Electronic transport in suspended rhombohedral few-layer graphene and 1T-TaS_2

Noelia Fernandez

SIGILL. UNIVERSITAT. LUDOVIC. MAXIM.

München 2023

Electronic transport in suspended rhombohedral few-layer graphene and 1T-TaS_2

Noelia Fernandez

Dissertation
der Fakultät für Physik
der Ludwig-Maximilians-Universität
München

vorgelegt von
Noelia Fernandez
aus Buenos Aires, Argentinien

München, den 20.01.2023

Erstgutachter: Prof. Dr. Thomas Weitz

Zweitgutachter: Prof. Dr. Alexander Urban

Tag der mündlichen Prüfung: 03.03.2023

Zusammenfassung

Durch Fortschritte in der experimentellen Messtechnik und der Probenherstellung ist eine präzise Kontrolle der elektronischen Eigenschaften von unterschiedlichen Materialien Realität geworden. In den vergangenen Jahren hat sich gezeigt, dass zweidimensionale Materialien eine ausgezeichnete experimentelle Plattform zur Untersuchung von Vielteilchen-Wechselwirkungsphysik und korrelierten Phänomenen darstellen. Die Vorhersage und anschließende Entdeckung von interaktionsgetriebenen gebrochenen Symmetriezuständen in mehrschichtigen Graphensystemen mit rhomboedrischer Stapelordnung motiviert die Realisierung von ultrareinen Proben dieses Materials, welche notwendig ist, um die Wechselwirkungsphysik innerhalb des Materials messbar zu machen.

Diese Dissertation präsentiert neue Ergebnisse zur Überwindung der Herausforderungen bei der Herstellung und Untersuchung von hochwertigen rhomboedrischen drei- und vierlagigen Graphenproben, die die experimentelle Beobachtung der Wechselwirkungsphysik innerhalb dieser Materialien ermöglichen. Das Graphen wird dabei in einer brückenartigen Struktur, die von zwei elektronischen Kontakten getragen wird, aufgehängt. Oberhalb und unterhalb werden Gate-Elektroden platziert. In dieser Probenkonfiguration kann das Graphen in situ auf höchste Qualität gereinigt werden. Außerdem findet im Vergleich zu anderen Probenkonfigurationen ein reduziertes Screening von Coulomb-Wechselwirkungen statt, was die Beobachtung von Wechselwirkungseffekten auf einer niedrigen Energiebandskala begünstigt. Mittels elektronischer und magnetischer Transportmessungen bei mK-Temperaturen werden die mehrschichtigen Graphenproben als Funktion der Ladungsträgerdichte, des äußeren elektrischen Feldes und des Magnetfeldes, welches sowohl senkrecht als auch parallel zur Probe ausgerichtet wird, untersucht.

Die Ergebnisse der Experimente mit drei- und vierschichtigem rhomboedrischem Graphen im Rahmen dieser Dissertation zeigen, dass in diesen Systemen isolierende Phasen spontan durch Wechselwirkungseffekte entstehen können. Diese wurden in zweilagigem Graphen bereits ausführlich untersucht und für mehrlagige Graphenlagen theoretisch vorhergesagt. Des Weiteren wurden weitere, nicht vorhergesagte, korrelierte Phänomene entdeckt. Beispielsweise wird in dieser Arbeit der Nachweis für magnetische Zustände in dreischichtigem ABC-Graphen erbracht, deren Abstimmbarkeit mit dem Ladungsträgertyp durch Anlegen eines Magnetfeldes in der Ebene verbessert wird. Darüber hinaus wurden auch in vierlagigen Graphenproben neuartige Zustände entdeckt, die von der Stärke eines angelegten Magnetfeldes abhängen. Außerdem wurde ein hysteretisches Verhalten bei der Messung von Quanten-Hall-Zuständen nachgewiesen.

Neben dreilagigem und vierlagigem rhomboedrischen Graphen wurde das Übergangsmetalldichalkogenid 1T-TaS_2 mit einem neuartigen experimentellen Ansatz untersucht. Die Realisierung von Proben für die gleichzeitige Untersuchung der elektrischen und strukturellen Aspekte im Zusammenhang mit einem Ladungsdichtewellen (CDW)-Phasenschalter im Material wird präsentiert. Dazu werden konventionell exfolierte 1T-TaS_2 Proben mit elektrischen Kontakten auf einer Transmissionselektronenmikroskopie (TEM)-Membran als Substrat hergestellt. Mit Hilfe von Beugungsmessungen sowie Hell- und Dunkelfeld-TEM-Bildgebung wird der strukturelle Charakter der CDW-Phasenübergänge nachvollzogen. Übergänge zwischen gleichartigen (C), fast gleichartigen (NC) und inkommensurierten (IC) CDW-Phasen in 1T-TaS_2 werden mit temperaturabhängigen und DC-vorspannungsgesteuerten Messungen an den hergestellten Proben untersucht. Der hier vorgestellte experimentelle Ansatz bietet neue Einblicke in die strukturellen Komponenten, die mit einem NC-/IC-CDW-Phasenübergang in 1T-TaS2 verbunden sind, indem er diesen im realen Raum abbildet, während der Übergang durch Anlegen einer Gleichspannung an die Probe ausgelöst wird. Darüber hinaus werden Signaturen eines Stabilisierungsmechanismus der C-CDW-Phase beim Anlegen einer DC-Vorspannung gezeigt, wenn das System sich an den temperaturgesteuerten Übergangspunkt zwischen dem NC-/C-CDW-Phasen befindet. Die hier vorgestellten Ergebnisse tragen zum grundlegenden Verständnis des Phasendiagramms von 1T-TaS_2 und der zugrunde liegenden Mechanismen seiner CDW-Phasenübergänge bei.

Abstract

With the advances of experimental and sample fabrication techniques, an outstanding control of the electronic properties of a material has become a reality. In the past years, two-dimensional materials have been demonstrated to constitute an exceptional experimental platform to investigate many-body interaction physics and correlated phenomena. The prediction and subsequent discovery of interaction-driven broken symmetry states in multilayer graphene systems with rhombohedral stacking order motivates the realization of ultraclean samples of this material, which is necessary to reveal its interaction physics.

This thesis presents novel results on overcoming the challenges in fabrication and investigation of rhombohedral few-layer graphene devices, in a platform that allows the experimental observation of interaction physics within the material. The platform consists of a sample configuration in which the graphene is suspended in a bridge-like structure supported by two electronic contacts, while placed in between a top and a bottom gate electrode. In such devices, graphene as well as few-layer graphene can be cleaned in-situ to the highest quality and is embedded in a platform with reduced screening of Coulomb interactions, which favours the observation of interaction effects at a low energy band scale. By means of electronic transport and magneto transport measurements at mK-temperatures, the few-layer graphene samples are studied with independent tunability of the displacement field and charge carrier density of the systems, under application of out of plane as well as in plane magnetic fields.

The outcomes of the experiments with few-layer rhombohedral graphene within this thesis reveal the presence of the interaction effect induced spontaneously gapped phase in the systems, which is predicted to be universal for rhombohedral graphene with more than two layers. In addition, further interaction phenomena which have not been revealed until now are brought to light. This thesis provides evidence for charge carrier density-tunable magnetic states in ABC trilayer graphene, whose tunability becomes enhanced upon application of an in-plane magnetic field. Additionally, quantum transport fingerprints of tetralayer ABCA reveal novel magnetic field tunable states in tetralayer graphene samples. Last but not least, a hysteretic behaviour when crossing quantum Hall conductance plateaus is revealed to be markedly present in the suspended samples.

Besides trilayer and tetralayer rhombohedral graphene, the transition-metal dichalcogenide 1T-TaS_2 has been studied by employing a novel experimental approach. The fabrication of samples for the simultaneous study of the electrical and structural aspects associated with a charge-density wave (CDW) phase switch in the material is presented.

To this aim, conventionally exfoliated 1T-TaS$_2$ samples with electrical contacts are fabricated with a Transmission Electron Microscopy (TEM) membrane as a substrate. By means of diffraction measurements as well as bright and dark-field TEM imaging, the structural character of the CDW phase transitions is followed. Moreover, transitions between commensurate (C), nearly-commensurate (NC) and incommensurate (IC) CDW phases in 1T-TaS$_2$ are investigated using temperature dependent and DC bias controlled measurements. The experimental approach presented here provides novel insights into the structural components associated with a NC-/IC-CDW phase transition within 1T-TaS$_2$ by imaging it in real space, while triggering the transition by applying DC voltage to the sample. Furthermore, signatures of a stabilization mechanism of the C-CDW phase upon application of a DC bias, when the system is at the temperature-driven transition points between the NC-/C-CDW phase switch, are revealed. The findings presented within this thesis contribute to the fundamental understanding of the phase diagram of 1T-TaS$_2$ and the underlying mechanisms of its CDW phase transitions.

Contents

Chapter 1

Introduction

For many years it was thought that a purely two-dimensional (2D) material was impossible to exist isolated in a laboratory [1]. With the first isolation of graphene in 2004 [2], this belief encountered an end. Shortly after, a broad range of 2D materials have been discovered and synthesized [3, 4] and a new field of research rapidly facilitated a wide range of applications. For instance, in flexible electronics [5–7], field effect transistors [8, 9], photonics and optoelectronics [10–12], spintronics [13–15] and energy storage [16, 17]. Because of their wide range of material properties, flexibility for device fabrication and the ability to host exotic states of quantum matter, 2D materials have been spotted as promising platforms for quantum-dot qubits, single photon emitters, superconducting qubits and topological quantum computing elements [18]. The experimental realization of 2D crystals also had an impact on the approach of several topics in fundamental physics. Graphene is an example of great relevance in this regard. Since quasiparticles in graphene can be described by a Dirac-type Hamiltonian [19], its particular properties are considered a bridge between quantum electrodynamics and condensed matter physics [1, 20].

Among the possibilities that 2D systems offer as an experimental platform to explore fundamental physics, many-body electron phenomena have recently been at the core of attention. With the advance of experimental and sample fabrication techniques, an outstanding control of the electronic properties of a material is nowadays achievable. For example, 2D van der Waals heterostructures with an interlayer twist angle have been demonstrated as a platform for observing correlated physics, both in graphene [21–23] and transition-metal dichalcogenide (TMD) structures [24–27]. These systems attribute in great part their underlying physics to the presence of a Moiré pattern in real space [28, 29]. This is because such patterns lead to an additional long-range periodicity in real space and therefore to a pronounced folding of bands in reciprocal space, which gives rise to flat bands at low energy, leading to a large (even diverging) density of states often referred to as a van Hove singularity [28–31]. Here, the presence of flat bands is the key to a low kinetic energy of the quasiparticles in the system, leading to a large ratio of Coulomb to kinetic energy and a high probability of strong electron correlations. From such arguments, an interesting question arises: are there 2D systems that intrinsically host sufficiently flat bands to observe correlated electron physics at accessible temperatures, without the need of Moiré patterns? The answer might come as a surprise, when finding that simple rhombohedral graphene with more than two layers offers a naturally occurring platform in which the low-energy band structure has a sharply peaked density of states with dispersion relation $E(k) \propto k^N$, where N is the number of layers of graphene, resulting in low energy flat bands which become increasingly flat for larger N [32–36]. While it is challenging to isolate rhombohedral graphene of any thickness, as it is less energetically favourable than its counterpart Bernal stacked graphene [19], efforts in isolating the rhombohedral stacking order have revealed a variety of correlation physics as well as the presence of flat bands in the system [29, 37–41], emphasizing the significance of this experimental platform.

The presence of interaction-driven broken symmetry states in rhombohedral few-layer graphene has been theoretically predicted [33, 42, 43] and later experimentally discovered [44–46] to be characterized by spin- and valley dependent spontaneous layer polarization. Due to their susceptibility to host a variety of broken chiral symmetry states, the study of few-layer rhombohedral graphene led to a growing interest in identifying possible many-body ground states of these systems [34]. However, samples have to be extremely clean to reveal its interaction physics, imposing additional challenges to the fabrication process. The work within this thesis overcomes many of the challenges in the fabrication and investigation of high quality rhombohedral few-layer graphene, in a platform that favours a regime which allows accessing interaction physics. The samples are fabricated in a dual-gated free-standing device configuration [45, 47], in which few-layer graphene can be cleaned in-situ to the highest quality [48]. Moreover, it is embedded in an environment with reduced screening of Coulomb interactions, which facilitates the observation of many-body interaction effects at the low energy band scale [49].

By means of magneto and electronic transport measurements at mK-temperatures, this thesis provides evidence for the existence of magnetic states in rhombohedral (ABC) trilayer graphene close to charge neutrality, which can be tuned by the charge carrier density of the system. Moreover, the fabrication of one of the most challenging rhombohedral few-layer graphene samples, tetralayer graphene, is achieved, in which not only the Bernal (ABAB) and rhombohedral (ABCA) stacking orders are present, but which can also host a hybrid stacking (ABCB) with completely different electronic properties. The investigation of this sample provides quantum transport fingerprints of tetralayer rhombohedral graphene as well as evidence of layer coherent and layer polarized states at finite magnetic fields. The presence of magnetic field driven transitions is also notable in this system. Perhaps the most intriguing result, a hysteresis behaviour when crossing quantum Hall conductance plateaus by scanning the charge carrier density, is revealed. The obtained results not only demonstrate the presence of interaction physics within the investigated samples, but also contributes towards the identification of the ground state of rhombohedral few-layer graphene systems, which is still debated. In addition, the insights provided here could help to elucidate the nature of correlation effects within the quantum Hall effect regime in rhombohedral graphene systems.

Although the main focus of this thesis is centred in investigating interaction physics in rhombohedral few-layer graphene, the transport physics of the 2D TMD 1T-TaS$_2$ has been intensively studied as well. Interestingly, 1T-TaS$_2$ hosts charge-ordered phases, with both Peierls and Mott physics [50] involved in some of its CDW states. Here, a fabrication pathway for using this material in a configuration that will reveal its more intriguing physics in a novel experimental approach is presented. These efforts intend to contribute to the complete understanding of the phase diagram of 1T-TaS$_2$, one of the richest among TMDs [51, 52], as well as the nature of its phase transitions. The experiments presented here follow a similar line of thought for studying the material reported by other groups, which study the effect of current-voltage measurements in 1T-TaS$_2$ flakes [53, 54]. The transitions between C-, NC- and IC-CDW phases are investigated under temperature dependent as well as DC bias controlled measurements. The structural components of a NC-/IC-CDW phase switch are followed in real space while applying a DC bias to the sample. This way, the structural change in the material associated with the phase switch on an electrically connected 1T-TaS$_2$ sample is revealed. Furthermore, an unexpected behaviour of the system at the transition points between the C-/NC-CDW phase switch is discovered, which reveals a stabilization of the C-CDW phase upon application of a DC bias. The findings within this work bring novel results relevant for understanding the 1T-TaS$_2$ CDW phase transition mechanisms. The experiments performed as part of this thesis with nano-thick 1T-TaS$_2$ connect the realm of electrical measurements with the structural change visualization of a CDW phase switch, providing detailed insights into the phase transitions of this material.

This thesis is composed of experimental work with two distinct 2D systems: rhombohedral few-layer graphene and the TMD 1T-TaS$_2$. The theory background which is essential for understanding the experimental results presented for each of the 2D materials is outlined in chapter 2. Chapter 3 is dedicated to describe the details on sample fabrication and experimental approaches to study the respective systems. Chapters 4, 5 and 6 are structured in such a way that distinct results of each investigated material are discussed in an independent manner, giving a short introduction to the topic, summarizing the experimental methods and discussing the respective results. An extended description of the content of each of the chapters of this thesis is outlined next.

In chapter 2, the theoretical foundations of this thesis are presented. First, the structure and electronic properties of the 2D layered materials investigated within this thesis, are introduced. The chapter begins with a description of the properties of graphene, followed by bilayer graphene and finally, trilayer and tetralayer graphene. Last but not least, 1T-TaS$_2$ is discussed. After introducing the basic structural and electronic properties in section 2.1, the most relevant concepts of the investigated phenomena in each of the systems are given. Section 2.2 begins with a description of the transport properties in few-layer graphene systems, starting with a general overview of the quantum Hall effect and Landau level quantization and then discussing these in rhombohedral stacked few-layer graphene. Next, some definitions with regard to quantum and classical phase transitions are given. At last, the topic of broken symmetry states in chiral graphene systems is discussed. In section 2.3, the underlying mechanisms of CDW formation are given from a general standpoint and concluded with a discussion of the 1T-TaS$_2$ case.

Chapter 3 presents the experimental methods to fabricate and characterize the samples investigated within this thesis. In section 3.1, a detailed description of the fabrication of high-quality rhombohedral graphene samples is given. Firstly, the methods to obtain, identify and isolate few-layer graphene with rhombohedral stacking order are outlined. Subsequently, the design and fabrication techniques of dual-gated suspended devices with this material are presented. In section 3.2, the details for fabricating samples with 1T-TaS$_2$ on a TEM membrane as a substrate are given, as well as the methods for electrical and structural characterization of CDW phases in the investigated samples. At the end of each section, the measuring setups and experimental approaches used to investigate the samples are given.

In chapter 4, results from the experiments with free-standing rhombohedral trilayer graphene are presented. Here, the focus is put on searching for correlated phases of the system. The discussion is centred on transport features observed at low charge carrier densities and low out of plane magnetic fields, although some higher magnetic field aspects are also discussed. Following an approach of independently scanning parameters of the system and investigating the influence of the application of a DC current bias, out of plane displacement field and magnetic fields, the study reveals possible spin-ordered magnetic states near charge neutrality. Furthermore, the discovery of a hysteretic behaviour around charge neutrality when applying an in-plane magnetic field provides evidence of magnetic states in the system which are tunable by changing the charge carrier type.

Chapter 5 presents the outcome from investigating tetralayer free-standing graphene with ABCA stacking order. The results shed light on the electronic and magneto transport fingerprints of naturally occurring rhombohedral tetralayer graphene. The experiments reveal signatures of magnetic field tunability of the transitions between quantum Hall effect states in the system. The discussion within this chapter is focused on the observation of layer coherent and layer polarized states at finite magnetic fields within rhombohedral tetralayer graphene, as well as a hysteretic behaviour when crossing quantum Hall conductance plateaus by scanning the charge carrier density of the system, which has not been shown until now.

In chapter 6, the structural and electrical characterization of CDW phases in 1T-TaS$_2$ flakes is presented. Novel results of tracing a structural CDW phase transition within 1T-TaS$_2$ in real space by means of dark-field TEM imaging, while triggering it by electrical means, are discussed. Moreover, signatures of a stabilization mechanism towards the C-CDW phase upon application of a DC bias when the system is at the transition points between the NC-/C-CDW phase switch are revealed and discussed with detail. To conclude, a summary and main conclusions of the work within this thesis, together with an outlook on future possible research directions are given in chapter 7. Besides, an appendix of the thesis is dedicated to two additional fabricated samples, namely, suspended graphene Josephson junctions and a 1T-TaS$_2$ electronic circuit with coplanar striplines and a photoconductive switch. Here, details on their fabrication as well as some outcome results relevant for future research on the respective topics are provided.

Chapter 2

Theoretical foundations

This chapter introduces the fundamental theoretical concepts and definitions which are most relevant for understanding the experimental results discussed within this thesis. First, section 2.1 provodes a brief introduction to the topic of 2D layered materials, together with a more in depth description of the structure and electronic properties of the 2D materials which are particularly relevant for this thesis: graphene, bilayer graphene, tri- and tetralayer graphene and, finally, the TMD 1T-TaS$_2$. In section 2.2, the focus is put on few-layer rhombohedral graphene to give an overview of the fundamentals of the electronic transport in such systems. The section begins with a general introduction about the quantum Hall effect (QHE), followed by a description of the Landau level (LL) quantization in 2D electron systems, to continue with the case of few-layer graphene with rhombohedral stacking order. This is followed by a discussion to define some concepts about the physics of classical and quantum phase transitions, to conclude with an introduction to the topic of broken symmetry states in rhombohedral graphene systems. Here, emphasis is put on the influence of electron-electron interactions on the electronic states and transport properties of few-layer graphene. Finally, in section 2.3, an introduction into CDW physics as well as the formation of CDW phases in 1T-TaS$_2$, is given.

2.1 Structure and electronic properties of selected 2D layered materials

Since the isolation of graphene, a single atomic layer of graphite [2] and the revelation of its fascinating properties [2, 19, 55], a rise in the field of 2D materials began [56]. Shortly after, many different 2D materials have been discovered and synthesized [3, 4] and the field of research rapidly broadcasted into a wide range of applications, such as flexible electronics [5–7], field effect transistors [8, 9], photonics and optoelectronics [10–12], spintronics [13–15] and energy storage [16,17], just to name a few [4,57]. A 2D material is defined as a crystalline material with a single layer or few-layers of atoms, in which the in-plane interatomic interactions are much stronger than those on the stacking direction. These type of materials show extended crystalline planar structures held together by strong in-plane covalent bonds and weak out-of-plane van der Waals forces. Consequently, the individual layers of the material are easily separated without structural damage, allowing the extraction of stable single and few layers of material by an exfoliation process [57]. Within this thesis, the 2D layered materials experimentally studied are few-layer rhombohedral graphene and the TMD 1T-TaS$_2$. This section provides a description of the most relevant aspects of their atomic structure as well as electronic properties.

2.1.1 Graphene

Graphene is a 2D material which consists of a single layer of carbon atoms arranged in a hexagonal lattice [55]. Its carbon atoms are linked between nearest neighbours by strong planar covalent σ-bonds, responsible for the outstanding mechanical strength of the graphene sheets [19]. The σ-bonds emerge from an sp^2 hybridization between one s- and two p-orbitals of neighbouring carbon atoms. The remaining electrons occupy p_z-orbitals perpendicular to the carbon plane forming π-bonds, which host delocalized electrons and shape the electronic properties of graphene [19, 58]. Until its first isolation in 2004 [2], graphene was thought to be an impossible material [59]. Despite that, it has been long ago a subject of theoretical study, being its unusual semi metallic behaviour already shown in the context of graphite studies in 1946 [60]. An interesting aspect of the graphene problem is that its low-energy excitations are massless Dirac fermions and, in neutral graphene, the chemical potential crosses exactly the so-called Dirac point. Moreover, thanks to its characteristic low-energy dispersion relation, graphene constitutes a platform for studying the physics of quantum electrodynamics in a solid state system [19]. The electronic structure of graphene from a simple nearest-neighbour, tight-binding approximation, takes as a starting point an hexagonal lattice with two atoms per unit cell, divided into two inequivalent triangular sublattices A and B [55, 58, 60], as represented in Figure 2.1 a). Figure 2.1 b) depicts the first Brillouin Zone with the highly symmetric points Γ, M, K and K', where K and K' belong to different sublattices and, therefore, are inequivalent. The tight-binding Hamiltonian for graphene, considering that electrons can hop to both nearest- and next-nearest-neighbour atoms reads [19]

$$\mathcal{H} = -\gamma_0 \sum_{<i,j>,\sigma} \left(a^\dagger_{\sigma,i} b_{\sigma,j} + H.c. \right) - \gamma'_0 \sum_{<i,j>,\sigma} \left(a^\dagger_{\sigma,i} a_{\sigma,j} + b^\dagger_{\sigma,i} b_{\sigma,j} + H.c. \right), \tag{2.1}$$

in units of $\hbar = 1$, where $a_{\sigma,i}$ ($a^\dagger_{\sigma,i}$) is the anihilation (creation) operator for an electron with spin σ ($\sigma = \uparrow, \downarrow$) on the $\mathbf{R}_i$ site of the sublattice A (analoge definition for the sublattice B), $\gamma_0 = 2.8$ eV is the nearest-neighbor hopping energy between different sublattices and γ'_0 is the next nearest-neighbor hopping energy in the same sublattice. The energy bands derived from this Hamiltonian result [60]

$$E_\pm(k) = \pm\gamma_0 \sqrt{3 + f(k)} - \gamma'_0 f(k), \tag{2.2}$$

with ± refering to the conduction and valence band and $f(k)$ defined as

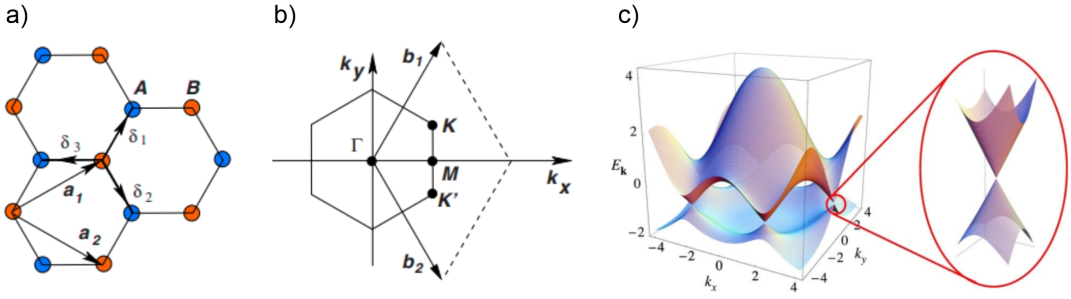

Figure 2.1: Crystal and electronic band structure of graphene, a) Hexagonal lattice of graphene with triangular sublattices A and B. The unit cell vectors are given by a_1 and a_2 and the nearest-neighbour vectors by $\delta_{1,2,3}$. b) Reciprocal lattice in the first Brillouin Zone with vectors given by b_1 and b_2. Dirac cones appear at the K and K' points. c) Electronic dispersion in the honeycomb lattice derived from the tight-binding approximation with $\gamma_0 = 2.7$ meV and $\gamma_0' = -0.54$ meV. Zoom-in of the energy bands close to one of the Dirac points. Image adapted from [19].

$$f(k) = 2\cos\left(\sqrt{3}k_y a\right) + 4\cos\left(\frac{\sqrt{3}}{2}k_y a\right)\cos\left(\frac{3}{2}k_x a\right). \tag{2.3}$$

Figure 2.1 c) shows the band structure for finite values of γ_0 and γ_0', this is, when nearest neighbour hopping is present. In the first Brilloun zone, the valence band and the conduction band touch each other at the K and K' points, forming linear low-energy bands (see zoomed in region in Figure 2.1 c)). This results from taking $\delta k = k - K$ as the displacement of the wave vector k from one corner of the hexagonal lattice at a wave vector K, with $\delta k a \ll 1$, which brings the dispersion relation

$$E_{\pm}(\delta k) = k v_F \mid \delta k \mid, \tag{2.4}$$

where $v_F = \frac{1}{2}\sqrt{3}\gamma_0 a/\hbar \approx 10^6$ m/s is the Fermi velocity [61]. In the low-energy regime, the electronic states have two components belonging to the two different sublattices A and B of graphene and, consequently, quasi-particles in graphene are described by a massless Dirac-like Hamiltonian, for which the low-energy excitations are massless, chiral, Dirac fermions and the speed of light is replaced by the Fermi velocity v_F [19]. The massless carriers in graphene are thus represented by a two-component electron wavefunction which obeys the 2D-Dirac equation [19, 61–63]

$$\pm v_F \begin{pmatrix} 0 & p_x - ip_y \\ p_x + ip_y & 0 \end{pmatrix} \begin{pmatrix} \Psi_A(r) \\ \Psi_B(r) \end{pmatrix} = E \begin{pmatrix} \Psi_A(r) \\ \Psi_B(r) \end{pmatrix}, \tag{2.5}$$

where ± refers to the conduction and valence bands, $\boldsymbol{p} = (p_x, p_y) = -i\hbar(\partial/\partial_x, \partial/\partial_y)$ is the momentum in the xy plane and $\Psi = (\Psi_A(r), \Psi_B(r))$ is a spinor with components associated with the sublatices A and B. From the massless Dirac-like Hamiltonian written as $H_K = v_F \boldsymbol{\sigma} \cdot \boldsymbol{p} = -i\hbar v_F \boldsymbol{\sigma} \cdot \boldsymbol{\nabla}$ for the momentum around the K point and $H_{K'} = H_K^T$

around the K' point, where $\boldsymbol{\sigma} = (\sigma_x, \sigma_y)$ is the vector of Pauli matrices, the wavefunctions in momentum space have the form [19, 62]

$$\Psi_{\pm,K} = \frac{1}{\sqrt{2}} \begin{pmatrix} e^{-i\phi/2} \\ \pm e^{i\phi/2} \end{pmatrix} \qquad \Psi_{\pm,K'} = \frac{1}{\sqrt{2}} \begin{pmatrix} e^{i\phi/2} \\ \pm e^{-i\phi/2} \end{pmatrix}, \tag{2.6}$$

where ϕ is the polar angle of the quasi-momentum $\boldsymbol{p}$ and ± refers to the conduction and valence bands.

It is important to note that the wave functions of equation (2.6) are related by time reversal symmetry and, if the phase is rotated by 2π, the wave function changes sign indicating a phase shift of π [19]. This change of phase under rotation is commonly referred in the literature as the Berry phase [64]. Additional to the spin, the charge carriers in graphene have a so-called valley or pseudospin degree of freedom, associated to the sublattices A and B and, specifically, to the K and K' points (Dirac points). Looking at the projection of the momentum operator along the pseudospin direction in a band, the later remains the same for both carrier types, while the direction of motion for electrons is opposite to the direction of motion for holes. This property, which holds only for the states of the system close to the Dirac points, is defined in the literature as the helicity or chirality of the states [19].

2.1.2 Bilayer graphene

Bilayer graphene consists of two coupled graphene monolayers which, in the most energetically stable configuration [19], are shifted with respect to each other such that one atom of the top layer is directly above the centre of the honeycomb of the bottom layer. This type of bilayer graphene crystal lattice, commonly referred in the literature as Bernal or AB-stacked bilayer graphene, contains four atoms per unit cell and is symmetric with respect to spatial inversion symmetry [65]. Figure 2.2 a) and b) shows a representation of the crystal lattice of AB-stacked bilayer graphene, with indexes A1, B1 for the lower layer and A2, B2 for the upper layer. Same as in monolayer, intrinsic bilayer graphene has no band gap between its conduction and valence bands, however, the low-energy dispersion relation is parabolic instead of linear and the charge carriers are therefore massive chiral quasiparticles [65, 66]. In the tight-binding description of bilayer graphene, not only intralayer, but also interlayer hopping parameters need to be considered. Following the notation of the Slonczewski-Weiss-McClure (SWM) model for bulk graphite [67, 68], the parameter γ_1 depicts the coupling between pairs of orbitals on the dimer sites B1 and A2 (nearest neighbour inter-layer coupling), γ_3 describes the interlayer coupling between non-dimer orbitals A1 and B2, while γ_4 the interlayer coupling between dimer and non-dimer orbitals A1 and A2 or B1 and B2 (both next nearest neighbour inter-layer coupling) and γ_0 represents the intralayer coupling (as for monolayer graphene) within a layer, i.e. between A1 and B1 sites as well as between A2 and B2 sites [19, 65]. A representation of all hopping parameters in AB-stacked bilayer graphene is shown in Figure 2.2 b).

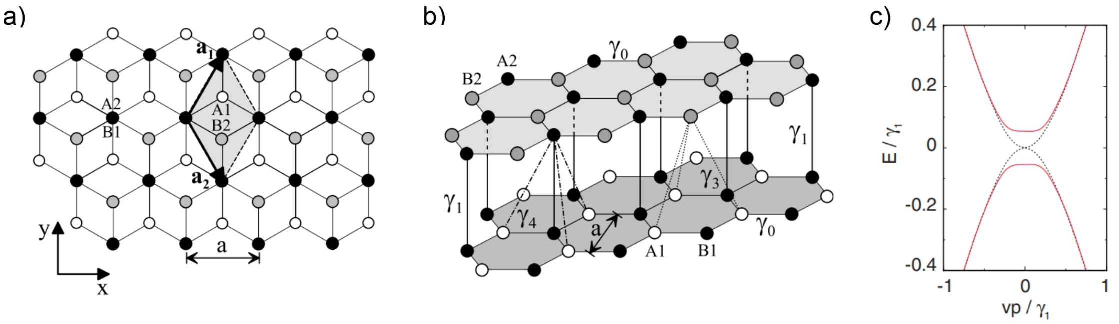

Figure 2.2: Crystal and band structure of bilayer graphene. a) Top view representation of the relative position of two graphene lattices conforming bilayer graphene. The shaded (grey) area encloses the conventional unit cell. b) Side view representation of the bilayer graphene crystal structure. Atoms from the sublattices A1 and B1 on the lower layer are shown as white and black circles, while from sublattices A2 and B2 on the upper layer are black and grey. γ_i with $i = \{0, 1, 2, 3, 4\}$ indicates the different hopping parameters. Image adapted from [65]. c) Low energy band structure of AB-stacked bilayer graphene at a finite (solid, red) and zero (dotted, black) external electric field. Image adapted from [36]

The tight-binding Hamiltonian for bilayer graphene reads [19]

$$\begin{aligned}\mathcal{H}_2 = &-\gamma_0 \sum_{<i,j>,m,\sigma} \left(a^\dagger_{m,i,\sigma} b_{m,j,\sigma} + H.c.\right) - \gamma_1 \sum_{j,\sigma} \left(a^\dagger_{1,j,\sigma} a_{2,j,\sigma} + H.c.\right) \\ &- \gamma_3 \sum_{j,\sigma} \left(b^\dagger_{1,j,\sigma} b_{2,j,\sigma} + H.c.\right) - \gamma_4 \sum_{j,\sigma} \left(a^\dagger_{1,j,\sigma} b_{2,j,\sigma} + a^\dagger_{2,j,\sigma} b_{1,j,\sigma} + H.c.\right),\end{aligned} \tag{2.7}$$

where $a_{m,i,\sigma}$ ($b_{m,i,\sigma}$) annihilates an electron with spin σ on sublattice A (B) within the layer $m = \{1, 2\}$ at the site $\mathbf{R}_i$. Thus, quasi-particles in bilayer graphene are described by a four-component spinor, with components for each of the lattices A and B and layer indexes $i = \{1, 2\}$ [19]. Same as in monolayer graphene, the electronic properties at low energies (i.e., when $\mid E \mid \ll \gamma_1$) are well described by taking only nearest neighbour couplings into account. Thus, neglecting γ_3 and γ_4 as well as higher order perturbation terms of the effective Hamiltonian

$$H_2 = -\frac{1}{2m} \begin{pmatrix} 0 & (p_x - ip_y)^2 \\ (p_x + ip_y)^2 & 0 \end{pmatrix}. \tag{2.8}$$

This resembles the Dirac-like Hamiltonian of monolayer graphene in Equation 2.5, but with a quadratic term in momentum instead of linear. As a consequence, the solutions of the bilayer graphene Hamiltonian are massive chiral electrons [65, 66, 69], with parabolic dispersion $E = \pm p^2/2m$, where $m = \gamma_1/2v^2$. The density of states is $m/(2\pi\hbar^2)$ per spin and per valley and the Fermi velocity $v_F = p_F/m$ is momentum dependent [65]. To illustrate the chiral nature of the charge carriers, the Hamiltonian in equation (2.8) may be re-written as $H_2 = (p^2/2m)\boldsymbol{\sigma} \cdot \hat{\boldsymbol{n}}$, where $\boldsymbol{\sigma} = (\sigma_x, \sigma_y, \sigma_z)$ are the Pauli matrices which act on the pseudo-spin degree of freedom and $\hat{n} = -(\cos 2\varphi, \pm \sin 2\varphi, 0)$ is a unit vector [65]. This results in the expression

$$H_2 = -\frac{(vp)^2}{\gamma_1}\left[\cos(2\phi_{\boldsymbol{p}})\sigma_x + \sin(2\phi_{\boldsymbol{p}})\sigma_y\right], \tag{2.9}$$

where $\cos(\phi_{\boldsymbol{p}}) = \pm p_x/p$ and $\sin(\phi_{\boldsymbol{p}}) = p_y/p$ with ± indicating the valeys K and K', respectively, and $v = \sqrt{3}a\gamma_0/2\hbar$ is an effective velocity. Markedly, for chiral quasiparticles in bilayer graphene, an adiabatic propagation along a closed orbit will result in a Berry phase change of 2π [66, 69].

It is important to remind that the quadratic dispersion relation described in the previous paragraphs and illustrated in Figure 2.2 c) (see dashed black curve), which has circular iso-energetic lines (i.e., circular Fermi lines around the valley points), is only valid at low energies and near the K and K' points, when $pa/\hbar \ll 1$. This regime is the investigated through the suspended graphene experiments within this thesis. It is still worth mentioning that, for higher energies and a momentum far from the valleys, a triangular perturbation of the iso-energetic lines, known as trigonal warping, occurs [65, 70, 71]. One source of trigonal warping is the momentum dependence of the energy bands derived from the tight-binding model, when considering that the band structure follows the symmetry of the crystal lattice [65, 72]. In bilayer graphene as well as in few-layer graphene and bulk graphite, a second source of trigonal warping is originated from the interlayer coupling parameter γ_3. Moreover, the interlayer coupling γ_4, between a non-dimer and a dimer site, produces an electron-hole asymmetry in the band structure [65]. Moreover, the inter-layer asymmetry, which accounts a difference in the on-site energies of the orbitals on the two layers, creates a gap between the conduction and valence bands. Since the gap between the conduction and valence bands arises from a layer asymmetry, contrary to monolayer graphene, it is possible to tune the magnitude of the gap by using external gates [19, 65, 71]. In Figure 2.2 c), the modification of the band structure of bilayer graphene in the presence of a finite external electric field is shown with a solid red line.

2.1.3 Tri- and tetra-layer rhombohedral graphene

In stacks with more than one graphene layer, it is energetically favourable for the atoms in the sublattices of each layer to arrange such that one of the atoms in one of the planes is at the centre of an hexagon from the lattice in the other plane [19, 35, 73], as illustrated in Figure 2.3 a). For more than two graphene layers, the three-dimensional representation of the honeycomb lattice onto the xy plane implies three distinct projections (A, B and C) and the stacking ordering acquires 2^{N-2} different N-layer stacking sequences [35]. A variety of stacking orders is possible because of the weak van der Waals forces between graphene layers. For a bigger number of layers, the sequences ABABA... (Bernal) are the most commonly found in nature, the sequences ABCABC... (rhombohedral) are found in a smaller fraction and other mixed stacking orders (e.g. ABCBA...) can also occur, although more rarely [19, 36, 73, 74]. Figures 2.3 b) and c) show a representation of all possible distinct stacks with $N = 3$ and $N = 4$ graphene layers. Noteworthy, both

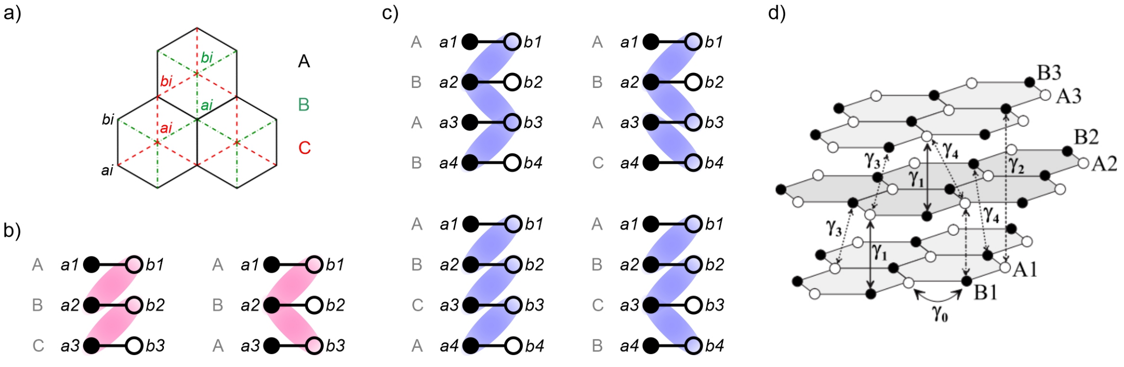

Figure 2.3: Unit cell and crystal structure of tri and tetralayer graphene. a) Sketch of the three non-equivalent orientations of graphene layers with respect to each other. Adapted from [19]. b) Stacking sequences for $N = 3$ and c) $N = 4$ layer graphene stacks. The coloured-shaded areas indicate the interlayer bonds with vertical γ_1 hopping parameter (strongest sublattice linkage in the SWM model). Adapted from [35]. d) Scheme of an ABC-stacked trilayer lattice showing the most relevant SWM model coupling parameters, γ_0 to γ_4. Adapted from [75]

monolayer and bilayer graphene can be viewed as either rhombohedral (ABC) or Bernal (AB) stacked few-layers with $N = 1$ and $N = 2$, respectively.

In multilayer graphene, the low energy electronic structure strongly depends on the stacking order of the individual layers as well as the number of layers, which has an impact in the observed electrical, optical and thermal properties [60, 67, 68, 73]. To begin with, rhombohedral multilayer graphene has a very different electronic structure from Bernal [36, 76]. For instance, the low-energy band structure for Bernal-stacked few-layer graphene consists of blocks of bilayer like and monolayer like bands [35, 36, 73, 75, 77] and the presence of an interlayer potential asymmetry produces hybridization (overlapping) of the bands [73, 75, 78]. In contrast, the low-energy bands of rhombohedral-stacked multilayers is given by the surface states localized at the outermost layers [73, 76] and the interlayer potential asymmetry opens an energy gap [73, 75, 76, 79] (see Figure 2.4). Importantly, the rhombohedral stacking order presents two low-energy sublattice sites localized in the outermost layers (A_1 and B_N) and the hopping between low-energy sites via high-energy states is an N-step process, leading to $\pm p^N$ dispersions in conduction and valence bands and a chirality related to a Berry phase $N\pi$. Moreover, as shown in Figure 2.4, the low-energy bands are increasingly flat for larger N, at least when weak remote hopping processes are neglected [34]. Because of these features, the electronic properties of N-layer rhombohedral graphene are well described by $\boldsymbol{k}\cdot\boldsymbol{p}$ band Hamiltonians [34, 65, 80]

$$H_N = -\frac{(vp)^N}{(\gamma_1)^{N-1}}\left[\cos(N\phi_{\boldsymbol{p}})\sigma_x + \sin(N\phi_{\boldsymbol{p}})\sigma_y\right], \tag{2.10}$$

where $\cos(\phi_{\boldsymbol{p}}) = \pm p_x/p$ and $\sin(\phi_{\boldsymbol{p}}) = p_y/p$, with ± addressing K and K' respectively and $v = \sqrt{3}a\gamma_0/2\hbar$ is the effective velocity. Note that the vector of Pauli matrices $\boldsymbol{\sigma}$ acts on the pseudospin degree of freedom, which addresses the two low-energy sublattices A_1 and B_N. As a consequence of the $\pm p^N$ dependence on the dispersion relations for the eigenvalues of

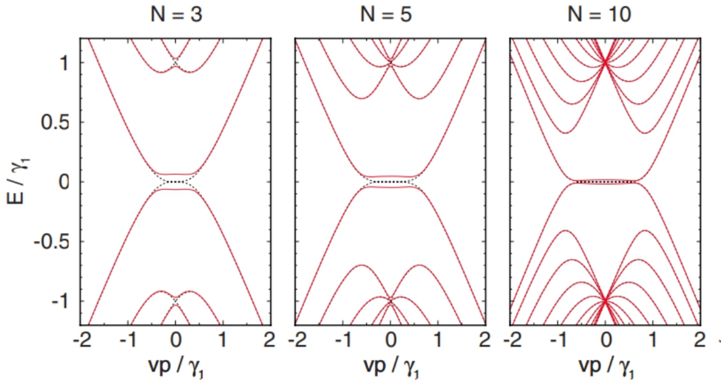

Figure 2.4: Low-energy band structure of multilayer rhombohedral graphene. Self-consistent band structures of rhombohedral graphene at a finite (solid) and zero (dotted) external electric field for $N = 3, 5$ and 10 layers. Image taken from [36]

the Hamiltonian in equation (2.10), the density of states at charge neutrality diverges, in contrast to monolayer ($N = 1$) and bilayer ($N = 2$) graphene, where the density of state at charge neutrality vanishes and remains finite, respectively [32, 81, 82]. As mentioned before, the wave function in a rhombohedral graphene stack is located on the upper and lower layers, and an electric field inducing a potential difference Δ will open a band gap [32, 40]. This can be modelled by adding the term $(\Delta/2)\sigma_z$ to the Hamiltonian in equation (2.10). Figure 2.4 a) shows the low energy band structure of rhombohedral few-layer graphene with $N = 3, 5$ and 10 under zero (dashed dotted line) and finite external electric fields (solid red line). Remarkably, the low energy bands become more and more flat with increasing layer number taking into account the interlayer electronic screening effects [36]. Moreover, in presence of an external electric field, an energy gap opens at low energy as in bilayer graphene. It has been shown from self-consistent calculations of the band structure of ACB multilayers [36], that the width of this gap becomes smaller for an increasing N, suggesting a stronger screening effect in larger stacks. Since the regime where trigonal warping dominates the physics of the system is not accessible by the experiments presented here, it will not be discussed with details. However, it is worth mentioning that, so far, only γ_0 and γ_1 are included in the discussion. When considering other hopping parameters, the surface flat bands acquire a finite bandwidth of the order of $2\gamma_4 4\gamma_1/\gamma_0$ as well as electron-hole asymmetry and trigonal warping due to γ_2 and γ_3 [40, 75]. In Section 2.2, electron-electron interaction effects at a low-energy band scale giving rise to non-trivial ground states of rhombohedral graphene are discussed.

2.1.4 The TMD 1T-TaS$_2$

TMDs are a class of 2D materials which consist of one layer of a transition metal atoms (such as Mo, W, or Ta) in between two layers of chalcogen atoms (like S or Se) [83]. They are layered materials with strong in-plane bonding and weak out-of-plane van der Waals interactions, which enables their exfoliation into 2D layers of single unit cell thickness [50, 84]. They exist in various structural phases characterized by different coordination

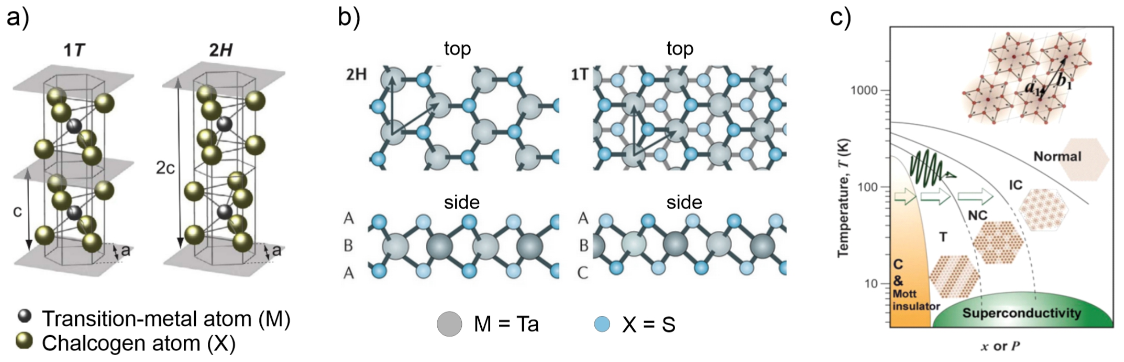

Figure 2.5: Crystal structure and structural phases of TMDs and generic phase diagram of the TMD 1T-TaS_2. a) Schematic of two structural polytypes of layered TMDs. In the 1T phase, the TMD atoms (M) are octahedrally coordinated by chalcogen atoms (X) and the thickness of the repeat unit in the c direction is one sandwich. In the 2H phase, the coordination is trigonal prismatic and the unit cell is two sandwiches thick. Image taken from [85]. b) Top and side views of the atomic structure of a single layer of TMD in the 1T and 2H phase, with labelling of the atoms exemplifying the TaS_2. Adapted from [83]. c) Phase diagram of 1T-TaS_2 under various physical conditions (temperature, doping x, or pressure P). Image adapted from [51]

spheres of the transition metal atoms, the most common being either a trigonal prismatic (2H) or an octahedral (1T) coordination of the metal atoms [83]. For multilayers and bulk samples, their structure is further defined by the stacking configuration of the individual layers and by possible distortions that lower the periodicity [83]. Figure 2.5 a) shows the basic undistorted TMD crystal structures of the 1T and 2H phases in the real space. In Figure 2.5 b), an equivalent description in terms of different stacking orders of the three atomic planes (chalcogen-metal-chalcogen, or, X-M-X) of the individual layers is represented. As indicated in the Figure, the 2H phases can be described as an ABA stacking order, where chalcogen atoms in different atomic planes and on the same relative position perpendicular to the layer are on top of each other. Besides, the 1T phases can be described as an ABC stacking, where no overlap of the atoms in different planes is found from a top view [83].

The band structure of many TMDs is similar in their general features, as shown by first principles and tight-binding approximations as well as by measurements with a variety of spectroscopy tools [1, 84, 86–88]. For this reason, taking into account some differences between them, they are separated into subgroups. As an example, MoX_2 and WX_2 are in general semiconducting while NbX_2 and TaX_2, metallic [86, 89–91], therefore they are grouped as such. Depending on the combination of transition metal and chalcogen elements as well as on their resulting crystal structure, the TMDs can have a broad range of electronic responses [1, 86–88, 90, 92] and, correspondingly, different applications. For example, the semiconducting phases are frequently employed for applications in photovoltaics, light-emitting diodes and field effect transistors [93–96]. Besides, metallic TMD phases have been demonstrated to exhibit exotic electronic excitations, leading to quantum spin Hall effects [97–99], CDW phases [85, 100], as well as significantly enhanced catalytic activity [101]. Worth mentioning, the TMD studied within this thesis, 1T-TaS_2, has one of the richests phase diagrams within its material class (Figure 2.5 c)), consituting a multitude of electronic responses and competing ground states under equilibrium conditions. Both a Mott state and various CDW phases have been found within this material [50,51,85,102,103], indicating that electron-phonon and electron-electron interactions are equally important for shaping its physics [50]. In addition, further nearby equilibrium states appear upon the application of external pressure or doping, both making the 1T-TaS$_2$ superconducting [51,52]. Even at ambient pressure a diversity of phases is present. As indicated in Figure 2.5 c), this includes a metallic phase (normal) at high temperatures, an IC-CDW phase below 550 K, a T phase which occurs only upon heating at ~280 K, a NC-CDW phase below 350 K and a C-CDW phase below 180 K [50]. The fundamental theory aspects about CDWs as well as a more in depth description of the charge-correlated and metastable phases in 1T-TaS$_2$, with focus on those explored within this thesis, are given in Section 2.3.

2.2 Transport in few-layer rhombohedral graphene

This section reviews the fundamental aspects about electronic transport in graphene and few-layer graphene with rhombohedral stacking order, which are relevant for the research on the present thesis. Both as motivation for the experiments and for the interpretation of the results. First, an introduction about the general aspects of the quantum regime of the Hall effect are given. Second, a more in depth explanation of this phenomena as well as the relevant definitions in terms of the LL quantization are given. Next, the expected LLs and conductance plateaus for the integer QHE, in particular, for the case of rhombohedral graphene systems, are discussed. To continue, a general overview about the physics of classical and quantum phase transitions is given. Last but not least, an overview about the origin and prediction of broken symmetry states in chiral graphene systems with more than two layers is presented.

2.2.1 Quantum Hall Effect

The classical Hall effect, discovered in 1879 [104], is a consequence of the motion of charged particles in a magnetic field. When a constant magnetic field perpendicular to a conductor with constant current flow is present, a transverse voltage in the conductor arises. This effect can be understood classically in terms of the Lorentz force acting on the charge carriers moving through the conductor, that causes charged particles to move in circles with a frequency given by $\omega_B = eB/m$ (the cyclotron frequency). In this context, the transverse (Hall) voltage V_H with associated transverse conductance $\sigma_{xy} = 1/\rho_{xy}$ are

$$V_H = \frac{IB}{nde} \qquad \text{and} \qquad \sigma_{xy} = \frac{ne}{B}, \tag{2.11}$$

where B is the magnetic field, d the thickness of the conductor in the direction of B, n the charge carrier density, e the elementary charge, I the current through the conductor and xy indicates that V_H accumulates in the transverse y direction, while I flows in the

x direction. In this regime, σ_{xy} is proportional to n and inversely proportional to B, and the resistance ρ_{xx} along the channel remains constant [105].

In the limit of a 2D electron gas (2DEG) and low temperatures, σ_{xy} becomes quantized [106] and its properties can only be explained through the laws of quantum mechanics. It is worth mentioning that two different quantum Hall effects (QHEs) associated to related phenomena are distinguished as the integer and fractional QHEs [105–107]. For what concerns this thesis, only the integer QHE will be discussed in detail. In 1980, the first experiments exploring the quantum regime of the Hall effect were performed [108], which showed the peculiarities of both the Hall resistivity ρ_{xy} and the longitudinal resistivity ρ_{xx} in that regime. By measuring V_H on a 2DEG realized with a Si-MOSFET, it was found that ρ_{xy} stays on a plateau for a range of magnetic fields before jumping suddenly to a next plateau, with values given by

$$\rho_{xy} = \frac{2\pi\hbar}{e^2}\frac{1}{\nu}, \ \nu \in \mathbb{Z} \qquad , \tag{2.12}$$

where ν is measured as an integer [106, 108], giving this phenomena the name of integer QHE. It can be shown that the centre of each plateau occurs at the values

$$B = \frac{2\pi\hbar n}{\nu e} = \frac{n}{\nu}\Phi_0, \tag{2.13}$$

where n is the electron density and $\Phi_0 = 2\pi\hbar/e$ is the flux quantum. Notably, while ρ_{xy} takes quantized values defining conductance plateaus, ρ_{xx} vanishes at the plateaus and exhibits spikes when the conductance increases from one to the next plateau [106, 108]. In this context, the vanish of ρ_{xx} can be understood as having a steady current flowing without doing any work and, correspondingly, without any dissipation [105]. More about the particular nature of ρ_{xx} will be discussed later.

Within this thesis, two-terminal devices are studied, where it is not practically accessible to measure independently σ_{xy} and σ_{xx}, but a combination of both defined as [109]

$$\sigma_{2T} = \sqrt{\sigma_{xx}^2 + \sigma_{xy}^2}. \tag{2.14}$$

The expression in equation (2.14), valid for squared samples, depends on their aspect ratio, with plateaus becoming distorted and the QHE obscured for higher and lower aspect ratios. As σ_{xx} is expected to vanish when the QHE occurs, σ_{2T} still exhibits the awaited conductance plateaus [109, 110].

2.2.2 Landau level quantization

The QHE can be explained by a quantization of the charge carrier energy into so-called Landau levels (LLs). In fact, the values of the magnetic field in equation (2.13) with $\nu \in \mathbb{Z}$ are those at which the first LLs are filled [105]. This can be seen from solving the Schrödinger equation with the Hamiltonian of a 2DEG of non-interacting spinless electrons in the presence of an external magnetic field,

$$H = \frac{1}{2m} \left(\mathbf{p} + e\mathbf{A}\right)^2, \tag{2.15}$$

where $\mathbf{A}$ is the vector potential with $B\hat{z} = \nabla \times \mathbf{A}$ and m the efective mass in the xy-plane. In the Landau gauge, $\mathbf{A} = (0, Bx, 0)$, the magnetic field forces the electrons to move in quantized cyclotron orbits. As a result, the energy continuum condenses into quantized energy (or Landau) levels, given by

$$E_N = \hbar\omega_B \left(N + \frac{1}{2}\right), \ N \in \mathbb{N}, \tag{2.16}$$

where $\omega_B = eB/m$. Here, the spin degree of freedom has been neglected for simplification. Its inclusion only increases the degeneracy of the LLs [105, 111] and will be introduced later, when necessary. It turns out that each LL can accommodate a number of states which increases with the magnetic field, given by $n_{LL} = eB/h$. The ratio between the density of states in a 2DEG and the density of states in the LLs, $\nu = n/n_{LL}$, is defined as the *filling factor*. When a LL is full, ν is an integer number i and the number of electrons per unit area is $n = in_{LL}$. Using that $R_H = B/en$ [104], it can be written [111]

$$R_H = \frac{h}{ie^2} = \frac{R_K}{i}, i = 1, 2, 3, ... \ . \tag{2.17}$$

So, an ideal 2DEG shows quantum Hall plateaus when the magnetic flux density is such that ν is an integer. On that condition, the Fermi level lies in a gap and the electronic scattering rate vanishes. Without scattering, the electrons cannot move perpendicular to both the electric and the magnetic fields, so σ_{xx} vanishes and the Hall conductivity becomes [106, 111]

$$\sigma_{xy} = \frac{en}{B} = \frac{ie^2}{h}, i = 1, 2, 3, ... \ . \tag{2.18}$$

To better understand the nature of the QHE and the behaviour of σ_{xy} and σ_{xx}, it is important to add two more aspects to their description: the presence of edge modes and disorder [105, 106, 111]. For a fixed magnetic field, all particles move in cyclotron orbits in one direction. At the edge of the sample, the particles collide with the boundary and produce a skipping motion, following one direction on the one-dimensional boundary (opposite on each side of the sample), as indicated in Figure 2.6 a). Since the bulk cannot carry current, the current flows entirely on the edges and, in the absence of an electric field, the net current vanishes [105]. From an energetic viewpoint, close to the edge of the sample, the energy of the LLs increases and, if the Fermi energy is placed between two LLs, edge channels appear at the crossing points as sketched in Figure 2.6 b). The calculations discussed on the previous paragraphs show that, if an integer number of LLs are filled, the longitudinal and Hall resistivities are those on the plateaus, but it does not explain why the plateaus happen nor why there are sharp jumps between them. Surprisingly, the plateaus exist thanks to the presence of disorder. In fact, without

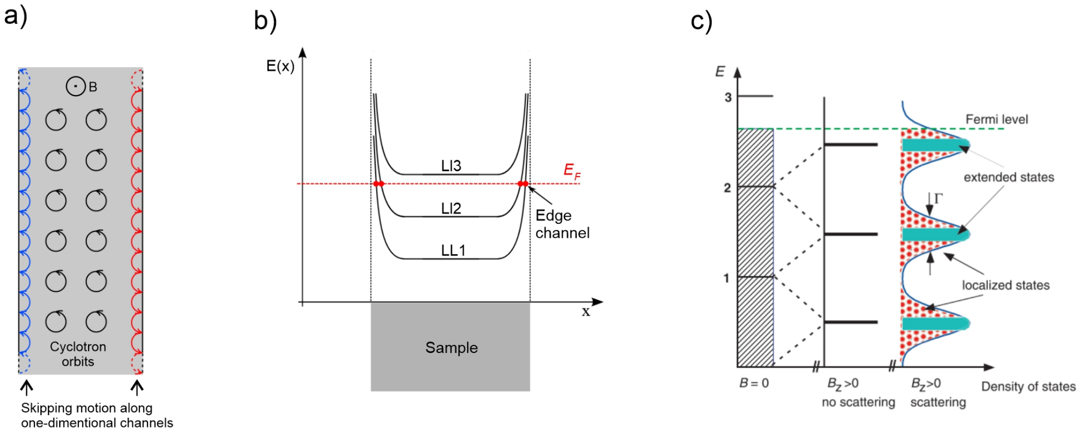

Figure 2.6: *LL* quantization of a 2DEG. a) Electron motion in a 2DEG exposed to an out of plane magnetic field B and the arise of edge channels. b) Energy spectrum of a 2DEG in a field B with a confining potential at the sample edges. Edge channels form at the intersection between *LL*s and the Fermi energy (E_F). c) *LL* quantization of a spinless 2DEG. The continuum of states at $B = 0$ (left) becomes quantized in *LL*s when B is on (centre). When disorder is added, the *LL*s broaden into localized and extended states (right). Image taken from [111].

disorder, the plateaus are expected to vanish completely [105, 106]. Disorder arises from impurities in the experimental samples and can be modelled by adding a random potential $V(x)$ to the Hamiltonian of the system. As drafted in Figure 2.6 c), the energy spectrum in the presence of weak disorder is expected to change from a picture without scattering to a picture including it. Additionally, the disorder can turn many of the quantum states from extended (spread throughout the system) to localised (restricted to some region of space). As a consequence, the states of either high or low energy at the far edge of a band are localised and only those states close to the centre of the band can be extended [105].

2.2.3 Rhombohedral few-layer graphene

As discussed in Section 2.1, mono- and few-layer graphene are distinct from a conventional 2D electron system (2DES) because of the chiral nature of their charge carriers and $N\pi$ Berry phases, with N the number of layers. For instance, the charge carrier movement on cyclotron orbits under an external magnetic field accumulates a phase shift of π in the wavefunction of chiral massless quasi-particles in monolayer graphene, while in rhombohedral N-layer graphene ($N > 1$), the wavefunctions of chiral massive quasi-particles obtain a phase shift of $N\pi$. This influences the properties of the QHE and, for example, it explains the existance of a *LL* at zero energy in monolayer graphene as well as the unconventional sequence of conductance plateaus in bilayer graphene [69], both illustrated in Figure 2.7.

As in a 2DEG, the *LL*s of a graphene system are obtained by replacing $\mathbf{p} \rightarrow \mathbf{p} - e\mathbf{A}$ in its Hamiltonian and calculating the eigenenergies [111, 112]. This way, the *LL*s of monolayer graphene result [69]

$$E^{(1L)}_{N_{LL}} = \pm\sqrt{2e\hbar\nu_F^2 B \mid N_{LL} \mid}, \tag{2.19}$$

where $N_{LL} = \{\pm 0, \pm 1, \pm 2, ...\}$ is the LL index with ± indicating the charge carrier type (positive for electrons and negative for holes). From equation (2.19) it is evident that the energy spacing between LLs in monolayer graphene is not equidistant, contrary to a conventional 2DEG. Besides, the emergence of a zero-energy LL is a clear consequence of the equal nature of electrons and holes with opposite pseudospin. Notably, the conductance in the context of the QHE in graphene, defined in equation (2.18), becomes quantized with integer values $\nu = \{1, 2, 3...\}$, resulting in

$$\sigma_{xy}^{(1L)} = \nu \frac{e^2}{h}, \qquad \nu = \pm\xi \left(N_{LL} + \frac{1}{2} \right) = \pm 2, \pm 6, \pm 10, ... \; , \tag{2.20}$$

where the value of ν includes various degrees of freedom, being $N_{LL} = \{0, 1, 2, 3...\}$ the LL index and ξ the valley and spin degree of freedom (spin up, spin down, K and K' for monolayer graphene, results in $\xi = 4$). It can be seen from equation (2.20) that the first quantum Hall plateau appears at the zeroth energy level, being half filled with electrons or with holes. This gives it the name of half-integer QHE in graphene.

For bilayer graphene, it is important to remember that its low-energy dispersion relation is parabolic instead of linear and the charge carriers are no longer massless, but have a finite mass. Considering this, the LL energies are given by [69]

$$E_{N_{LL}}^{(2L)} = \pm\hbar\omega_B \sqrt{N_{LL}(N_{LL} - 1)}, \tag{2.21}$$

where $N_{LL} = \{0, 1, 2, ...\}$ is the LL index and ω_B the cyclotron frequency. Accordingly, the conductance plateaus result in

$$\sigma_{xy}^{(2L)} = \nu \frac{e^2}{h}, \qquad \nu = \pm\xi \left(N_{LL} + 1 \right) = \pm 4, \pm 8, \pm 12, ... \; . \tag{2.22}$$

Here, an eight-fold degeneracy of the zero energy LL ($N_{LL} = 0$) originates from the inclusion of both 0 and 1 orbital states among the zero-energy solutions of equation (2.21). Together with the valley and spin degeneracies (giving again $\xi = 4$), a set of eight nearly degenerate LLs known as the $N_{LL} = 0$ octet is defined. Because of this near degeneracy, interaction driven effects are predicted to occurr in graphene bilayers [113, 114]. Noteworthy, in the case of trilayer ABC graphene, a twelve-fold degeneracy of the zeroth LL can be expected, due to the inclusion of a degenerate set of triplet orbitals 0, 1 and 2 [115, 116].

Figure 2.7 shows the conductance plateaus for the integer QHE in a conventional 2DEG compared to those in graphene, bilayer graphene and trilayer graphene. As introduced in section 2.1, few layer graphene systems stacked in different ways give rise to different electronic properties at the corresponding energy scales, so it is to expect that the particular stacking order will have an influence on the resulting QHE properties. From now on, the discussions will be focused on the stacking order investigated during this thesis, namely, rhombohedral few-layer graphene. Two examples have been already introduced when discussing mono and bilayer graphene. At low energies, they represent the $J = 1$

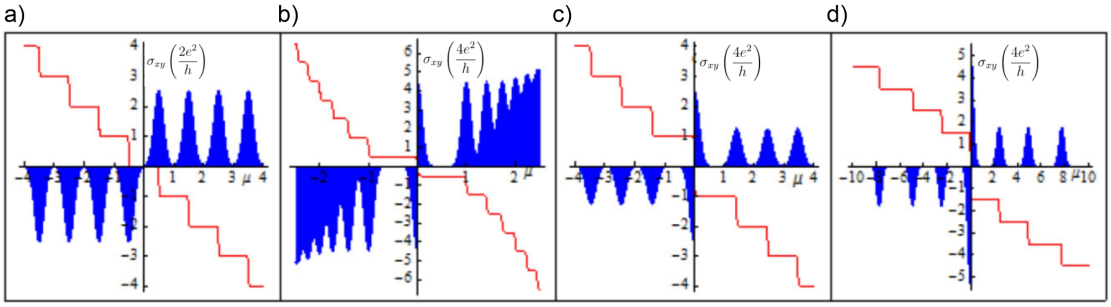

Figure 2.7: *LL* quantization of 2DEG systems. a) Conventional 2DEG, b) monolayer graphene, c) bilayer graphene and d) ABC stacked trilayer graphene as a function of chemical potential μ measured from the carrier neutrality point for fixed magnetic field. The Hall conductivity σ_{xy} is shown by the red (solid) line and the longitudinal conductivity in blue. The shaded blue areas indicate the disorder broadened *LL* density of states, inverted on the holes side for visualization. The chemical potential μ in a) is in units of $\hbar^2/\left(ml_B^2\right)$ and, in b), of $1/\gamma_1^{J-1}(\sqrt{2}\hbar\nu_D)^J$ with J the chirality degree of freedom. Image adapted from [113].

and 2 instances of a chiral 2DES [79], with J a chirality degree of freedom. Describing rhombohedral trilayer graphene with a single $J = 3$ chiral 2DEG model [35, 79, 113], it can be shown that its conductance plateaus appear at $4\left(N + J/2\right)e^2/h$ integer multiples of e^2/h with $J = 3$, where N is an integer and J the 2DEG chirality, which for rhombohedrally stacked systems is equal to the number of layers [35, 113]. Notably, as shown in Figure2.7, the LL separation decreases with energy for $J = 1$, is independent of energy for $J = 2$ and increases with energy for $J = 3$. In addition, the disorder broadening of the LL density of states has roughly the same form as the longitudinal conductivity except that its peaks are typically less sharp [113].

As a final remark, it is worth mentioning that the chirality degree of freedom J can be deduced in terms of the low-energy band and the LL structure from the stacking diagrams in Figure 2.3, by partitioning a given stack in terms ABC and AB repetitions blocks [35]. This way, it can be shown that in N-layer cyclic ABC there is a single $J = N$ partition, while an AB stacking results in $N/2$ partitions with $J = 2$ if N is even and an extra $J = 1$ partition if N is odd. Between these two limits, a diversity of qualitatively distinct low-energy behaviours exists. As an example, for ABCB stacked tetralayer graphene, ABC results a $J = 3$ doublet and the remaining B layer gives a $J = 1$ doublet ($J_{\text{ABCB}} = 3 + 1$). Therefore, the low-energy band and LL structure of this stack is predicted to have two sets of bands with dispersion $|E| \propto k, k^3$, LLs with $|E| \propto B^{1/2}, B^{3/2}$ and four zero-energy LLs per valley and per spin [35]. A detailed description of the partitioning rules for different N layer stacks can be found in Refs. [35] and [79].

2.2.4 Quantum and classical phase transitions

Within this thesis, distinct phase transition phenomena is commented and discussed in different contexts, therefore a few definitions are introduced. From a classical perspective, a phase transition occurs upon variation of an external control parameter, which results in a qualitative change in the system properties. Common examples are the melting of ice as well as the transition of a metal into a superconducting state upon lowering the temperature. In such phase transitions, which occur at a finite temperature, a macroscopic order (e.g. the crystal structure in the case of melting) is destroyed by thermal fluctuations [117]. Following the traditional classification, first-order phase transitions are those in which the two phases co-exist at the transition temperature (e.g. ice and water at 0 °C), while second-order phase transitions are those in which the two phases do not co-exist [118]. A main difference between the two is that there are large fluctuations before a second-order phase change, while first order phase changes occur abruptly and without any prior fluctuations [119]. In the latter, the observability of accompanying phenomena such as hysteresis is often a useful sign of a first-order phase change [120]. One important example of a second-order phase transition, which is mentioned in chapter 3 of this thesis, is the critical end-point of carbon dioxide. This is the end-point of the line that separates the liquid and gaseous states in the pressure-temperature plane, which can also be interpreted in terms of competition between order and thermal fluctuations [117, 118].

In the last decade, attention was driven to phase transitions which are qualitatively different from the previous examples. These are quantum phase transitions, which occur only at the absolute zero of temperature [118]. The transition happens at the "quantum critical" value of some parameter such as pressure or magnetic field strength [118]. When the co-operative ordering of the system disappears, this loss of order is driven solely by the quantum fluctuations demanded by the Heisenberg's uncertainty principle [117, 118]. A common approach to studying quantum phase transitions is to determine the lowest energy or "ground" state of the material at zero temperature and a fixed value of some variable such as pressure. To do this, it is also important to know the low-energy excitations of the system. It is often found that the ground state will be qualitatively different at different values of the relevant variable. This means that the material must undergo a phase transition as this variable is changed, even at absolute zero, being this the quantum phase transition [118]. The study of quantum phase transitions tuned by system parameters rather than temperature, has enlarged the research domain of phase-transition physics. In electronic systems, transitions to ordered ground states can occur when interactions between particles (rather than single-particle potentials) play a dominant role in selecting the ground state. This situation is frequently encountered in the quantum Hall regime owing to the quantization of in-plane kinetic energy into macroscopically degenerate LLs [121]. In the next section, a more in depth discussion about finding the ground state of the main system studied within this thesis, is given.

2.2.5 Broken symmetry states in chiral graphene systems

With an appropriate tuning of the Fermi energy as well as the electric and magnetic fields, a wide range of physical phenomena can be experimentally studied and understood by treating particles as non-interacting. If the kinetic energy of the electrons becomes comparable to the Coulomb interaction energies, electron-electron interactions can no longer be neglected and the single-particle picture breaks down [122]. When this happens, a very rich scenario is open, where many-body interactions lead to spontaneous symmetry breaking and other interesting phenomena such as fundamental particles' mass generation, superconductivity and magnetism [34,37–39,82,122]. In the next paragraphs, the influence of interactions on the many-body ground state of rhombohedral (chiral) few-layer graphene is discussed. Focus is given on the class of broken symmetry states most relevant for this thesis, which are distinguished by their charge, spin and valley quantized Hall conductance, by their orbital magnetizations and by their edge states properties.

Beacuse of the large density of states and $N\pi$ Berry phases near low-energy band touching points (see section 2.1), chiral 2DES with $N > 1$ at zero external fields are prone to manifest broken symmetry states [34]. Especially for $N \geq 2$, electron-electron interactions make the scenery even more exciting, as the energy bands become increasingly flat near charge neutrality [33]. As discussed in section 2.1, the low-energy electrons in N-layer rhombohedral graphene systems are concentrated on the top and bottom layers, so its low-energy physics is approximately described by a band model with a p^N dispersion relation and correspondingly large Berry curvatures [33, 123]. In a pseudospin language description, this implies broken symmetry states characterized by a momentum-space vortex with vorticity N and a vortex core polarized in the top or bottom layers [33, 42].

An interesting example of interaction driven effects in a chiral graphene system is the one of AB-stacked bilayer graphene. Here, a spontaneous gap with charge transfer between the top and bottom layers, proposed theoretically and observed experimentally, constitutes an interaction-induced broken symmetry ground state of bilayer graphene [33,42,43,45,124]. Because of its flatter bands, ABC-stacked trilayer graphene is expected to be even more inclined to embody interaction-driven broken symmetries [33]. In general, for an N-layer rhombohedral stacked graphene system, the interaction effects near charge neutrality are well described by a mean-field Hamiltonian of the form [33, 43, 124],

$$H_N = \frac{(vp)^N}{(-\gamma_1)^{N-1}} \left[\cos(N\phi_{\boldsymbol{p}})\sigma_x + \sin(N\phi_{\boldsymbol{p}})\sigma_y\right] + \lambda\sigma_z, \tag{2.23}$$

this is, the low-energy single-particle Hamiltonian from equation (2.10) with an extra term to account an interlayer interaction-induced gap, associated to the direction of layer polarization in the momentum space vortex core [33]. Again, the vector of Pauli matrices $\boldsymbol{\sigma}$ acts on the pseudospin degree of freedom, which tells in which layer the states are.

While an external electric field introduces a potential difference Δ to explicitly break chiral-symmetry and opens a band gap [32], spontaneous chiral-symmetry breaking opens a gap in the electronic spectrum originating a giant Berry curvature in the vicinity to the band minima [43]. For each spin $(\uparrow, \downarrow)$ and valley (K, K'), symmetry is broken by choosing the sign of λ in equation (2.23) [33]. Counting all possible degree of freedom combinations with individually allocated λ sign, chiral trilayer graphene comes up with sixteen broken symmetry states. Notably, six of those states can be grouped into three doublets with no net charge transfer between top and bottom layers, being only discernible by layer inversion in every spin-valley. The three fundamentally distinct states, theorized

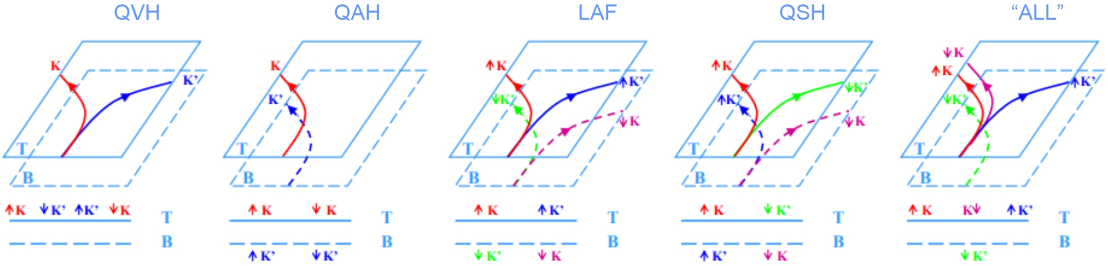

Figure 2.8: Broken symmetry states in chiral N-layer graphene. The lower panel indicates the sense of layer polarization (top (T) or bottom (B)) for each spin-valley combination and the upper panel shows with arrows the Hall conductivity contributions for the quantum valley Hall (QVH) insulator; the quantum anomalous Hall (QAH) insulator; the layer antiferromagnetic (LAF) insulator; the quantum spin Hall (QSH) insulator and the "ALL" state. Adapted from [33].

as competing broken symmetry ground states, are the anomalous Hall state (QAH), in which the sign of λ depends on the valley but not on the spin, the layer antiferromagnetic state (LAF), where λ is only spin-dependent and a quantum spin Hall (QSH) state (often called 2D topological insulator), which shows λ both spin and valley dependence. Besides, two additional states with net layer charge transfer between top and bottom layers can be favoured by a potential difference between the layers. These are the valley Hall state (QVH), with neither valley nor spin dependent λ and the “ALL” state, for which λ depends on both valley and spin [33, 34, 125].

Noteworthy, the five broken symmetry states drafted in Figure 2.8 are predicted to be universal in rhombohedral multilayer graphene stacks [34]. As summarized in Table 2.1, they can be distinguished by their charge, spin, and valley Hall conductivities, as well as by their orbital magnetizations and broken symmetries [34]. Until now, experiments in bilayer graphene systems seem to have given definitive proof that the ground state of bilayer graphene at very weak external magnetic fields is the QAH state [44,45], both the LAF and QVH states have been revealed in bilayer and few-layer graphene [39, 40, 74, 126–128] and more recent experiments appear to grant evidence of the existence of the so-called “ALL’ state in bilayer graphene [46]. Nevertheless, a full phase diagram for few-layer graphene remains undiscovered, presumably, because samples that are clean enough to reveal its interaction physics, which is expected to dominate at low carrier densities [32, 125], are difficult to implement. This thesis has been dedicated to fabricate and investigate such samples.

$K\uparrow$	$K\downarrow$	$K'\uparrow$	$K'\downarrow$	$\sigma^{(\mathrm{SH})}$	$\sigma^{(\mathrm{VH})}$	$\sigma^{(\mathrm{CH})}$	$\sigma^{(\mathrm{SVH})}$	Insulator	Broken Symmetries
T	T	T	T	0	$2N$	0	0	QVH	$\mathcal{P}$
T	T	B	B	0	0	$2N$	0	QAH	$\Theta, \mathcal{Z}_2$
T	B	T	B	0	0	0	$2N$	LAF	$\Theta, \mathcal{P}, SU(2)$
T	B	B	T	$2N$	0	0	0	QSH	$\mathcal{Z}_2, SU(2)$
T	T	T	B	N	N	N	N	ALL	$\Theta, \mathcal{P}, \mathcal{Z}_2, SU(2)$

Table 2.1: Spin-valley layer polarizations (as in Figure 2.8) and their charge, spin, and valley Hall conductivities (in units of e^2/h), as well as their insulator types and broken symmetries, namely, time-reversal (Θ), inversion ($\mathcal{P}$), valley Ising $\mathcal{Z}_2$ and spin ($SU(2)$). Adapted from [34]

2.3 Charge Density Waves in 1T-TaS$_2$

This section gives an introduction to the basic ideas behind CDW formation in low dimensional systems. To this aim, a model commonly used in the literature to explain the origin of the CDWs in layered TMDs is introduced. Moreover, the particular case of 1T-TaS$_2$ and its hosting of different CDW phases are discused.

2.3.1 Definitions and concepts behind CDW formation

A CDW is a Fermi-surface driven phenomena consisting on a static modulation of the conduction electrons, usually accompanied by a periodic lattice distortion (PLD) [85,129]. A basic scenario to visualize this is a quasi-1D metal made of a linear chain of atoms separated by a distance a, as sketched in Figure 2.9 a). In such a system, a so-called Peielrs instability towards a CDW/PLD formation occurs as a consequence of strong electron-phonon interactions [85]. This can be explained by the Peierls model, which considers the CDW/PLD as a modulated electron density [85,129]

$$\rho(\mathbf{r}) = \rho_0(\mathbf{r}) \left[1 + \rho_1 \cos\left(\mathbf{q}_0 \mathbf{r} + \phi\right)\right], \tag{2.24}$$

where $\rho_0(\mathbf{r})$ is the unperturbed electron density and the second term between square brackets is called the CDW, with amplitude ρ_1, wavevector $\mathbf{q}_0$ and phase ϕ. This standing wave with wavelength $\lambda_0 = 2\pi/|\mathbf{q}_0|$ makes each ion in the chain see a different potential, which modifies their equilibrium positions. A PLD of the form

$$u_n = u_0 \sin\left(n|\mathbf{q}_0|a + \phi\right), \tag{2.25}$$

where $n \in \mathbb{Z}$ labels the ions positions and u_0 is an amplitude smaller than the lattice constant a, sets up a potential that opens a gap at the Fermi surface, lowering the energy of the occupied electron states and raising the energy of the empty ones [85, 129], as shown in Figure 2.9 b). The subsequent net energy gain overcompensates the Coulomb and elastic energy costs, so the CDW/PLD is self-sustaining [85]. It is worth mentioning that, for an arbitrary band filling, the period of the CDW/PLD is incommensurate with the underlying lattice, i.e., λ/a is irrational [129]. Last, it should be noted that a CDW and PLD modulation are intrinsically coupled and the question of which one is the driving force remains an open debate.

Remarkably, the Peierls instability is an instability of a coupled electron-lattice system, which in essence is a structural phase transition driven by strong electron-phonon coupling [85]. The main features of a Peierls transition, from a metal above a transition temperature T_0 to a CDW/PLD ground state at temperature $T = 0$, can be described quantitatively by a mean-field theory of a 1D electron-lattice system in the weak-coupling limit with independent electron, harmonic and adiabatic approximations [85,129]. Such modelling, which will not be derived here, is expected to become non appropriate when the electron–phonon coupling and energy gapping are large and Fermi surface geometry

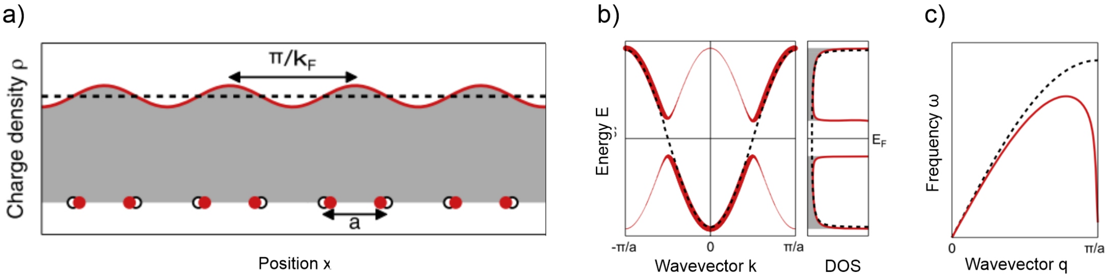

Figure 2.9: Peierls instability of a 1D metal. a) CDW/PLD scheme of a 1D metal showing the conduction electron density modulation (solid red line) and ion positions (red circles). The normal state has constant charge-density (dashed black line) and undistorted chain (black circles). b) Band structure and density of states in the metallic state (dashed black lines) and in the CDW state at $T = 0$ (solid red lines with thickness proportional to the spectral weight of the electron states in the CDW phase). c) Corresponding acoustic phonon dispersions. Adapted from [85].

is not 1D-like [85]. In spite of that, when realistic calculations are not available, the Peierls model provides a theoretical framework for comparing experimental data with a semiquantitative prediction, and certainly helps to identify and understand CDW/PLD transitions in real materials, in particular, quasi-1D solids [85, 129].

2.3.2 CDW phases 1T-TaS$_2$

The prerequisites for a Peierls transition can be fulfilled in materials where the basic structural units form chains with strongly overlapping electronic wave functions along the chains and weak overlap in the perpendicular directions [129]. In fact, materials in which CDW phases are observed have commonly chain-like or layered structures [129]. For example, various CDW phase transitions have been reported in experiments with quasi-1D organic conductors [130–132] as well as in quasi-2D layered compounds (e.g. TMDs) [85, 133, 134]. During this thesis, the CDW material 1T-TaS$_2$ is subject of study, whose crystalline and electronic structure as well as its phase diagram have been commented in section 2.1, Figure 2.5. As often seen in strongly correlated systems, the electrons in 1T-TaS$_2$ have a tendency to self-organize into an ordered insulating state at low temperatures and, for the case of this layered material, the ordering implicates the formation of a C-CDW [51]. Figure 2.10 a) shows the atomic structure of the C-CDW phase with the well-known star of David (SD) cluster unit cell, in which 12 among 13 Ta atoms of a cluster become distorted toward the central one forming a $\sqrt{13} \times \sqrt{13}$ supercell [85]. As represented in Figure 2.10 b), upon cooling or heating, several distinct CDW phases are distinguished in terms of their lattice structure and the presence of SD supercells. The CDW phase transitions are generally strongly first order transitions, exhibiting a correspondingly strong hysteresis [51]. Figure 2.10 c) shows a map of the resistivity (ρ) of 1T-TaS$_2$ as a function of the temperature, in a cooling and warming cycle. Notably, the hysteretic behaviour of the CDW phase transition depends on the material thickness as well as on the cooling and warming rates (see Ref. [53]). From higher to lower temperatures (see Figures 2.10 b) and c)), bulk 1T-TaS$_2$ undergoes a transition from an IC-CDW phase,

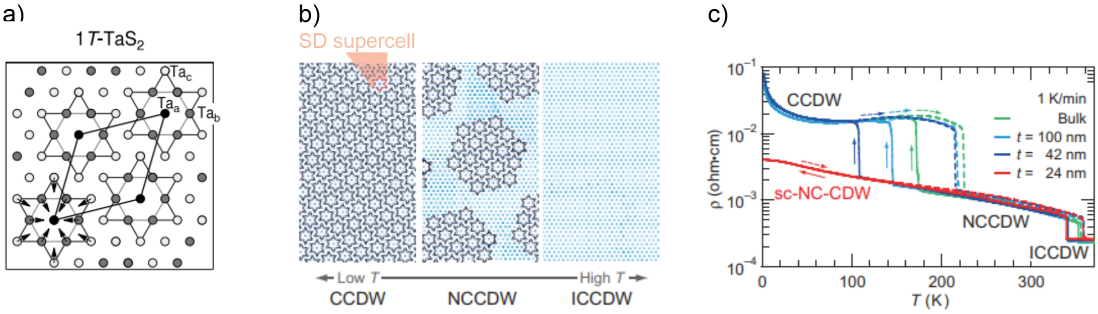

Figure 2.10: a) Real-space unit cell for the commensurate superlattice of 1T-TaS$_2$ with only Ta atoms shown. The arrows illustrate in-plane displacements of the atoms from their original positions, forming a star of David (SD) supercell. Adapted from [85]. b) Sketch of a Ta atom network in the C-CDW (left), NC-CDW (middle) and IC-CDW (right) phases. The dark blue circles represent the Ta atoms in an SD cluster. Adapted from [53]. c) Temperature (T) dependence of the resistivity (ρ) for bulk and nano-thick crystals of 1T-TaS2. The solid and broken lines represent the ρ in the cooling and warming cycle, respectively. The notation sc-NC-CDW represents supercooled NC-CDW (see Ref. [53]). Image adapted from [53]

a domain-free state with incommensurate CDW order (see Figure 2.10 b), right), to a NC-CDW phase at ∼350 K, with hexagonally ordered domains (see Figure 2.10 b), centre). Following, the system goes from an NC-CDW to the C-CDW phase at ∼180 K (Figure 2.10 b), left) [51, 53, 85, 134]. Notably, in 1T-TaS$_2$, within the C-CDW phase the Mott state is simultaneously developed [135]. Furthermore, a hidden electronic state emerges at low temperatures upon shining a single intense femtosecond laser pulse on the 1T-TaS$_2$ insulating ground state [136–139]. In addition, it has been shown that controlled optical or electromagnetic perturbations can induce an amorphous phase [140].

The richness of the electronic properties of the CDW material 1T-TaS$_2$ makes it of great interest for technological applications. In particular, because of the robustness of the phase switching, there is a growing interest on applications in memristive systems [53] as well as device integration for CDW phase switch control [141, 142]. Therefore, identifying the origins of the emergence of the correlated ordering in 1T-TaS$_2$ is of great relevance. Contributing to the understanding of some open questions on the formation of CDW phases in 1T-TaS$_2$ is a goal of this thesis. To this aim, the experiments presented on this thesis are directed to address the nature of the CDW emergence in low dimensions under certain environmental conditions. For instance, by investigating the underlying stabilization mechanisms and the structural character of mixed CDW domains, in particular, under an external electrical stimulus. Other approaches include studying the system in a controlled dielectric environment or preserving the intrinsic properties of atomically thin flakes by encapsulation with hexagonal boron nitride (see Ref. [103]).

Chapter 3

Fabrication and methods

This chapter provides a detailed description about the fabrication and design of the samples investigated within this thesis. Moreover, the experimental setups, the electrical characterization methods and the calibration measurements used during this thesis are depicted. In section 3.1, the fabrication procedure of dually gated free-standing rhombohedral graphene devices is given, starting with a description of the methods used to identify the rhombohedral stacking order in trilayer and tetralayer graphene. Next, the focus is put on the fabrication and design of electrical contacts to the sample and a first characterization of the devices at room temperature in a probe-station. Following, a description of the chip-carrier integration and cleaning process of free-standing devices is given, together with a description of the experimental setups used to perform the electron transport studies at temperatures down to 10 mK and magnetic fields up to 14 T. Last but not least, a description of the relevant calibrations and transport measurements to obtain the results reported within this thesis is detailed. Section 3.2 presents the guidelines for the fabrication of devices with both bulk and thin-films of 1T-TaS$_2$ using a TEM membrane as a substrate. The most important characterization methods for this material to make devices for the exploration of CDW phases are given. The section concludes with a description of the temperature dependent electron transport measurements in a closed-cycle probe station, as well as of the setup and its measuring modes used for bright and dark-field TEM imaging.

3.1 Free-standing dual-gated rhombohedral graphene devices

The experiments with few-layer graphene reported on this thesis are performed in a sample configuration where the graphene is suspended (free-standing) between a top and a bottom gate. The fabrication of a dual gated device enables the independent tuning of the charge carrier density (n) and the displacement field (D) on the system, by changing the top and bottom gate voltages [45,47]. This facilitates the experimental study of electronic transport under controlled system parameters. Making free-standing graphene instead of the most common encapsulated samples in hexagonal boron nitride has two main reasons: On the one side, it constitutes an experimental platform to study multilayer graphene in a low dielectric environment. On the other side, it lowers the screening of the Coulomb interactions in the system, which favours the observation of correlated phenomena [49]. Furthermore, free-standing graphene devices are demonstrated to be of the best quality [48], which is needed to study interaction physics in graphene. In what follows, the steps to obtain rhombohedral few-layer graphene flakes and fabricate free-standing dual-gated graphene devices with them are given. The relevant device characterization and measurements techniques used within this thesis are also introduced.

3.1.1 Finding rhombohedral multilayer graphene

Multilayer graphene flakes are obtained from highly oriented pyrolytic graphite (HOPG, HQ Graphene) by mechanical exfoliation, which is known to deliver very high-quality flakes [143]. This technique consists in using an adhesive tape (Magic Tape, Scotch) to peel-off or exfoliate graphene flakes from a piece of graphite. An adequate number of iterations of this process separates thin layers of the material which, as mentioned in chapter 2, are weakly bonded by van der Waals forces. As a result, graphene and few-layer graphene flakes end up on the adhesive tape. In order to transfer the flakes onto a substrate, the tape containing material is gently pressed on the upper face of the substrate and carefully removed after a few seconds. The substrate used on this thesis is a 4 mm×4 mm cut from a commercially available degenerately p-doped Si wafer with a 300 nm SiO_2 top layer. The SiO_2 layer thickness is chosen to provide good visibility of the graphene flakes in an optical microscope [144] and a high doping level is chosen to ensure low gate resistivities at temperatures close to absolute zero. To facilitate the localization of flakes on the substrate, a marker system is patterned onto the wafers using standard Electron Beam Lithography (EBL) [145] and Physical Vapor Deposition (PVD) of thin metal films (thermal or e-beam, upon availability). The material used for the markers is 2 nm Cr and 30 nm Au. Before transferring the graphene flakes on the substrates with marker system, the substrates are thoroughly cleaned. First, they are dipped in acetone at room temperature in a sonicator for 10 min at maximum power. Second, they are rinsed with acetone and then dipped in isopropanol for 10 min, then rinsed with isopropanol again and blown dried with a N_2 gun. Afterwards, they are plasma cleaned for 5 min at 50 W in 10 sccm O2 (PICO Plasma Cleaner, Diener). Last, they are pre-heated several minutes on a hot plate at 100 - 120 °C to evaporate any residual acetone, isopropanol and water. In order to find multilayer graphene with rhombohedral stacking order among the several transferred flakes, different microscopy and spectroscopy characterization methods are performed. In the next paragraphs, each of them is described with detail.

Optical microscopy

The first step to locate the exfoliated multilayer graphene flakes on the substrate is looking for them at an optical microscope (LC EC Epiplan-Neofluar 100x, Zeiss). An ex-

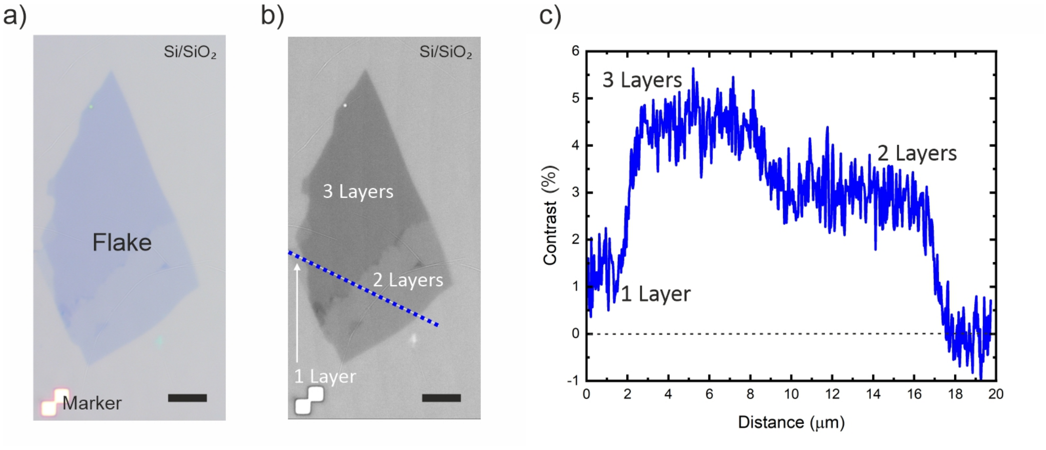

Figure 3.1: a) Optical microscope image of a multilayer graphene flake on a Si/SiO$_2$ substrate, with 300 nm oxide thickness. Scale bar 5 µm. b) Background-corrected grayscale image using the green channel, where a distinction between 1, 2 and 3 layers of graphene can be noted by comparing the contrast with respect to the substrate (background). Scale bar 5 µm. c) Profile measurement following the blue dotted line in b), showing a contrast increase with respect to the background (substrate set as 0 level of contrast) for a higher number of graphene layers.

ample on how this is done is shown in Figure 3.1. Given that monolayer graphene absorbs a part of the incident white light [146] and that the amount of absorbed light increases linearly with the number of layers of graphene for a low number of layers [144], the contrast observed on an optical microscope image can be used to estimate the number of layers of graphene within a flake. It is important to note that the optical contrast of graphene depends on the characteristics of the substrate. In order to make graphene visible with white light, a substrate with a 300 nm SiO$_2$ layer is most convenient [144]. Figure 3.1 a) shows a few-layer graphene flake located by optical microscopy next to a Cr/Au marker and, Figure 3.1 b)-c), its corresponding contrast analysis. The optical contrast of the green channel, which provides the highest contrast, divided by the background channel is taken as a measure for the analysis. For a graphene flake suspended, the fine structure constant defines the opacity of the flake, which is known to absorb about a 2.3 % fraction of incident white light [146]. Thanks to this property, as shown in Figure 3.1 c), a small increase in the percentage of light absorbed is enough to distinguish one layer of graphene from the substrate. Besides localizing and identifying on a first approximation the graphene flakes with a desired number of layers, optical microscope images of the entire substrate are used to have information of the surroundings of the pre-selected flakes. In order to facilitate the fabrication of good quality electrical contacts, flakes found in the middle region of the 4 mm x 4 mm substrate and isolated as much as possible from other nearby flakes are of preferred choice. Among them, flakes with a size bigger than 1 µm width and 4 µm length are pre-selected. Once suitable flake candidates are located, the exact number of layers as well as stacking order are determined by a combination of Raman spectroscopy and scattering-type Scanning Near-Field Optical Microscopy (s-SNOM). A detailed description of both characterization techniques is given on the next paragraphs.

Raman spectroscopy

Once the most promising flake candidates are pre-selected, Raman spectroscopy is performed in order to confirm the number of graphene layers and to gain additional information of the stacking order. Raman spectroscopy is a technique based on the inelastic scattering of light by matter and it is highly sensitive to the physical and chemical properties of the materials, as well as to the environmental effects that have an impact on these properties [147, 148]. For the case of graphene, the secondary D peak (2D peak) of the Raman signal is the most sensitive to the electronic and phonon band structure changes [149–151]. This is because it has origin on a second-order Raman process that involves two transverse optical phonons [149, 152]. Its line shape is determined by the relative contributions of different scattering paths involving both conduction and valence bands, thus, it encodes information of the electronic band structure [149, 152]. Since the band structure of multilayer graphene depends on both the number of layers and the stacking order, the 2D Raman peak contains information about the structural properties of the system [152, 153]. Figure 3.2 a) shows the result of measuring the 2D Raman peak in mono-, bi-, tri-, and tetra-layer graphene for the case of both Bernal and rhombohedral stacking orders. The measurements are taken with an excitation wavelength 532 nm (Torus 532, Laser Quantum). The laser is focused onto the sample through an optical microscope objective (MPlanFL N 100x/0.90na, Olympus), resulting in a laser spot size of $\sim 1\mu$m diameter. The spectra are recorded using a spectrometer (iHR550, Horiba Scientific) with 1800 lines per mm grating. In the result shown in Figure 3.2 a), it can be noted that the greater the number of layers of graphene, the broader the 2D Raman peak becomes. Moreover, the 2D peak of graphene has a different line shape for mono-, bi-, tri- or tetra-layer graphene. For the case of tri- and tetra-layer graphene, an additional difference in the spectra can be assigned to the Bernal or the rhombohedral stacking order: the 2D peak for rhombohedral graphene stacked flakes is remarkably asymmetric, in contrast to the more symmetric 2D peak characteristic of flakes with Bernal stacking order. These results are in good agreement with the literature [152, 154].

The stacking order in one multilayer graphene flake is known to change among the surface area of the flake [154]. This can be seen on the result shown in Figure 3.2 b). On the top, an optical microscope image of a few-layer graphene is shown. The portion of the flake encircled by the dashed line has three layers, as determined by optical contrast and Raman spectroscopy. On the bottom, a complete Raman map of the trilayer graphene portion of the flake is depicted. The map is measured by scanning the laser over the sample, moving a motorized piezoelectric stage and taking a Raman measurement at each point. The datapoints that constitute the map correspond to a measure the Full Width at Half Maximum (FWHM) of a single Lorentzian fit of the 2D Raman peak at each xy position on the flake. Noteworthy, despite the fact that a single Lorentzian function does not reproduce with accuracy the full shape of the Raman spectra, it is good enough to account the difference between a 2D peak of Bernal and rhombohedral graphene stacking order. This way, a single Lorentzian fit serves the purpose of having a first quick approach to coarsely discern which are the areas of the flake that will be of interest for making a

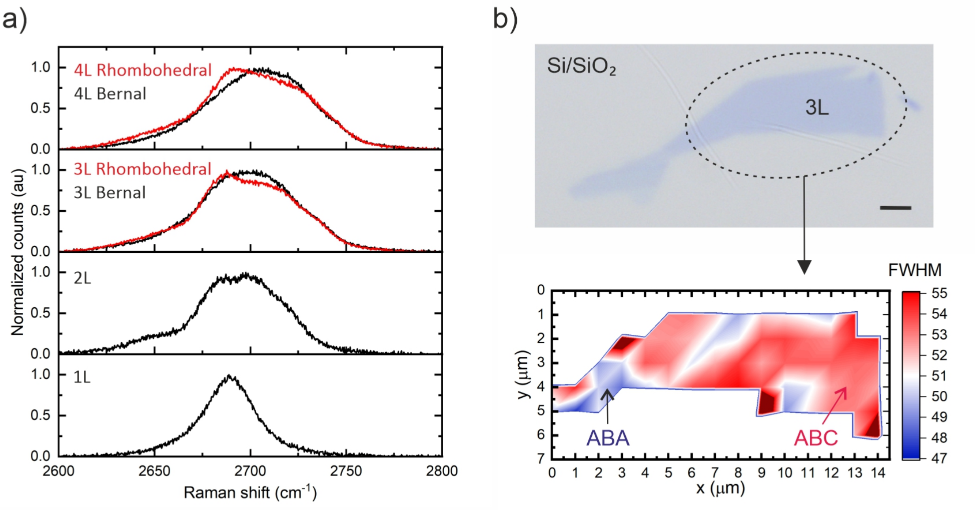

Figure 3.2: a) Normalized 2D-peak Raman spectra of flakes with 1 to 4 layers (L) of graphene. Bernal and rhombohedral graphene 2D Raman peak signal for 3L and 4L graphene are shown in black and red, respectively. b) Top: optical microscope image of a few-layer graphene flake. The enclosed dashed area corresponds to 3L on an optical contrast analysis. Scale bar 5 µm. Bottom: Raman spectroscopy map of the flake, showing the FWHM of a single Lorentzian fit of the Raman spectra measured at each xy position over the scanned area. Higher FWHM (red) corresponds to rhombohedral stacking order and lower FWHM (blue), to Bernal.

device. As indicated in Figure 3.2 b), bottom, higher FWHM is assigned to rhombohedral stacking order while lower FWHM, to Bernal. Importantly, as introduced in chapter 2, section 2.1.3, for the case of tetralayer graphene, beyond rhombohedral (ABCA) and Bernal (ABAB), additional (hybrid, ABCB) stacking orders can occur. Up to four layers, Bernal and rhombohedral stacking orders are still distinguished by the asymmetry of the 2D-peak, as can be seen in Figure 3.2 a). The distinction between ABCA and ABCB stacking orders is subtler [155] and will be commented with the results discussed in chapter 5. Last but not least, it should be noted that the lateral spatial resolution of the Raman measurements, in particular for the Raman map, is limited by the spot size of the laser as well as by the resolution of the piezoelectric stage and, ultimately, by the diffraction limit. This is why the Raman measurement, while delivering an accurate measure of the number of layers and stacking order of a few-layer graphene flake, it does not provide the best possible spatially resolved map of the properties of a flake. To overcome this limitation, a s-SNOM technique is used as a complement, as described on the next paragraph.

Scattering-type Scanning Near-field Optical Microscopy (s-SNOM)

The work on this thesis is aimed at investigating trilayer and tetralayer graphene with rhombohedral stacking order. Experiments in bilayer graphene have shown that the presence of ripples and domain walls have a strong influence in the electronic properties of the resulting system [156, 157]. For this reason and within the framework of this thesis, it is important to resolve flake areas of a given staking order with the best achievable

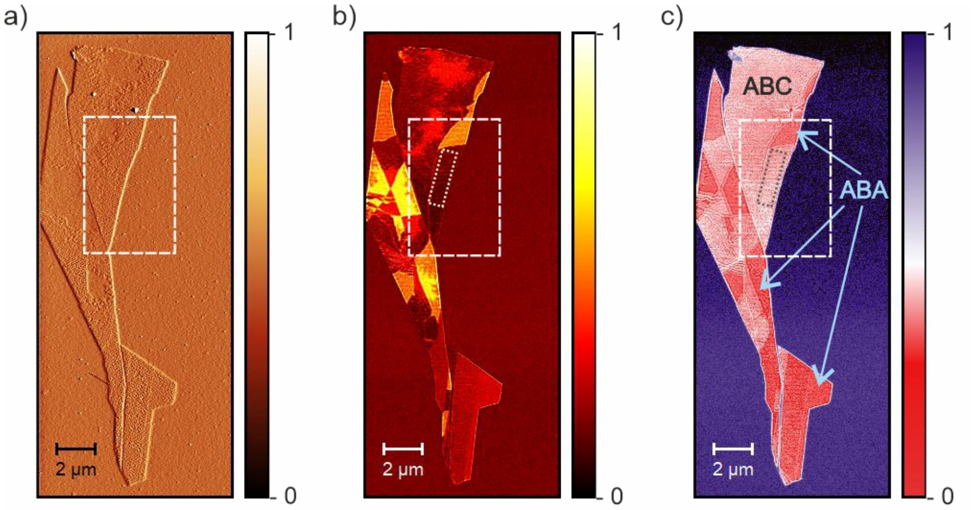

Figure 3.3: s-SNOM measurement for the identification of different stacking domains in trilayer graphene. Colour scales in arbitrary units. Optical images modulated at the third harmonic of the tapping frequency. a) Mechanical amplitude. The dashed white line encloses a flake portion to study. b) Reflectivity (optical amplitude). Domains with different optical responses are enclosed by the white dashed line. The dotted line marks a portion of the flake with a homogeneous reflectivity response, free of ripples and cracks. c) Absorption (optical phase). By comparison with the Raman map, ABC and ABA graphene domains can be assigned to the regions where there is a change in the absorption phase. This is represented in the image in different shades of red, where lighter corresponds to ABC and darker, to ABA stacking order.

spatial resolution, to identify inhomogeneities on the flake surface as well as the edges of the stacking domains. To this purpose, a s-SNOM method is used to obtain a material-characteristic map of the chemical and optical properties of the sample surface at a spatial resolution below the diffraction limit. The measurement on a s-SNOM setup is founded on an asymmetric interferometer where an Atomic Force Microscope (AFM) tip and the sample are located in one of the interferometer arms. During the measurement, the sample is moved underneath a sharp AFM tip to raster-scan across the sample surface and map the topography, while the tip is being illuminated with the focus of a Near Infrared (NIR) laser. This creates a strong near-field nano-focus at the apex of the tip, which probes the optical properties of the sample below the tip, making the measurement sensitive to the local optical properties. The light scattered from the tip-sample is recombined with a reference beam at a detector. An interferometric detection based on varying the reference phase with a mirror position, allows for simultaneous recording of the phase and the amplitude of the tip-scattered light, which relate to the local reflectivity and absorption of the sample. Modulating the reference phase also enables complete suppression of scattering background. This way, s-SNOM returns pure optical/chemical near-field maps simultaneously with AFM topography and phase [158–160].

On this thesis, s-SNOM measurements are done with a commercially available setup (neaSNOM, neaspec), provided with a step-tunable MIR laser (CO_2). Figure 3.3 shows the measurement data which corresponds to the trilayer graphene flake in Figure 3.2 b). First, in Figure 3.3 a), the AFM topography (mechanical amplitude) measurement is shown. Here it can be observed that the area of the flake previously identified as trilayer graphene has some inhomogeneities on its topography. This can be attributed to different origins such as dirt, cracks or ripples among the surface of the flake. A portion of the flake free of inhomogeneities is identified and pre-selected to use. Figure 3.3 b) and c) are the results of the reflectivity (optical amplitude) and the absorption (optical phase) of the NIR field on the sample surface (CO_2 laser tuned at a 10.551 µm wavelength). Here, a difference in the absorption line as a consequence of a change in the electronic band structure is measured and identified from a change of contrast in the optical conductivity. Such changes can be designated to the presence of ABC and ABA stacking areas among the flake, using both measurements shown in Figure 3.3 b) and c), which provide a clear identification of different domain regions among the flake surface. Here, it is important to keep in mind that a s-SNOM measurement only delivers information of a change in the optical absorption and reflection of the sample surface, from which is possible to distinguish lower-scattering and higher-scattering amplitude domains. In order to assign these domains to a specific stacking order, the s-SNOM measurement needs to be compared with the Raman spectra of the flake to confirm the domain assignment for either rhombohedral or Bernal stacking order. This way, from a combination of all the measurements and characterizations presented in this section, the rhombohedral and Bernal stacking order areas of a few-layer graphene flake are revealed and identified. In the following section, the fabrication procedure of a free-standing dual-gated device with a rhombohedral graphene flake is described with detail.

3.1.2 Design and fabrication of devices

Structuring and contacting

A first step for fabricating free-standing graphene devices is structuring and contacting the graphene flakes. To do this, a standard EBL technique [145] is used, for which a layout design of a mask is made. Figure 3.4 a) shows a mask design on the area close to the graphene flake. A total of five lithography masks are used for different fabrication steps. As enumerated in Figure 3.4 a), a first mask is used for shaping the graphene flake as a rectangle, with Reactive Ion Etching (RIE). A second mask is used for patterning the source and drain (SD) contacts on the graphene flake. For the case of dual gated devices, a third mask is used to make a spacer between the previous layers and the top gate. The top gate is then fabricated using a fourth lithography mask. Finally, a fifth lithography mask is used to pattern the leads to the contact pads on the substrate, for connecting bond-wires to the graphene devices. All the EBL steps are performed using an e-Line system (Raith), as described on the next paragraph.

Before starting, the substrates with the graphene flakes of interest are cleaned with acetone and isopropanol, about 3 minutes in each solvent, followed by rinsing them and blow drying them with a N_2 gun. Figure 3.4 b) shows a scheme of the EBL procedure in an example to evaporate metal contacts. After cleaning, the substrates are pre-heated for several minutes at 150 ºC on a hot plate and then spin coated with a positive polymer

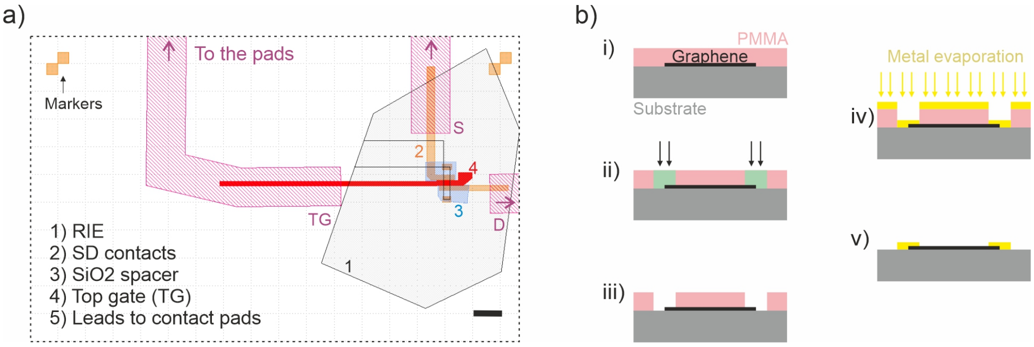

Figure 3.4: Electron Beam Lithography procedure. a) EBL mask design for a dual-gated free-standing graphene device. Scale bar 4 µm. b) Procedure for EBL patterning and fabrication of metal contacts. i) PMMA spin coat on the substrate containing the flakes. ii) e-beam beam exposure. iii) Developing to dissolve the e-beam exposed parts of the PMMA. iv) PVD deposition of metals. v) Resulting sample after removing the PMMA during lift-off.

resist (PMMA 950k 4,5 %) for 65 s at 4000 rpm. This results in a PMMA layer of 250 nm, represented in pink in Figure 3.4 b), i). After spin coating the resist, the samples are soft-baked for 3 minutes at 150 ºC in a hot plate. The masks are designed such that an electron beam (e-beam) exposes the area which is going to be etched or covered by a material. For smaller structures (designed within a 100 µm x 100 µm area), the beam parameters used are ETH 10kV, dose 120 $\mu C/cm^2$, write-field 100 µm, step size 2 nm and aperture 10 µm. For bigger structures (designed within a 1000 µm x 1000 µm area), 10 kV and 170 $\mu C/cm^2$, 1000 µm write-field, 60 nm step-size and 60 µm aperture are used. After e-beam exposure, the structures are developed in a 1:3 mixture of metyl isobutyl keton (MIBK) and isopropanol (IPA), for 2 minutes if one layer of PMMA is used and 3:30 minutes when two layers are used. This dissolves the parts of PMMA which have been exposed by the electron beam, represented in green in Figure 3.4 b), ii). The developing process is stopped by dipping the substrates in IPA, resulting as illustrated in Figure 3.4 b), iii). After development, the samples are treated with UV-Ozone (UV Ozone Cleaner, Ossila) for 1:30 min, to improve the contact resistance [161–163].

The first EBL mask used is intended to etch some parts of the graphene flake which are not of interest (i.e. with unwanted thickness or stacking order), leaving it with a rectangular shape. This is performed using one PMMA layer. The EBL mask is defined such that a rectangular area of width 1 µm and length 4 to 8 µm is protected by the PMMA while the remaining (non-protected) part is exposed to a dry etching process. The rectangle mask length is designed to take advantage of the biggest surface possible of the flake which possess the desired characteristics. The width is planned for a 1 µm × 1 µm square channel on the final device. This is important in order to study the QHE in samples with two-terminal contacts, for the reasons pointed out in chapter 2, section 2.2. The dry etching process consists of RIE (Oxford PlasmaLab) with a flow of 40 sccm of O_2 at 80 W and 40 mTorr during 18 seconds. The etching parameters are tested to efficiently remove few-layer graphene flakes exposed. Also included in the recipe, a PMMA etching rate of 100 nm/min ensures that the mask protects the flake until the end of the etching process. The second EBL step is made to pattern metallic contacts to the multilayer graphene flake and is performed with one PMMA layer. In this step, 4 nm Cr and 60 nm Au are deposited, as pictured in Figure 3.4 b), iv). The third EBL step is made using 2 layers of PMMA to thermally evaporate 150 nm of SiO_2 as a spacer between the graphene and the top gate. The fourth and fifth lithography steps are also performed with 2 layers of PMMA. Here, 4 nm Cr and 160 nm Au are deposited to make the top gates and the bigger contact pads for bond-wiring the devices on a chip. For the bigger contacts, additionally to the UV-Ozone cleaning, the sample is also treated for 1 min with RIE (with same parameters as in the first lithography step). This improves the adhesion of the contacts to the SiO_2 surface by removing PMMA residues from previous lithography steps as well as glue residues from the exfoliation and transfer of flakes. After material deposition (and after the first RIE), a lift-off process in hot acetone (< 48 ºC) is performed. This process removes the non-exposed areas of PMMA as well as the evaporated material thin-films on top of these areas, leaving a result as exemplified in the sketch on Figure 3.4 b), v). After the lift-off is completed, the samples are immersed one more time in acetone and then a few minutes in isopropanol to clean them, after which they are blown dry with a N_2 gun. It is worth mentioning that both Cr (adhesion layer) and Au are used as they are stable in hydrofluoric acid (HF) [164], which is used for the “suspension” technique described in the following paragraph.

Suspension

Figure 3.5 a), top, shows a scheme of a dual-gated few-layer graphene sample as it results after the EBL and PVD steps described in the previous paragraphs. To make the graphene free-standing between the top gate and the bottom gate, the sample is dipped into a buffered oxide etchant (BOE) for 100 seconds to remove ∼150 nm of SiO_2. The etching rate is achieved using BOE 7:1 (HF : NH4F = 12.5 : 87.5 %, VLSI-quality). The process occurs isotropically for the areas which are not covered by the metallic Cr/Au contacts and faster around the graphene [48]. In the resulting bridge-like structure, the metallic contacts which hold the graphene are supported by a SiO_2 column, as schematized in Figure 3.5 a), bottom, and shown in the false-coloured Scanning Electron Microscopy (SEM) image on Figure 3.5 b). To stop the etching reaction after 100 s, the samples are immersed in water two times for a few seconds, then in acetone and lastly in ethanol. To avoid surface-tension-induced collapse of the suspended graphene structures [48], the samples are dried using a Critical Point Dryer (CPD, Leica EM CPD300). The working principle of the CPD technique makes use of the thermodynamic end point of the liquid-vapor critical point, which is the end point of the pressure-temperature curve that sets the conditions for a liquid and its vapor to coexist. At the critical point, the physical properties of liquid and gaseous phases are not distinguishable [165]. So, compounds which are at the critical point can switch into liquid or gaseous phases without crossing the interfaces between each phase, thus avoiding surface tension induced damage effects of a specimen immersed in the liquid phase of the compound [165]. To start, the samples which were kept in ethanol are transferred into the CPD sample chamber, which is also

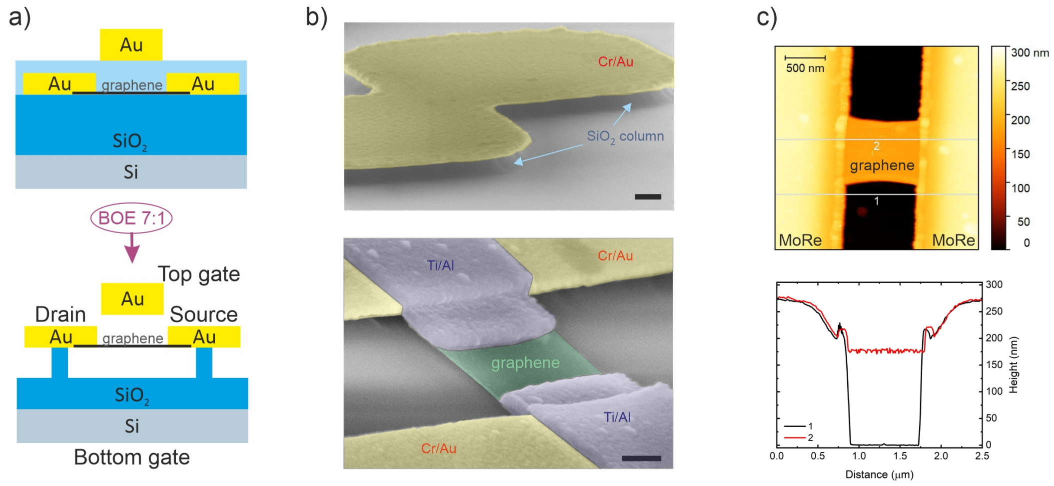

Figure 3.5: Fabrication of free-standing samples. a) Sketch of the structures before and after wet etching for dual-gated suspended few-layer graphene devices. b) SEM false-coloured images (10 kV, 8 mm work distance, 90° tilt, aperture 20 µm, in-lens), scale bar 200 nm. Top: Cr/Au marker showing the SiO_2 column that supports the metallic structure. Bottom: free-standing graphene device with superconducting contacts (Ti/Al) and Cr/Au contacts for structural support, without a top gate. c) AFM image of graphene free-standing between superconducting contacts (MoRe), without a top gate, and profile line cuts along the graphene junction channel.

filled with ethanol. Inside the chamber, the ethanol is replaced against liquid carbon dioxide (CO_2), whose critical point is at 31 °C and 74 bar. After completely replacing the exchange fluid (ethanol) with liquid CO_2, the liquid CO_2 is brought to its critical point and converted to the gaseous phase by decreasing the pressure at constant critical point temperature. Figure 3.5 b), bottom, and Figure 3.5 c) show respectively a false-coloured SEM and a AFM images of fully processed graphene-based free-standing devices (without a top gate), after drying them in the CPD. Further free-standing devices which have been fabricated during this thesis are shown in chapters 4 and 5, as well as in the appendix A.1 of this thesis.

3.1.3 Chip carrier integration and current annealing

To perform experiments at cryogenic temperatures, successfully fabricated samples are fixed with silver conductive paste (Ferro GmbH) onto a home-made chip carrier with 24 gold pins. Figure 3.6 a) shows a photograph of a sample on a home-made chip carrier. As indicated in the Figure, the silver paste is also used to build an electrical connection between the bottom gate and two of the chip carrier gold pins. The Cr/Au contact pads leading to the drain-source terminal contacts and the top gate of the device are connected to the chip carrier pins with gold wires, using a wedge bonder (K&S 4523 Wedge Bonder). In order to avoid gate leakages and possible breaking of the wires when cooled down to very low temperatures, a wire bond with a bend loop shape is made, as sketched in the inset of Figure 3.6 a). Once the connections to the chip carrier are done, the electrical contacts of the bonded devices are first tested in a probe station setup at room temperature. This

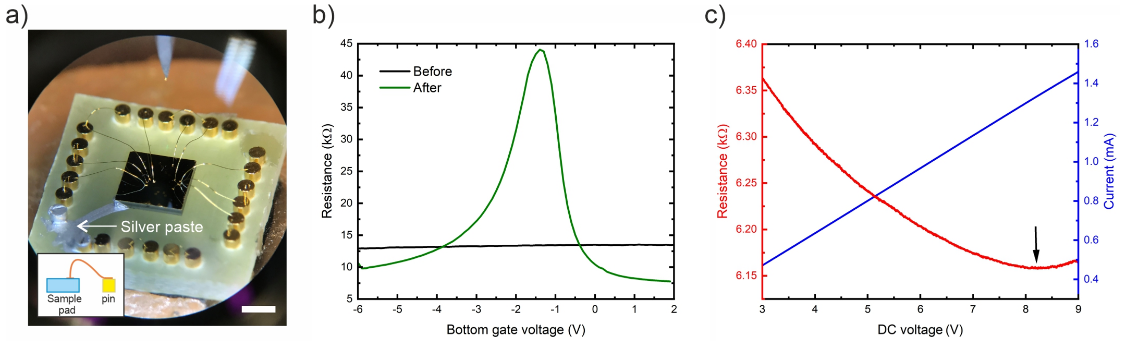

Figure 3.6: Chip carrier integration and current annealing. a) Photograph of a sample mounted on a chip carrier at a bond wiring machine. The Cr/Au pads of the sample are bonded with a gold wire to the gold pins of the chip carrier. Scale bar 2 mm. Inset: sketch of a bond wire loop. b) Two-contact resistance vs bottom gate voltage for a graphene sample before (black) and after (green) current annealing, when the CNP of graphene is observed. c) Annealing curves before measuring the green plot in b). A DC current is applied until the voltage difference between contacts surpasses around 1 V the saturation point of the resistance, indicated by the black arrow on the red curve. The step-size for the voltage ramp is 0.002 V.

setup consists of needle probes that are used as electrical contacts, for instance, to the source, drain and gates of the devices. By applying a small voltage difference between two needles using a source-measure device (SourceMeter 2450, Keithley), an I-V curve of the relevant connections to the chip carrier pins is measured. An important check is to ensure that the connections are working and that there is no unwanted electrical shortcuts or leakages. Additionally, this measurement serves to verify that the room temperature resistance on the multilayer graphene channel is as low as possible from fabrication. This is between 500 Ω and 20 kΩ, considering the best and worse acceptable limits. A low measured magnitude of this resistance is taken as a selection criterion for promising fabricated devices.

At the end of the fabrication processes described in section 3.1.2, it is inevitable that the few-layer graphene flakes result contaminated with PMMA residues. Nonetheless, in free-standing graphene it is possible to remove in-situ contaminants on the graphene surface and greatly improve the device quality by a cleaning process of current annealing [166, 167]. This technique consists in forcing a large current flow through the suspended device, between the source and drain contacts to the flake, to remove adsorbed contaminants [166]. Figure 3.6 b) shows a measurement of the two-terminal resistance as a function of the bottom gate voltage for a free-standing graphene flake, before and after current annealing. The cleaning process should result in the observation of the Charge Neutrality Point (CNP) in a resistance versus gate voltage measurement. Once the CNP is observed, additional iterations of the current annealing are performed in order to improve the sample quality. This results on a better centering of the CNP with respect to the zero top and bottom gate voltage values and a sharper peak of the resistance around charge neutrality. To avoid the risk of breaking the device by the strong current flow, it is advisable to perform the current annealing process carefully. This is, by ramping up and down the voltage difference from zero to an upper fixed value, increasing the upper limit step-wise until the saturation point in the resistance is observed. This point is marked with an arrow on Figure 3.6 c). Usually, several iterations of the current annealing curve are performed until observation of the CNP. After every iteration, it is a good check to measure the resistance as a function of both top and bottom gates, to verify that there are no gate leakages nor collapse of the suspended structures. The best cleaning results are achieved when reaching DC voltages up to approximately 1 to 1.5 V beyond the saturation point of the resistance. This assumes current values around 1 mA for devices with a (few-layer) graphene channel of 1 µm × 1 µm surface area. The current annealing process is performed after loading the samples in the measuring setup of use, at temperatures between 1.6 K and 2.5 K for the dilution refrigerator system and around 4 K for measurements in a Helium Dewar. These setups are described in the following section.

3.1.4 Measuring setups: dilution refrigerator system and 4K station

Within this thesis, the electrical transport measurements in free-standing dual-gated graphene devices are performed in a cryogen-free dilution refrigerator system (Dilution Refrigerator BF-LD250, Bluefors). The system is equipped with a superconducting magnet that delivers magnetic fields up to 14 T. The magnetic fields can be applied perpendicularly or parallel to the sample, by rotating the sample holder when loading. Moreover, a heater control (Lakeshore) allows setting fix temperatures within a range between 10 mK and 40 K. To reach probe temperatures down to 10 mK, the DR obtains cooling power from the heat produced by mixing the 3-He and 4-He isotopes. Figure 3.7 a) shows a scheme of its main constituting parts. Inside the cryostat, represented by the area enclosed with a black dashed line in Figure 3.7 a), several stages are cooled down in sequence by transferring heat between each other until the lowest temperature is reached at the last stage. This is done with two closed-cycle cooling systems. One is a pulse-tube refrigerator system, which uses 4-He at a pressure of few hundred mbar as a refrigerant and provides cooling power down to ∼3 K. This is possible thanks to a phase transition from a normal fluid into a superfluid of pure 4-He at saturated vapor pressure. The other is a dilution refrigerator system (or dilution unit), where 4-He is mixed with 3-He and, instead of forming two separate pure phases, an amount of 3-He in the 4-He phase remains finite [168], constituting a diluted phase. By pumping on this phase, 3-He atoms evaporate and additional atoms from an 3-He-rich phase are transferred to the diluted phase [168]. This process costs energy and, since this energy is taken from a well-isolated environment (the mixing chamber), cooling occurs. Working at such low temperatures imply challenges on the electrical wire design inside the cryostat. In particular, the wires that connect the sample to the measurement units introduce heating and must be thermalized properly. This is done through a series of thermalization stages provided by Bluefors, indicated by the grey horizontal lines in Figure 3.7 a), and by several filters stages, not shown in the Figure, self-made by Dr. Felix Winterer (see details in Ref. [169]). A total of 24 con-

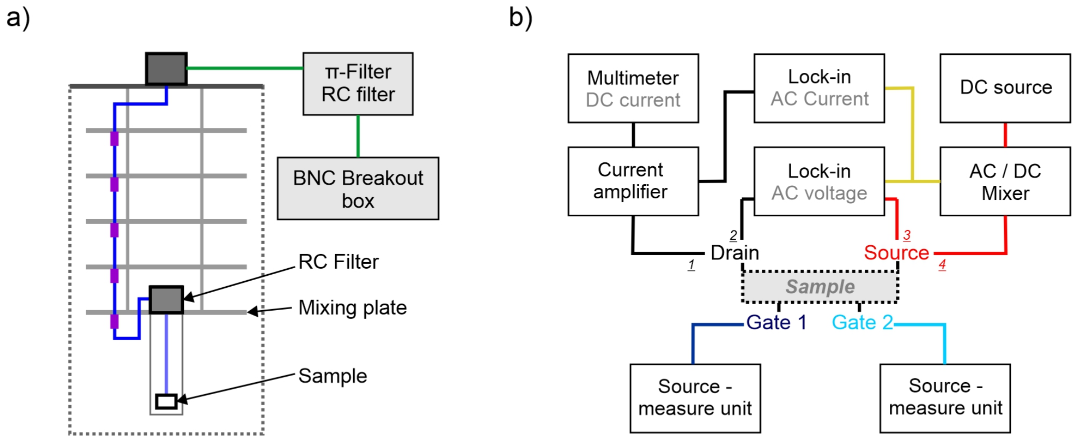

Figure 3.7: Measuring setup for the experiments on free-standing graphene. a) Wiring of the cryostat. The blue (*green*) lines indicate twisted (*non-twisted*) pairs. The wires pass through a π-filter, starting from the breakout box, and then through an RC filter before entering the cryostat (black dotted area). Inside the cryostat the wires are thermalized at every temperature stage (grey horizontal lines) through bobbins (purple). Then they pass through another RC filter at the mixing plate, to reach the sample. b) Quasi-four point measuring electronic components.

nections reach out the sample and each of them constitute individual probes; 20 of them have regular filters and are used as probe terminals to contact the sample and 4 of them, equipped with stronger filters, are used as gate connections [169]. All lines are grouped into twisted pairs to minimize electromagnetic noise. Additionally, for the gate wires, a π-filter coupled to an RC filter prevents high-frequency noise from entering the cryostat. Inside the cryostat, the wires are thermalized at every temperature stage through bobbins (provided by Bluefors), represented in violet in Figure 3.7 a). At the mixing plate, a low-pass RC filter stage (also home-made as part of Ref. [169]) is positioned to maximize thermalization. Measurements in the dilution refrigerator are performed for the experiments that require temperatures as low as 10 mK. For device testing and other experiments that were proposed on the span of this thesis, for example, on graphene samples with superconducting contacts of critical temperatures in the K order of magnitude (see appendix A), a so-called 4K station is used. This setup consists on a vacuumed stick with electrical connections to the sample that is inserted into a He-Dewar. Once inside the Dewar and after thermalization, measurements can be performed at the fixed temperature of liquid He. In the following section, details on the electrical measuring configuration used for both setups are given.

3.1.5 Electrical measurements and calibration

The electrical measurements for the free-standing graphene devices investigated during this thesis are preformed using two-point and quasi-four-point configurations. Figure 3.7 b) shows a scheme of the electrical measurement setup as it is implemented for both the dilution refrigerator system and the 4K station, in a quasi-four point configuration. To apply external gate and bias voltages and to track the current or voltage drop in

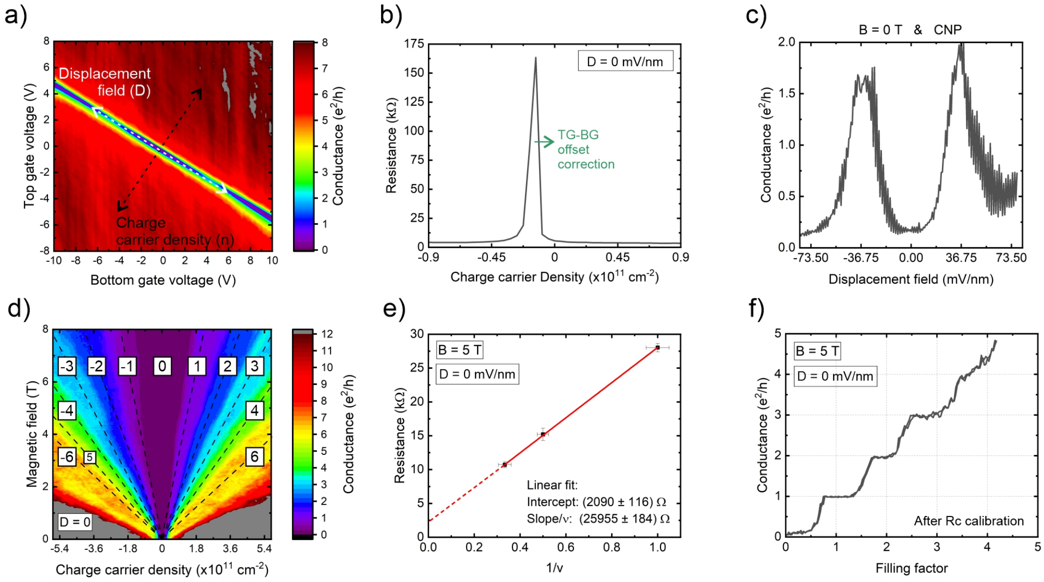

Figure 3.8: Electron transport calibration measurements for dually-gated suspended trilayer graphene. a) Differential conductance at B =0 T as a function of the top and bottom gate voltages. The white (black) dashed line indicates the D (n) scan axis. b) Resistance as a function of n at $D = 0$. Adjusting the top and bottom gate voltage offsets corrects for the CNP centring. c) Conductance as a function of D after correcting the offsets to centre the CNP at $n = 0$. d) Fan diagram between 0 and 8 T. The numbers inside white boxes indicate the calculated filling factors according to their slopes traced to 0 T (black dashed lines). e) Resistance of the QHE plateaus as a function of the inverse filling factor to obtain the contact resistance (intercept). e) Conductance plateaus as a function of filling factor after subtracting the contact resistance.

the graphene devices, source-measure units (SourceMeter 2450, Keithley) are used. A standard lock-in amplifier technique with four contact points to the sample constitutes a quasi-four-point measurement, as shown in Figure3.7 b). Starting at the upper right paths of the measuring circuit represented in Figure3.7 b), a home-made AC/DC mixer inductively modulates the AC reference signal from the lock-ins (78 Hz and 2 Vpp) onto a DC bias (SourceMeter 2450, Keithley), before it reaches the sample. By means of different resistances for the AC and DC component, the voltages are converted to a combination of AC and DC currents that can be applied on the sample source contact. At the drain contact, the current goes through a current amplifier (Model 1211, DL Instruments) and is measured simultaneously with a lock-in (Lock-in SR830, Stanford Research Systems) and a multimeter (Multimeter 34461A, Keysight). At the same time, the voltage drop over the device is measured by an additional lock-in (Lock-in SR865, Stanford Research Systems) building this way the a quasi-four-point measuring geometry (contacts 1, 2, 3, 4 in Figure 3.7 b)). For automation of the measurements as well as to calculate useful output parameters of the system (e.g. differential conductance and charge carrier density), a python-based measuring interface (SuperFunAnalyzer, SFA) developed by Dr. Felix Winterer as part of his doctoral thesis (see Ref. [169]), is used.

After the current annealing process explained in section 3.1.3, a conductance map as a function of the top and bottom gate voltages (V_T and V_B, respectively) is measured.

Figure 3.8 a) shows this result on a trilayer free-standing graphene sample, as an example. By sweeping V_T and V_B, both D and n are simultaneously tuned. An advantage of a dual gated device is the possibility of disentangling D and n to tune them independently [45,47]. To begin, n can be decomposed into contributions from both V_T and V_B as

$$n = (n_T + n_B) = \frac{C_T V_T + C_B V_B}{e} = \frac{C_B}{e}\left(\alpha V_T + V_B\right), \tag{3.1}$$

with C_T and C_B the capacitances per unit area for the top and bottom gates, respectively, e the electron charge and $\alpha = C_T/C_B$ [47]. To follow, D, which points perpendicular to the graphene channel in the free-standing device, is given by

$$D = \frac{1}{2}\left(D_T + D_B\right) = \frac{C_B}{2\epsilon_0}\left(\alpha V_T - V_B\right), \tag{3.2}$$

i.e., the mean value of the D from the V_B and V_T electrodes perspectives [47]. For the experiments, it is useful to combine the equations (3.1) and (3.2 to facilitate setting arbitrary combinations of n and D by choosing a value of V_B and V_T. This results in

$$V_B = \frac{1}{2C_B}\left(en - 2\epsilon_0 D\right) + V_{B0} \quad and \quad V_T = \frac{1}{2\alpha C_B}\left(en + 2\epsilon_0 D\right) + V_{T0}, \tag{3.3}$$

with V_{B0} (V_{T0}) a voltage offset to balance the effect of charge traps screening of the bottom (top) gate field. The first step to make practical use of equation (3.3) is to know α. This is obtained from a measurement of the slope of the line at charge neutrality (white dashed line in Figure 3.8 a)). To do this, a Gaussian fit of the resistance as a function of V_B (V_T) at fixed V_T (V_B) is used to know the position of the maximum resistance points. These points are fit with a linear function, whose slope is $1/\alpha$. Figure 3.8 b) shows a measurement as a function of n at $D = 0$, done using equation (3.3) after replacing the value of α. The offsets are used to adjust the resistance maximum (CNP) to $n = 0$. Figure 3.8 c) shows the conductance as a function of D at $n = 0$, measured after compensating the voltage offsets in the measurement. To conclude with the calibrations, the value of C_B is adjusted. First, a rough estimation from geometrical arguments is used. Then, from a measurement of the fan diagram, shown in Figure 3.8 d), the position of the conductance plateaus is forced to match the values given by $n = \nu eB/h$ (see chapter 2, section 2.2.2). This is done by adjusting the scaling factor of the n axis, which is proportional to C_B in equation (3.1), making the slope of each ν traced to $B = 0$ T be at the right n value. Using this calibration, the resistance of the QHE plateaus are plot as a function of $1/\nu$, as shown in Figure 3.8 e). A linear fit of these data points yields the contact resistance (R_C) of the device which corresponds to the intercept and, if the calibration is correct, the slope/ν value of this fit overlaps with the von Klitzing constant, $R_K = h/e^2 = 25812.80745...\ \Omega$. To conclude, Figure 3.8 f) shows a measurement of the QHE conductance plateaus as a function of ν, after all calibrations are done and R_C is subtracted.

3.2 Devices for the investigation of Charge Density Wave phases in 1T-TaS$_2$

The experiments to study CDW phases in the TMD 1T-TaS$_2$ presented within this thesis are part of a collaboration project between the group of Prof. Dr. Thomas Weitz and the group of Prof. Dr. Claus Ropers (Max Planck Institute for Biophysical Chemistry and University of Göttingen). This section presents the work for the optimization of the sample design and environment realized as part of this thesis in the context of the collaborative research project. The most important aspects for fabricating electrically contacted samples with bulk and thin films of 1T-TaS$_2$ on a TEM membrane as a substrate are given. By the end of this section, the main setups for the experiments performed on this topic as well as the measurement techniques that were used, are described.

3.2.1 Obtaining 1T-TaS$_2$ flakes

To conduct experiments for simultaneous structural and electrical characterization of CDW phases in 1T-TaS$_2$, devices of this layered van der Waals material are fabricated on commercially available TEM membranes. Figure 3.9 a), top, shows a photograph of a TEM substrate as the used on this thesis from a bottom view. It consists of a 200 µm thick Si frame of 3 mm diameter size, covered by a SiNx membrane of thickness 20 nm. As sketched in Figure 3.9 a), bottom, the Si frame has squared windows whose area is covered only by the SiNx membrane. A TEM substrate can have a single window or an array of windows, as shown in Figure 3.9 a). For the fabrication of 1T-TaS$_2$ two-terminal devices, substrates with an array of 3×3 windows of size 100 µm × 100 µm each is used. For the fabrication of free-standing samples on a circuit configuration with coplanar strip lines and a Si photoconductive switch, an array of 4×4 windows of size 20 µm × 20 µm each is used. These substrates also have a 1 µm diameter hole in the centre of the windows, made with a Focused Ion Beam (FIB). To obtain 1T-TaS$_2$ flakes on the substrates, the fabrication methods of exfoliation and transfer as well as stamping are performed, as described in the next paragraphs. Before starting any fabrication step, the substrates are cleaned by dipping them in acetone and isopropanol for several minutes and carefully rinsing and drying them with an N$_2$ gun. Afterwards, they are heated on a hotplate for several minutes at 150 ºC to evaporate further residues. The TEM substrates are also exposed to an oxygen plasma for 5 min at 50 W in 10 sccm O2 (PICO Plasma Cleaner, Diener). This last step is skipped for the 1T-TaS$_2$ flakes on Si/SiO$_2$ substrates which are meant be picked-up for stamping. Given the fragility and small dimensions of the TEM membranes, some aspects for their use in fabrication of devices with thin films of 1T-TaS$_2$ should be considered and will be commented on the span of this section.

Exfoliation and transfer

Thin films of 1T-TaS$_2$ are obtained from the bulk crystal (1T phase Tantalum Disulfide, HQ graphene) by mechanical exfoliation, as described in section 3.1. Two different

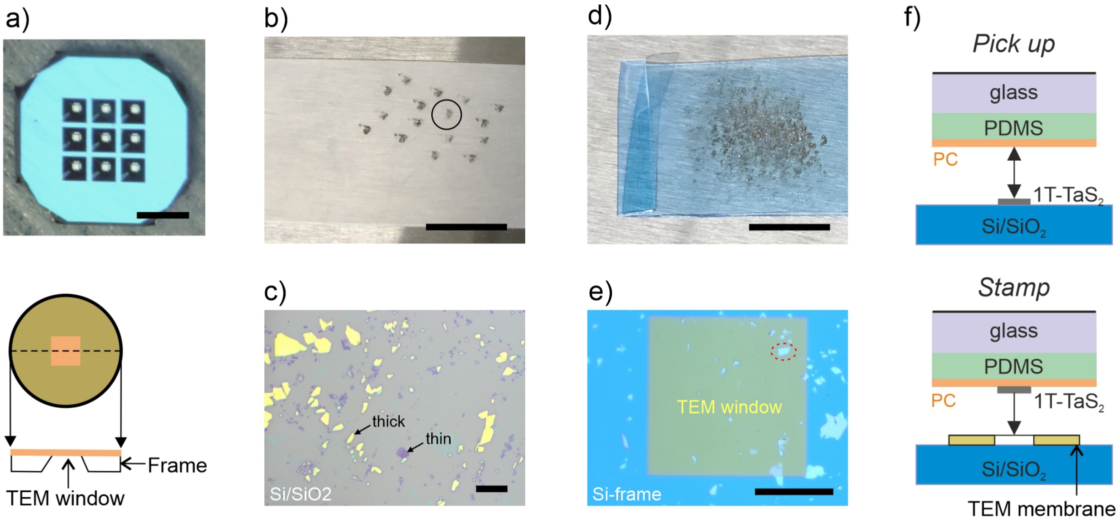

Figure 3.9: Exfoliation, transfer and stamping of 1T-TaS$_2$ flakes. a) Photograph of an upside-down TEM membrane with 9 windows (photo adapted from [170], scale bar 1 mm) and a draft of a cross section of a TEM grid with 1 window on a 3 mm diameter dimension. b) Photograph of a Magic tape with exfoliated 1T-TaS$_2$ flakes. Scale bar 500 mm. c) Optical microscope image of the transferred 1T-TaS$_2$ flakes from the Magic Tape onto a Si/SiO$_2$ substrate (300 nm oxide). Scale bar 100 µm. d) Photograph of a blue Nitto tape with exfoliated 1T-TaS$_2$ flakes. Scale bar 500 mm. e) Optical microscope image of transferred 1T-TaS$_2$ flakes from the blue Nitto tape onto a TEM membrane. The TEM window is covered by a 20 nm thick SiNx membrane. Scale bar 50 µm. f) Image adapted from [171]. Scheme of the stamping method for placing 1T-TaS$_2$ flakes on a TEM membrane.

adhesive tapes have been tested for the exfoliation of 1T-TaS$_2$ flakes: The blue Nitto tape (SWT20+, Nitto inc.) and the commercial adhesive tape (Magic Tape, Scotch). As a result, it is found that the commercial adhesive tape is convenient for obtaining a higher proportion of mono- and few-layer 1T-TaS$_2$ flakes when directly transferring them onto a SiO$_2$ substrate. This tape is nevertheless not adequate to use on a TEM membrane, not only because of the amount of glue residues delivered after the transfer process, but also it has been found that the adhesion of this tape can easily damage the SiNx membrane on the windows. For TEM membranes, the Nitto tape not only brings the benefit of a final result with no glue residuals, but also allows a softer transfer of the flakes onto the delicate SiNx membranes, avoiding possible collapse of the windows after the transfer process. Figures 3.9 b) and d) show a photograph of the tapes with exfoliated 1T-TaS$_2$ flakes before transferring them onto a substrate. For both tapes, the starting point for the mechanical exfoliation procedure is a small piece of the commercial crystal not bigger than 1 mm × 1 mm. When using commercial tape, the exfoliation is performed by folding the tape on itself and peeling it off several times, taking care that for each iteration the peeled off crystal layers end up on different regions of the tape. This is, without overlap of crystal layers from a previous fold and unfold sequence. The process is repeated until the areas of the tape which contain the material appear visible to the naked eye as a homogeneous pale-grey area rather than shiny silver, as it is the case when starting the procedure. Then, a pale-grey area on the tape is chosen to transferring flakes onto a

Si/SiO$_2$ substrate, e.g. the encircled in Figure 3.9 b). For the blue Nitto tape, the exfoliation procedure is slightly different. Here, the tape with a small piece of 1T-TaS$_2$ crystal is folded and unfolded several times on itself to produce a region on the tape covered with the material, without considering overlap of material layers. This method is found best suited when the goal is to transfer a big quantity of bulk flakes. For transferring the flakes from the adhesive tapes to a substrate of choice, the tape is gently pressed on and peeled off the substrate. The best transferring results are found by heating the substrates at 110 ºC before transferring the flakes. Figure 3.9 c) and e) show an optical microscope image of the result of transferring 1T-TaS$_2$ flakes onto Si/SiO$_2$ and a TEM membrane, respectively. For the flakes on Si/SiO$_2$, a quick distinction between very thin and bulk flakes is possible by observing a difference in the optical contrast. To show an example, thinner and thicker flakes are pointed with an arrow Figures 3.9 c). A study of the real thickness is done using AFM imaging, as described in section 3.2.2. For the experiments within this thesis, bulk flakes in the TEM window area are localized and pre-selected. An example of a candidate flake is enclosed by a red dashed line in Figure 3.9 e). More details about the selection criterion and techniques for finding the flakes of interest are given in the section 3.2.2.

Stamping

To have an accurate control on the position in which a 1T-TaS$_2$ flake will be on a substrate, a stamping method is used [171, 172]. Figure 3.9 f) shows a schematic of the technique. For the work within this thesis, the flakes to be stamped are first obtained by exfoliation and transfer onto a Si/SiO$_2$ substrate, as described before. To pick up a flake of interest from the substrate, a stamp constituted by a piece of glass with a block of polydimethylsiloxane (PDMS) covered by a polycarbonate (PC) film is used. The PDMS (Sylgard 184, Dowsil) is prepared beforehand in a petri dish by mixing a base-curing agent ratio 10.5:1, which is then let dry at 5 mbar for 24 hours. The resulting PDMS has a thickness of approximately 2 mm. The PC films are prepared using a film application machine (ZAA 2300, Zehntner) with an 8 wt. % solution of Poly-Bisphenol A carbonate (Sigma-Aldrich) diluted in chloroform. This delivers a final thickness between 10 and 20 µm. A blade (ZUA 2000, Zehntner) is used to make the films uniform with a pre-set height of 1675 µm and speed 6 mm/s. As a final step, the PC films are dried at room temperature in air for at least one hour. To prepare the stamp, a microscope (glass) slide is cleaned with isopropanol and blown dried with a N$_2$ gun, and a squared area ($\sim$ 2 mm×2 mm) in the centre of a double-sided adhesive tape is cut using a scalpel. The tape, now with a cut-out window, is adhered to the glass slide. After removing the protection layer of the tape to make it double-adhesive, a PDMS block is positioned in the window area. The PDMS block is obtained by cutting it with a scalpel from the petri dish, making it slightly smaller than the squared window on the tape. On this step, it is important to check that the PDMS area to cut is clean and free of bubbles. This is done either by naked eye or by inspecting it under an optical microscope. Another piece of tape is prepared as before but with a bigger window area ($\sim$ 4 mm×4 mm) and placed on top of a glass slide covered with PC film. The sides of the PC layer around the tape are cut to easily detach the PC from the glass slide with sharp edges. As a result, an adhesive tape with a window covered by PC film is obtained. This is placed on top of the PDMS block on the previous glass slide while the two adhesive tapes are kept in place. Finally, the stamp (glass/PDMS/PC) as illustrated in Figure 3.9 f) is ready to use.

A first step on the stamping procedure consists in picking up the flake of interest from a Si/SiO$_2$ substrate using the described stamp. Figure 3.9 f) illustrates the type of setup used for this purpose. It consists on a motorized X-Y-Z arm which holds with vacuum the stamp facing downwards (towards the upper face of the sample). In addition, the Si/SiO$_2$ with the 1T-TaS$_2$ flake of interest is fixed with vacuum onto a temperature-controlled motorized X-Y-Z stage, which is set at 40 °C. With an optical microscope, the vertical alignment between the stamp and the substrate is controlled, while the stamp is moved towards the substrate. When the stamp is almost touching the substrate and well aligned with the flake, using a fine position step-size, the stamp is gradually brought in contact with the substrate and the flake until the appearance of interference fringes are visible under the optical microscope. This indicates that the stamp is in contact with the sample. Then, by means of a temperature ramp, the contact between stamp and sample is driven in a controlled manner. Setting the stage temperature to 80 ºC, the 1T-TaS$_2$ flake sticks to the stamp. After releasing the contact between stamp and sample by cooling down from 80 ºC to 40 ºC, the motorized arm with the stamp can be driven up again. After this, the flake is picked-up from the Si/SiO$_2$ substrate and found on the stamp.

To stamp the picked-up flake, a new substrate is fixed onto the temperature-controlled motorized X-Y-Z stage with vacuum. For the sample prepared within this thesis, a 3 mm diameter size TEM substrate with a 4×4 array of 20 µm×20 µm size windows and a 20 nm thick SiNx membrane is used. The aiming spot to stamp the flake is a 1 µm diameter pin hole at the centre of a TEM window. To provide a better handling of the small and fragile TEM membrane, this substrate is pasted with carbon tape on top of a bigger Si/SiO$_2$ substrate for fixing it with vacuum on the temperature-controlled stage. On this second step of the dry transfer procedure, the hotplate with the substrate is first heated up to around 150 °C. Then, the stamp is taken close to the substrate while controlling the alignment of the flake with respect to the pin hole with an optical microscope. The stamp is gradually brought in contact with the substrate until interference fringes are seen and the substrate is almost fully covered by the stamp. Then, the substrate is heated up to 180 °C. After a waiting time of around 5 minutes, the PC on the stamp containing the flake should meld down on the substrate. Then, the motorized arm with the PDMS can be moved upwards. As a result, the PC film and the flake stays on the TEM membrane. Last, the substrate is immersed in chloroform for some minutes to remove the PC film.

As a remark, it should be noted that the stamping procedure which has been described and used in this thesis is a standard one. Based on the accomplished results, some aspects are recommended to modify in the future for the specific work with TEM membranes. For instance, contamination clusters are observed on the TEM membrane surface for the fabricated sample after immersing it in chloroform (see appendix A.2). For the sample

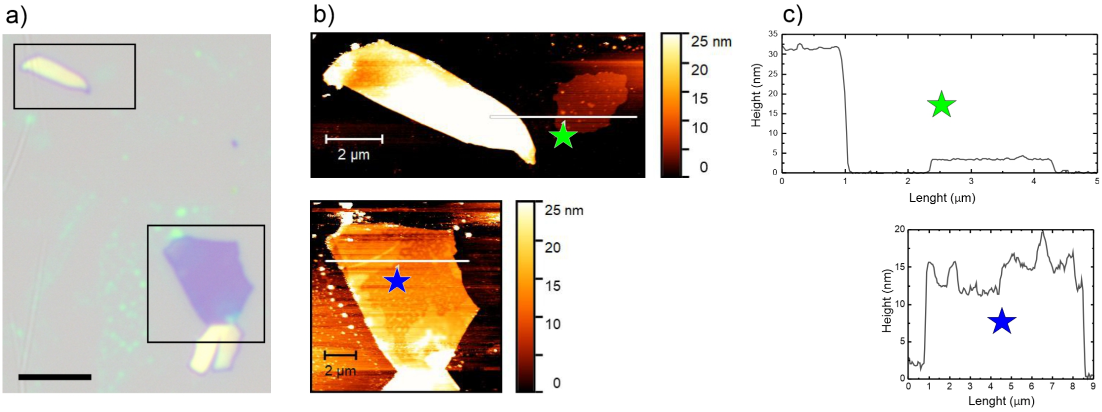

Figure 3.10: Optical and Atomic Force Microscope (AFM) images of different 1T-TaS$_2$ flakes. a) Optical microscope image of 1T-TaS$_2$ flakes on a Si/SiO$_2$ substrate exfoliated at air atmosphere. Scale bar 10 µm b) AFM images of the flakes enclosed on a). c) Measured profile of the AFM images, for the line profiles indicated in b) with a blue and a green star.

made within this thesis, the contamination found after dipping the sample in chloroform could be considerably removed by cleaning the samples several times in isopropanol, but some contaminated regions remained. In order to avoid this trouble, a stamping method without PC films could be implemented. This consists on skipping the pick-up step on the previously described stamping method by exfoliating and transferring flakes directly onto the PDMS to stamp them immediately afterwards on the targeted substrate [173].

3.2.2 Finding suitable flakes

Both for the case of 1T-TaS$_2$ flakes transferred onto Si/SiO$_2$ wafers and onto a TEM substrate, an optical microscope is used in a first place for localizing flakes. Once they are localized, their thickness is determined using an AFM. For the case of flakes on a TEM substrate, as shown in Figure 3.9 e), only bulk flakes are clearly visible under an optical microscope. On a Si/SiO$_2$ of a given oxide thickness, both thick (bulk) and thinner flakes are visible with an optical microscope in reflection configuration and their contrast can be correlated with the flake thickness, as for the case of graphene [144]. Figure 3.10 a) shows an optical microscope image of 1T-TaS$_2$ flakes on Si/SiO$_2$ with 300 nm oxide thickness using white light. Here, a rough distinction between bulk flakes and thin films of 1T-TaS$_2$ can be done by comparing their colours: thicker flakes appear yellow while thinner flakes on different shades of violet. For the experiments within this thesis which are intended to study bulk 1T-TaS$_2$ flakes, yellow flakes which look homogeneous on the optical microscope and have a width $\sim$ 1 µm and a length $\sim$2 µm are chosen for making devices with them. For the work with very thin films of 1T-TaS$_2$, it is important to know that the thinner the flakes, the more reactive in air atmosphere they become and, as they start to degrade, they lose optical contrast [141]. It has been reported that no degradation occurs for flakes thicker than 7 layers, a discoloration is observed as a function of time for flakes below 6 layers and the contrast decreases more quickly for thinner flakes [141].

To avoid degradation, the fabrication of samples with few-layer 1T-TaS$_2$ should be done inside a glovebox.

The AFM measurements within this thesis are performed in tapping mode with the commercial systems available (Dimension 3100 and Dimension Icon, Bruker; Jupiter XR, Asylum Research AFM). The tapping mode is a dynamic AFM technique that images the sample topography by scanning its surface with an oscillating cantilever. With this technique, the sharp AFM probe tip is not scanned across the sample surface while being in contact. Instead, the cantilever vibrates near its resonance frequency making the tip oscillate up and down. Under this condition, the probe comes into close contact with the surface intermittently while the amplitude of the cantilever oscillation is measured, detecting changes in the tip-sample interaction forces and thereby the sample topography [174]. Figure 3.10 b) shows AFM images of thin and bulk 1T-TaS$_2$ flakes exfoliated at air atmosphere onto a Si/SiO$_2$ wafer, which were first located using an optical microscope. The results on this Figure b) and c) also show that the very thin films (below 5 nm) are almost invisible under the optical microscope but revealed on an AFM measurement, while thicker flakes are easier to spot.

3.2.3 Design and fabrication of devices

To simplify the manipulation of the delicate TEM substrates on the subsequent fabrication steps, they are attached to the centre of a bigger Si/SiO$_2$ wafer, which plays the role of a supporting holder. To make this compatible with the following fabrication, the attachment is done by spin coating PMMA (950k 4,5 %) for 65 s at 3000 rpm and placing the TEM substrate immediately after, on the centre of the Si/SiO$_2$ wafer covered with PMMA. After gently pressing the TEM substrates with tweezers and baking at 150°C for a few minutes, the TEM grids with 1T-TaS$_2$ flakes are prepared for the following fabrication steps. First, the samples are spin coated with a positive polymer resist (PMMA 950k 4,5 %) for 65 s at 4000 rpm, resulting in a PMMA layer of thickness 250 nm on the TEM substrate. After this, they are soft-baked for 3 minutes at 150 ºC in a hot plate. A conventional EBL technique is then used to write electrical contacts to the 1T-TaS$_2$ flakes as explained in subsection 3.1.2. The smaller structures near the flake are written with ETH 10 kV, dose 120 µC/cm2, write-field 100 µm, step size 2 nm and aperture 10 µm, while the bigger structures like bond pads and connecting leads with ETH 10 kV, dose 170 µC/cm^2, write-field 1000 µm, step size 60 nm and aperture 60 µm. Then, the structures are developed in 1:3 MIBK:IPA for 2 min. This process dissolves the parts of PMMA which have been exposed by the electron beam and is stopped by immersing the substrates in pure IPA. Noteworthy, this does not remove the PMMA attachment of the TEM grid to the bigger Si/SiO$_2$ substrate, which is kept until the final fabrication step. After development and rinsing the samples with isopropanol, they are blown-dried with a N2 gun and next they are exposed to PVD of materials. For the two terminal contact devices, only one EBL step is implemented to evaporate 2 nm Ti / 40 nm Au contacts. For the devices with coplanar striplines and a photoconductive switch, a first EBL step

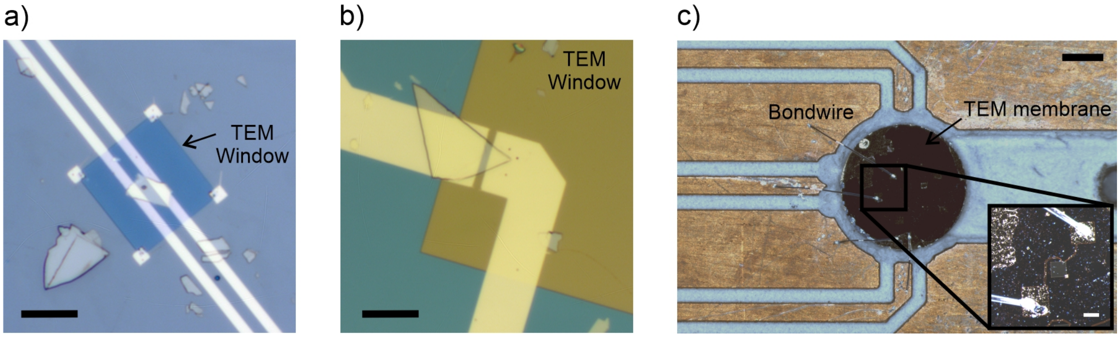

Figure 3.11: 1T-TaS$_2$ devices on TEM membranes. a) Optical microscope image of a 1T-TaS$_2$ flake contacted with coplanar strip lines. The flake is stamped on top of a 1 µm diameter hole at the centre of the TEM window, before fabrication of contacts. Scale bar 10 µm. b) Optical microscope image of a two-terminal device with a 1T-TaS$_2$ flake. The flake is obtained on the TEM windows by direct exfoliation and transfer, before fabricating metallic contacts. Scale bar 10 µm. c) Optical microscope image of the TEM holder with one sample electrically connected via aluminium bond wires. Scale bar 1 mm (black, top right). Inset: Two-terminal 1T-TaS$_2$ device on a TEM window bonded to the sample holder. Scale bar 100 µm (white, bottom right).

is performed to pattern the circuit, followed by PVD of 2 nm Ti / 90 nm Au. Then, a second EBL step is implemented to evaporate 100 nm Si, which constitutes a photoconductive switch. After each PVD step, the samples are dipped in acetone at 40 °C for several minutes, until the lift-off process is completed. This detaches the TEM substrate from its Si/SiO$_2$ support. Figures 3.11 a) and b) show optical microscope images of the two-terminal and coplanar strip lines devices fabricated with 1T-TaS$_2$ flakes on a TEM membrane. Additional microscope images of the devices with a photoconductive switch are given in the appendix A.2 of this thesis. As a final step, the fabricated devices are bonded with aluminium wires using a wedge bonder (K&S 4523 Wedge Bonder) on a chip carrier with chromium connectors, as shown on the optical microscope image in Figure 3.11 c). To do this, the TEM substrates are fixed at the middle of the sample holder, which has an opening for the TEM windows, with PMMA. In the following section, the measuring setups used during this thesis to investigate the 1T-TaS$_2$ samples are described.

3.2.4 Measuring setups: Closed-cycle Probe Station and Ultrafast Transmission Electron Microscopy setup

The experiments to study CDW phases in 1T-TaS$_2$ presented on this thesis involve two different experimental approaches. On the one hand, electron transport measurements in a closed-cycle Lakeshore probe system are performed in order to explore the critical parameters such as transition temperatures between C and NC phases in 1T-TaS$_2$ two-terminal devices. On the other hand, dark-field (DF) imaging in an Ultrafast Transmission Electron Microscopy (UTEM) setup, operating at room temperatures, is used to visualize the real space evolution of the dynamics of between the IC- and NC-CDW phases in a 1T-TaS$_2$ flake under application of external DC voltages. In what follows, the two experimental setups are described.

Closed-cycle Probe Station

To study the dependence of the resistance on 1T-TaS$_2$ devices as a function of the temperature, a probe station (Probe Station CRX-VF, LakeShore Cryotronics) is used. The system operates at a vacuum pressure $< 5\times10^{-6}$ mbar and is provided with up to four needle probes, which are used to build electrical connections between the device pads and an external voltage source (SourceMeter 2450, Keithley). By means of a self-contained closed cycle refrigerator (CCR), the probe station cools down to cryogenic temperatures unassisted. A temperature controller (Cryogenic Temperature Controller 336, Lake Shore Cryotronics) is used to set the temperature in a range between 5 K and 400 K. The samples studied in the probe-station are pasted with silver conductive paste in order to improve the thermal coupling between the sample and the thermal plate. As an additional safety measure, the TEM grids are kept in place by pressing them from the upper surface with an additional needle. Figure 3.12 a) shows a picture of the open setup with two loaded samples, indicating some of its components.

Dark-field imaging in Ultrafast Transmission Electron Microscope

Figure 3.12 b) shows a schematic view of the main constituting parts of the UTEM setup developed in the group of Prof. Claus Ropers. The setup is based on laser-triggered electron emission from a nanoscale photocathode, which provides a high-coherence ultrafast electron source. Among a range of possible applications for this setup, such as studying spatiotemporal dynamics with sub-nanometre spatial resolution [175], specifically tailored DF imaging was employed in the experiments presented here, to gain explicit contrast sensitivity to local modulations of the NC-CDW amplitude in 1T-TaS$_2$. To do such measurements on electrically connected 1T-TaS$_2$ samples (described in section 3.2.3), the specimen is placed between the electron source and a DF aperture array, implemented to filter the NC-CDW wave vector components in the back-focal plane of the objective lens, where a first electron diffraction pattern is formed. The high coherence character of the electron beam source ensures that diffraction spots are small enough to allow filtering with sufficiently small DF apertures. This prevents the image quality to be blurred or even dominated by inelastic scattering, as well as it prevents that the IC-CDW spots contribute to the image contrast. Finally, the real-space image is captured either on a direct detection camera (Direct Electron DE-16 in “counting mode”), or a conventional scintillator-coupled CCD (Gatan UltraScan 4000), to result as shown in the end of the column schematized in Figure 3.12 b) [176]. For the experiments performed within this thesis, the DF data are recorded using a camera system (TVIPS XF416, TVIPS) behind an energy filter (CEFID, CEOS). The DF mask used to obtain the results reported in chapter 6 of this thesis was designed by Till Domröse and fabricated in collaboration with Felix Kurtz, both from the group of Prof. Ropers. It consists on a home-made FIB etched tailored array of 72 small apertures, aimed at selecting the brightest second-order satellite reflections and block all other diffraction peaks. When the DF aperture array is inserted into the column of the electron microscope, only electrons scattered into NC-

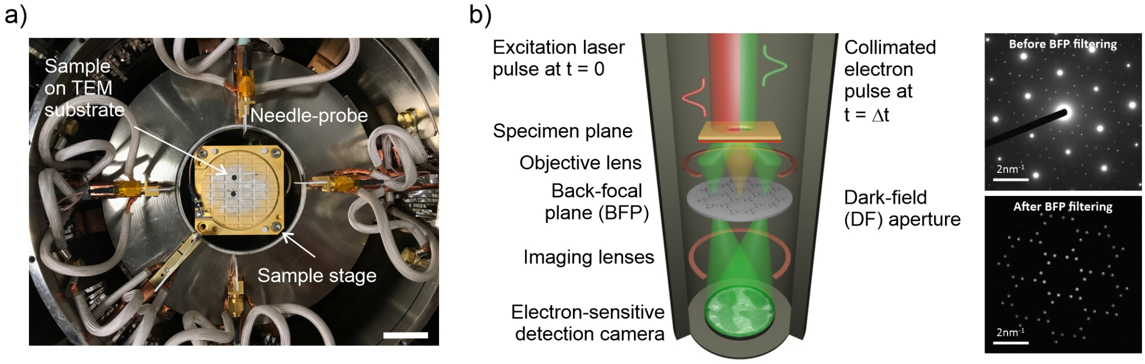

Figure 3.12: Closed-cycle Probe Station and DF mask configuration of the UTEM setup. a) Photograph of the probe-station load chamber with a two 1T-TaS$_2$ samples. The TEM substrates are pasted with silver paste to the sample stage of the Probe-Station for thermal contact improvement. A total of four needles can be used in the setup to electrically contact the sample. Scale bar 4 cm. b) Left: Diagram of the UTEM setup main parts. Electron (green) and optical (red) pulses are incident close to perpendicular on the specimen. A DF aperture array is placed in the BFP and can be rotated for alignment. Right: Electron diffractograms of a 1T-TaS$_2$ thin film at room temperature, without the DF aperture array (top) and with the DF aperture array on the electron beam path (bottom). Only superstructure reflections of the NC-CDW phase are transmitted through the aperture array. Image adapted from [176].

CDW satellite diffraction peaks reach the detector and contribute to the image contrast, while the elastically scattered electrons into main lattice peaks and IC-CDW diffraction peaks are blocked. The DF images reflect the local order parameter of the NC-CDW with a spatial resolution below 5 nm while inelastic scattering contributions account for some background in the image (even in the IC phase) [177]. As a result, direct imaging of CDW dynamics in the material is obtained, with a contrast unreachable by conventional bright-field imaging [176].

Chapter 4

Searching for correlated phases of rhombohedral trilayer graphene

One of the richest scenarios in quantum mechanics takes place when the physics of many-body interactions emerge. Since some years ago, rhombohedral graphene has been proven a suitable platform to study interaction effects in two dimensions. Such effects are predicted to be even richer when the system has more than two layers, because of the low energy bands becoming flatter for an increasing number of layers, with correspondingly large associated Berry phases. In spite of the recent advances for fabricating high quality graphene samples, experimental studies with rhombohedral graphene systems with more than two layers remain scarce. In this chapter, electron and magneto transport measurements on trilayer ABC graphene in a dual-gated free-standing device configuration are presented. This work has been dedicated to the search of correlated phases within trilayer ABC graphene. Following an approach of scanning different parameters of the system, the study leads to the revelation of spin magnetic states at charge carrier densities below 5×10^{10} cm^{-2} for rhombohedral trilayer graphene in a low dielectric environment. Moreover, when turning on an in-plane magnetic field, a hysteretic behaviour found when measuring the conductance as a function of the charge carrier density provides evidence of magnetic states in the system which are tunable by changing the charge carrier type. The efforts within this thesis to achieve the highest sample quality on a free-standing few-layer graphene device shed light on novel phenomena near the low-energy band touching points of rhombohedral trilayer graphene.

The results discussed within this chapter are currently being prepared for publication. The s-SNOM images have been made by F. Falorsi and the Raman spectroscopy measurements by F. Winterer. The sample optical characterization, design and fabrication of devices as well as their electrical characterization, electron transport measurements and experiments at very low temperatures as well as the data analysis have been done as part of this thesis.

4.1 Introduction

Rhombohedral graphene systems increasingly grow of interest as they constitute a versatile platform to study many-body interaction effects. An important example is bilayer graphene, which has been demonstrated a naturally occurring platform for the investigation of strong interaction behaviour, showing a family of spontaneously broken symmetry phases such as the anomalous quantum Hall effect (QAH), the canted antiferromagnetic (CAF) effect and, recently, suggesting evidence of the existence of the so-called ALL state [45, 46]. As discussed in chapter 2 (section 2.2), the presence of strongly correlated phenomena in bilayer graphene is attributed to the flattens of its low energy bands near charge neutrality and large Berry curvatures [33]. Noteworthy, such a scenery is predicted to be universal for rhombohedral graphene with N-layers ($N > 2$) and, in addition, it has been theoretically predicted that an increasing number of layers delivers even flatter bands and larger Berry phases with divergent density of states at charge neutrality [33]. Thus, as discussed in chapter 2 of this thesis, it is expected that a bigger number of layers should give place to larger many-body interaction effects, and this is the case of rhombohedral trilayer graphene [32, 33, 35, 36]. In the past years, different experiments with rhombohedral graphene have revealed a variety of correlation physics, such as superconductivity and ferromagnetism, as well as the presence of flat bands in the system [29, 37–41]. Nevertheless, an experimental study on the search of broken symmetry states as well as electron and magneto transport in trilayer rhombohedral graphene at low charge carrier density and low magnetic fields remains little explored, with many of the reported experiments limited to single-gated structures [74, 115, 178, 179]. Presumably, because of the challenges for fabricating dual-gated samples of the quality required to observe correlated phenomena on this energy scale. Here, high quality ABC trilayer graphene is investigated in a dual-gated free-standing device configuration, in which graphene not only can be clean in-situ to the highest standard [166, 167], but it is also part of a platform with a reduced screening of Coulomb interactions, favouring the observation of many-body effects.

This chapter is organized as follows. In section 4.2, details on the sample fabrication and characterization are given. In section 4.3, the results of electron and magneto transport measurements at temperatures down to 10 mK are discussed. Here, the effect of varying independently n, D, the out of plane and the in-plane magnetic fields ($B_\perp$ and $B_\parallel$, respectively) is outlined. First, the discussion is centred on the search of broken symmetry states of the system at low magnetic fields and the tunability of QHE states in the system by means of an out of plane magnetic and displacement fields. Next, results on DC bias spectroscopy measurements are discussed. This is done in a similar fashion as in Refs. [74, 180–182], with the motivation of find correlated phases within the system. Last, a discussion about the application of a $B_\parallel$, which provides evidence of n tunable very low magnetic states in the rhombohedral trilayer graphene system, is given. In particular, a strong hysteretic behaviour is found at $B_\perp$=0 when measuring the conductance as a function of n, which is enhanced upon application of a higher $B_\parallel$. A conclusion and summary of the findings presented within this chapter is given in section 4.4.

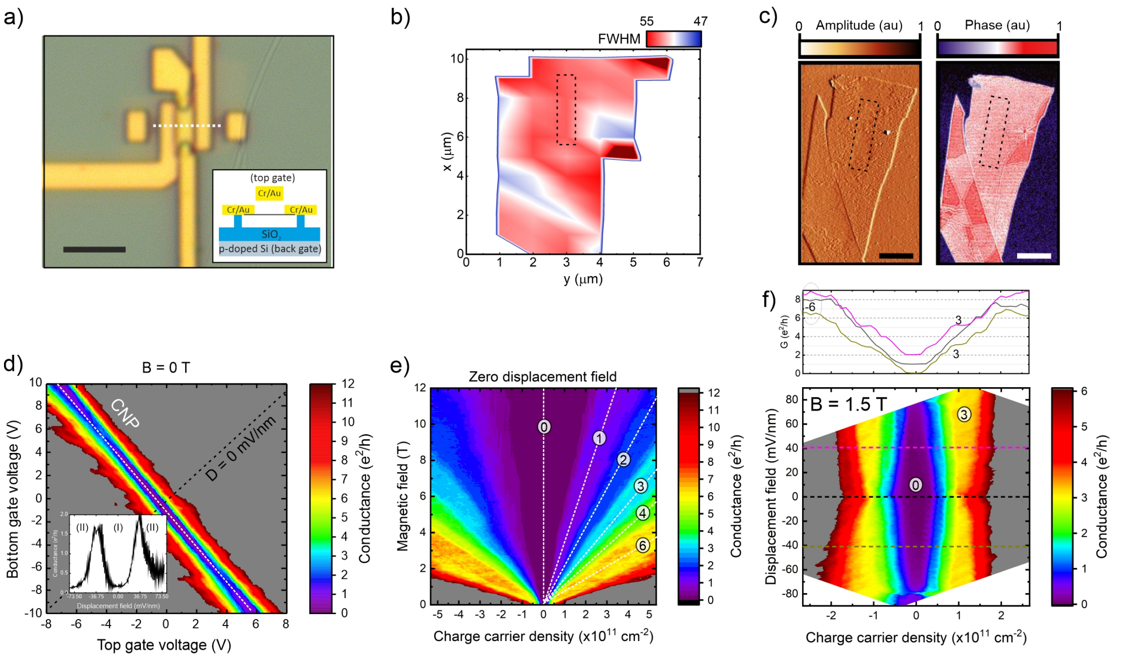

Figure 4.1: Sample fabrication and transport measurements. a) Optical microscope image of the device. Scale bar 5 µm. Inset: sketch of a cross-section along the white dotted line. A rectangular portion of ABC graphene, marked with a dashed line in b) and c) (not in scale), is isolated by RIE. b) Raman map from a single Lorentzian fit of the 2D-peak signal collected at every point on the flake. Red areas have ABC stacking order and blue areas, ABA. c) s-SNOM measurement. Right: AFM topography and left: optical phase. Colour scales in arbitrary units. Scale bar in both images 2 µm. d) Conductance map as a function of V_B and V_T at zero external magnetic field. Inset: conductance as a function of the displacement field at charge neutrality (white dashed line). (I) indicates the LAF/CAF phase and (II) layer the polarized phase. e) Fan diagram at $D = 0$. The encircled numbers indicate the calculated filling factors of the conductance plateaus. f) Conductance map as a function of n and D at $B = 1.5$ T. The profile measurement lines (along coloured dahsed lines) have an offset of 1 e^2/h for visualization.

4.2 Fabrication and methods

The samples presented here have been fabricated and characterized as described in chapter 3. In short, graphene flakes are exfoliated from highly oriented pyrolytic graphite (HOPG, HQ Graphene) and transferred onto a Si wafer with a 300 nm SiO_2 layer. Their number of layers as well as stacking order are identified by optical microscopy and Raman spectroscopy. Additionally, s-SNOM is used to ensure stacking order homogeneity with nanometre spatial resolution and to confirm the absence of domain walls. Suspended dual-gated structures with trilayer rhombohedral graphene are fabricated as follows: First, the flake regions with homogenous stacking order are etched in a rectangle shape using standard EBL and RIE with O_2 as an etchant gas. Electrical contacts (6 nm/70 nm Cr/Au), a spacer for the top gate (140 nm SiO2) and the top gate (6 nm/160 nm Cr/Au) are fabricated using EBL and PVD. To reduce the contact resistance, the samples are treated in a UV/Ozone environment for 1:30 min prior to metal evaporation. Subsequently, samples are dipped into a buffered oxide etchant (BOE 7:1) for 100 s to remove the SiO_2

spacer as well as 150 nm SiO_2 from the initial substrate. After stopping the wet etching process in water, the samples are transferred into ethanol and dried in a CPD. An optical microscope image of the sample and a draft of a cross-section to illustrate its vertical structure are shown in Figure 4.1 a). Figures 4.1 b)-c) show the s-SNOM and Raman measurements indicating the regions of the flake with rhombohedral (or ABC) stacking order: red on the Raman map, light red on the s-SNOM optical phase. All transport measurements are performed in a dilution refrigerator system at probe temperatures around 10 mK (unless specified otherwise) with a standard lock-in measurement technique, with AC frequency of 78 Hz and current <2 nA. The samples are investigated under external out of plane and in plane magnetic fields, which in the text are noted as $B_\perp$ and $B_\parallel$, respectively. For the case of zero total magnetic field, the notation B is used. In order to apply a finite $B_\parallel$ field, the sample is loaded into the cryostat tilting its holder to 90 degrees. This setup configuration is tested to not show any significant contribution of a perpendicular component, therefore, the influence of $B_\perp$ and $B_\parallel$ is studied and discussed independently within this chapter. Prior to any measurements, the devices are cleaned in-situ by current annealing. The results of this process are shown in the supplementary material in section 5.5, Figure 4.6 a). Adjusting the bottom and top gate voltages (V_B and V_T, respectively) enables independent tuning of both n and D, respectively defined as $n = C_B\left(\alpha V_T + V_B\right)/e$ and $D = C_B\left(\alpha V_T - V_B\right)/2\epsilon_0$ [45], where, C_B is the capacitance per unit area of the bottom gate, $\alpha = C_T/C_B$ the ratio between top and bottom gate capacitances, e the electron charge and ϵ_0 the vacuum permittivity. The contact resistance R_C and the bottom gate capacitance are extracted from the quantum Hall plateaus at $B = 3$ T and $D = 20$ mV/nm. The relevant calibrations are outlined in the supplementary material of this chapter (see Figure 4.6). Four different rhombohedral trilayer graphene samples were fabricated as outlined here. Two samples which resulted of highest quality were investigated in depth, whose results are shown in the next section as well as in the supplementary material in section 4.5.

4.3 Results and discussion

To begin, a few aspects of the physics at a the full n and B range accessible on the experiment with a suspended trilayer graphene are discussed. Figure 4.1 d) shows the two-terminal differential conductance $G = dI/dV$ in units of e^2/h as a function of V_B and V_T and $B = 0$. The interaction induced spontaneous gapped phase at charge neutrality, predicted to be universal for multilayer graphene with rhombohedral stacking order [33], is measured. As discussed in chapter 2, section 2.2, this phase is the result of electron-electron interactions opening a spontaneous gap near the CNP at zero electric and magnetic fields and has been since many years theoretically pointed out [42, 43, 183, 184]. Same as in previous experimental work with bilayer graphene and trilayer graphene [39, 45, 46, 169, 185], here it is observed that the spontaneous gapped phase closes upon application of a finite D field (see Figure 4.1 d), inset). Additionally, as it can be seen from Figures 4.1 e) and f), the spontaneous gapped phase extends to an insulating state by application of a finite $B_{\perp}$. This is consistent with previous results reported by several groups on rhombohedral few-layer graphene, in which the low conductance regions have been identified as the layer antiferromagnet/canted antiferromagnet (LAF/CAF) quantum phases [39, 45, 169, 185–187] (see also chapter 2, section 2.2). As it can be seen in Figure 4.1 f) at $B_{\perp} = 1.5$ T, conductance plateaus with filling factors ν from 0 to 8 are well resolved, with numbers assigned by tracing their slopes down to $B_{\perp} = 0$ in Figure 4.1 e). The calibration of ν is given in the supplementary material in section 4.5, Figures 4.6 b) and c), which is also used to calculate the contact resistance. This resistance value is subtracted in all of the measurements discussed within this chapter, unless specified differently. Figure 4.1 f) shows the conductance map after calibration of n and D scanning parameters of the system. An interesting aspect to observe here is that the conductance plateau at $\nu = 3$ emerges upon application of a D field. This is unlike the behaviour at $B = 0$, where the charge neutral LAF/CAF state jumps to a layer polarized state at some critical D field. While this might remind to previous results reported for bilayer graphene, where $\nu = 2$ is prominent at some finite D fields but disappears at zero and very high negative D fields [46], the results presented here show that, for trilayer ABC graphene, $\nu = 3$ not only can be activated at a finite D field but it also becomes present at $D = 0$ upon application of an out of plane B field (see Figure 4.1 e), 2 T and above). Further measurements for the states close to charge neutrality from $B_{\perp} = 0$ T to $B_{\perp} =$ 2 T are given and discussed in the supplementary material (Figures 4.7 a)-h)), as well as a measurement of the $B_{\perp}$ dependence of G at charge neutrality as a function of D (Figure 4.7 i)) and a measurement of the conductance map at $B_{\perp} = 8$ T. In the latter, an hysteretic behaviour observed when scanning D at a fixed n suggests that crossing the $D = 0$ line implicates a change in layer polarization (Figures 4.7 j)-l)) [33]. This is based on the assumption that the top and the bottom layers have different effective couplings to the electrical contacts (as discussed in Ref. [169]). Since $\nu = 3$ presents quite distinctive displacement and magnetic field responses, it is interesting to see what ground state of the system at small magnetic field this could be. A discussion with focus on this aspect is given next.

To identify the electronic ground states of the system, it is useful to explore the symmetries that might be preserved in them (see discussion in chapter 2 and Ref. [127]). In particular, to elucidate the nature of the ground state of trilayer ABC graphene at $B = 0$ and $D = 0$, further measurements of the QHE states at low B field are performed (see Figure 4.2). Here, it is useful to think what filling factors should be expected to see at very low B fields, in accordance to the degeneracies of the system. For trilayer graphene, the degrees of freedom to be considered are spin (up, down), valley (K, K'), and orbital LL (0, 1, 2) (see chapter 2, section 2.2 for a discussion about LL quantization in multilayer graphene). The degeneracy between the $N = 0, 1$ and 2 LLs, together with the spin and valley degrees of freedom, yield a 12-fold degeneracy of the lowest LL [115]. This is consistent with the observation of well-resolved conductance plateaus with integer filling factors $-6 \leq \nu \leq 6$ in the measurement shown in Figure 4.1 a). Interactions and/or single particle effects lift the 12-fold degeneracy and the order at which the degeneracy is

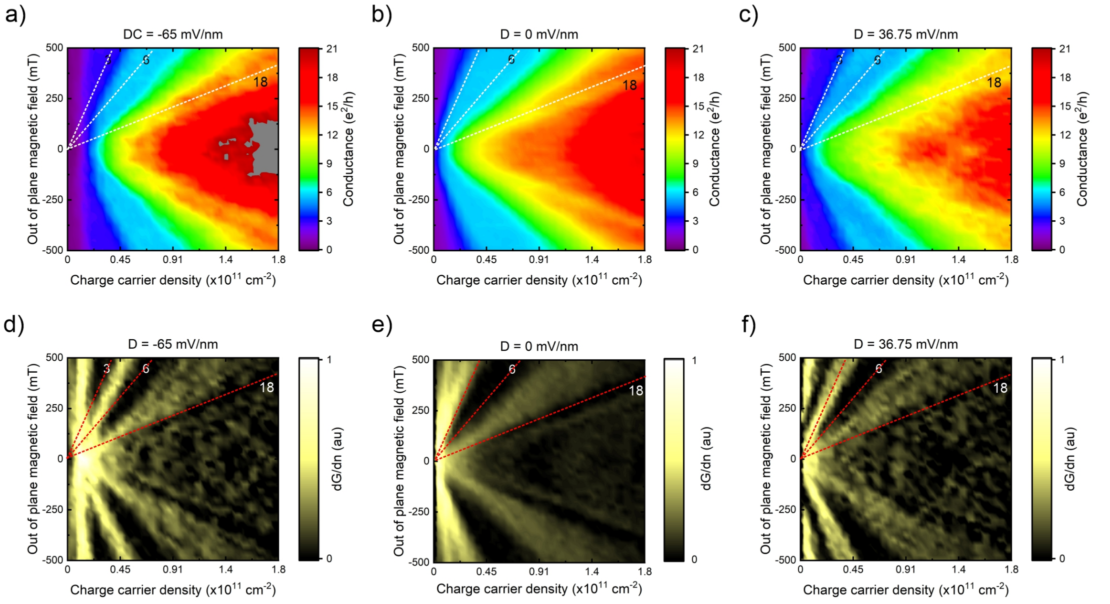

Figure 4.2: a)-c) Fan diagrams at low B for different D fields and, d)-f), their associated first derivative of the conductance with respect to the charge carrier density. The numbers inside the plot area label the position of the calculated filling factors. $\nu = 3$ arises upon application of a large displacement field. $\nu = 6$ and 18 are visible in all of the plots.

broken reflects the underlying competing symmetries [115, 188]. Considering this, several observations can be done for the results with suspended rhombohedral trilayer graphene. Figures 4.2 a)-c) reveal that, while $\nu = 6$ is present at zero and finite D, $\nu = 3$ emerges only at a finite D field. This can also be seen from Figures 4.2 d)-f), where a plot of the derivative of G with respect to n as a function of n and B is shown. In these plots, no change in the derivative indicates a conductance plateau. As a result, it can be observed that the strongest the D field, the more pronounced the plateau at $\nu = 3$ becomes. The fact that, at $D = 0$, $\nu = 6$ appears earlier than $\nu = 3$ (see Figure 4.1 f) and discussion about $B_\perp = 1.5$ T) is consistent with previous experiments exploring the fine LL splitting of the degeneracy in suspended trilayer graphene [178] and it also follows the Hund's rules proposed for ABC-staked trilayer graphene [113, 116]. However, the tunability of $\nu = 3$ with the D field is remarkable. Recalling the discussion about broken symmetry states in chiral graphene systems given in chapter 2 and the summary in table 2.1, the measurement of $\nu = 3$ (odd number) being favoured at the presence of an external B field and having charge Hall conductivity 3 e^2/h suggest it could be related with the "ALL" state at high displacement fields, predicted to have non-zero orbital momentum [33, 34]. This observation is as well consistent with the findings reported in [169]. It is notable from the measurements presented here, that conductance plateaus are visible at B fields as low at 100 mT. Using the definition of magnetic lenght $l_B = \sqrt{\hbar/eB}$ [105], this results in $l_B \sim 80$ nm, which speaks for the high quality of the sample. Another interesting aspect is that a QHE plateau at $\nu = 18$ (as calculated from the LL calibration) is also clearly visible on the plots on Figure 4.2, at both zero and finite displacement fields.

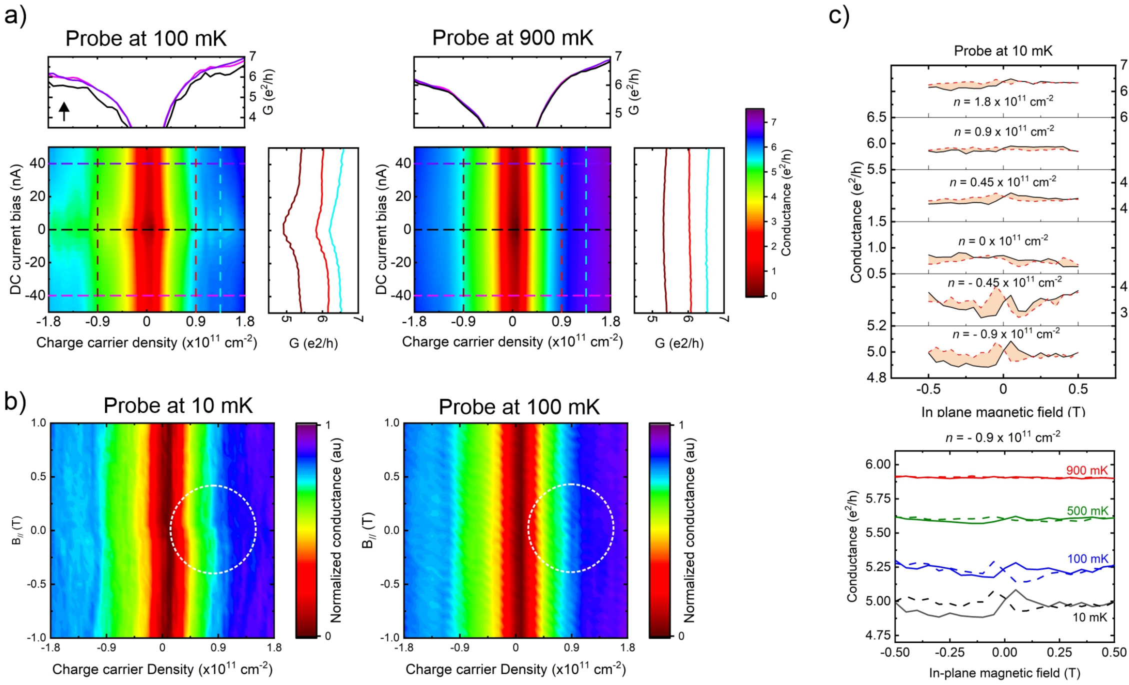

Figure 4.3: Low n conductance map upon application of a DC current bias and a $B_{\parallel}$ field. $B_{\perp} = 0$ and $D = -60$ mV/nm. a) Differential conductance as a function of n and DC bias, at 100 mK and 900 mK. The dashed lines indicate a measurement at fixed n or DC bias (see right and top plots for each map). The black arrow points out the fluctuations in G which are not present at higher temperatures. b) Normalized G as a function of n and $B_{\parallel}$, at 10 mK and 100 mK. The dashed white circle points out a fluctuation in the conductance map, which is not present at higher temperatures. c) Top, hysteresis measured at 10 mK when crossing $B_{\parallel} = 0$ on a trace (solid) and retrace (dashed) scan at fixed n (the hysteresis area is shaded for visualization). Bottom, same measurement at different temperatures for $n = -0.9 \times 10^{11}$ cm^{-2}.

It has been predicted that in high quality suspended ABC trilayers, $\nu = 0, \pm 3, \pm 6$ are likely to persist down to zero magnetic field and smoothly connect with electron-electron interaction driven broken symmetry states [33, 116]. So far, this is consistent with the findings discussed here. However, a clear observation of a conductance plateau at $\nu = 18$ is intriguing. The experimental observation of this filling factor has been reported before in rhombohedral graphite with 9 layers [40] using magnetic fields above 4 T, where it is to expect given the degeneracy from the zero-th LL. The observation of $\nu = 18$ in the trilayer ABC sample opens a question about its origin. Further theory analysis might be required for determining to which LL it belongs and, in particular, if it provides additional information about the ground state of the system.

With the motivation of looking for correlated phases at larger n within the band, DC bias spectroscopy has been used to identify the phases, similar as in Refs. [74, 180–182]. Using this approach, it has been shown before that in encapsulated bilayer and trilayer graphene some correlated states occur at the flat band positions [38, 182]. Here, the question is if something similar is accessible in suspended samples as well. To this point, it is important to note that in suspended graphene samples a high density of states (such as those shown in Ref. [38], where correlated phases have been reported) is not accessible, because it is limited by the maximum D field which can be applied in suspended graphene devices before they break. However, as discussed before in this thesis, since correlations are expected to be stronger because of the low dielectric constant of the suspended devices, it is worth trying to explore this direction. Figure 4.3 a) shows the result of a DC bias spectroscopy measurement at two different temperatures on the same suspended graphene device. Although it seems there are no clear signatures of a phase change upon application of a DC bias at different n values, as seen on the other works, there are specific regions of the conductance map where there is some pattern in the conductivity at very low temperatures. Figure 4.3 a) shows a measurement pointing out one pattern (see black arrow). While a line cut at zero DC bias shows fluctuations in G (black solid line in Figure 4.3 a)), at finite DC current bias the fluctuations are not present (pink and blue solid lines). In addition, by increasing the temperature of the probe from 100 mK to 900 mK, the fluctuations in G in general disappear. The latter is also observed by comparing the line cut measurements at fixed n. Here, G shows a dip around zero DC bias at 100 mK, which is gone at 900 mK. These results indicate that the fluctuations in G at $B = 0$ could be either correlations or Coulomb blockades. Further measurements which investigate the influence of an external DC bias signal in the system are shown in the supplementary material, in chapter 4.5. In particular, the results shown in Figure 4.3 correspond to a finite D field. The same set of measurements at $D = 0$ is given in section 5.5, Figure 4.8, showing similar results. Since no clear signatures of correlated phases were found on the DC spectroscopy bias study, the variation of other parameters of the system was explored. This is discussed in the following paragraphs.

A different experiment parameter used to explore the magneto transport in the present sample is the application of a $B_{\parallel}$ field. To begin, the conductance map shown in Figure 4.3 b) is measured. The result is given with the same scale for a measurement at 10 mK and 100 mK. Here, it has been noted that turning $B_{\parallel}$ on has an apparent effect in the conductance of the sample (compare, for example, dashed enclosed area in the Figure). To explore further this, a measurement of trace and retrace line scans of G as a function of $B_{\parallel}$ at different n values, is made. The results are shown in Figure 4.3 c). Remarkably, an hysteretic behaviour is found when crossing $B_{\parallel} = 0$ back and forth at finite n values. In particular, it has been found that $n = -0.9 \times 10^{11}$ cm^{-2} shows the most pronounced hysteresis and, in general, the hysteresis appears to be more pronounced for negative than positive n. In Figure 4.3 c) (top) it can be seen that, for $B_{\parallel}$ increasing (decreasing) between -500 and 500 mT, G rises when $B_{\parallel} = 0$ crosses zero, reaching a maximum at about 60 mT (-60 mT), before it decreases again. Moreover, repeating the same measurement at different temperatures for a fixed n (see Figure 4.3 c), bottom) results in the hysteretic behaviour becoming less prominent, until completely vanishing at a probe temperature of 900 mK. Similar results have been reported before for suspended few-layer rhombohedral and Bernal graphene in Ref. [128]. This excludes the possibility of the hysteresis observed being a measurement artefact and it supports its interpretation as an intrinsic property of the trilayer rhombohedral graphene sample, also given in [128].

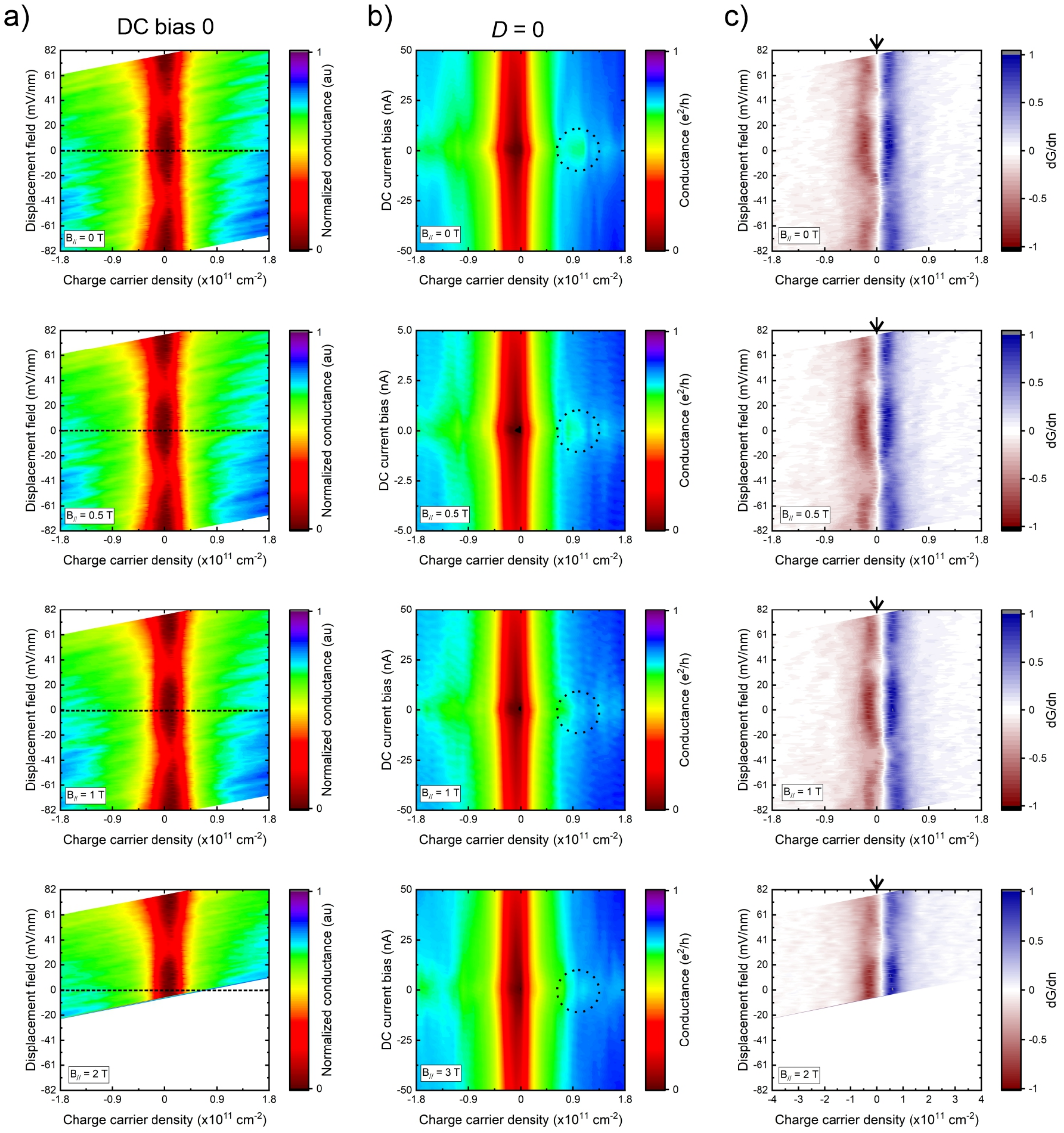

Figure 4.4: Magneto transport data for $B_{\|}$ at $D = 0$, $B_{\perp} = 0$ and cryostat $T = 10$ mK. a) Normalized differential conductance map as a function of n and D. b) DC bias spectroscopy measurement at $D = 0$ shows fluctuation regions in the conductance, e.g., the region enclosed with the dotted black line, which change upon application of a $B_{\|}$ field. c) First derivative of G with respect to n evidences a phase transition at $n = 0$ if $B_{\|} = 0$. This position is marked with the black arrow on the top axis on the plots, to point out a shift in the transition line to positive n values when increasing $B_{\|}$.

The work in Ref. [128], however, shows the results on a single-gated device, where no independent tunability of n and D can be practically measured on a gate voltage scan. The results presented here using a dual-gated device show the phenomena by scanning independently n and D, demonstrating that the hysteretic effect in $B_{\|}$ is both present at zero and finite displacement field (see supplementary material, section 5.5). The fact that the hysteresis in Figure 4.3 c) appears to be stronger for negative than positive n suggests that the charge carrier type could play a role in the observed phenomena. This observation could also explain some of the results reported in Ref. [128], where a difference in the magneto conductance and hysteresis in $B_{||}$ is observed as the devices become more electron- or hole-doped. To explore more in depth the effect of applying a $B_{||}$ field and reveal the actual nature of its influence in the present rhombohedral trilayer graphene sample, the set of measurements shown in Figure 4.4 was taken. First, in Figure 4.4 a), a measurement of the conductance map at $B_{\perp} = 0$ is shown. For comparison, G is normalized with respect to the values measured at $B_{||} = 0$. As a fist observation, it can be noted that the map does not show clear changes when turning on a $B_{||}$ field. Moreover, the same phases as discussed with Figures 4.1 e) and f) at the beginning of this section (LAF/CAF and layer polarized) are visible in the map at $B_{||} = 0$ and up to $B_{||} = 2$ T. For completeness, a measurement of the conductance map of the system as a function of n and DC current bias is taken at different fixed $B_{||}$ values and $D = 0$. From this result it is interesting to note that the fluctuations in the conductance discussed earlier with Figure 4.3 b) are modified upon application of a $B_{||}$ field. To determine if this has an origin in scattering and disorder, or rather a quantum mechanical origin, an in-depth analysis of the phenomena as a function of the temperature is necessary. Unfortunately, the attempt to perform such measurements within this thesis delivered no clear results. The reach of this study in the present work is discussed in the supplementary material in section 4.5. Looking at the result shown in Figure 4.4 c), the fact that $\mathrm{d}G/\mathrm{d}n$ does not change for n between 0.45×10^{11} cm^{-2} and 1.8×10^{11} cm^{-2} might suggest that all the states within this density range are in the same phase. Aside that, an interesting effect is noted from the plots in Figure 4.4 c). Here, a black arrow marks as a reference the centre of the phase transition (seen as a change in the sign of the derivative) which is present at the CNP and zero external B. Interestingly, the centre of the transition, found at $n = 0$ for $B_{||} = 0$, shifts in n upon application of a finite external $B_{||}$ field. Further measurements dedicated to explore this result are discussed in the following paragraph.

Strikingly, the shift at the CNP commented in the previous paragraph and shown in Figure 4.4 c) is accompanied by an hysteretic behaviour in n, which becomes strongly enhanced if the magnitude of the externally applied $B_{||}$ field is higher (see Figure 4.5 a)). Notably, this effect also depends on the temperature. As it can be seen on Figures 4.5 b) and c), the hysteresis becomes less prominent when increasing the temperature from 10 to 100 mK and it is suppressed at a temperature of 500 mK. Previous experimental works which have shown magnetism in rhombohedral few-layer graphene have reported strong hysteresis in the systems by scanning $B_{||}$ and $B_{\perp}$ [128]. Here, the phenomena is observed in a novel manner, by varying n. In order to compare the results presented here with those in Ref. [128] and determine how both results are related, it is tempting to note that in the quantum Hall regime, scanning n should be equivalent to scanning $B_{\perp}$ (see chapter 2, equation (2.2.2)). However, the results shown in Figure 4.5 are measured at $B_{\perp} = 0$ where no QHE is present, so this observation does not apply. It is also clear from the plots in Figure 4.5 that the QHE conductance plateaus are not present when turning on $B_{||}$ within the studied n range (see Figures 4.1 e) and 4.2 for comparison), so it can be excluded that a parasitic component of $B_{\perp}$ reaches the sample. Considering this,

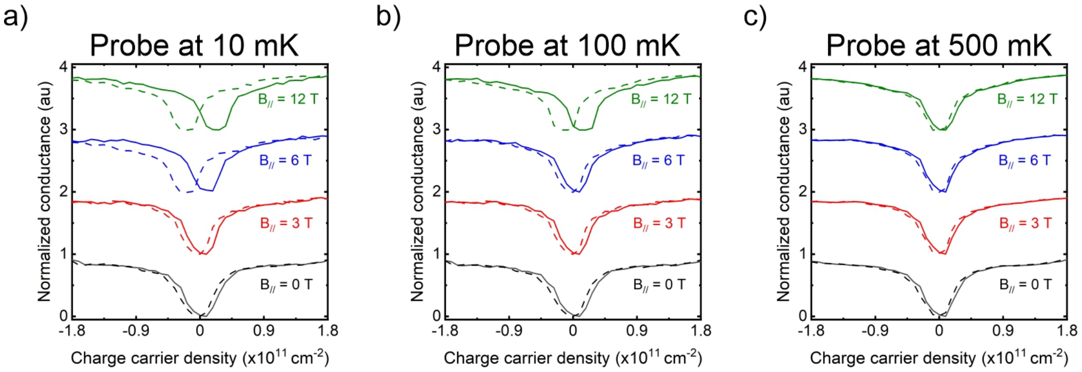

Figure 4.5: Normalized conductance with respect to the values at $B_{\|} = 0$ as a function of n and upon application of a $B_{\|}$ field, for the system at $D = 0$ and very low temperatures. An offset in an arbitrary unit of G is added for visualization. a) Trace (solid) and retrace (dashed) measurements at 10 mK show a hysteretic behaviour which becomes more prominent the larger a $B_{\|}$ is applied. b) Same measurement at 100 mK shows the same effect, but less prominent. c) Same measurement at 500 mK shows the hysteretic behaviour suppressed.

the results here show the peculiarity of tuning intrinsic magnetic states in the system by the charge carrier type and might bring novel insights about broken symmetry states in the system. Noteworthy, the results shown in Figure 4.5 are present at zero as well as at finite D fields (see results in supplementary material, section 4.5, Figure 4.11). The findings from the work presented here open a question about the role of the charge carrier type in the tunability of orbital-magnetism within the investigated system. Moreover, the results seem to provide signatures of a spin-ordered phase at charge neutrality as a ground state of rhombohedral trilayer graphene, such as it has been proposed for bilayer graphene [127]. Further theoretical efforts will be required to address this point.

4.4 Conclusions

The experimental study which conforms the present chapter shows results on transport measurements within high quality dual-gated suspended ABC trilayer graphene, which reveal the presence of magnetic states at low n. This main result has been achieved by following an investigation pathway on the search for correlated phases within the sample. To begin, transport measurements at $B = 0$ demonstrate the presence of the insulating LAF/CAF phase at charge neutrality and D fields near zero, as well as the layer polarized phase at higher D fields, in agreement with the results found in the literature. Furthermore, the observation of distinct QHE conductance plateaus at low $B_\perp$ indicate the presence of spontaneous quantum Hall states with non-zero charge Hall conductivity. In particular, conductance plateaus at $\nu = 3$ and $\nu = 6$ are traced down to $B = 0$, being clearly distinguished on their slopes at $B_\perp$ below 100 mT. Notably, the conductance plateau at $\nu = 3$, with measured conductivity 3 e^2/h, is stabilized upon application of a D field at low B and it also emerges upon application of $B_\perp$ at $D = 0$. This suggests that it could be one of the broken symmetry states which have been theoretically predicted for rhombohedral graphene with more than 2 layers [33, 34], which also supports the findings in Ref. [169]. In the sample which has been fabricated here, the additional observation of a conductance plateau at low B with $\nu = 18$ is ramarkable. Theoretical efforts are necessary in order to address the question about the role of higher LLs in the ground state of the system.

On the way to search for correlated phases within rhombohedral trilayer graphene, a map of the conductance as a function of different experimental parameters has been investigated. At first, fluctuations in the conductance have been noticed at $B_{\perp} = 0$, which have a dependence on an externally applied DC current bias and $B_{\parallel}$ field, as well as on the temperature. Although their appearance has been found more pronounced in the cleanest ABC graphene samples, no clear signatures of correlated phases in relation to these fluctuations in G could be determined. Next and presumably the most interesting result from the experiments discussed within this chapter, a hysteretic behaviour as a function of $B_{\parallel}$ and also as a function of n when turning on a $B_{\parallel}$ field is revealed. This phenomena is observed near charge neutrality at $B_{\perp} = 0$. Remarkably, the hysteretic behaviour in n becomes more pronounced the higher the $B_{\parallel}$ field. Moreover, it is present for both finite and zero D fields and it becomes less prominent (until disappearing) when increasing the probe temperature from 10 mK to 500 mK. These findings seem to provide evidence of a spin-ordered phase at charge neutrality in rhombohedral trilayer graphene. Moreover, the discovered magnetic states at low n show a tunability with the charge carrier type. Further theory analysis is required in order to elucidate the role of the n doping at the low energy band scale of trilayer rhombohedral graphene as well as a possible spin-ordered nature of its ground state.

4.5 Supplementary material

This section presents further measurement and calibration data not shown within sections 4.2 and 4.3. This data shown as supplementary material supports and extends the results presented within this chapter and is shown for completeness and reference.

Current annealing and LL calibration

Figure 4.6 a) shows the trace and retrace of subsequent current annealing cycles performed in-situ to clean the graphene-based devices, at a cryostat (probe) temperature of $T_{\text{cryo}} = 2.5$ K. The cleaning process is concluded when the trace and retrace annealing curves overlap and the CNP is observed when measuring the resistance as a function of one of the gate voltages. The cleanest result is obtained when the DC current surpasses about 1 V beyond the saturation point of the resistance (see chapter 3). Figure 4.6 b) shows the resistance of the QHE plateaus as a function of $1/\nu$, measured at $B_{\perp} = 5$ T and $D = 0$. The slope of the linear fit, resulting $(25955 \pm 184)\ \Omega$, overlaps with the von Klitzing constant and yields a contact resistance of $R_C = (2090 \pm 116)\ \Omega$. Figure 4.6 c) shows the conductance plateaus of the QHE at $B_{\perp} = 5$ T and $D = 0$ after subtracting the

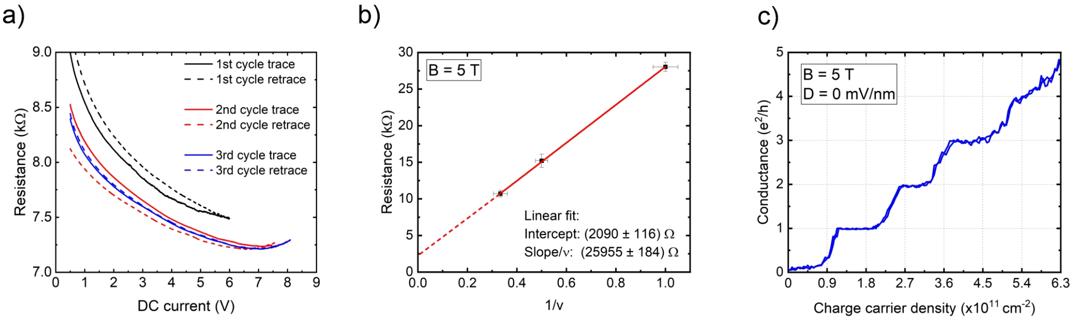

Figure 4.6: Current annealing and LL calibration. a) Resistance as a function of DC voltage for several annealing cycles. $T_{\text{cryo}} = 2.5$ K. b) Resistance of the QHE plateaus as a function of inverse filling factor at $B_\perp = 5$ T, $D = 0$ mV/nm and $T_{\text{cryo}} = 10$ mK. c) QHE conductance plateaus as a function of n at $B_\perp = 5$ T, $D = 0$ mV/nm and $T_{\text{cryo}} = 10$ mK, after subtracting the contact resistance (Intercept in b)).

contact resistance. The measurement shows well define conductance steps as a function of n, with plateaus at integer factors of e^2/h. The contact resistance is subtracted from all of the plots shown within this chapter, unless specified differently.

Magneto transport at higher B fields and inversion of the layer polarization

Figures 4.7 a)-h) show a map of the differential conductance as a function of n and D for different $B_\perp$ fields between 0 and 2 T, for D values around the gap-close, i.e. at the boundary between the LAF/CAF and layer polarized phase. This measurement is intended to show the low n states behaviour around the gap closing when increasing the $B_\perp$ field. Figure 4.7 i) shows the differential conductance at charge neutrality as a function of $B_\perp$, to complement the data in Figure 4.1. Figure 4.7 j) shows a map of G as a function V_T and V_B at $B_\perp = 8$ T, the dashed-dotted lines mark the fix n values for the trace and retrace scans in D, which are shown in Figure 4.7 l). In this Figure, a hysteretic behaviour symmetric with respect to D=0 suggests a change in layer polarization when crossing the $D = 0$ line. This effect is less pronounced at higher n values.

Additional magneto transport data and temperature dependence at finite D

Figure 4.8 shows additional data at $D = 0$, complementary to the results shown in Figure 4.3 for a finite D. Additionally, Figure 4.9 shows a study of the temperature dependence of one of the states at $B_\perp = B_\parallel = 0$, enclosed by a solid line in Figure 4.9 a). A point within a region of a low temperature feature in the conductance map, as the encircled in Figure 4.9 a), is chosen to read the value of G at different temperatures T. This results in the plot shown in Figure 4.9 b), which has been fit using an arbitrary allometric function in order to elucidate the T dependence of G through a power law. The resulting power coefficient of 0.11 ± 0.05 of this fit suggests an insulating behaviour of the state enclosed in Figure 4.9 a). A similar study on the nearby states at low n values shows a non-trivial temperature dependence. Because of time constrains, this study could not be performed more in depth. Further temperature dependant measurements and data points at additional T values are necessary to confirm the nature of the states which are present at every n value at $B_{\perp} = B_{\|} = 0$.

Reproducibility of the results in a second sample

Similar results as those discussed in the main text have been found on a second fabricated sample, which are shown in Figure 4.10. It is worth mentioning that this second sample did not result as clean as the presented in section 4.3. This can be seen from its low B fan diagram, where the ν=3 and ν=6, although traceable down to $B = 0$, are less pronounced compared to the results shown in Figure 4.2, which are measured on a cleaner sample. This could be a sign that the low n fluctuations of the conductance discussed in section 4.3 this chapter are not due to disorder, but correlated phases. A more complete analysis of the temperature dependence of these states would help to conclude this accurately.

DC current bias effect at higher $B_{\perp}$ fields

Figures 4.11 a)-l) show a measurement of G as a function of n, for different $B_{\perp}$ values. Here, some aspects are to be commented. First, an hysteretic behaviour becomes evident when comparing the trace and retrace of G for $B_{\perp}$ bigger than 7 T. Second, an external DC current bias supresses the conductance plateaus. Following the trace and retrace of the biased measurements, a hysteretic behaviour and jumps in G where the plateaus were is seen. This effect occurs as soon as conductance plateaus are well resolved on a non-biased scan. In the present sample, this is at $B_{\perp} = 3$ T. Figure 4.11 m) shows G as a function of n at $B = 10$ T, with the area of the hysteresis is shaded for better visualization. Figure 4.11 n) shows the normalized G at charge neutrality as a function of D and DC current bias, at $B_{\perp} = 1$ T. Different tendencies in the G values are measured before and after the transition to layer polarized states and also when comparing zero and finiete n.

Hysteresis in n upon application of a $B_{\|}$ at different D fields

Figure 4.12 shows additional data at finite D fields, complementary to the results shown in Figure 4.5 for a finite $D = 0$. A hysteretic behaviour in G is measured as a function of n, being enhanced upon application of a $B_{\|}$ field. The effect becomes less prominent until completely vanishing upon a temperature increase.

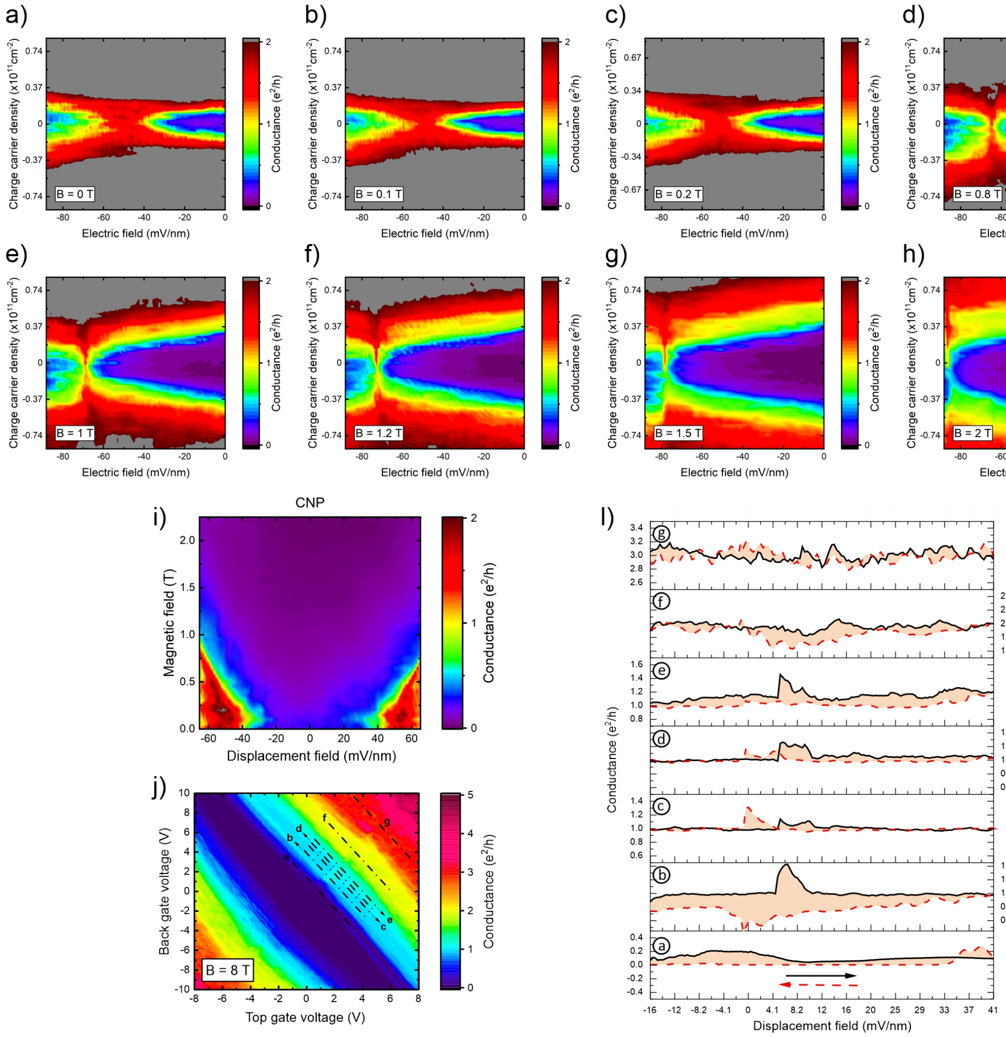

Figure 4.7: Magneto transport at higher B fields and inversion of the layer polarization. a)-h) Differential conductance at the border of the gapped CAF and layer polarized phases for different $B_\perp$ values. i) G as a function of D and $B_\perp$ at charge neutrality. j) G map at $B_\perp = 8$ T. The labelled dashed-dot lines correspond to the trace and retrace measurements shown in l), where an hysteretic behaviour is observed when scaning along the D axis on the respective conductance plateaus.

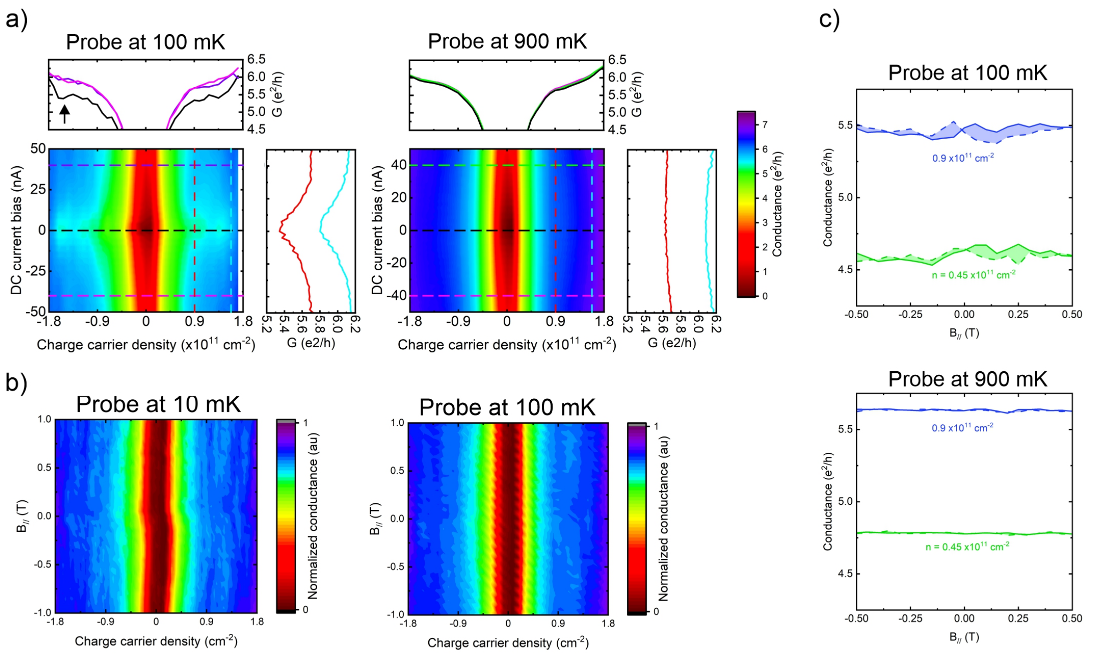

Figure 4.8: Low n conductance map upon application of a DC current bias and a $B_{\|}$ field at very low and low temperatures. $B_{\perp} = 0$ and $D = 0$ mV/nm. a) G as a function of n and DC current bias, at 100 mK and 900 mK. The dashed lines indicate a measurement at fixed n or DC bias, which are plotted on the right and top of each map. The black arrow points out the fluctuations in the conductance which are not present at higher temperatures. b) Normalized G as a function of n and $B_{\|}$, at 10 mK and 100 mK. c) Top, hysteresis measured at 100 mK when crossing $B_{\|} = 0$ on a trace (solid) and retrace (dashed) scan at fixed n values (the hysteresis area is shaded for visualization). Bottom, same measurement at 900 mK does not show a hysteresis.

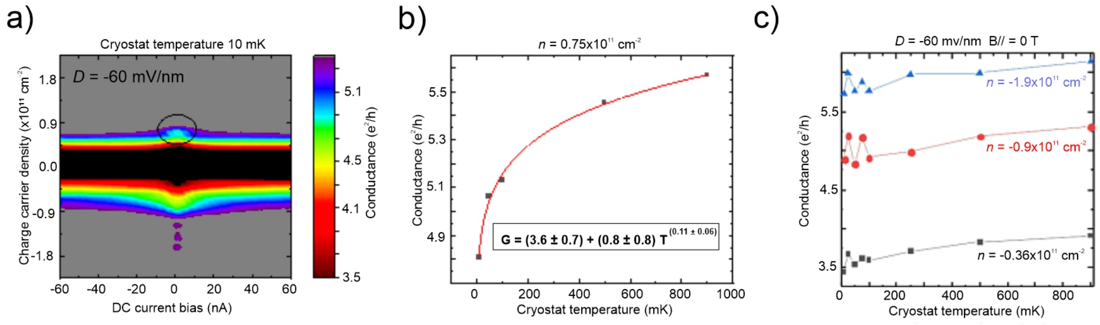

Figure 4.9: Temperature dependence of G points from a DC spectroscopy map at D=-60 mV/nm a) Conductance map as a function of DC current bias and charge carrier density. b) Temperature dependence of the insulating state encircled in a) (black data points) and allometric non-linear fit (red solid line). c) Temperature dependence of conductance points at the vicinity of the region encircled in a) at different n and temperature values.

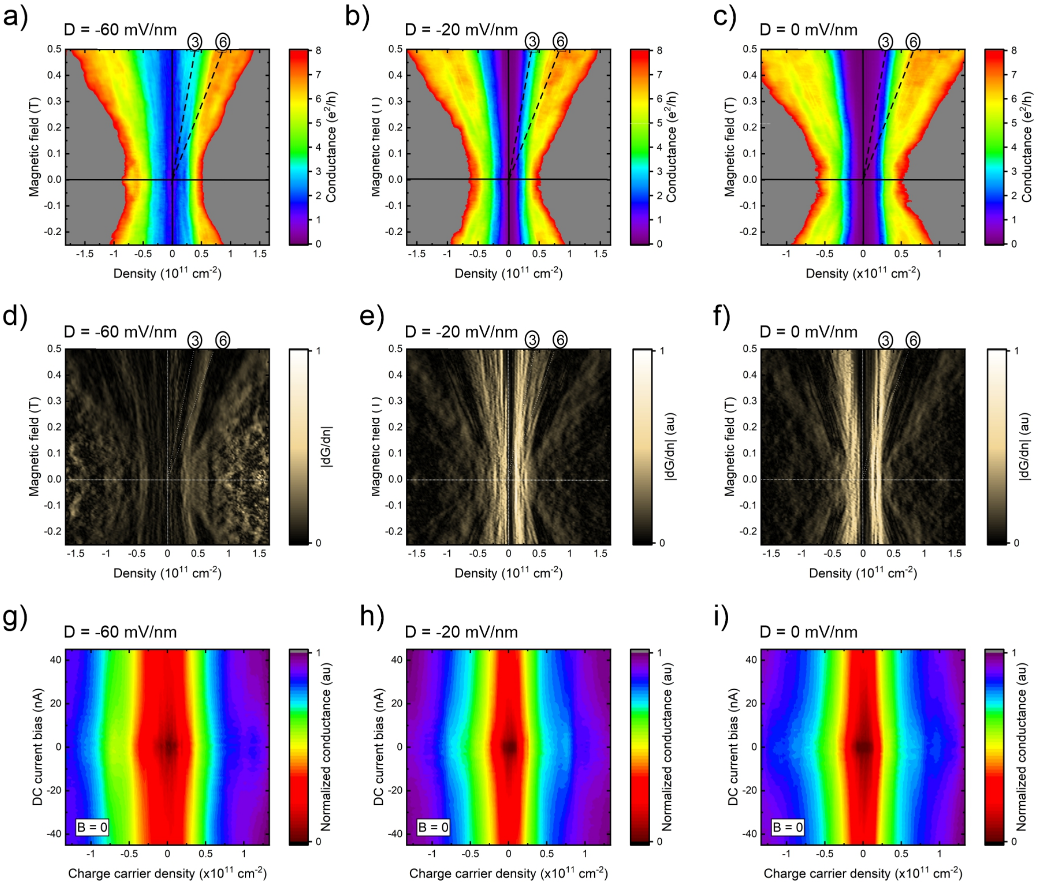

Figure 4.10: Results on a second sample. a)-c) Fan diagrams at low $B_\perp$ for D fields and, d)-f), corresponding first derivatives. The encircled numbers label the position of the calculated filling factors (ν). $\nu = 3$ arises upon application of a large displacement field. c) Normalized conductance map as a function of DC current bias ad charge carrier density at $B_\perp = 0$ shows fluctuations in the conductance as in the other reported sample.

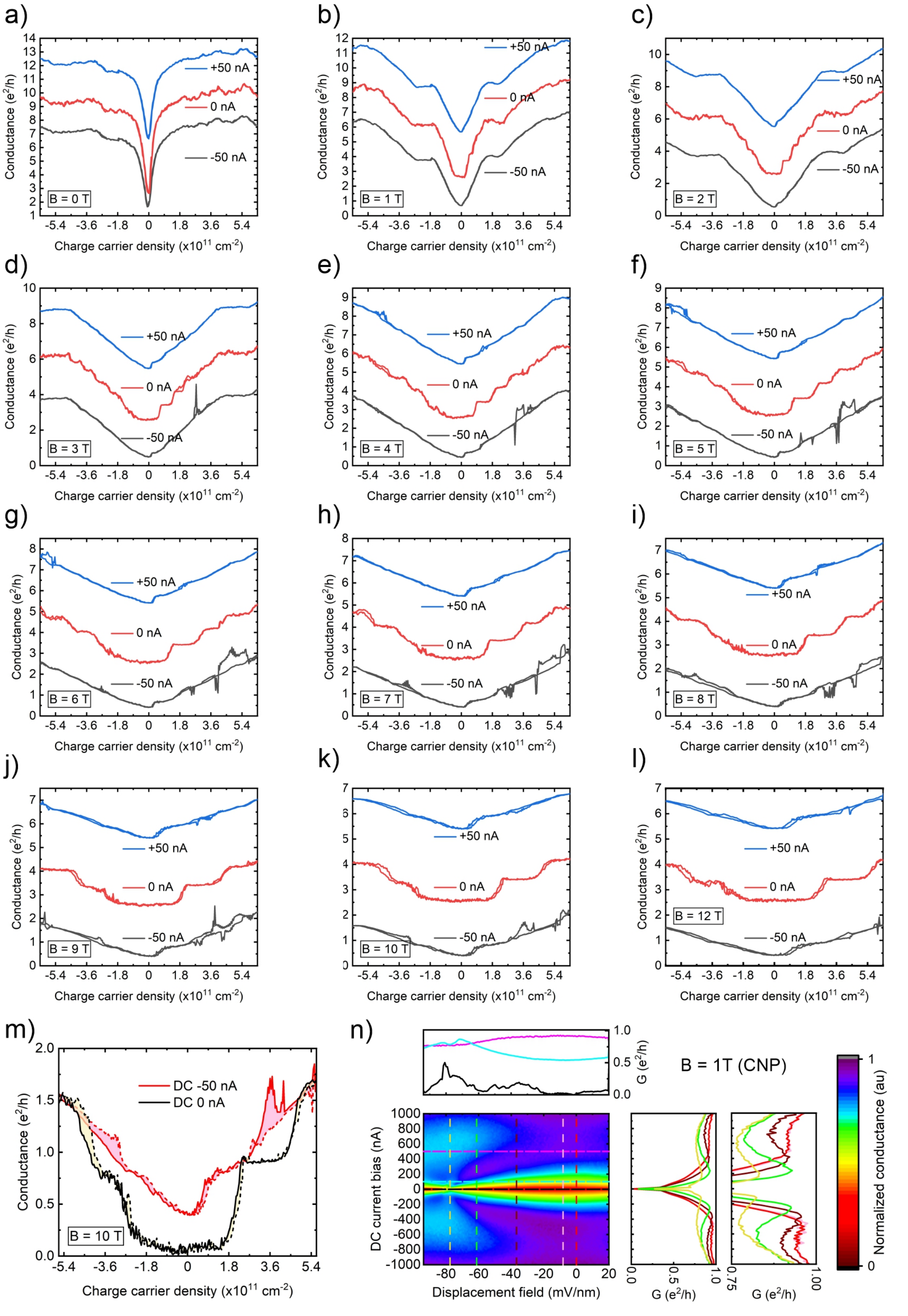

Figure 4.11: DC current bias effect at higher $B_\perp$ fields. a)-l) Differential conductance as a function of n for different $B_\perp$ fuelds, with (black and blue) and without (red) applied DC bias. An offset of 2.5 e^2/h is added between curves for visualization. Trace and retrace are shown for each individual scan. m) Highlight of the hysteretic behaviour at 10 T. Trace and retrace are shown with solid and dashed line, respectively. The hysteresis area is shaded for visualization. n) Normalized G as a function of D and DC current bias at the neutrality point and $B = 1$ T.

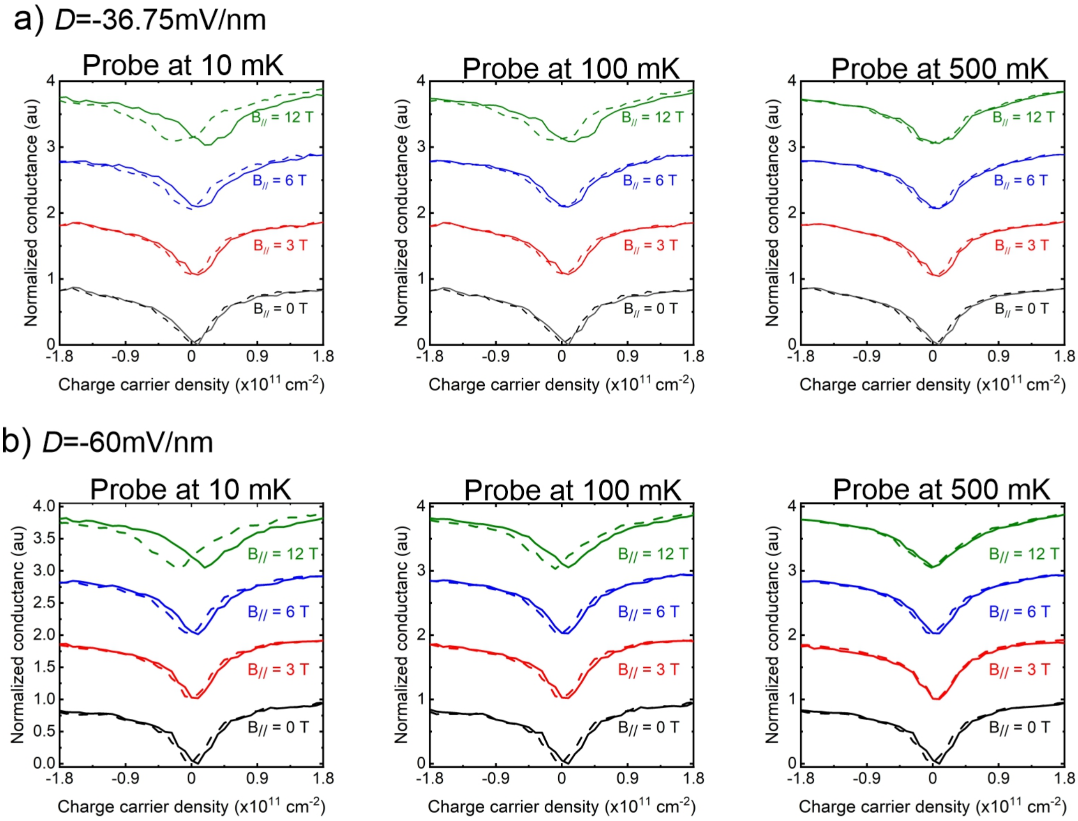

Figure 4.12: Hysteresis in n upon application of a $B_{\parallel}$ at different D fields. Normalized conductance with respect to the values at $B_{\parallel} = 0$ as a function of n and upon application of $B_{\parallel}$. An offset in an arbitrary unit of G is added for visualization. Left, trace (solid) and retrace (dashed) measurements at 10 mK show a hysteretic behaviour which becomes more prominent the larger a $B_{\parallel}$ is applied. Middle, same measurement at 100 mK shows the same effect, but less prominent. Right, same measurement at 500 mK shows the hysteretic behaviour suppressed. a) $D = -36.75$ mV/nm. b) $D = -60$ mV/nm.

Chapter 5

Quantum transport fingerprints of tetralayer rhombohedral graphene

Being it because of its less probable natural occurrence or its tendency to shift to the more energetically stable Bernal stacking order, naturally occurring few-layer rhombohedral graphene with more than three layers remains little experimentally explored. In the past years, experiments with rhombohedral bilayer and trilayer graphene reported an intriguing variety of correlated phases that make worth the efforts in preserving its stacking properties in a electronic device configuration. When looking at tetralayer graphene, additionally to the Bernal (ABAB) and rhombohedral (ABCA) stacking orders, the possibility of finding the material in an hybrid (ABCB) stack comes into play. Because the crystallographic stacking order of few-layer graphene has a strong impact in the electronic properties, distinguishing stacking ordering from an electron transport standpoint should become a standard characterization tool. Given the scarce experimental evidence on electron and magneto transport full characterization of tetralayer rhombohedral graphene in the literature, the results presented within this chapter shed light on the electronic transport fingerprints of naturally occurring rhombohedral tetralayer graphene.

The results presented in this chapter are currently being prepared for publication. The Raman Spectroscopy measurement has been done by F. S. Winterer, the scattering scanning near-field optical microscopy images have been made by F. Falorsi. Furthermore. The sample fabrication and experimental work as well as the data analysis has been done as part of this thesis.

5.1 Introduction

During the past years, rhombohedral multilayer graphene systems have fulfilled the promise of being a suitable platform for exploring electron-electron interaction physics in the laboratory. As it has been predicted theoretically, this has basis on the property of its low energy band structure with nearly flat bands, which become even flatter with an increasing number of graphene layers [33, 36]. At the moment of experimentally studying rhombohedral few-layer graphene, an important aspect to have in mind is how to realize the system. Having in mind that the most common and energetically favourable stacking order of few-layer graphene is Bernal (ABAB), while rhombohedral (ABCA) is less common, for tetralayer graphene one should add the possibility of finding the system in a hybrid staking configuration, usually noted as (ABCB) [19, 36, 73, 74]. Although recent experiments have been exploring tetralayer graphene systems and demonstrated the presence of correlated physics [29] as well as an accurate localization of all possible different stacking domains among a single tetralayer graphene flake [155], a complete electron and magneto transport study of naturally occurring tetralayer rhombohedral graphene is still missing. Here, such study is provided using high quality free-standing rhombohedral graphene. The results discussed within this chapter bring insights that pave the way towards a complete understanding of the quantum transport fingerprints of the few-layer graphene systems for revealing their stacking order from electron transport measurements. As an interesting outcome to remark, the study which has been performed here led to a revelation of layer coherent and layer polarized states at finite magnetic fields within rhombohedral tetralayer graphene, as well as a pronounced hysteresis behaviour when crossing LLs by scanning n, which has not been shown until now.

This chapter is organized as follows. First, in section 5.2, details on the sample fabrication are given. In section 5.3, the results of electron and magneto transport measurements on free-standing tetralayer rhombohedral graphene are presented. The discussion starts commenting unusual features observed in a measurement of the fan diagram and it continues by analysing the effect of the application of an external D field perpendicular to the sample. Next, the discovery of a strong hysteretic behaviour when scanning n across QHE conductance plateaus is discussed. Last, the results from studying the system at low B fields are commented. In section 5.4, a conclusion on the experimental findings discussed within this chapter is given.

5.2 Fabrication and methods

The samples presented within this chapter have been fabricated and characterized as described in the chapter 3, section 3.1. Here, only tetralayer ABCA free-standing graphene samples are discussed, whose fabrication method is equivalent as for the trilayer ABC samples presented in chapter 4. In brief, few-layer graphene is exfoliated from highly oriented pyrolytic graphite (HOPG, HQ Graphene) and transferred onto a Si wafer with a 300 nm SiO_2 layer. Tetralayer rhombohedral graphene flakes are identified by optical microscopy and Raman spectroscopy. A s-SNOM technique is used to verify the stacking order homogeneity with nanometre spatial resolution and the absence of domain walls. Results on this characterization measurements are shown in the supplementary material in section 5.5, Figure5.7 a) and b). Suspended dual-gated structures are fabricated as follows: First, regions with homogenous stacking order are sectioned in a rectangle shape using standard EBL and RIE with O_2 as an etchant gas. Electrical contacts (6/70 nm Cr/Au), a spacer for the top gate (140 nm SiO_2) and the top gate (6/160 nm Cr/Au) are fabricated using EBL and PVD. The lithography layout is shown in section 5.5, Figure5.7

c). To improve the contact resistance to the graphene flakes, the samples are treated in a UV/Ozone environment for 1:30 min prior to PVD. After lift-off, the samples are dipped into a buffered oxide etchant (BOE 7:1) for 100 seconds to remove the SiO_2 spacer and 150 nm of SiO_2 from the substrate. After stopping the wet etching in water, the samples are transferred into ethanol and dried in a CPD to prevent collapse of the graphene free-standing structure by capillary forces. All measurements are performed in a dilution refrigerator system at probe temperatures of 10 mK (unless specified otherwise), using a standard lock-in measurement technique at an AC frequency of 78 Hz and currents of <5 nA. Prior to any measurements, the devices are cleaned in-situ via current annealing. By adjusting the voltages V_B and V_T of the silicon back gate and the gold top gate, respectively, both the charge carrier density $n = C_B\left(\alpha V_T + V_B\right)/e$ and the displacement field $D = C_B\left(\alpha V_T - V_B\right)/2\epsilon_0$ are tuned independently [45]. Here, C_B is the capacitance per unit area of the bottom gate, $\alpha = C_T/C_B$ the ratio between top and bottom gate capacitances, e the electron charge and ϵ_0 the vacuum permittivity. The calibration used is shown in section 5.5, Figure5.7 d) and e). The contact resistance R_C and the bottom gate capacitance C_B are extracted from quantum Hall plateaus at $B = 4$ T and $D = 20$ mV/nm, and it has a value of $R_C \sim 1537\ \Omega$. This value is subtracted in all of the measurements presented here, unless specified differently. All the results in the present chapter are studied under application of an out of plane B field, when used.

5.3 Experimental results

Figure 5.1 a) shows the resistance of a free-standing dual gated tetralayer rhombohedral graphene sample as a function of n, after current annealing. While at higher n the graphene flake has the well-known metallic behaviour, approaching the CNP at $n = 0$ shows an increase of the resistance. The fact that at charge neutrality a resistance of the order of $10^7\ \Omega$ is measured speaks for the high quality of the sample and gives the sample an insulating character at charge neutrality. In Figure 5.1 b) it can be seen that the insulating region extends over a large range of D field. This is the interaction induced gapped phase discussed in chapter 4 for the suspended trilayer graphene sample and also in Refs. [39, 45, 46, 169, 185] for bilayer and trilayer graphene. As argued in chapter 2 of this thesis, this spontaneous gapped phase is predicted to be universal for multilayer graphene with rhombohedral stacking order [33, 34]. Evidence of this phase has been shown in tetralayer graphene before [74, 128], but here the outstanding quality of the sample seems to provide additional information about this phase. First, as can be seen from Figure 5.1 a), the increase in the resistance towards charge neutrality is not uniform, but it presents lowering points. Something similar has also been observed in very high-quality free-standing bilayer graphene samples [45]. The effect can be attributed to Coulomb blockades due to interaction effects, because of having a spatially varying gap in the system [18,189,190]. The observation of this blockades in the tetralayer rhombohedral graphene sample supports the assumption that the insulating region in Figure 5.1 b) is the interaction-induced insulating gapped phase, which is proposed to be a LAF/CAF

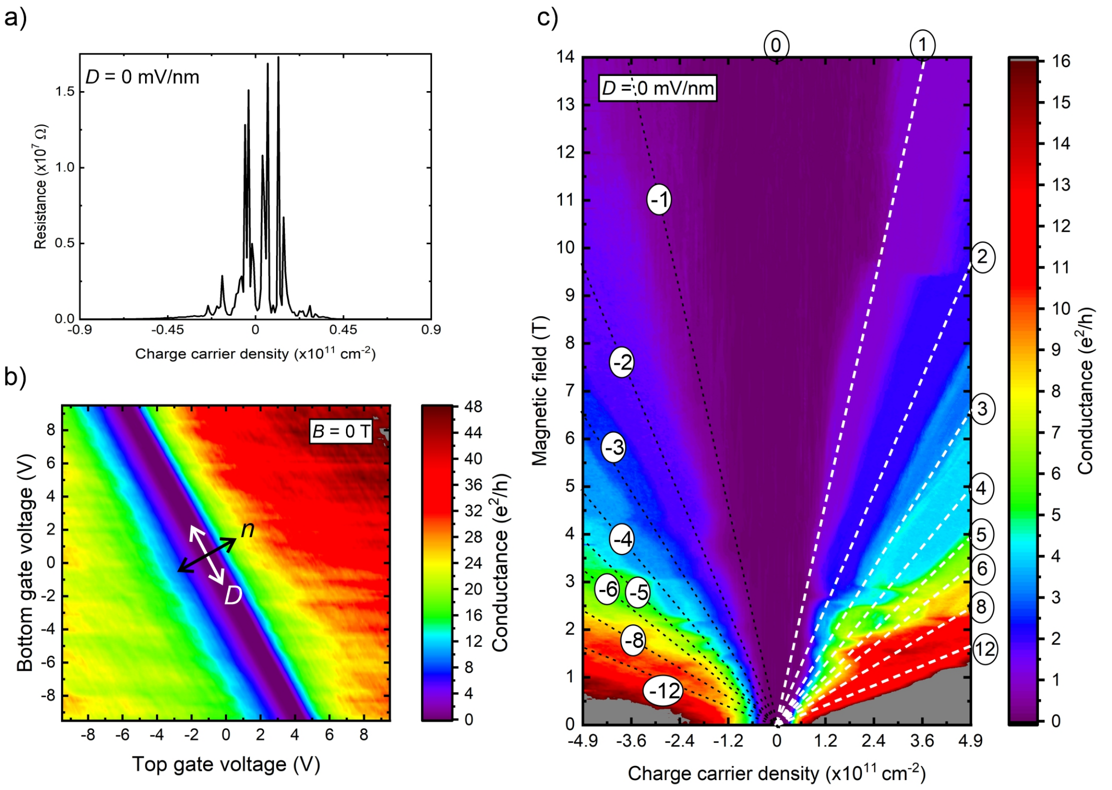

Figure 5.1: Electron and magneto-transport results in free-standing dual-gated rhombohedral tetralayer graphene. a) Resistance as a function of the charge carrier density n at $D = 0$ after in-situ current annealing. b) Differential conductance map in units of e^2/h as a function of top and bottom gate voltages. A spontaneous insulating phase is present for the full range of D accessible by the experiment. c) Fan diagram of the fabricated tetralayer rhombohedral graphene sample at $D = 0$.

phase state with broken time reversal and spin rotation symmetries [33,34] (see chapter 2, section 2.2.5)). In fact, previous transport studies with tetralayer rhombohedral graphene have measured the gap of this insulating phase resulting bigger than in the bi- and trilayer counterparts [74], which agrees with the theoretical prediction of a continuing the trend of increasing interaction in thicker rhombohedral few-layer graphene up to 6 layers [74,127]. This is also validated by observing that thicker rhombohedral few-layer graphene has even larger density of states at the CNP that are ever more unstable against electronic interactions, thus favouring the formation of a larger gap (see discussion chapter 2). Here, the interplay between a larger screening effect in large stacks [36] and a stronger interaction effect in tetralayer rhombohedral graphene [191], given that its low energy bands are even flatter than the case of bi- and trilayer [36] (see as well chapter 2) explain this phenomena. From the sample prepared within this thesis, as can be seen in Figure 5.1 b), this phase remains stable for the entire range of D fields accessible on the experiment, which is enough to close the gap in an equivalent experiment with bilayer [45, 46] and trilayer graphene (see section 4, Figure 4.1). Additionally, the insulating character at $D = 0$ seems to extend to a larger n range than in the trilayer graphene sample measured

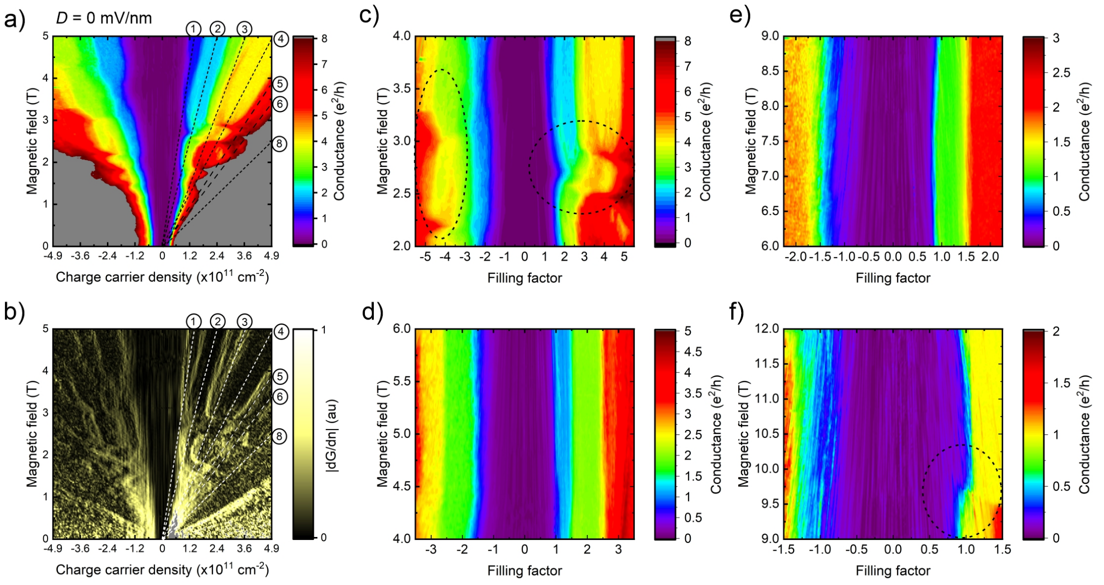

Figure 5.2: a) Fan diagram at $D = 0$ mV/nm. The encircled numbers are the filling factor values calculated from the slope of the conductance plateaus as a function of B. b) Derivative of the conductance G with respect to the charge carrier density n at $D = 0$ mV/nm. c)-f) Differential conductance map as a function of the filling factor different B fields. The dashed enclosed areas point out the regions with changing conductance as a function of B at a fixed ν.

within this thesis (see chapter 4). Last, to provide a complete transport study, the fan diagram of the ultra-clean rhombohedral tetralayer graphene sample is measured. Figure 5.1 c) shows this result at $D = 0$ up to a B field of 14 T which, noteworthy, has not been reported to date. Surprisingly, as it can be seen in the Figure, rhombohedral tetralayer free-standing graphene, instead of showing LLs with a large scale uniform (lineal) slope towards higher B fields, as it is the case for trilayer (see Figure 4.1 in chapter 4) and bilayer free-standing graphene (see Ref. [46]), the fan diagram of rhombohedral tetralayer graphene shows non-linear features that suggest crossings of LLs. This result is reproducible in the measured sample on different cooldowns (after which is necessary to do again current annealing) as well as on a second fabricated sample, both shown in the supplementary material in section 5.5, Figure 5.8. On the next paragraph, the discussion is centred in the non-linearities observed at different B field ranges.

Figure 5.2 a) shows the fan diagram at $D = 0$ up to $B = 5$ T and Figure 5.2 b) the first derivative of G with respect to n as a function of n and B. The filling factors are assigned by tracing their slopes down to $B = 0$. As discussed previously in chapter 4, it is useful to know what filling factors should be expected to see, in accordance to the degeneracies of the system. For tetralayer graphene, the degrees of freedom to be considered are, once more, spin (up, down), valley (K, K') and orbital (0, 1, 2, 3) (see chapter 2, section 2.2). The degeneracy between the $N = 0, 1, 2$ and 3 LLs, together with the spin and valley degrees of freedom, yield a 16-fold degeneracy of the lowest LL in tetralayer graphene [115]. This is in agreement with the observation of well-resolved conductance plateaus with integer filling factors $-8 \leq \nu \leq 8$ in Figures 5.1 c) and

5.2 a)-b). Noteworthy, the calibration of the conductance plateau slopes in B delivers filling factors with matching values for the conductance in integer units of e^2/h after subtracting the contact resistance. It is interesting to note that $\nu = 5$ and 6 are not so clearly distinguished in the fan diagram. Besides, the fact that the $\nu = 1$ to 4 are clearly visible indicates the presence of interaction physics on the sample, since these are attributed to exchange splitting instead of Zeeman splitting, in analogy to the case of bilayer graphene [114]. Another aspect that can be observed in Figures 5.2 c)-f), in a plot of G as a function of ν and B is that, up to $B = 4$ T, an apparent mixture between LLs in the conductance map is clearly visible. In particular, between 4 T and 6 T, the conductance plateaus uniformly follow their filling factor calibration lines, similarly between 6 T and 9 T. Whereas on a range between 2 T and 4 T as well as between 9 T and 12 T, crossings and shifting of the conductance plateau slopes become apparent (see dashed encircled areas as an example). Theory works have provided models to predict the LL spectrum of multilayer graphene samples [35, 80], showing that they are very distinct if one considers Bernal, rhombohedral or an hybrid stacking order as well as different number of layers, due to the different chiral decompositions of their energy spectrum (see discussion in chapter 2, section 2.2.2, and Ref. [35]). Similar as for rhombohedral graphite films study in Ref. [40], the results shown here provide a full experimental picture of the LL quantization in the so far less explored tetralayer ABCA graphene. These results could be used as adjusting parameters of a theoretical model (e.g. as the given in [35]) to determine from transport measurements which stacking order of the system is present. Theoretical efforts in this direction could be interesting to that aim.

To have a complete picture of the QHE transport characteristics of the sample, it is interesting to study its response upon application of a D field. Figure 5.3 a) shows line scans of G as a function of ν at different B fields and $D = 20$ mV/nm. The calibration of the filling factors using the slopes from the fan diagram at $D = 0$ fits well and all the QHE plateaus (starting at filling factor 1) are clearly discernible at B fields above 2 T. Figures 5.3 b)-f) show the D field dependence of the states at different fixed B. As a first observation, for $B = 4$ T, where conductance plateaus are well resolved with conductance values proportional to their calculated filling factor (see Figure 5.3 d) and g)-(ii)), and D does not have a influence in the conductance measured. This is contrary to the case of $B = 8$ and 12 T, where the application of a D field has an influence in the conductance within a plateau. Since a D field should not change filling factor, the changes in the conductance could be attributed to a transition between two different phases. Interestingly, the influence of D observed in the conductance map at 12 T, visible for $\nu = 1$, 2 and 3, resembles the case of trilayer graphene at 8 T (see Figure 4.7 and Ref. [169]). This situation is very different when observing the map at 8 T for D values between 0 and 50 mV/nm. Here, $\nu = 1$ and 2 are not affected by a D field, while $\nu = 3$, 4 and 5 experience conductance jumps. It seems that at 4 T there is no phase transition as a function of D, because there is no region of clear increase in the conductance. However, at 8 T, an increase in the conductance at a fixed n is seen (see enclosed area in Figure 5.3 e)), suggesting there is a transition as a function of D (see discussion about layer

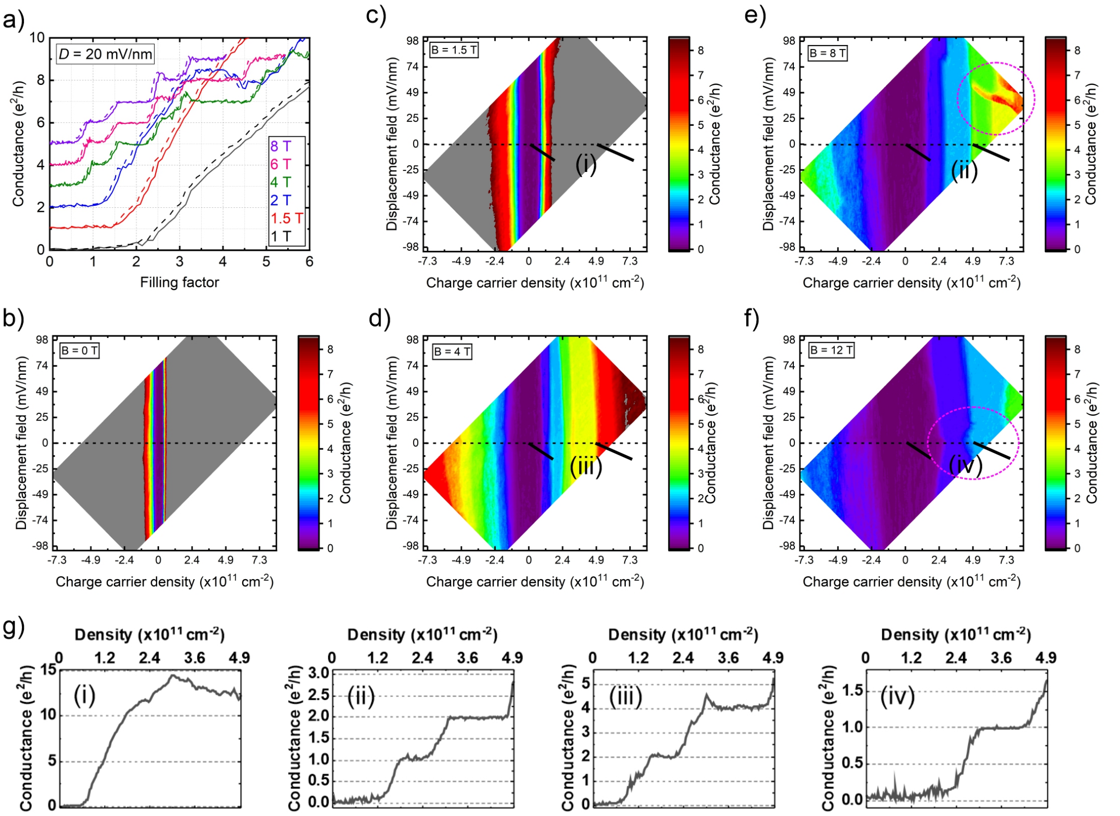

Figure 5.3: a) QHE conductance plateaus as a function of filling factor at $D = 20$ mV/nm. b)-f) Differential conductance map as a function of D and n for different out of plane magnetic field B values. The dashed pink lines in e) and f) enclose the region of the map with changes in the conductance along the D axis. g) Single line traces along the dashed black lines ($D = 0$), between the limits indicated with solid black diagonal lines.

polarized phases within trilayer graphene in chapter 4 and within bilayer graphene in Ref. [46]). From these results, it seems that the quantum numbers of the ν do not change as a function of D, but rather as a function of B. This raises the question of what states these are, e.g. layer polarized or unpolarized. From private communications with Dr. Fan Zhang (University of Texas at Dallas, USA), it turned out that it is hard to tell, since the states are too close in energy. There are different ways in which the valleys, spins and orbital degrees of freedom could order and what the energy of the different combinations is as a function of D and B is unknown. The results provided here show that the ordering apparently changes as a function of B. On a concrete example, this can be seen by comparing the maps at 4 T and 8 T, where $\nu = 3$ seems to be layer polarized at 8 T, as it shows a jump in the conductance (see also Figure 5.4 a)), and layer unpolarized at 4 T, as no conductance jumps along the D axis are observed. In the next paragraph, the picture at 8 T is discussed with further details.

Figure 5.4 a) shows the result of measuring the trace and retrace of a D field scan at different fixed ν values (i.e., within a conductance plateau), with the aim of identifying a possible phase transition when crossing $D = 0$. As a result, it is found that for $\nu = 1$ (blue

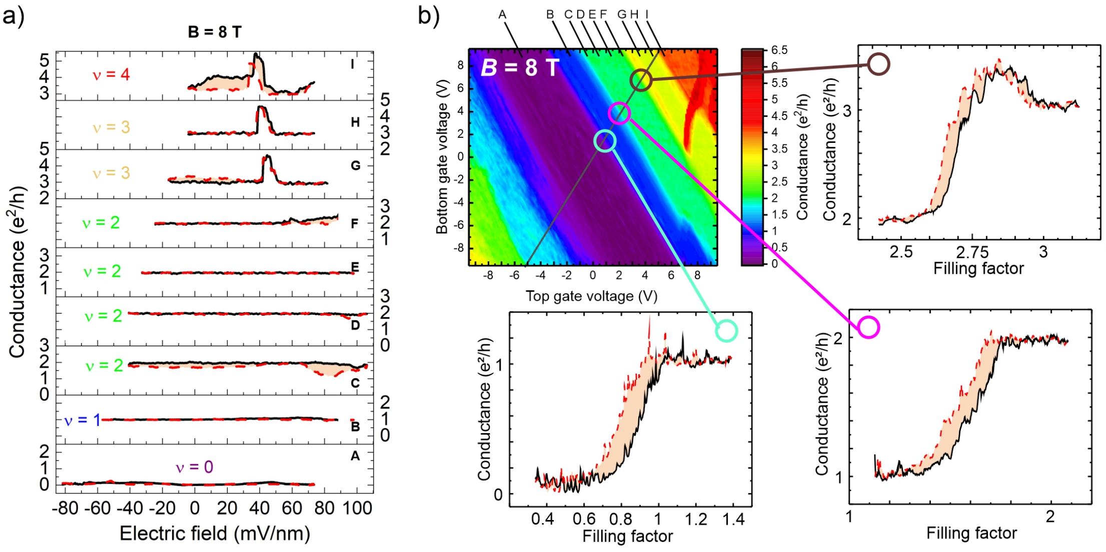

Figure 5.4: a) Trace (solid, black) and retrace (dashed, red) of D line scans at fixed ν values and $B = 8$ T. An hysteretic behaviour is seen starting at $D > 60$ mV/nm when scanning close to the plateaus boundaries and on the full accessible range at $\nu = 4$. b) Differential conductance map at $B = 8$ T. The capital letters indicate the fixed n values associated to the scans on the plot in b). Scanning n at $D = 0$, crossing from one to the following QHE conductance plateau shows a hysteretic behaviour. Trace and retrace are shown in black (solid) and red (dashed), respectively. In every line scan plot, the area of the hysteresis is shaded in orange for visualization.

region in the map in Figure 5.4 b)), the trace and retrace measurements overlap for a wide range of D field accessible on the experiment. For $\nu = 2$ (green region), a hysteretic behaviour in D is observed only at the limits before jumping to a next conductance plateau and at large D, but not in the centre of the plateaus for a wide range of D (between -60 mV/nm and 60 mV/nm). $\nu = 3$ (yellow) does not show a pronounced hysteretic behaviour in D, despite crossing a region of increment in conductance in one unit of e^2/h. $\nu = 4$ (red), shows a hysteretic behaviour in D. As discussed in chapters 2 and 4, this hysteretic behaviour should be attributed to a phase change, in particular of first order. More specifically, to a change between layer polarized states [46]. From this result, it can be argued that, in tetralayer ABCA graphene, the phases at filling factors $\nu = 1, 2$ and 3 are layer coherent, while $\nu = 4$ is layer polarized. Although, $\nu = 3$ should be treated more carefully, as a slightly hysteretic behaviour could be claimed to be present at $D = 0$. Additional measurements showing the effect of D field in the conductance plateaus at 7 T are shown in the supplementary material in section 5.5, Figure 5.9. Remarkably, Figure 5.4 b) shows that the boundaries between conductance plateaus should be treated carefully, since trace and retrace of an n scan do not overlap, leaving some margin of error when assigning a filling factor close to the boundary of a plateau. This behaviour in the conductance, seen in the line traces in Figure 5.4 b) at fixed D and changing n (ν is assigned after calibrations), is however surprising and therefore worth of a separated discussion, which given next paragraphs.

An interesting aspect discovered when characterizing this sample is what happens

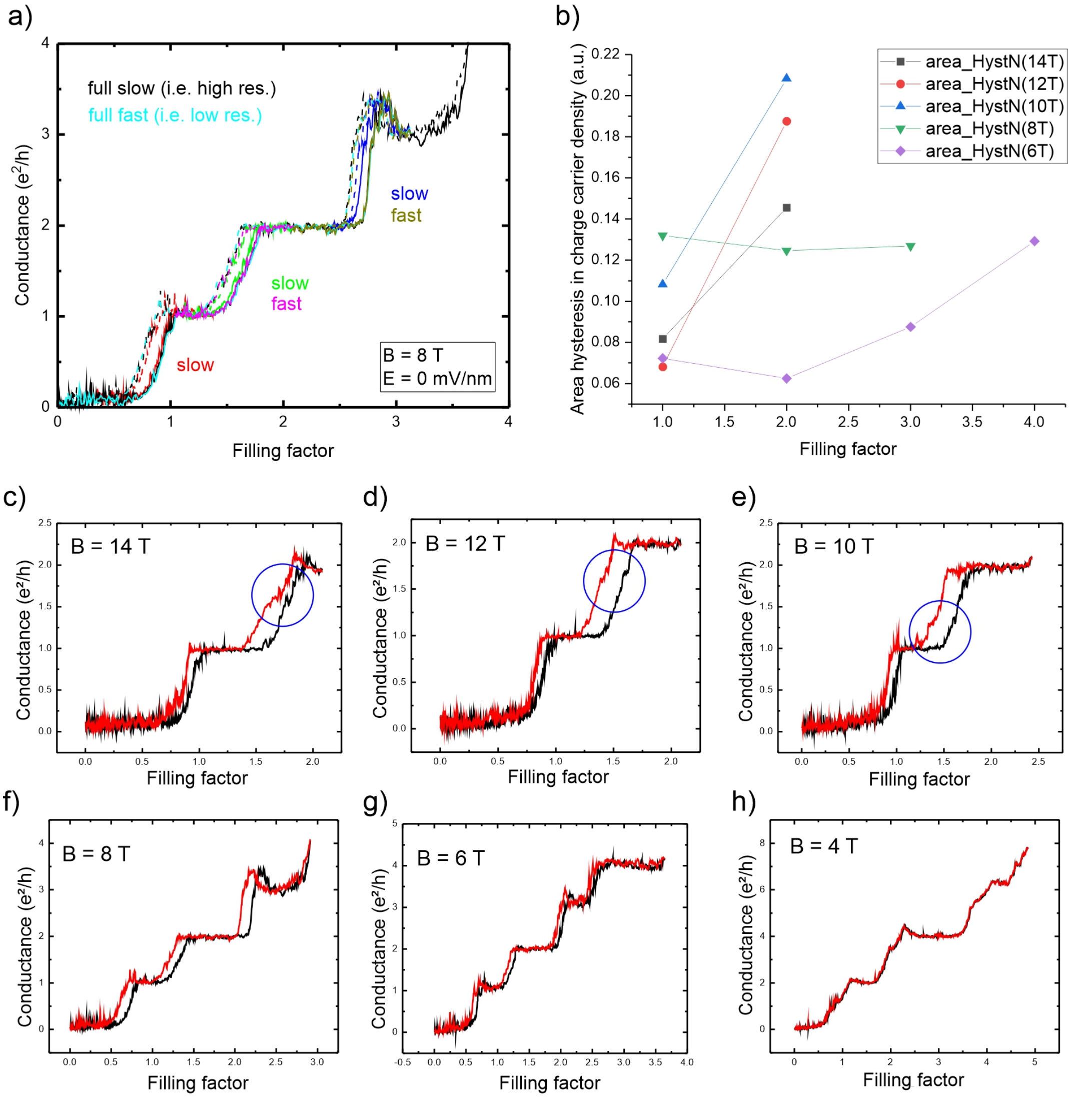

Figure 5.5: a) Trace (solid) and retrace (dashed) line scans at $D = 0$ and $B = 8$ T crossing from one plateau to the other, at different scanning rates: fast meaning larger n step size and slow, smaller n step size. The individual scans overlap with a general scan from $\nu = 0$ to 4 and back. b) Area of the hysteresis loop as a function of ν. The points at $\nu = 1$ correspond to the hysteresis measured from 0 to 1, and so on. c)-h) Hysteresis in n (equivalent, ν) in a scan covering the full range accessible by the experiment at different B fields. Trace is shown in black and retrace in red. The blue circles mark additional features discussed in the main text.

when crossing conductance plateaus at a fixed D field. This is done in the experiment by scanning n back and forth, setting D to a fixed value. As shown in Figure 5.4 b) in a measure of G as a function of ν (calculated with the slope calibration from the fan diagram in Figure 5.1, section 2.2.4), crossing conductance plateaus on a trace and retrace measurement evidences a hysteretic behaviour. This suggests that the transitions between QHE plateaus on this system are first order phase transitions (see discussion about quantum and classical phase transitions in chapter 2). Noteworthy, the cases in the literature which show experimentally similar behaviour are rare. Only two closely related experiments proving evidence of a first order phase transition character for transitions between conductance plateaus have been reported to date. One studies QHE states confined to a wide gallium arsenide quantum well, demonstrating the occurrence first-order phase transitions in a quantum Hall ferromagnet [121], another investigates correlated states and orbital magnetism in twisted monolayer-bilayer graphene, showing first-order phase transitions at high field upon sweeping B [192]. Noteworthy, both works observe the phase transition phenomena by scanning a B field. The findings presented here bring novel insights about the nature of the LL transitions in rhombohedral few-layer graphene, showing a first-order phase transition character by scanning the parameter n of the system. Noteworthy, this effect has been observed as well in the trilayer rhombohedral graphene samples prepared within this thesis (see results section 5.5 as well as Figure 4.11 in the supplementary material of chapter 4).

Further measurements of the hysteretic behaviour when crossing conductance plateaus by scanning n are given in Figure 5.5. To start, Figure 5.5 b) shows that the hysteresis in n does not depend on the starting point for the first two conductance plateaus (red, green and pink curves), but it does when crossing from $\nu = 2$ to $\nu = 3$ (blue and golden curves). Moreover, a full scan varying the scanning rate, i.e., comparing finer step-size in n (shown black, indicated as slow) with a coarser step-size in n (shown in cyan, indicated as fast) shows a perfect overlap of trace and retrace when continuously crossing plateaus from $\nu = 0$ up to $\nu = 3$, back and forth. An additional aspect to note on the measurement in Figure 5.5 a) is the width of the hysteresis loops in n. These are summarized in Figure 5.5 b). Although comparing the area of the hysteresis assigned to a plateau crossing (in the Figure, datapoint at $\nu = 1$ represents the crossing from 0 to 1, at $\nu = 2$, crossing from 1 to 2, and so on) does not show a clear general tendency, it seems that in some cases the hysteresis is rather stronger at higher than lower B. This tendency is also present in the results shown on Figures 5.5 c)-h), where trace and retrace of a scan in n are represented with solid black and red lines respectively. Noteworthy, the hysteresis is very clear starting at $B = 8$ T and above, while it is hard to observe (almost not visible) below $B = 4$ T. It is worth mentioning, a comparison of the areas of the hysteresis above 8 T (and in the sense of comparing between plateaus with integer filling factors) should be taken more carefully, since additional steps appear between the conductance plateaus, which are not present at lower B fields (see blue circles in Figures 5.5 c)-e)). Further investigation is necessary to elucidate the nature of this hysteresis by comparing its characteristics at different ν, D and B fields. This could be useful to gain insights on the understanding of a QHE phase transition from a perspective of domain pining of the electronic states before the system jumps from finding itself at one filling factor to another.

Last but not least, it is interesting to analyse the behaviour at low magnetic fields, for instance, to look for broken symmetry states (and ground states) of the system, as discussed in chapter 4. Figures 5.6 a) and b) show the fan diagram at B fields bellow 500 mT. Notably, the filling factors 8 and 16 can be traced down to $B = 0$ at $D = 0$, while only the filling factor 8 shows a clear trace to $B = 0$ at a finite value, $D = 24.5$ mV/nm. Not only the stronger presence of the filling factor 16 is a low B feature at $D = 0$, a

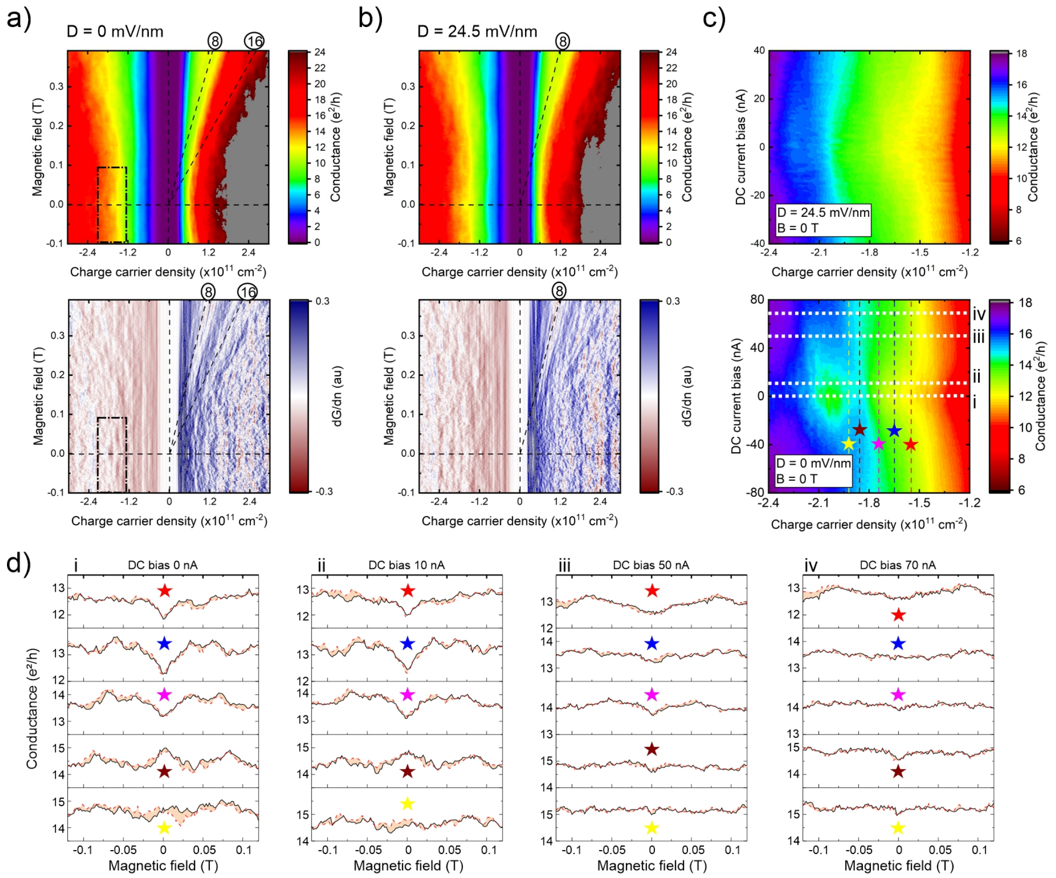

Figure 5.6: a)-b) Low B fan diagrams (top) and corresponding derivatives (bottom) at $D = 0$ and D=24.5 mV/nm. The encircled numbers are the filling factors traced down to $B = 0$ (marked with a black dashed horizontal line for reference). c) DC bias spectroscopy measurement for negative low n values at 0 and finite D. d) Trace (black, solid) and retrace (dashed, red) of a magnetic field scan (within black dash-dotted enclosed region in a)) at $D = 0$, at the charge carrier density values indicated with coloured stars (with reference on c), bottom) for different DC bias values (white dashed lines in c), bottom).

DC bias spectroscopy measurement (Figure 5.6 c)) shows as well additional regions with conductance fluctuations at $D = 0$ (similar as those discussed for trilayer graphene in chapter 4), rather than at finite D. Taking this observation as starting point, a further study focusing on the features at $D = 0$ and low B field, region enclosed in the black dash-dotted rectangle in Figure 5.6 a), is perform with results shown in Figure 5.6 d). Here, the response of the system at $D = 0$ and different fixed n values (indicated with stars and referred to Figure 5.6 c), bottom), for different DC current bias lines evidences a hysteretic behaviour in B as well as a change in the nature of the states approaching $B = 0$. This can be followed on an increase or decrease tendency in G when approaching $B = 0$, which is different at different DC biases. Interestingly, the trace (solid, black) and retrace (dashed, red) of the B field scan does not always show an hysteresis. This encourages further investigation of possible magnetic states localized at certain n values in the map shown in Figure 5.6 c), bottom, for the system at $B = 0$ and $D = 0$.

5.4 Conclusions

The results discussed within this chapter provide a detailed electron transport study of suspended tetralayer rhombohedral (ABCA) graphene. First, a measurement of the interaction induced spontaneous gapped phase in the sample is shown to have a larger gap in D as its counterparts with two and three layers, as theoretically predicted. This is a sign of stronger interaction effects within the system of study. Next, a measurement of the fan diagram of the sample at $D = 0$ and from 0 to 14 T provides experimental evidence of crossings between LLs. This data could be useful to fit a model of the LL energy dependence on the magnetic field, such as found in Ref. [35], for an identification of the stacking order of tetralayer graphene from a transport viewpoint. In addition, distinct features in the conductance map at different B and D fields are revealed, in particular at higher n values. These results suggest the presence of layer coherent and layer polarized states in the system, which can be identified by the absence or the presence of a hysteretic behaviour in D and/or jumps in the conductance at a fixed D within a QHE plateau. Noteworthy, these distinct states appear to be tuned by a B field. On a specific example, the results in the present chapter show evidence of $\nu = 3$ being layer polarized at $B = 8$ T and unpolarized at 4 T in a reproducible manner. These results constitute novel evidence of B tuneable states in a rhombohedral few-layer system. In addition, a pronounced hysteretic behaviour is revealed when crossing LLs at a fixed D, scanning n. This evidences a first-order phase transition character associated to the transitions between QHE conductance plateaus, from a novel perspective which is scanning n instead of B. A theoretical description of the observed phenomena could contribute to understand the competition between different order parameters of the few-layer graphene system, before transitioning from one QHE conductance plateau to another. The findings presented here could contribute elucidate the nature of correlation effects [193], in particular, within the QHE regime in rhombohedral graphene systems. Last but not least, the observation conductance plateaus with $\nu = 8$ and 16 are tracked down to $B = 0$, with $\nu = 16$ being suppressed by a finite D field. Notably, this seem to be opposite the phenomena observed in trilayer, where the application of D activates the lower ν conductance plateau at low B (see chapter 4). In addition, a DC spectroscopy measurement at $B = 0$ reveals features in the conductanc map which are present at $D = 0$ but not at a finite D. These results could help to determine the nature of the ground state of rhombohedral tetralayer graphene. Further investigation of the low B states in rhombohedral tetralayer graphene samples and theory interpretation of the ν values observed is necessary to determine the origin of this result.

5.5 Supplementary material

This section presents further measurement and calibration data not shown within Sections 5.2 and 5.3. This data shown as supplementary material supports and extends the results presented within this chapter and is shown for completeness and reference.

Fabrication and device quality

Figure 5.7 a) shows a Raman spectroscopy map (2D-peak) of the flake used for the devices presented within this chapter, where a measurement of the FWHM at every point over the flake distinguishes between Bernal and rhombohedral stacking order. In the Figure, darker blue and red areas correspond to ABAB and ABCA stacking order, respectively. White regions are undefined, although individual points on these regions are determined to be ABCA or ABCB by the presence or absence of a modulation of the asymmetric profile of the 2D-peak towards lower wavenumbers [155]. Figure 5.7 b) shows the s-SNOM measurement of the mechanical amplitude and optical phase for the flake in a). A comparison of this measurement with the corresponding Raman map determines with nm spatial resolution the regions of the flake of a given stacking order. Based on this comparison, a portion of the flake containing rhombohedral stacking order is isolated by RIE. Figure 5.7 d) shows a layout design with the different EBL masks used for fabricating contacts to the isolated rhombohedral multilayer graphene flake (now with rectangular shape). d) shows the resistance of the QHE plateaus as a function of the inverse of the filling factor (ν), measured at $B_\perp = 4$ T and $D = 20.4$ mV/nm, after current annealing (same as described for trilayer graphene on the result shown in Figure 4.7 a)). The slope of the linear fit, calculated (25365 ± 437) Ω overlaps with the von Klitzing constant, yielding a contact resistance of $R_C = (1537 \pm 55)$ Ω. Figure 5.7 c) shows the conductance plateaus of the QHE at $B_\perp = 4$ T and $D = 20.4$ mV/nm after subtracting the contact resistance. The measurement shows well defined conductance steps, with conductance plateaus at integer factors of e^2/h as a function of ν.

Results reproducibility

Figures 5.8 a)-c) show a differential conductance map as a function of bottom and top gate voltages and, Figures 5.8 d)-f) fan diagrams at a finite and zero externally applied displacement field. The results belong to a second fabricated sample and reproduce the findings for the sample discussed in the main text. Figures 5.8 g) shows the reproducibility of the fan diagram of Figures 5.1 c) on a different cool down of the sample. This implicates taking the sample outside of the cryostat and loading it again, after which it is always necessary to perform a new current annealing process, which usually requires a new calibration for the transport measurements. This leaves the sample with different initial conditions for the electron and magneto transport studies, but with results proving that the sample preserves its rhombohedral stacking order.

Additional transport and hysteresis data

Figure 5.9 a) shows additional transport data to complement the discussion of the results in Figure 5.4. A measurement of the trace and retrace of a D field scan at different fixed ν (within a conductance plateau) shows a hysteretic behaviour for $\nu = 3$ and no hysteresis visible for $\nu = 1$ and 2. Thus supports the statement in the main text for $\nu = 1, 2$ as layer coherent states, and introduces $\nu = 3$ as a layer polarized state at a different B field. Figure 5.9 b) shows the presence of an hysteresis in n for zero and finite displacement field. One more time, despite the presence of a displacement field, the hysteresis in n appears to be more pronounced for higher magnetic fields, as well as in the main text. Figures 5.10 and 5.11 show additional hysteresis data measured, respectively, in suspended tetralayer and trilayer rhombohedral graphene when crossing QHE conductance plateaus by sweeping the parameter n of the systems, for zero as well as finite D fields. Last, Figure 5.12 a) is an extension of the bias spectroscopy study discussed with Figure 5.6, showing higher n values. Figure 5.12 b) shows an hysteresis in B for certain n and D conditions when crossing the zero perpendicular magnetic field on a trace and retrace scan at a fixed n.

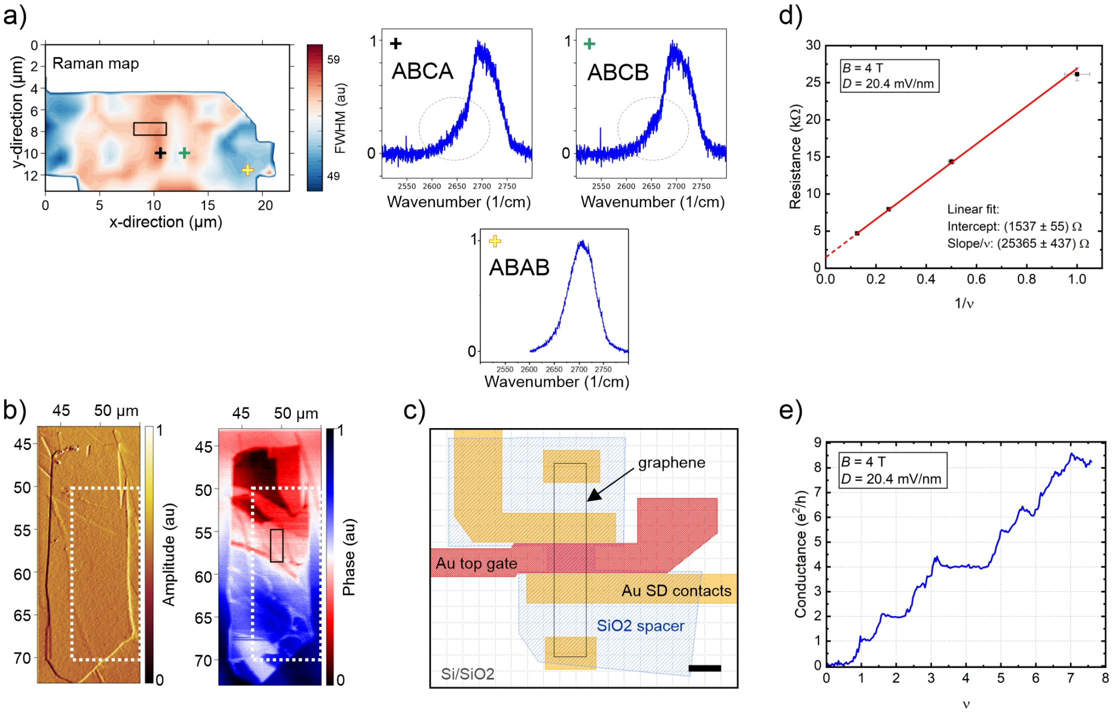

Figure 5.7: Fabrication and device quality. a) Raman spectroscopy map of the tetralayer graphene flake, from a single Lorentzian fit of the 2D-peak Raman signal. Bigger FWHM (red) corresponds to Rhombohedral (ABCA) stacking order and, lower (blue), to Bernal (ABAB). Values in between correspond to ABCB stacking, distinguished from ABCA by a difference in the shape of the 2D-peak signal, as encircled with a dotted line on the single peak plots (see Refs. [154, 155]). b) s-SNOM measurement of the flake. The area enclosed by the white dashed line corresponds to the area of the Raman map shown in a). c) Layout design for the fabricated dual gated tetralayer rhombohedral graphene device. In yellow are represented the source and drain contacts to the flake (SD). The gold pads on the flake extremes are for preventing it to break/fold on itself during suspension. Scale bar 1 μm. d) Resistance of the conductance plateaus after in-situ current annealing as a function of the inverse of their calculated filling factors. The contact resistance is extracted from the intercept, resulting in $R_C \approx 1537\ \Omega$. e) QHE conductance plateaus as a function of the filling factor after subtracting the contact resistance.

5.5 Supplementary material

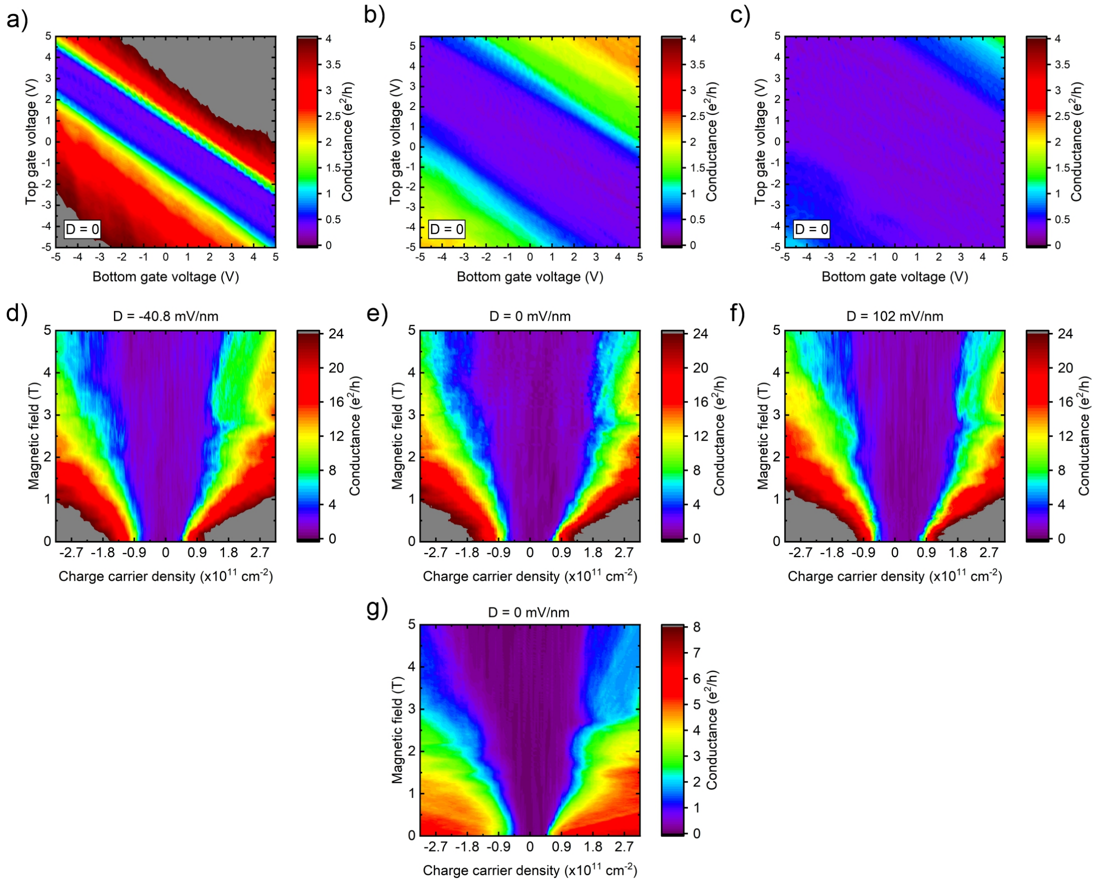

Figure 5.8: a)-f) Magneto-transport measurements on a different fabricated dual-gated tetralayer rhombohedral graphene sample. Here, the contact resistance is not subtracted. g) Fan diagram at $D = 0$ for the sample discussed in the main text (section 5.3), measured on a different cooldown. This implicates taking the sample out of the cryostat, loading it again and performing again current annealing.

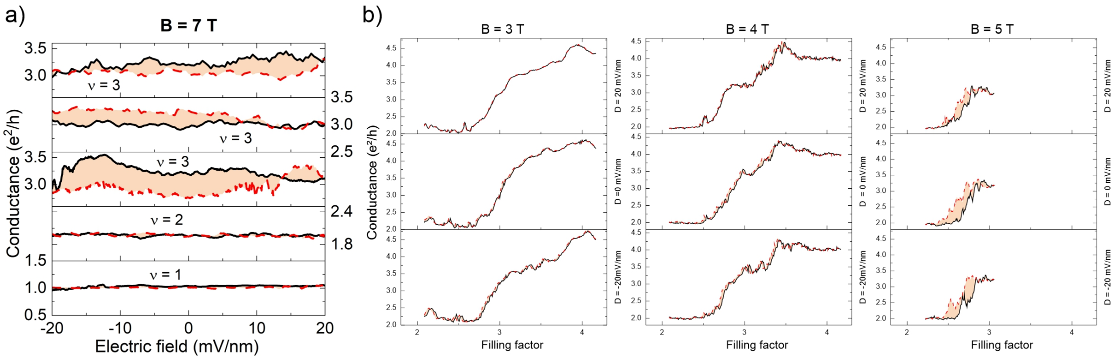

Figure 5.9: a) Trace (solid, black) and retrace (red, dashed) of a D scan at the indicated fixed n values, at $B = 7$ T. b) Trace (black, solid) and retrace (red, dashed) of a filling factor scan (crossing conductance plateaus) at different B and D fields. The area of the hysteresis is shaded for visualization. Results on the sample discussed in section 5.3.

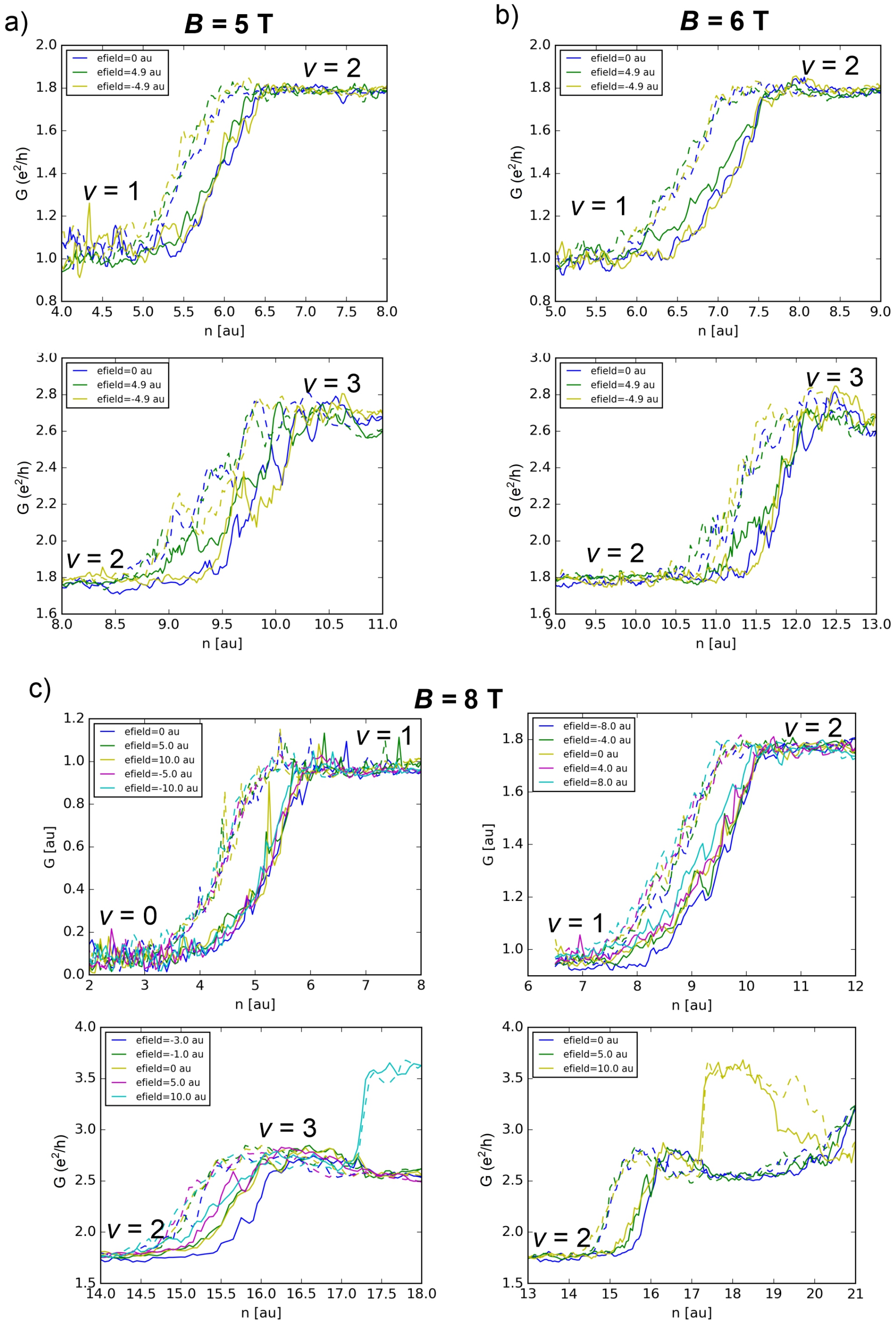

Figure 5.10: Additional hysteresis data taken when measuring the conductance as a function of n for zero and finite D and increasing B fields in the suspended rhombohedral tetralayer sample discussed in the main text (section 5.3). Trace (retrace) are indicated with solid (dashed) lines. The n and D values are given in arbitrary units. The contact resistance is not subtracted.

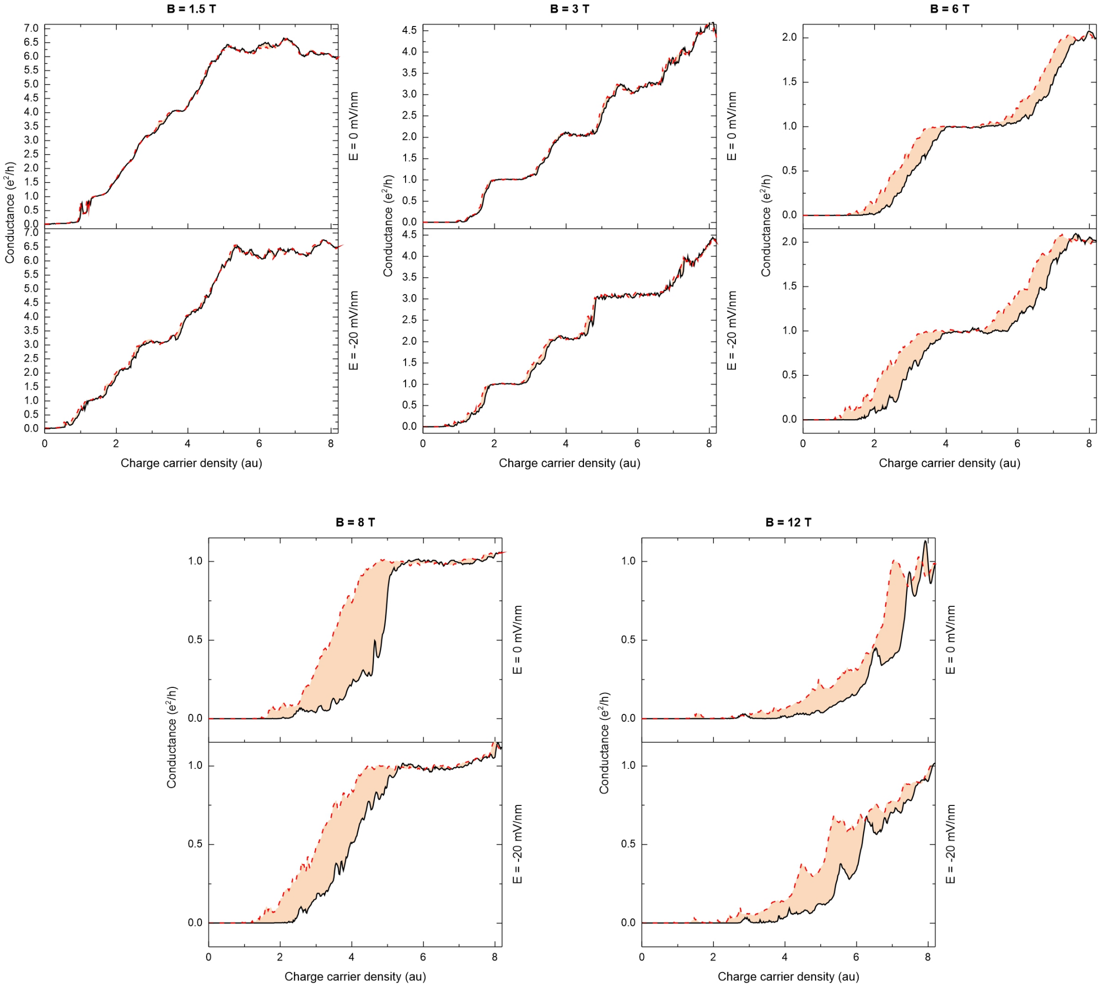

Figure 5.11: Hysteresis behaviour when measuring the conductance as a function of n for zero and finite D and increasing B fields in a suspended rhombohedral trilayer sample, fabricated using the trilayer rohombohedral graphene portion of a graphene flake, identified and isolated as described in chapter 3. Trace (retrace) are indicated with solid black (dashed red) lines. The area of the hysteresis is shaded for visualization. The n values are given in arbitrary units.

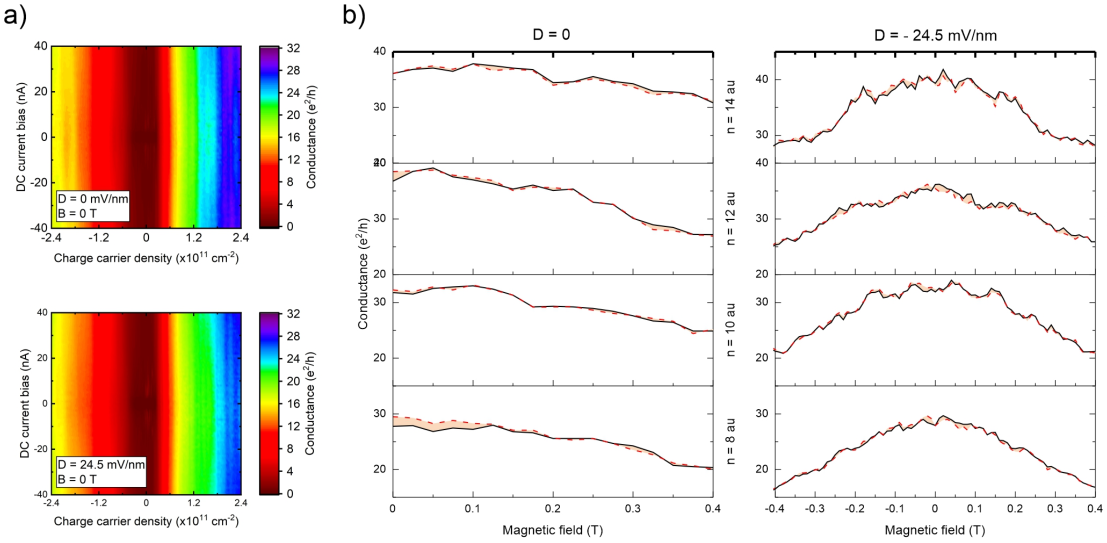

Figure 5.12: Extended data of Figure 5.6. a) Differential conductance as a function of the DC current bias charge carrier density n 0 and finite D fields. b) Trace (black, solid) and retrace (dashed, red) of a magnetic field scan at 0 and finite D fields and 0 DC current bias, for the indicated fixed n values.

Chapter 6

Landscape of a Charge Density Wave phase transition in 1T-TaS$_2$

The experiments discussed within this chapter are part of a collaborative research project between the group of Prof. Dr. Thomas Weitz and the group of Prof. Dr. Claus Ropers, which aims at understanding the microscopic origins and mechanisms behind CDW phase transitions in the TMD 1T-TaS$_2$. To do this, elucidating the impact of intrinsic and external parameters such as layer thickness, dielectric environment and electrostatically induced charge carrier density on the system is a key. As a starting point to address this topic, bulk 1T-TaS$_2$ samples ($\sim$ 35 nm thick) are prepared in a two-terminal device configuration using a TEM membrane as a substrate. This enables to investigate the structural and electrical signatures of a CDW phase transition by both electron transport and diffraction measurements on the same sample, independently as well as simultaneously. For the simultaneous experiments, a novel type of TEM setup developed by the group of Prof. Claus Ropers at the University of Göttingen is used. With this setup, the influence of a DC current flow on the phase switch between NC- and IC-CDW phases in two types of 1T-TaS$_2$-based devices (two-terminal and shorted) is investigated by means of diffraction measurements as well as bright and dark-field (DF) TEM imaging. While the electrical transport measurements reveal novel properties of the system at the transition boundary between a C-/NC-CDW phase switch, real space DF imaging of a NC-/IC-CDW phase switch allows following the structural changes associated to a controlled CDW phase switch in a 1T-TaS$_2$ flake. The results shown on this chapter contribute towards a complete understanding of the active control mechanisms and evolution of CDW phase transitions within 1T-TaS$_2$. Moreover, light is shed onto the pathways for a controlled metastability of a CDW phase switch.

The results presented in this chapter are currently being prepared for publication. The bright and DF TEM images as well as the diffraction measurements have been done by Till Domröse. The fabrication of the DF mask has been made by Till Domröse and Felix Kurtz. The sample design and fabrication, its characterization, electron transport measurements as well as the data analysis has been done as part of this thesis.

6.1 Introduction

Already since the 1980s, the CDW material 1T-TaS$_2$ has been centre of considerable attention. In the past years, the richness of its phase diagram, which hosts a diversity of charge-ordered phases, has been a reason for the renewed investigation interest. It is noteworthy that, within 1T-TaS$_2$, both Peierls and Mott physics are involved in some of its CDW states [50]. Moreover, the transitions between CDW phases in 1T-TaS$_2$ present a first order nature [50,53,194], making the material interesting for applications in nanoscale devices based on a controlled phase switch, for instance, for quantum communication, computation technologies and memristive systems. Despite the many approaches to study the phase diagram of 1T-TaS$_2$, such as by charge transport, scanning probe and spectroscopic experiments [53,141,195], the true nature and origin of the material phases and transitions between them remains a debate. An interesting aspect in relation to some open questions is the impact of intrinsic and external parameters, excitations, stabilization and transitions of CDW phases in 1T-TaS$_2$. This includes the influence of stationary current densities and induced thermal effects. In the past years, experiments dedicated to trigger CDW phase transitions by applying external voltages to 1T-TaS$_2$ flakes [196,197] have suggested a thermal origin of the CDW phase switching while demonstrating a phase switch control on the samples by externally applying electrical signals. However, other studies reveal peculiarities around the CDW phase switching, which are linked to the influence of the application of electrical signals. For example, it has been shown that the application of an in-plane voltage can trigger the appearance of metastable states in 1T-TaS$_2$ flakes of reduced thickness [53]. This suggests it is worth considering other mechanism besides Joule heating to understand some of the CDW phase switch behaviour in 1T-TaS$_2$. The results discussed within this chapter intend to address this aspect in particular. Morever, while most of the previously reported experiments investigate the CDW phase switching within 1T-TaS$_2$ only from the electrical transport or the structural characterization viewpoint, the experiments presented here are aimed to combine the two approaches. The structural changes associated to CDW phase transitions in 1T-TaS$_2$ triggered via temperature have been imaged in the real space via STM [198], AFM [194] and s-SNOM [199], showing the formation of clusters on the sample surface and expansion of domain walls extending over the flakes as the origin of an overall phase switch. The experiments presented here connect the realm of electrical measurements with the structural change visualization of a CDW phase switch, providing a complete panorama of the transitions in the material and demonstrating a control of a NC-CDW to IC-CDW phase switch in an electronic device configuration.

The chapter is organized as follows. First, in section 6.2 the methods developed during this thesis for fabricating samples which allow simultaneous electrical and structural characterizations of CDW phase transitions in 1T-TaS$_2$ flakes are introduced. Next, in section 6.3, a study of the basic electronic transport and structural properties of the fabricated samples is shown. This is taken as a starting point for next experiments by proving that the fabricated samples host the expected CDW physics. While doing these measurements, a surprising behaviour of the current-voltage (I-V) characteristics of the 1T-TaS$_2$ two-terminal devices is found, which is discussed with details. In particular, the results reveal a stabilization mechanism towards the C-CDW phase, which occurs upon application of a DC current bias at the interface between a C-/NC-CDW thermally driven phase switch. To continue, the experiments of simultaneous electrical and structural characterization of an NC-/IC-CDW phase transition are presented. The influence of an externally applied DC voltage between two terminals on the samples is revealed in a real-space image of the phase transition. To do this, a technique of DF-TEM imaging is implemented (see Ref. [176] and chapter 3, section 3.2.4, of this thesis). This study provides a complete picture of the controllable and reversible features associated to the IC-/NC-CDW phase switch on a 1T-TaS$_2$ flake with electrical contacts. Last, in section 6.4, a conclusion and future prospects are outlined.

6.2 Fabrication and methods

The samples presented within this chapter are fabricated and characterized as described in chapter 3 (section 3.2). In brief, thin films of 1T-TaS$_2$ are obtained by mechanical exfoliation with blue Nitto tape (SWT20+, Nitto inc.) from a bulk crystal (1T phase Tantalum Disulphide, HQ graphene) and transferred onto a TEM substrate. Figure 6.1 a) shows an AFM image of a flake as used for the experiments presented here. Flakes with thicknesses between 20 nm and 50 nm found on the centre of a TEM window (20 nm thick SiNx membrane) are localized with an optical microscope and pre-selected according to their thickness. Two-terminal contacts (4 nm Ti/ 60 nm Au) are fabricated on top of the selected flakes using standard EBL and PVD. Figure 6.1 b) shows an optical microscope image of a two-terminal 1T-TaS$_2$ device and Figure 6.1 c) shows the same device on a bright field TEM image, together with a scheme of a cross-section of the device on the TEM substrate (side view representation). Devices with a shorted channel constituted by a $\sim$200 nm wide metallic wire in contact to the flake outer edge on the two-terminal channel are fabricated by over-exposing the PMMA during EBL. Details about this fabrication together with an optical microscope image of the overexposed PMMA mask and an AFM image of the resulting short channel (without a 1T-TaS$_2$ flake for better visualization) are shown in the supplementary material of this chapter, in section 6.5 (see Figure 6.7). Successfully fabricated devices are fixed onto a holder with Cr pads, as described in chapter 3, section 3.2.3. Aluminium bond wires are made with an ultrasonic wedge bonder (K&S 4523 Wedge Bonder) to build electrical connection between the sample and the holder. Quantum transport measurements for tracing the temperature dependance of the resistance associated to a CDW phase transition in 1T-TaS$_2$ two-terminal devices are performed in a closed-cycle Lakeshore probe system with a temperature scanning range between 5 K and 400 K. For the simultaneous structural and electrical characterization, in particular, to trace the evolution of a structural phase transition in real space, the samples are measured in the UTEM setup at the group of Prof. Dr. Claus Ropers, operating at room temperature. A description of the setup and its measuring modes used

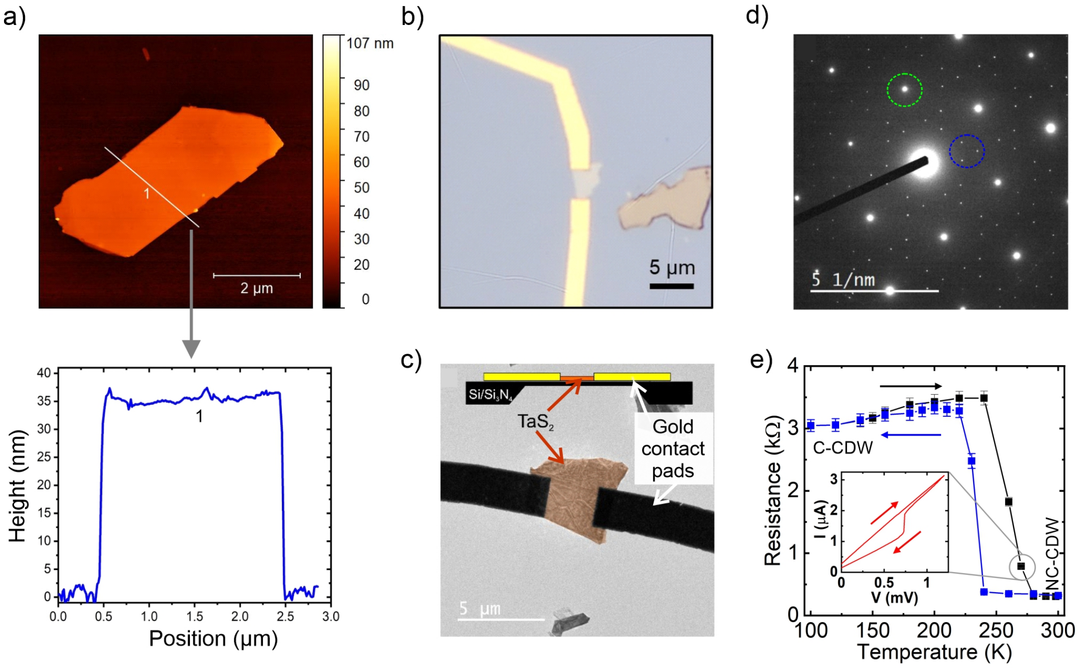

Figure 6.1: Sample fabrication and characterization. a) AFM image of an exfoliated 1T-TaS$_2$ flake, ∼ 35 nm thick. b) Optical microscope image of a two-terminal 1T-TaS$_2$ device on a TEM substrate. c) Bright-field TEM image of the device and a side-view scheme. The flake with gold contacts sits on the SiNx membrane on a window of the TEM substrate. d) Diffraction image of the contacted flake at room temperature shows the characteristic satellite points (e.g. enclosed by blue dashed circle) around the main Bragg points (e.g. enclosed by green dashed circle) of the NC-CDW phase. e) Resistance of the 1T-TaS$_2$ flake as a function of temperature showing the transition between the NC-CDW and C-CDW phases upon cooling (blue) and heating (black), with hysteretic behaviour. The inset shows the current-voltage characteristic at a transition point with hysteretic switching of the resistivity. The arrows indicate the directions of the scans.

during this thesis are given in chapter 3 (section 3.2.4). In the supplementary material in section 6.5 of this chapter (Figure 6.8), details on the DF aperture array, tailored to filter the periodicities of a CDW at the diffraction plane of the microscope, are given. Figure 6.1 d) shows a diffraction measurement at room temperature of the fabricated two-terminal 1T-TaS$_2$ sample, where clear diffraction spots from the NC-CDW phase are observed. This measurement ensures that the flake contains CDW phases. Together with the C-CDW to NC-CDW phase transition observed for the same flake when measuring the resistance as a function of the temperature (Figure 6.1 e)), these measurements prove that conventional exfoliated flakes can be used in a suitable geometry as required for the experiments discussed within this chapter. An extended discussion on the electrical characterization result shown in Figure 6.1 e) is given in the following section.

6.3 Experimental results

For the initial identification of CDW phases, independent electrical and structural characterization of the same sample are performed. As mentioned in the previous section, a diffraction measurement of the flake on the fabricated device is taken in the first place to confirm that the flake hosts CDW phases. Figure 6.1 d) shows that this is the case for the sample discussed here, since the diffraction spots characteristic for a NC-CDW phase in 1T-TaS$_2$ are present at room temperature (see theory background in chapter 2, section 2.3). After this measurement, the sample is loaded into the Lakeshore probe station to study the dependance of its resistance as a function of the temperature. Figure 6.1 e) shows the result of this measurement for the ~ 35 nm thick 1T-TaS$_2$ flake in a two-terminal device configuration on a TEM membrane. Here, an abrupt change in the resistance associated to a phase transition between the NC-CDW (at higher temperature) and C-CDW phases (at lower temperatures), each with respectively lower and higher resistance values, is observed. Moreover, a hysteretic behaviour is measured upon variations of the temperature around the NC-/C-CDW phase switch. This indicates that the phase transition between NC- and C-CDW phases is of first order, in the sense of the traditional classification of phase transitions, being of first order those in which two phases co-exist at the transition temperature (see Ref. [118] and chapter 2, section 2.2.4 of this thesis). This result for the C-/NC-CDW phase switch is consistent with previous experiments by other groups which studied the CDW phases in 1T-TaS$_2$ by measuring the resistance of the material as a function of the temperature (e.g. Refs. [50, 51]). Comparing the results presented here with those in the literature, it is worth noting that the temperature central value of the hysteresis loop in Figure 6.1 e) is shifted in about +50 K with respect to the experimental results reported by other groups on bulk and nano-thick 1T-TaS$_2$ samples [50, 51, 53, 103, 141]. This is attributed to a poor thermal coupling between the probe-station setup and the sample on the TEM membrane, given the fact that the 1T-TaS$_2$ flake is only in contact with the 20 nm thick SiNx membrane and the gold leads, each of them not directly touching the probe-station sample holder. As a consequence, the NC-CDW to IC-CDW phase transition, expected to occur at temperatures between 350 K and 400 K (close to the measuring limit of the setup), could not be observed in a measurement of the resistance as a function of the temperature. For this reason, the temperature dependant experiment with samples on a TEM membrane discussed in this chapter is limited to the observation of the C-/NC-CDW phase transition only.

While performing the experiments to investigate the CDW transitions which can be induced by a temperature change in 1T-TaS$_2$, an interesting behaviour of the I-V characteristics of some points in the curve shown in Figure 6.1 e) was noticed. As it can be observed in the inset of Figure 6.1 e), a bias-dependant hysteretic resistance switching seems to be present at the transition points between the C-CDW and the NC-CDW phases. Figures 6.2 b)-h) show the I-V curves associated to the datapoints on the measurement branch upon heating in Figure 6.1 e) (plotted separately in Figure 6.2 a) for better visualization). An analogous compilation of results is shown in the supplementary material of this chapter, in section 6.5 (Figure 6.6), for the branch upon cooling. While the system is at a well-defined CDW phase, namely, the higher (lower) resistive C-CDW (NC-CDW), the I-V characteristics of the sample at the temperature points for each phase have a linear behaviour with a perfect overlap between trace and retrace measurements.

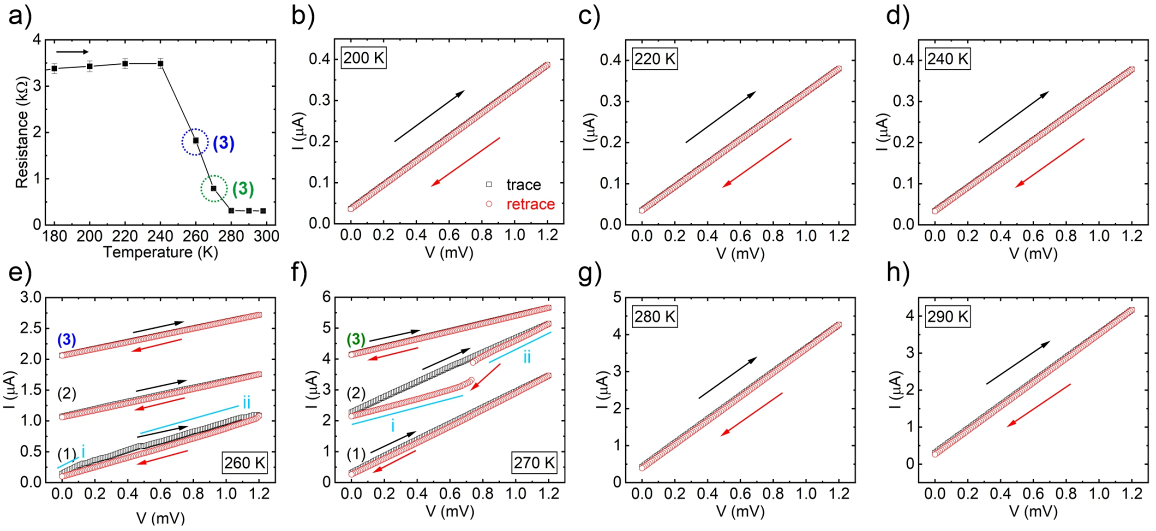

Figure 6.2: I-V characteristics of the two-terminal 1T-TaS$_2$ device at different temperature values. In all cases, the arrows indicate the direction of the scan. a) Resistance as a function of the temperature for the C-/NC-CDW phase transition upon heating. The resistance values of the encircled data points are extracted from the slope of the curves in e) and f) with same coloured number. b)-h) I-V curves of the data points in a). The open black squares (open red circles) correspond to the trace (retrace) scans. In e) and f), (1), (2) and (3) indicate first, second and third consecutive measurements on a same voltage range. In e) (f)) an offset of I = 2 µA (I = 1 µA) is added between the curves for visualization. The cyan lines (i and ii) indicate the datapoints set for the linear fit used to calculate the resistance values in Table 6.1.

This result is reproducible, as discussed in the supplementary material and shown in Figure 6.6. However, for the points in between two phases (see dashed encircled points in Figure 6.2 a)), a non-linear behaviour is observed for a first (1) and a second (2) consecutive measurements, until the resistance is stabilized on a third (3) measurement, to finally show both linear behaviour and perfect match between trace and retrace. It is interesting to note that, when the I-V fluctuations at the transition stop, the final resistance value results in between the higher and lower resistance states. Moreover, by extracting the resistance values from the slope of the I-V curves for the system at each consecutive measurement shown in Figures 6.2 e) and f), a tendency of stabilization towards the C-CDW phase becomes aparent. As listed in Table 6.1, in a measurement of the resistance as a function of the temperature upon heating, starting with the system at the C-CDW phase at 200 K, a higher resistance value is measured. At a temperature of 260 K, the resistance jumps initially to a lower value, as extracted from the slope of the trace of the I-V curve. The retrace, however, results in a higher resistance value. On a following scan, the slope of the I-V curve markedly changes and the resistance becomes higher, getting stabilized at a higher resistance value. A similar behaviour is seen at 270 K, at which temperature the system is in a first measurement at a lower resistance state, but the measurement stabilizes the system towards higher resistance values on consecutive DC bias scans. At 280 K, the system switched completely to the lower resistive state NC-CDW and the non-linear behaviour of the I-V characteristics is no longer observed. Upon cooling, a

CDW phase	**T (K)**	**(1): dV/dI (Ω)**	**(2): dV/dI (Ω)**	**(3): dV/dI (Ω)**
C	200	t: 3426.8 ± 0.5 r: 3423.0 ± 0.5		
C	220	t: 3484.5 ± 0.5 r: 3479.4 ± 0.4		
C	240	t: 3489.8 ± 0.4 r: 3478.8 ± 0.4		
Transition	260	t: $(784.4 \pm 0.3)_{\mathrm{i}}$ $(1275.0 \pm 3.0)_{\mathrm{ii}}$ r: 1290.0 ± 1.0	t: 1755.0 ± 3.0 r: 1728.0 ± 1.0	t: 1821.6 ± 0.5 r: 1814.4 ± 0.9
Transition	270	t: 382.4 ± 0.2 r: 375.8 ± 0.6	t: 419.2 ± 0.5 r: $(708.5 \pm 1.5)_{\mathrm{i}}$ $(385.0 \pm 2.0)_{\mathrm{ii}}$	t: 791.5 ± 0.3 r: 788.8 ± 0.3
NC	280	t: 312.3 ± 0.1 r: 309.5 ± 0.1		
NC	290	t: 311.0 ± 0.1 r: 307.3 ± 0.1		
NC	298	t: 306.8 ± 0.1 r: 304.2 ± 0.1		

Table 6.1: Resistance values calculated from a linear fit of the data shown in Figure 6.2 b)-h). The results extracted from the slope of the linear fit of the trace (t) and retrace (r) are listed for each temperature value, corresponding to a CDW phase or to a point in between the two phases (named Transision). (1), (2) and (3) label the consecutive scans shown in Figure 6.2 e) and f). For the case of discontinuous jumps within a scan, the data points of the I-V curves are separated in two different subsets i and ii (see cyan lines in Figures 6.2 e) and f)).

stabilization of the system towards higher resistance values when measuring the I-V curve is also observed (see discussion in section 6.5). This result suggests that the application of a DC bias at the transition points between NC-CDW and C-CDW phases stabilizes the system towards the C-CDW phase. Although different groups have reported studies on the effect of current-voltage measurements in 1T-TaS$_2$ flakes [53, 54], the results discussed with the experiments presented here, which are found exactly at the transition boundary between the NC-CDW and C-CDW switch, remained overlooked until now. A more in-depth study of the electron transport characteristics of the transition points, eventually in combination with ultrafast time-resolved measurements, could be of interest to gain more insights about the nature of the discussed behaviour.

Having a sample with two-terminal contacts on a TEM substrate enables a simultaneous structural and electrical characterization of the system. Results on such a study at room temperature are shown in Figure 6.3. Here, a constant DC voltage difference is applied between the contacts of the sample while taking a diffraction image, before changing to a next voltage point. Figure 6.3 a) shows an upwards scan. Starting at a voltage difference of 287 mV (green arrow in Figure 6.3 a), left), the system is found initially on the NC-CDW phase. This is confirmed by the observation of the characteristic satellite points in the diffraction image (see white circled dots in Figure 6.3 a), middle). By increasing the voltage, an abrupt change in the resistance is measured (see orange arrow in Figure 6.3 a)) and the satellite points are no longer visible in the diffraction pattern (Figure 6.3 a), right). Such change in less of an order of magnitude in the resistance, under

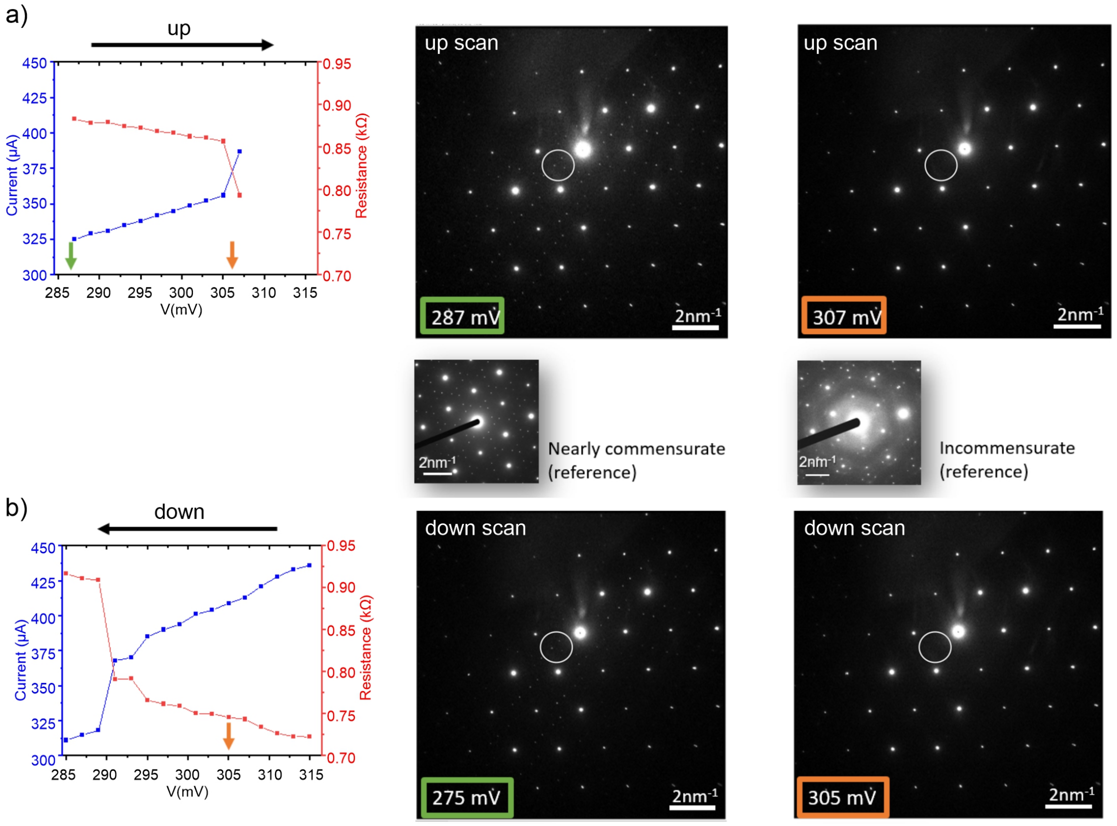

Figure 6.3: Simultaneous electrical and structural characterization of a CDW phase transition on a two-terminal 1T-TaS$_2$ device. a) Two terminal resistance measured from lower to higher DC bias (left). For each data point, a diffraction image is taken. Before the resistance jump (middle), the satellite diffraction points of the NC-CDW phase are visible and, after the resistance jump (right), not anymore. b) Same measurement from higher to lower DC bias.

an environment at which an increase in the temperature sample could be involved (e.g., from Joule heating), can be attributed to a transition of the system towards the IC-CDW phase [50, 53, 196, 197]. In the experiments discussed here, this is further confirmed by a measurement of the diffraction pattern of the 1T-TaS$_2$ flake in the device. Moreover, in Figure 6.3 b), scanning the voltage downwards shows a retardation of the resistance jump, after which the satellite points of the NC-CDW phase become again visible. The retardation in the resistance switch agrees with the expected hysteretic behaviour associated to a NC- to IC-CDW phase switch [53, 196, 200, 201]. Thus, this experiment constitutes an in-situ control of a reversible CDW phase switch in a nano-thick 1T-TaS$_2$, while tracing its structural change associated to the phase transition. In the results discussed on the following paragraph, this aspect is explored from a novel perspective.

Figure 6.4 a) shows a false-coloured bright field TEM image of a second type of device fabricated with a 1T-TaS$_2$ flake on a TEM substrate. This consists on a similar two terminal device as in Figure 6.1 b) and c), but this time the 1T-TaS$_2$ channel (coloured green in Figure 6.4 a)) is connected through a thin metallic wire (blue in Figure 6.4 a)), which shortcuts the channel while touching a side of the flake. First, it should be noted

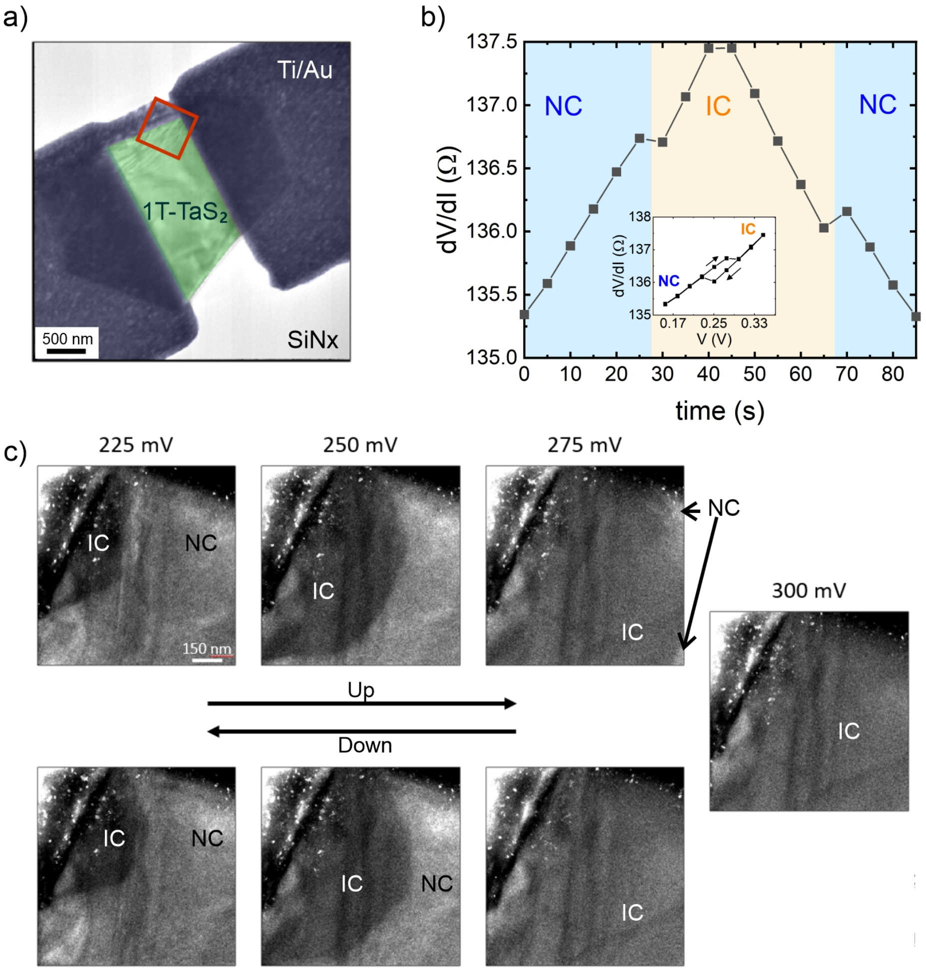

Figure 6.4: DF TEM imaging of a CDW phase transition upon application of DC current bias on a shorted device. a) Bright-field TEM image of the device showing the gold shortcut. The red square indicates the area for the DF measurements shown in c). b) Resistance of the sample measured within time intervals of 10 s. The inset shows the datapoints taken as a function of the voltage applied between the two contacts. The arrows indicate the direction of the scan. c) DF TEM imaging for the datapoints shown in b). By increasing the voltage applied between gold contacts, a front of IC-CDW phase originates on the shortcut and extends over the flake. The IC-CDW front extension over the flake is reversed by decreasing the applied voltage.

that the differential resistance values in Figure 6.4 b) of the order of 100 Ω indicate that most of the current flows through the metallic wire. This assumption is consistent with a rough estimation of the metallic wire resistance at room temperature as $R_{\text{wire}} \approx 2$ Ω, by assuming it as a free-standing gold wire (lenght 1 μm, width 200 nm and height 60 nm) with the resistivity of gold at room temperature $\rho \approx 2 \times 10^{-8}$ Ω·m [202]. As already seen in the two-terminal sample discussed with Figure 6.3, when the system overcomes a transition from the NC-CDW to the IC-CDW phase, a sudden drop in the resistance is measured. This is also observed in the shorted device when increasing the externally applied DC voltage (see Figure 6.4 b) and inset), indicating that some of the current should also flow through the material. For each data point in Figure 6.4 b) and

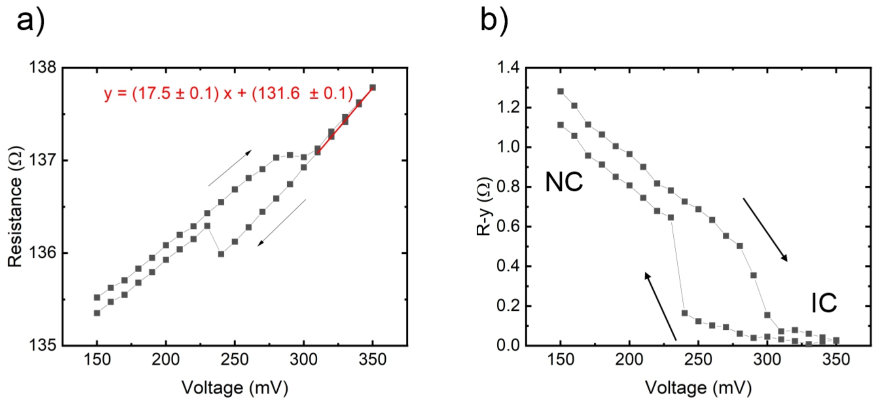

Figure 6.5: Shorted device resistance as a function of the DC voltage applied. a) Linear fit (red, solid line) of the "metallic-like" part of the device: wire plus IC-CDW portion of the flake. b) Result after subtracting the metallic contribution (y) to the overall measured resistance (R) shows a typical NC-/IC-CDW phase transition curve profile.

within the time intervals indicated in the lower axis of the plot, a DF TEM image is taken. Results of this measurement are shown in Figure 6.4 c), where it can be seen that increasing the voltage difference on the device is accompanied by the propagation of an IC-CDW front, which begins on the area of the flake in contact with the thin metal wire and extends over the entire flake. The phase-switching on this device is controllable, reversible and reproducible. Additionally, it presents an associated hysteretic behaviour, which is pointed out in the inset of Figure 6.4 b).

Given the sample configuration, this experiment suggests that the Joule heating on the thin metallic wire plays an important role as a seed for triggering the NC-CDW to IC-CDW phase transition in the 1T-TaS$_2$ flake. More interestingly, the findings presented here indicate that spatial localization of the structural phase change associated to the NC-CDW to IC-CDW transition can be controlled over the sample dimensions on a specific device design. The non-linear character of the 1T-TaS$_2$ resistance change, specially towards the NC-CDW phase, has been reported in previous electronic measurement works (see for instance Ref. [53]). Here, the simultaneous DF imaging gives additional information on what areas of the flake have one or the other CDW phase and make possible to assign which region should have which resistance value. Unfortunately, for the experiment presented here, the DF imaging is constrained to a corner of the sample. DF-TEM imagining of bigger areas could be of interest for an accurate modelling of the electrical parameters for shorted devices with dimensions as given here. With the results presented, a further step can be given in order to identify with precision the triggering of the CDW phase transition in the shorted devices. Assuming that the IC-CDW phase has a metallic character and therefore the current in the device should also flow preferably in the portion of the flake at the IC-CDW phase, the "metallic background" of the device can be subtracted from a measurement of resistance as a function of DC bias, to leave as a result the contribution only of the NC-CDW parts of the flake on the resistance change. The result of this reasoning is shown in Figure 6.5. Notably, the curve in Figure 6.5

b) resembles those of an NC- to IC-CDW phase switch measured by other groups (see Ref. [53]). Importantly, the assignment of CDW phases in Figure 6.5 b) is corroborated by the corresponding DF-TEM image at each data point (refer to Figure 6.4 c)). This way, with proper optimization of the DF mask alignment and TEM integration times, a hysteretic behaviour of the phase switch could also be traced structurally on a DF image, by following the propagation of the IC-CDW front while the two phases coexist spatially in a 1T-TaS$_2$ flake. This way, a complete picture of the electrical and structural components of the phase switching can be provided. Additional data that supports this statement is given in section 6.5 (Figure 6.9).

6.4 Conclusions

The experiments shown in this chapter investigate CDW phase transitions in 1T-TaS$_2$ nano-thick flakes, fabricated on a two-terminal device configuration on top of a TEM membrane as a substrate. A preliminary electron transport characterization shows the presence of CDW-phases in the material. In particular, the NC- to C-CDW phase transition is revealed on a measurement of the device resistance as a function of the temperature upon cooling, while the C- to NC-CDW phase transition is observed upon heating. The phase switch is accompanied by an abrupt change in the resistance between lower resistance at the NC-CDW to higher resistance values at the C-CDW phase. The resistance difference between the phases is of one order of magnitude and the switch presents a hysteretic behaviour as a function of the temperature, which evidences the first order phase transition character of the switch. An interesting behaviour of the I-V characteristics of the system at the transition temperature is discovered in the same experiment, which reveals a stabilization of the system towards the C-CDW phase upon application of a DC bias. Further investigation on the effect of applying DC biases to the system at the transition points of the C-/NC-CDW phase switch could contribute new insights relevant for understanding the 1T-TaS$_2$ first order phase transition mechanisms. A measurement of the diffraction pattern at room temperature on the same flake shows the presence of satellite points around the main Bragg points of the 1T-TaS$_2$ lattice, indicating that the flake is at the NC-CDW phase when no external stimulus is applied. A novel experimental approach is presented within this chapter for the simultaneous structural and electrical characterization of the flakes, being this a main motivation for fabricating devices on a TEM substrate. A study of the samples inside a TEM setup while externally applying DC voltages to the terminals of the sample reveals a controllable NC-/IC-CDW phase transition. The phase switch is reversible and reproducible for two-terminal devices with a 1T-TaS$_2$ bulk flake in the channel, as well as for a sample configuration with a metallic wire along the channel. The latest configuration has been investigated under DF TEM imaging. Such measurements reveal the propagation of an IC-CDW front on the flake surface, which originates on the metallic wire and grows over the flake as long as the voltage difference between the terminals of the device increases. This scenario is reverted to the original state of the entire flake on the NC-CDW phase when decreasing the voltage difference. The findings presented here shed light on the structural nature of a NC-/IC-CDW phase transition, when triggering it via externally applied electrical signals. An interesting follow up of the experiments presented here would be to study the system in a device configuration with a metallic wire next but not in touch to the flake, to decouple the influence of the Joule heating from the wire and electrical current flow in the flake on the nucleation and propagation of the IC-CDW phase front. Last, having control over the structural character of the phase transition could be of interest for three-dimensional integration as well as for usage of the material features in device applications. The results achieved with the samples presented and discussed here demonstrate a controllable and reversible switching between CDW phases which have distinct resistance values and present a hysteretic behaviour, making 1T-TaS$_2$ promising, for instance, in quantum information technologies and memristive switching device applications.

6.5 Supplementary material

This section presents further measurement and calibration data not shown within Sections 6.2 and 6.3. This data shown as supplementary material supports and extends the results presented within this chapter and is shown for completeness and reference.

C-CDW to NC-CDW transition point

To study the temperature dependence of the resistance of 1T-TaS$_2$ flakes, the sample in a two-terminal device configuration is brought to a fixed temperature and the I-V curve of the device is measured. The resistance of the 1T-TaS$_2$ flake at each temperature is extracted from the slope of the I-V measurements. Figure 6.6 a) shows the result of upon cooling for the sample discussed in section 6.3 (see Figure 6.1 e)). When the system is at a well-defined CDW phase at a fixed temperature, for example, starting at the NC-CDW phase at 300 K, the trace and retrace of the I-V curve perfectly overlap (see 6.6 b)), having a slope of around 300 Ω. When the sample is at a stable CDW phase, the results of the I-V curve is reproducible in several consecutive measurements at a same temperature and voltage range, as seen in Figures 6.6 d), e), h) and l). At a temperature of 240 K, where the system is stable at the NC-CDW phase and the slope of the I-V curve is sitll well-defined with resistance values around 300 Ω. When the system is at a transition point between NC-CDW and C-CDW (see dashed circled datapoint in Figure 6.6 a)), the trace and retrace of the I-V curve are mismatched on a first (1) measurement, until the trace and retrace match on a second (2) and third (3) one (Figure 6.6 g)). Interestingly, the I-V curve has initially a lower resistance (see value for black datapoints, trace, on measurement (1)), then it is undefined between lower and higher resistance values (see red datapoints, retrace, on measurement (1)), lastly, it stabilizes towards a higher resistance (see measurements (2) and (3) on the same plot). Afterwards, at 230 K, the system is found at the C-CDW phase with resistance values of around 3 kΩ. It is worth mentioning that this result found at the transition points is counterintuitive, if one considers that the higher resistance state associated to a C-CDW is a phase stable at lower temperatures and applying a DC bias to the flake might introduce Joule heating. These findings suggest that the application of external electrical signals (in particualr a DC bias) when the system is about to overcome a NC-/C-CDW phase transition, stabilizes the system towards the C-CDW phase.

Fabrication of shorted devices

Figure 6.7 a) shows the result of overexposed EBL structures. This is achieved by from having an inhomogeneous PMMA spin coating on the TEM substrate, resulting an improper adjustment of the EBL writing parameters and/or developing times, when following the recipe given in chapter 3, section 3.2.3. After development, cracks on the PMMA surface appear which get filled with material during PVD. For the sample presented within this chapter, an inhomogeneous PMMA layer was obtained by spin-coating the TEM substrates for 30 s at 4000 rpm, which was cleaned only with acetone and isopropanol before exfoliation and transfer of 1T-TaS$_2$ flakes. Figure 6.7 b) shows an AFM image of the result after PVD and lift-off.

Dark field mask design and alignment

Order parameter sensitivity is obtained by means of a DF aperture array, tailored to filter the periodicities of the CDW at the diffraction plane of the microscope of the UTEM setup. TEM images taken with the DF mask result brighter if NC-CDW satellite diffraction points are present and darker when they are not. The latter occurs, for instance, when the 1T-TaS$_2$ flake is at the IC-CDW phase. Details about the setup for performing DF TEM imaging are given in chapter 3 (section 3.2.4).

Additional electron transport and DF imaging data

Figure 6.9 a) shows additional measurements of the resistance as a function of the externally applied voltage to the shortcut device. The width of the hysteresis loop associated to the NC-/IC-CDW phase transition remains similar for different scanning rates and waiting times between datapoints. Surprisingly, for a slower scanning rate (step size 5 mV and waiting time between datapoints 0.1 s), the hysteresis loop is not measured, although there is a signature of the phase switch at the positions of the measurement shown in Figure 6.9 a) (see resistance jumps in Figure 6.9 b)). Figure 6.9 c) shows the DF-TEM measurement of the sample with scanning rate given by a 10 mV step size and waiting time between voltage points 20 s, selected for usign an integration time of the TEM imaging of 10 s. The blue arrow signalizes the expansion direction of the IC-CDW phase front from lower to higher voltage applied.

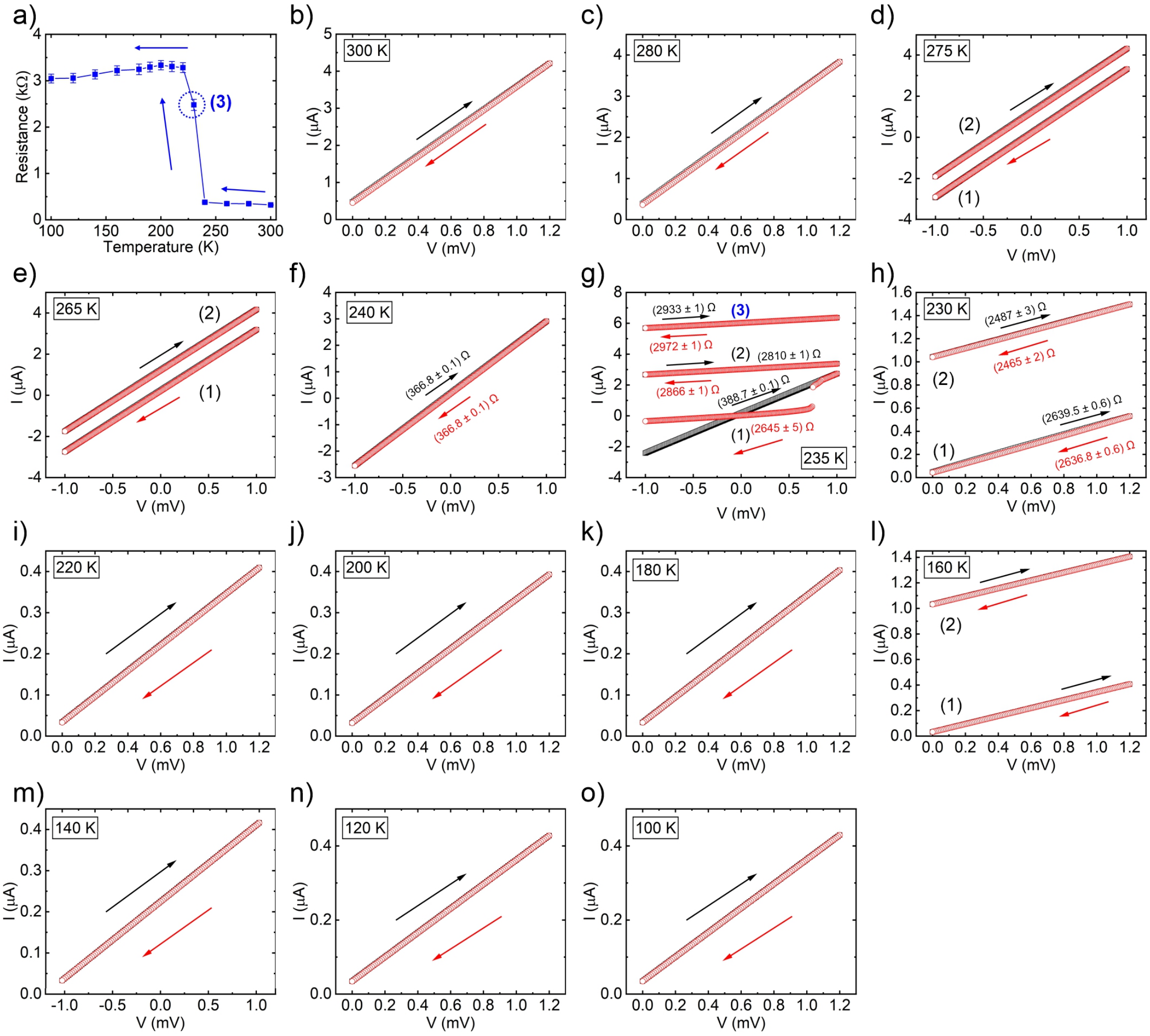

Figure 6.6: I-V characteristics of a two-terminal 1T-TaS$_2$ device at different temperature values. In all cases, the arrows indicate the direction of the scans (black for trace and red for retrace data points). a) Resistance as a function of the temperature for the C-CDW to NC-CDW phase transition upon cooling. b)-o) I-V curves of the data points shown in a). In all plots, the open black squares (open red circles) are datapoints of the trace (retrace) scans. The numbering (1), (2) and (3) indicates first, second and third consecutive measurements on the same voltage range. The measurements are shifted with an offset of I = 2 μA for visualization, when more than one measurement is shown. The resistance values extracted from the slopes of the I-V curves is indicated with black (red) numbers for the trace (retrace) scan in some of the plots.

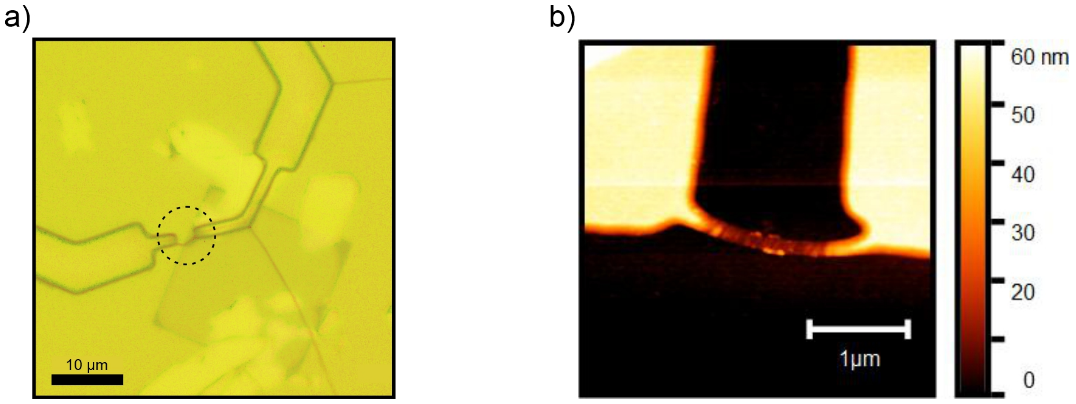

Figure 6.7: Fabrication of shorted devices. a) Optical microscope image of a test two-terminal device after developing the e-beam exposed PMMA. The dotted circled area encloses the region where the image in b) belongs. The cracks on the PMMA get filled during metal evaporation and produce a shortcut between terminal contacts. b) AFM measurement of the test device after evaporation of 2 nm Ti / 60 nm Au, showing the fabricated shortcut (∼ 200 nm width wire).

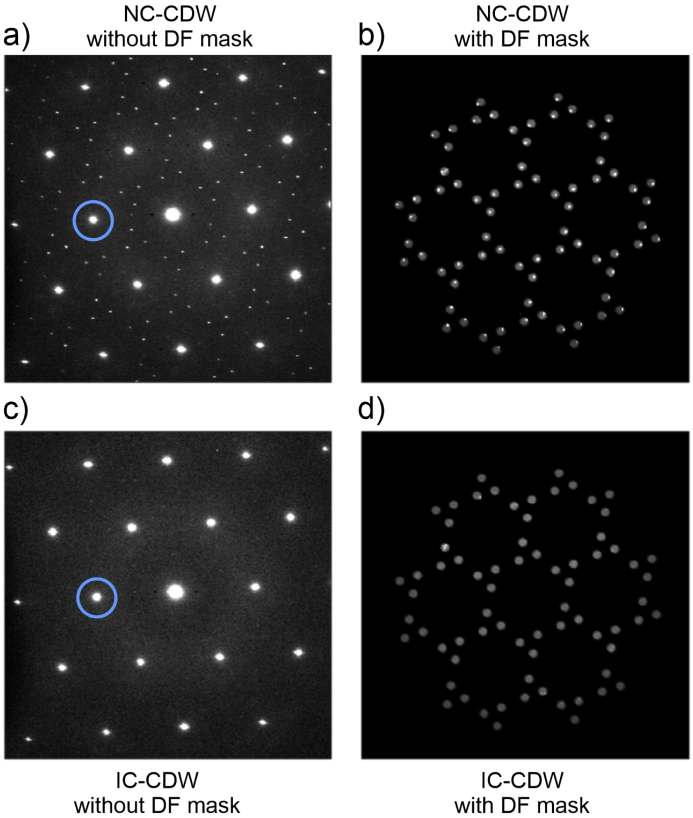

Figure 6.8: DF mask alignment. a) Diffraction pattern of a 1T-TaS$_2$ flake in the NC-CDW phase without and b) with the DF mask. The signal from the NC-CDW satellite diffraction points goes through the DF mask while the main Bragg lattice diffraction points (encircled in blue) are blocked. c) Diffraction pattern of a 1T-TaS$_2$ flake in the IC-CDW phase without and d) with the DF mask. No signal from the diffraction points goes through the DF mask.

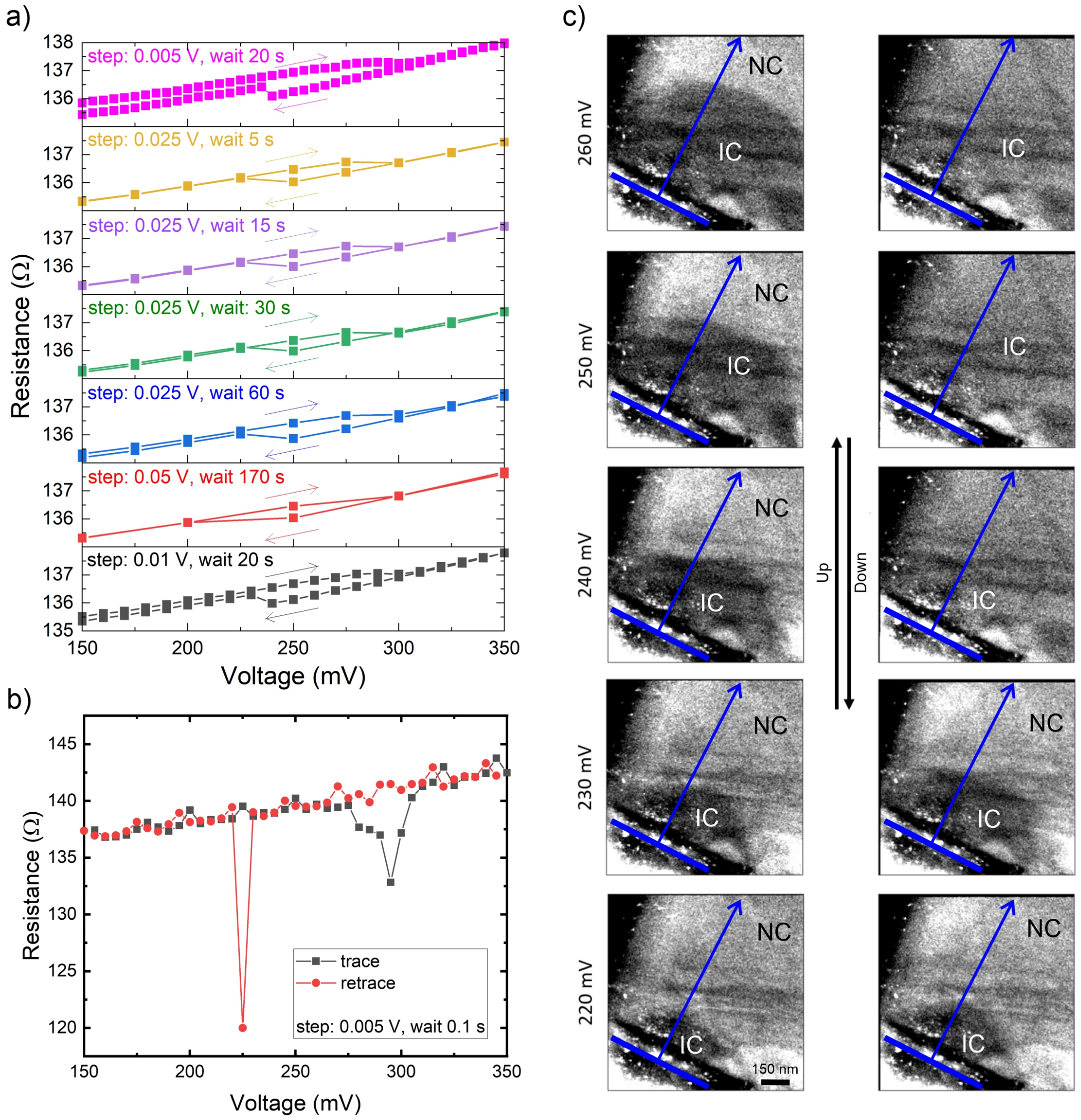

Figure 6.9: Further measurements on the shorted device. a) Resistance as a function of the DC voltage difference applied between the two terminals of the device for different scanning rates and waiting times between data points. No substantial difference is observed in the position and width of the resistance jump for trace and retrace (indicated with arrows). b) Resistance as a function of the DC voltage for a fast scan (waiting time 0.1 s). c) Observation of the IC-CDW phase front originated on the shortcut side of the flake for an up and down voltage sweep, showing the reversibility of the process in a real space image. TEM measurement taken with DF mask and 15 seconds integration time. The blue arrow is added as a reference with origin on the metallic wire and pointing towards the growing direction of the IC-CDW phase front (darker).

Chapter 7

Conclusions

During this thesis, high-quality suspended rhombohedral few-layer graphene and nano-thick 1T-TaS$_2$ samples were investigated. On a first part, by overcoming the challenges in the fabrication and investigation of naturally occurring rhombohedral trilayer and tetralayer graphene, the experiments within this thesis reveal the presence of interaction physics in the few-layer graphene systems. The stacking order is brought to light by a combination of Raman spectroscopy and s-SNOM, and confirmed by electron and magneto transport measurements. The samples are fabricated in a dual-gated free-standing device configuration, which shows that few-layer graphene can be cleaned in-situ to the highest quality. In addition, this allows to independently tune charge carrier density and displacement field in the few-layer graphene samples for the magneto transport measurements at mK-temperatures. Moreover, the sample environment has reduced screening of Coulomb interactions, which facilitates the observation of many-body interaction effects at the low energy band scale. On a second part of the thesis, the fabrication of 1T-TaS$_2$ samples on TEM substrates allows investigating this CDW material using a novel experimental approach. The transitions between C-, NC- and IC-CDW phases are explored by means of temperature dependant as well as DC bias-controlled measurements. Simultaneously, diffraction measurements as well as bright- and DF-TEM imaging, e.g. while applying a DC bias to the sample, are possible with the presented sample design. In the next paragraphs, the main experimental results of this thesis are summarized.

First, by means of electron and magneto transport measurements at mK-temperatures, the presence of magnetic states at low n in suspended rhombohedral trilayer graphene is revealed. Transport measurements at $B = 0$ show the insulating LAF/CAF phase at charge neutrality and vanishing D, as well as a layer polarized phase at higher D fields. Furthermore, the observation of QHE conductance plateaus at low $B_\perp$ shows the presence of spontaneous quantum Hall states with non-zero charge Hall conductivity. In particular, conductance plateaus at $\nu = 3$ and $\nu = 6$ are followed with their slopes down to $B = 0$, being clearly distinguished at 100 mT. Notably, $\nu = 3$ has conductivity $3e^2/h$, it becomes stable upon application of D at very low B and it emerges upon application of $B_\perp$ at $D = 0$. The measured Hall conductivity for $\nu = 3$ as well as its layer-polarization character suggests evidence of the "ALL" broken chiral symmetry state in rhombohedral trilayer graphene. The clear observation of $\nu = 18$ at very low B in the cleanest sample requires a more in-depth theory analysis in order to explain its appearance. Besides, fluctuations in the conductance have been noticed at $B_\perp = 0$, which depend on an externally applied DC current bias and $B_\parallel$, as well as on the temperature. Despite these fluctuations are more pronounced in the cleanest samples, no clear signatures of correlated phases in relation to them could be determined. Last, a hysteretic behaviour as a function of $B_\parallel$ and also as a function of n when turning on a $B_\parallel$ field is discovered around charge neutrality at $B_\perp = 0$. The hysteresis in n becomes more prominent for a higher $B_\parallel$. Moreover, it is present at both finite and zero D fields and it becomes less prominent (until disappearing) when increasing the temperature from 10 mK to 500 mK. These results suggest evidence of a spin-ordered phase at charge neutrality in rhombohedral trilayer graphene. Surprisingly, the discovered magnetic states at low n are tuneable with the charge carrier type. An in-depth theory analysis could be of great relevance to elucidate the role of the n doping at the low energy band scale of trilayer rhombohedral graphene, as well as a to confirm a possible spin-ordered nature of its ground state.

Next, a detailed electron transport study of suspended tetralayer ABCA graphene is provided. To begin, the interaction induced spontaneous gapped phase in the sample is shown to match the theoretical prediction of a larger gap in D as its counterparts with two and three layers. This is a sign of stronger interaction effects in tetralayers. Following, a fan diagram of the sample at $D = 0$ and from 0 to 14 T provides experimental evidence of LL crossings in tetralayer ABCA graphene. Using this data to fit a model of the LL spectrum could be a way to identify the stacking order of tetralayer graphene from a quantum transport standpoint. The conductance maps at different B and D indicate the presence of layer coherent and layer polarized states in the system, which are tuned by a B field. For instance, $\nu = 3$ is found layer polarized at $B = 8$ T and unpolarized at 4 T in a reproducible manner. A change in layer polarization is identified by the observation of a hysteresis in D, as well as jumps in the conductance at a fixed D within a QHE plateau. Strikingly, a hysteresis is also observed when crossing LLs at a fixed D, scanning n, both in tri- and tetralayer rhombohedral graphene samples. This constitutes evidence of a first-order phase transition character associated to a change between QHE conductance plateaus. The novelty of the results here is to find the phenomena scanning n instead of B. These findings bring new insights to elucidate the nature of correlation effects within the QHE regime in rhombohedral graphene systems. Theory contributions might help to understand the competition between different order parameters within the graphene systems, before transitioning from one QHE conductance plateau to another. Last, the observation conductance plateaus at $\nu = 8$ and 16 are tracked down to $B = 0$, with $\nu = 16$ being suppressed by a finite D field, opposite to the phenomena observed in trilayers, where D activates a lower ν state at low B. Further investigation and theory interpretation of the ν values observed are necessary to determine the origin of this result. In addition, a DC spectroscopy measurement at $B = 0$ reveals features in the conductance map which are present at $D = 0$ but not at a finite D. These studies could help to determine the nature of the ground state of rhombohedral tetralayer graphene.

Finally, different CDW phases within 1T-TaS$_2$ were investigated using temperature dependant electron transport as well as TEM measurements. First, the NC- to C-CDW phase switch is observed by measuring the sample resistance as a function of the temperature upon cooling and the C- to NC-CDW transition, upon heating. The phase switch shows an abrupt change in the resistance, showing lower (higher) values for the NC-CDW (C-CDW) phase. The associated hysteresis as a function of the temperature evidences the first order phase transition character of the switch. A measurement of the diffraction pattern at room temperature on the same flake shows satellite points around the main Bragg points of the 1T-TaS$_2$ lattice, indicative of the NC-CDW phase when no external stimulus are present. Surprisingly, a stabilization towards the C-CDW phase upon application of a DC bias is discovered, when the system is at the limit of a temperature-driven C-/NC-CDW phase switch. This brings new insights relevant for understanding the 1T-TaS$_2$ first order phase transition mechanisms. A study of the samples inside a TEM setup while externally applying DC voltages to the terminals of the sample reveals a controllable NC-/IC-CDW phase transition. The phase switch is reversible and reproducible for two-terminal devices with a 1T-TaS$_2$ in the channel, as well as for samples with a metallic wire along the channel. The latest type of device has been investigated using DF TEM imaging, to reveal the propagation of an IC-CDW front on the flake surface originated at the metallic wire. The IC front grows over the flake as long as a voltage difference on the sample increases, coming back to the original state (NC-CDW) when decreasing the voltage difference. These findings bring new insights on the structural nature of a NC-/IC-CDW phase transition, when triggering it via externally applied electrical signals. These results demonstrate a controllable and reversible switching between CDW phases which have distinct resistance values and present a hysteretic behaviour, making 1T-TaS$_2$ promising, for instance, in memristive switching device applications.

To conclude, this thesis demonstrates few-layer rhombohedral graphene as an outstanding tuneable platform to investigate many-body interaction physics and correlated phenomena. The presented results contribute to pave the way for using the potential of rhombohedral graphene systems in applications such as low dissipation electronics and quantum information technologies. Future research directions might include repeating the experiments on Bernal graphene as well as ABCB tetralayers. This will define with experimental evidence if the phenomena discussed belongs to the realm rhombohedral stacked graphene. Looking for the hysteresis in n when crossing conductance plateaus on mono- and bilayers could be of interest too, e.g. to see if the chirality number influences the phenomena observed. The fabrication of four-terminal devices is necessary to extend the studies with disentangle of the longitudinal and Hall conductance. Last, an interesting follow up of the experiments with 1T-TaS$_2$ could be to fabricate the samples with a metallic wire next but not in touch to the flake, to decouple the influence of the Joule heating from the wire and electrical current flow on the CDW phenomena discussed. Time resolved measurements could provide unique complementary insights, e.g. from monitoring the out-of-equilibrium dynamics of the CDW phase switch.

Appendix A

Additional samples

In addition to the samples presented in chapters 4, 5 and 6, free-standing graphene devices with superconducting contacts and a 1T-TaS$_2$ sample in a coplanar stripline circuit with a photoconductive switch have been fabricated during this thesis. The results shown here are not discussed with bigger detail, because they are beyond the scope of the thesis. However, the motivation for their fabrication as well as the results achieved with each type of sample are given, as they could be useful as a possible starting point for future research in the topics.

A.1 Free standing graphene Josephson junctions

The Josephson effect, originally a discovery in a tunnel junction [203], occurs when two superconductors are placed in proximity while coupled by a weak link. Within this frame, a supercurrent flows dissipationless across a device known as a Josephson junction (JJ). Any weak link between two superconductors can support a dissipationless current in equilibrium, as long as the dimensions of the weak link are sufficiently small [204]. Since graphene became available, its implementation as a weak link on a JJ has opened the doors to explore the interplay between superconductivity and relativistic quantum dynamics [205, 206]. Moreover, using graphene or other 2D materials as the weak link between two superconducting electrodes presents the advantage of having the I-V characteristics of the JJ devices easily tuned by the gate voltage [207]. Different sample fabrication approaches to investigate graphene JJs are found in the literature. One example consists in having single layer graphene on a SiO$_2$ substrate connected with superconducting contacts [208, 209]. Others use the graphene encapsulated [210–212], while a few place the graphene in a free-standing device configuration [213–215]. The latest type of device assumes several challenges for fabrication, but also has advantages, as it has been discussed on previous chapters of the present thesis. Among the challenges, one of the biggest is that the most usual recipes for making the graphene free-standing involve the use HF-based wet etching (see Chapter 3), a process which is not compatible with most of the superconducting materials, as they are attacked by HF [164]. To overcome this problem, two different fabrication designs of suspended graphene JJs were proposed and

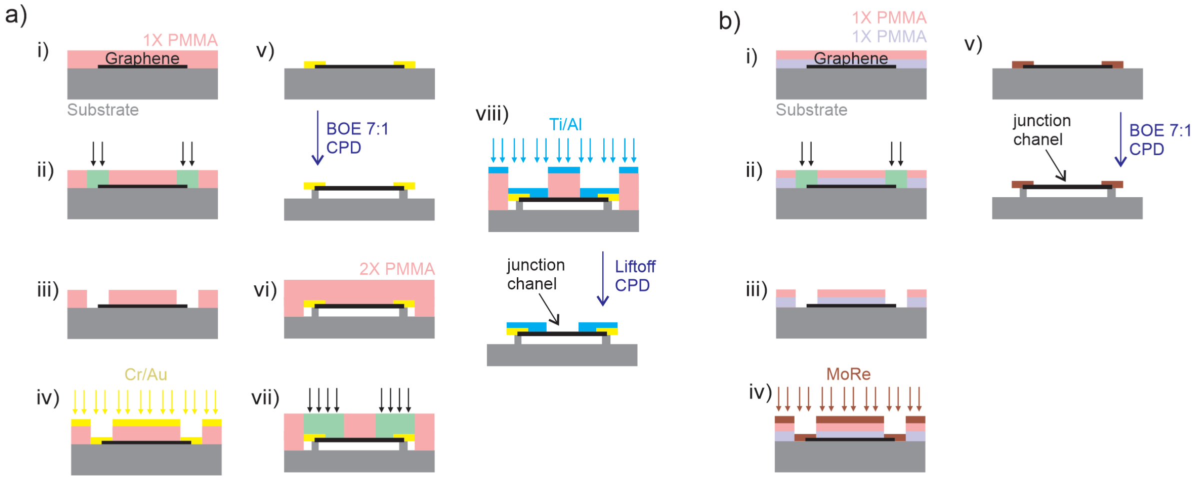

Figure A.1: Sketch of the fabrication steps for free-standing graphene JJs. a) JJ constituted by a 500 nm longitudinal channel between Al contacts in touch with free-standing graphene flake after making it suspended with Cr/Au contacts. b) JJ constituted by a 500 nm to 1 µm longitudinal channel between MoRe contacts in touch with a free-standing graphene flake. Here, the suspension is done only using MoRe contacts as structural support. The individual steps enumerated with roman numbers are discussed in the main text.

fabricated within this thesis. One uses Aluminium (Al) as a superconductor supported by a Cr/Au structure and the other uses Molybdenum Rhenium (MoRe) as both superconducting contact and structural support of the free-standing graphene bridge. Although the resulting JJ samples did not succeed in showing superconducting characteristics, the insights gained from this work are relevant for future research in this direction, therefore are presented here.

Figures A.1 a) and b) show a sketch with a general overview of the fabrication steps for the two different samples. To fabricate free-standing graphene JJs with Al contacts, an approach inspired by the description of the sample discussed in Ref. [213] is taken, where a structure of Cr/Au contacts is used as structural support for the superconducting Al contacts. In the procedure used in this thesis, the first step consists in making a conventional free-standing graphene sample with Cr/Au contacts, as described in chapter 3. Therefore, the steps i) to v) in Figure A.1 a) follow the same recipe given in section 3.1.2. As usual, after etching the sample with BOE 7:1 to make the graphene free-standing, the sample is dried inside a CPD. Once a free-standing graphene sample with Cr/Au contacts is fabricated, a next step consists in adding superconducting contacts to the graphene flake. Same as before, this is done by using conventional EBL (Figure A.1 a) vi)-viii)) to pattern the contacts directly on top of the suspended sample. To do this, vi) two layers of PMMA are used as described in section 3.1.2, to make sure that the substrate is completely covered and no opening areas towards the substrate are present, in particular next to the flake. vii) The structures are exposed by an e-beam and, after developing the EBL structures, viii) 10 nm Ti/70 nm Al contacts are deposited by PVD. Importantly, after lift-off the samples should only be dried using a CPD to avoid collapse of the suspended structures by capillary forces [48]. The graphene JJ is constituted by the two Ti/Al contacts with a separation of 500 nm in touch with the suspended graphene flake (see Figure A.1 a) viii), bottom). Here it is important to note that the width of the JJ channel is adequate for JJs with 2D materials as a weak link [207]. A simpler fabrication and sample design is proposed using MoRe contacts as illustrated in Figure A.1 b). Again, conventional EBL is used to pattern the contacts. The only difference is that two layers of different PMMA are used to facilitate lift-off and minimize the accumulation of material in the contact edges, since the MoRe is deposited on the samples via DC sputtering (Ar atmosphere, pressure of 2×10^{-2} mbar). So, for the fabrication step in Figure A.1 b) i), first, one layer of PMMA (200 k) is spin coated with a ramp of 15 seconds at 1000 rmp during 60 seconds at 4000 rpm. After soft baking for 1 minute at 150 °C, a second layer of PMMA (950 k) is spin coated with a ramp of 1 second at 800 rpm during 40 seconds at 4000 rpm. As illustrated in Figure A.1 b) ii), conventional EBL is used to pattern contacts to the graphene. This is done using ETH 10 kV, aperture 20 µm, dose 120 µC and step size 5 nm. iii) The development is done in IPA:MIBK (3:1) for 3:30 minutes, followed by rinsing the substrates with IPA and blow dry them with a N_2 gun. Before sputtering MoRe, the samples are exposed for 1 minute to an UV O3 atmosphere. iv) The sputtering is performed during 3 minutes at 40 W DC power to achieve a 100 nm thick MoRe layer. v) Since MoRe is stable in HF [164,216], it can be directly etched using BOE 7:1 to make a free-standing graphene sample as described in chapter 3. Notably, using MoRe as superconducting contact to the graphene flakes has the fabrication advantage of sparing one use of the CPD and several EBL lithography steps.

Figure A.2 shows SEM and AFM images of the free-standing graphene JJs fabricated during this thesis. Although mechanically stable suspended samples were successfully fabricated with both Al and MoRe as superconducting contacts, a higher risk of collapse of the delicate graphene bridges has been found for those fabricated with Al contacts, in comparison with the simpler suspended graphene structures contacted and structurally supported with only Au or MoRe. Figure A.2 a) shows images of free-standing graphene JJs with Al contacts for a collapsed structure, where it can be seen that the graphene channel is broken. Figure A.2 b) shows a free-standing sample. As it can be seen from the AFM profile measurement, the suspended graphene devices with Al contacts present a small bend towards the SiO_2 substrate. Despite that, the graphene-Al structure is free-standing and electrical contact between the metals and the graphene is provided, as discussed in the next paragraph. Figure A.2 c) shows AFM images of different attempts of fabricating free-standing graphene JJs with MoRe contacts. The successful fabrication of a suspended sample shows that using only this material without any extra adhesion layer is sufficient to keep the graphene in a free-standing structure and also electrically connected, as discussed in the following paragraphs. While working with this material aiming at a graphene JJ channel of 500 nm width, it has been noted that its deposition via sputtering generates a broadening of the EBL written structures, therefore the fabricated channel results filled with material (see Figure A.2 a), left). To solve this issue, the obtained broadening is compensated in the EBL mask design. With the fabrication recipe outlined in the previous paragraph, designing an EBL mask with a graphene channel of

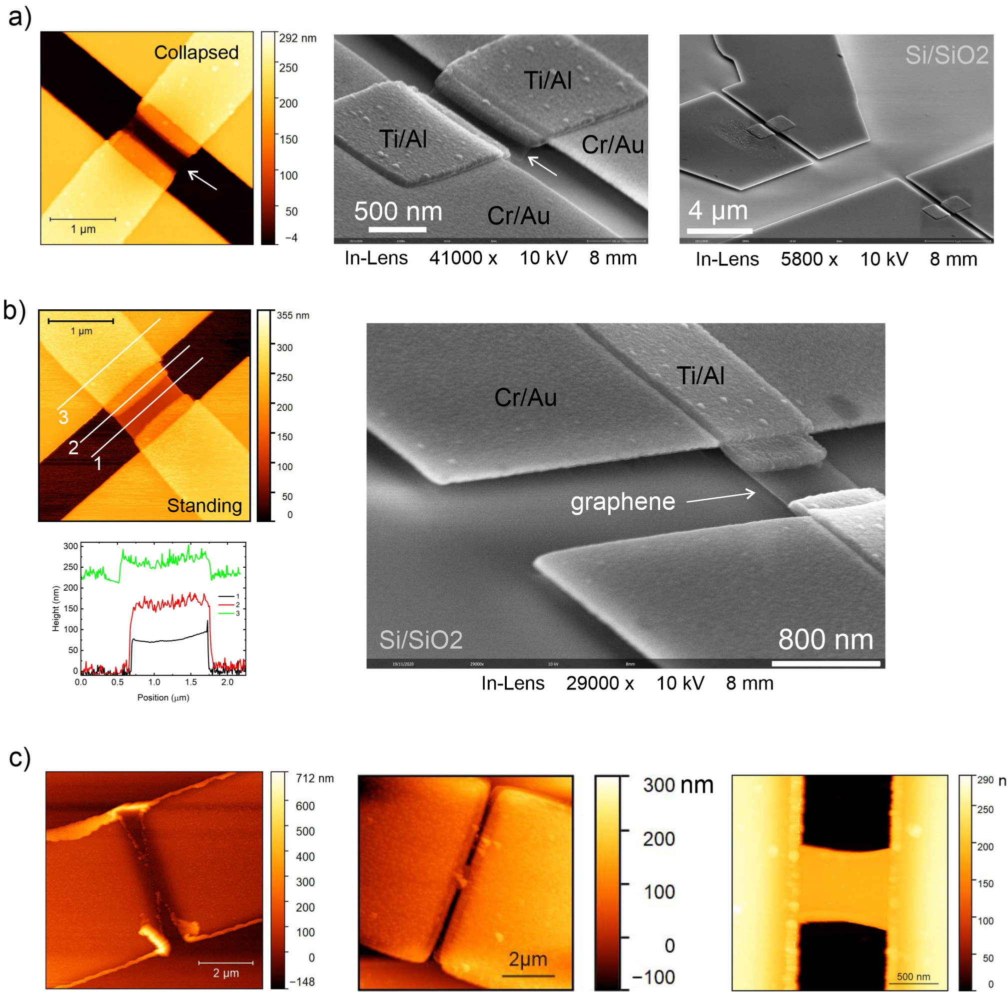

Figure A.2: AFM and side-view SEM images of several free-standing graphene JJs. a) Images of a collapsed structure. The broken free-standing graphene bridge is pointed by a white arrow in an AFM (left) and SEM images of a single junction (middle). Additionally, two other collapsed graphene junctions are shown in an SEM image (right). b) AFM (left) and SEM (right) images of a successful free-standing graphene sample with superconducting Al contacts. The AFM profile lines (1, 2, 3 in left image) show that the graphene is suspended (see line profile 1). This can be seen from the side view SEM image (left) as well. c) AFM images of free standing graphene devices with MoRe contacts. Result after sputtering MoRe. EBL mask design of the junction channel with a width of 500 nm (left), 1 µm (middle) and 1.5 µm (right).

1.5 µm width results in a 500 nm width channel after sputtering. Figure A.2 c) shows the resulting structures from a design with (right) and without (left) compensation of the channel broadening after sputtering MoRe, together with an intermediate design (middle). Respectively, they correspond to an EBL mask design with a graphene channel of 500 nm, 1 µm and 1.5 µm. An additional AFM image of a MoRe JJ including a profile measurement is shown in chapter 3, Figure 3.5 c).

To understand the behaviour of the superconductors used for the graphene JJs, the superconducting properties of the materials were tested on their own. A first measurement consists in verifying that the material used on the graphene devices is superconduct-

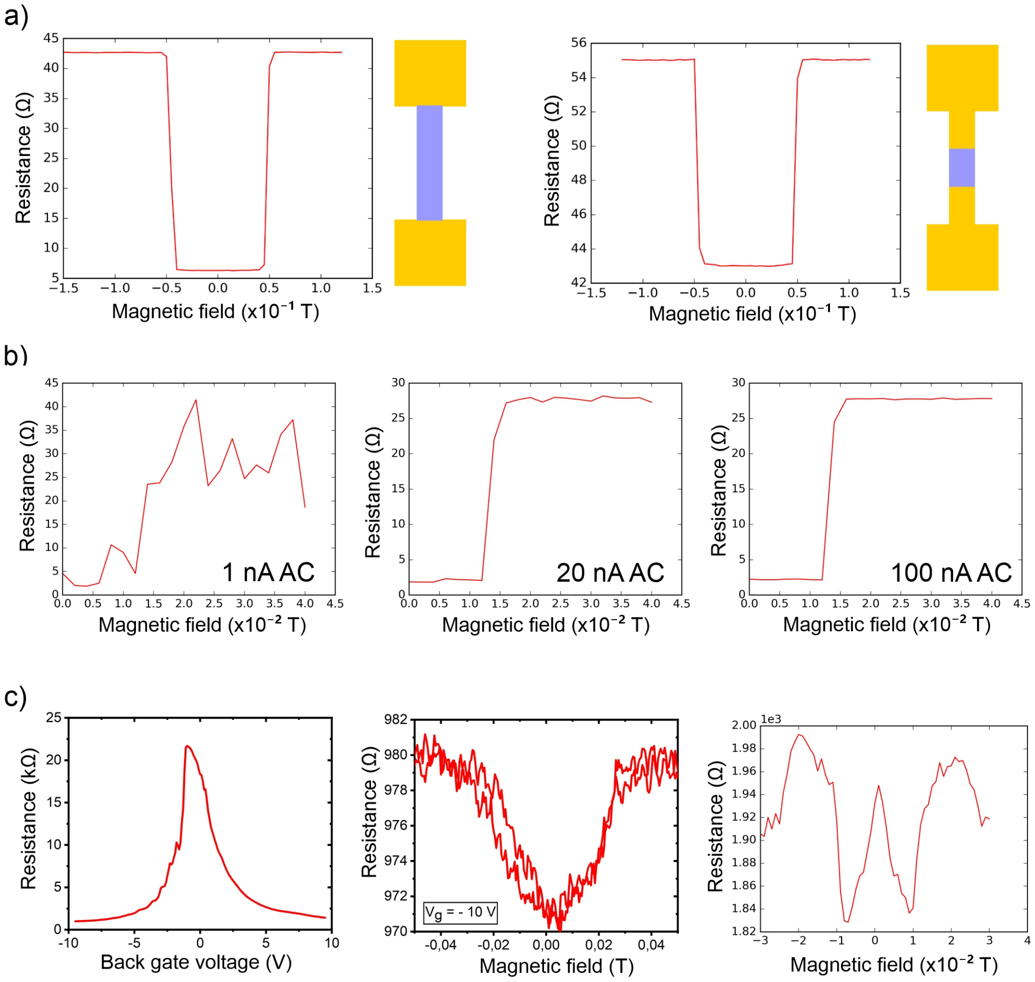

Figure A.3: Superconductivity test of Al leads and graphene JJ. a) B_C for a longer Al lead (length of few hundreds of µm, width 7 µm, thickness 70 nm) and for a shorter Al lead (length $\leq$ 10 µm, width 7 µm, 70 nm thick). In yellow is illustrated the Au used for the leads and the bond pads, while in violet the Al. b) B_C measured with different reference signals of the lock-in amplifier. c) Electron transport for a suspended graphene JJ with Al contacts. Left, CNP after current annealing. Middle, resistance as a function of the magnetic field for a finite gate voltage shows a drop in the resistance of about 10 Ω between ±0.02 T. Right, resistance as a function of the magnetic field for zero gate voltage shows fluctuations in the resistance between ±0.02.

ing. This is done by measuring the resistance between two terminals of the material (see sketches in Figure A.3 a)) at temperatures below its critical temperature T_C (temperature under which a material acts as a superconductor). When the material is in a superconducting state, its resistance between two terminals drops to zero. For Al, $T_C \sim 1$ K, therefore all measurements are performed in the dilution refrigerator system operating at 10 mK. For MoRe, $T_C \sim 6.5$ K and can become higher upon annealing of the material [216], therefore this material has been studied both in the dilution refrigerator and the 4K station setup (see chapter 3 for a description of the setups). If the material is superconducting, a second measurement consists in characterizing it critical magnetic field B_C, i.e., the maximum magnetic field strength below which a material remains superconducting. Additionally, a measure of the critical current I_C, this is, the maximum current that a wire can carry with zero resistance, can also be done. Figure A.3 a) shows a measurement of B_C for two different Al leads, a longer (left) and a shorter (right). Here, longer means an Al lead that covers several hundreds of µm length, measured from the graphene sample to the bond pads on the SiO_2 wafer. Shorter means an Al piece only in the vicinity of the graphene, with total length not bigger than 10 µm (see Figure A.2 a) as a reference). The result shown in Figure A.3 a) shows that the amount of Al in the circuit has an influence on the final result for measuring superconductivity. It has been found that for Al leads of same thickness (70 nm) and width (7 µm) but different length (longer or shorter), the longer leads show a resistance drop down to zero while the shorter, not completely, although the values of B_C are consistent in both cases (see plots in Figure A.3 a)). The measurement of same B_C values suggests that the drop in the resistance, although not completely down to zero, is related to the transition between normal conductor and superconductor states of the material. Additionally, as shown in Figure A.3 b), it has been noted that the reference signal used for the lock-in measurements is also important in order to measure superconductivity in the devices. From this result is concluded that a reference signal bigger than 20 nA should be used in order to resolve well the resistance jump at B_C. Last, Figure A.3 c) shows the results of the electrical transport characterization for the sample shown in Figure A.2 b). Worth mentioning, the current annealing process on free-standing samples with Al contacts resulted a lot more delicate and prone to the risk of collapse of the structure, than for suspended graphene samples with only Au contacts, such as those discussed in chapters 4 and 5. In the measurements discussed here, the observation of the saturation point of the resistance was usually immediately followed by breaking the device, seen as a sudden drop to zero of the current flow through the channel while measuring the I-V curve. For the devices that successfully overcame several cycles of current annealing without breaking them, the CNP is observed on a resistance as a function of the back gate voltage measurement, as shown in Figure A.3 c), left. This result indicates that the free-standing graphene flake is electrically connected and relatively clean. Taking this as a starting point to follow the type of measurements in Ref. [213] for characterizing the graphene JJ, a measurement of the resistance as a function of the magnetic field is performed. The result, shown in Figure A.3 c) (middle and right plots), shows a drop (or a fluctuation) in the resistance for magnetic fields lower than a critical value of 20 mT. In spite that only a resistance drop to zero is indicative of a superconducting junction, having in mind the result discussed earlier for shorter Al leads (Figure A.3 a)), the resistance fluctuations to lower values in Figure A.3 c) (middle and right plots) might suggest that too little Al was implemented in the fabrication of this particular sample. Therefore, only a small drop in the resistance was measured instead of its vanishing below B_C. Besides, considering that the current annealing did not deliver the best possible cleaning of the graphene flake, the failure on measuring superconductivity in this device could also have origin in a bad quality of the graphene flake and its contact with the superconductor. Further fabrication tests are necessary in order to determine the reason of this result.

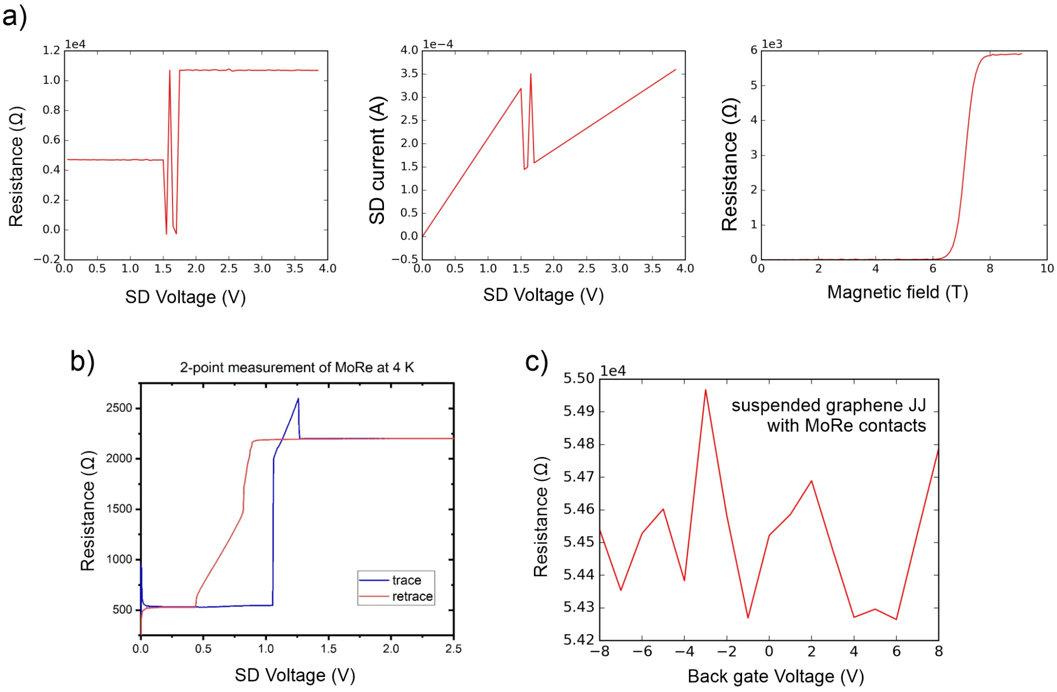

Figure A.4: Superconductivity test of MoRe leads and graphene JJ. a) Left, resistance as a function of the source-drain (SD) voltage for a MoRe lead shows an abrupt jump from zero to 10 kΩ. Middle, the jump can be seen in a plot of the SD current as a function of the SD voltage, to measure I_C at about 0.2 mA. Left, measure of B_C resulting in about 8 T. b) a second measurement of the resistance as a function of SD voltage reveals a hysteretic behaviour associated with the superconducting transition. c) Resistance as a function of the back-gate voltage for a suspended graphene sample with MoRe leads after current annealing does not reveal the charge neutrality point, although there is transport through the graphene channel.

Figure A.4 a) shows the I-V characteristics of a MoRe lead (length of the order of hundreds of µm, width 7 µm, thickness 100 nm) and a measurement of its B_C. As a result, I_C and B_C are about 0.2 mA and 8 T, respectively. Such values are similar as the reported in the literature (see Ref. [216]). Figure A.3 c) shows the results of measuring the JJ devices fabricated with MoRe. It has been found that, although the fabrication of suspended graphene JJ with MoRe contacts is straightforward, it brings other challenges. One of them is shown in Figure A.3 b), where an hysteretic behaviour around the superconducting transition is measured. This constrains the work with the material to much lower and much higher limits of current for defining the system at a superconducting or not superconducting state. Another challenge is that the critical temperature of MoRe is around 7 K, which might sound as a positive aspect if one wishes to study the material without the need of a dilution refrigerator, but it is a disadvantage in order to clean in-situ the graphene in the measuring setup operating at cryogenic temperatures. To avoid the MoRe being superconducting while attempting to clean the graphene in-situ by current annealing, the current annealing process has been tested at room temperature. Although several annealing cycles were possible to implement without destroying the sample, the observation of the saturation point in the annealing curve as well as the CNP in a resistance as a function of the back gate voltage measurement was not achieved. This could be related to a poor quality of the graphene-superconductor contact when using MoRe and requires further investigation. Although further research is needed to implement MoRe as a superconducting contact for free-standing graphene JJs, it is worth noting that a mechanically stable and electrically contacted free-standing graphene structures have been here proven possible to fabricate with MoRe.

A.2 Ultrafast electronic circuit with 1T-TaS$_2$ on a TEM substrate

With the motivation of performing time-resolved ultrafast electronic experiments with 1T-TaS$_2$ at the UTEM setup (see description of the setup in chapter 3), a sample with the characteristics that suit this purpose was designed and fabricated on a TEM substrate. In particular, the sample is designed to be used in an on-chip time-resolved pump-probe spectroscopy scheme [217, 218]. To this aim, the design of the sample follows the guidelines given in Ref. [219], which provides a study of the pulse propagation characteristics in coplanar striplines fabricated on different substrates for experiments that combine femtosecond optics and on-chip electronics to generate electric pulses in the THz domain (1 THz = 10^12 Hz). For the sample prepared within this thesis, the 1T-TaS$_2$ flake is connected by coplanar striplines to a photoconductive semiconductor switch, in a circuit configuration that enables the use of an ultrafast laser to generate sub picosecond pulses of electromagnetic radiation that reach the flake [218, 220, 221]. The novelty of the work presented here is the sample preparation on a TEM substrate, for which some challenges have been encountered and will be discussed below, with a suggestion for an alternative fabrication approach.

Figure A.5 a) shows an optical microscope image of the starting point for the sample fabrication, which is stamping a 1T-TaS$_2$ flake to cover a pinhole placed at the middle of a TEM window. As it can be seen in Figure A.5 b), although it was possible to stamp the 1T-TaS$_2$ flake using the stamping method described in chapter 3, the result is not optimal. Figures A.5 b)-d) show an optical microscope image of the TEM substrate after stamping the flake and immersing the sample in chloroform, following the standard stamping method. The result is a TEM membrane surface with contamination from the stamp, as well as some regions where it looks like the SiNx membrane was damaged. Figure A.5 e)-f) show optical microscope images of the sample after cleaning it for several hours in isopropanol. As it can be seen, the cleaning delivered the formation of contamination clusters extended over the TEM substrate. Since the area around the stamped flake could be cleared, the fabrication of the sample was continued from this point for testing purposes. Figure A.6 a) shows an optical microscope image of the sample after EBL patterning of the coplanar striplines and PVD of 4 nm Ti/40 nm Au. Figure A.6 b) shows a closer image of the striplines connecting the flake. In both images, a layer of PMMA covers the sample for a next EBL step which is perform after evaporating Ti/Au.

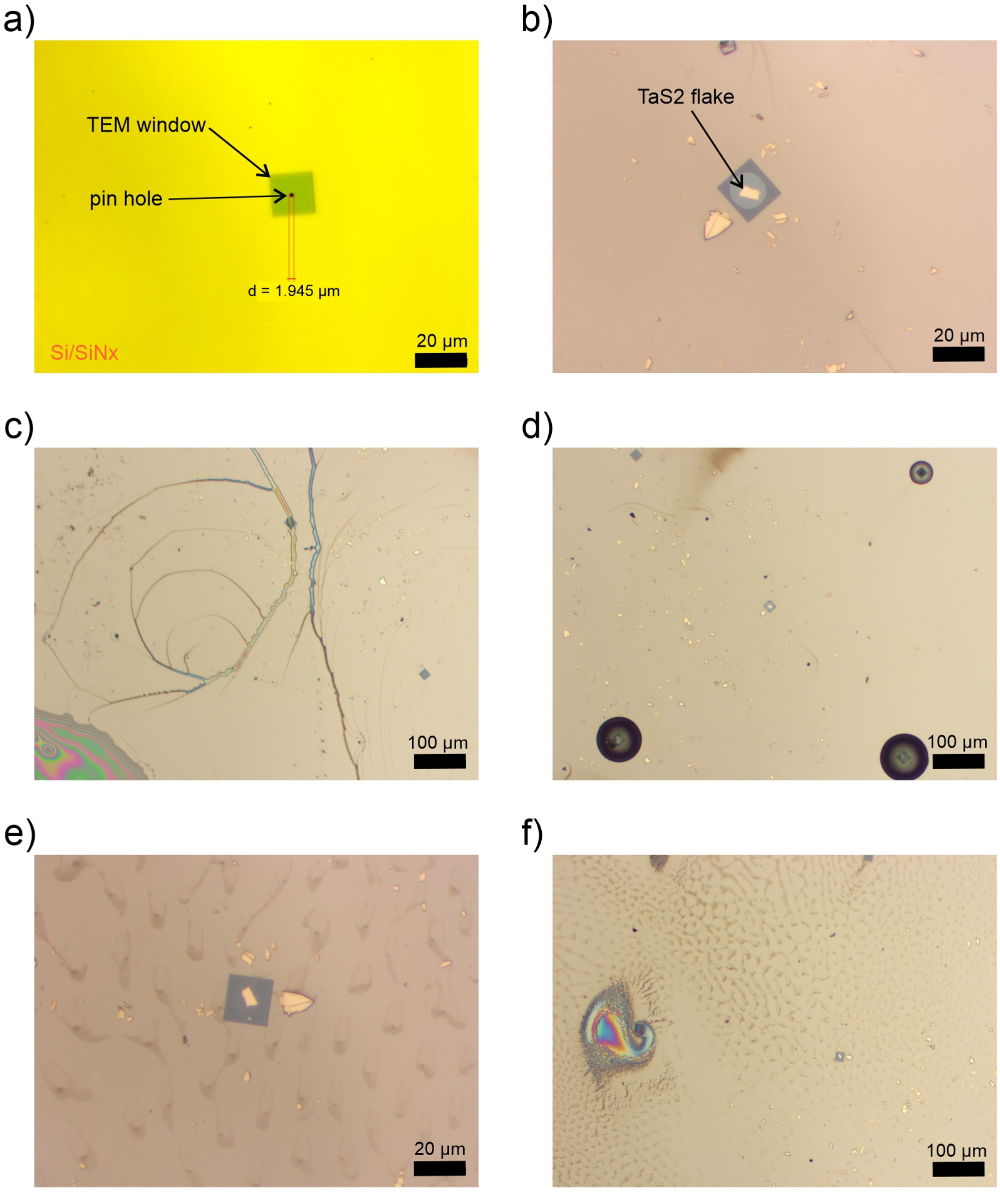

Figure A.5: Optical microscope images before and after stamping a 1T-TaS$_2$ flake on a TEM substrate. a) Image of the clean substrate with the target window having a ~1 µm diameter hole at its centre. b) 1T-TaS$_2$ flake after stamping it on top of the pinhole. c)-d) Overview of the substrate's surface after removing the stamp with chloroform. e)-f) Substrate's surface after cleaning with isopropanol.

Details on the EBL and PVD recipes for this sample are given in chapter 3 of this thesis. Figure A.6 c) shows an optical microscope image of the sample after development of the EBL pattern for the photoconducting switches. As it can be seen on these images, cracks on the PMMA are visible before and after development. This could be attributed to an inhomogeneous PMMA covering of the substrate and can be improved by starting with a cleaner surface of the TEM substrate. Figure A.6 d) shows the result after evaporating Si as the photoconductive switch. One more time, the result is not optimal, in part, because a contaminated substrate was used as a starting point. In spite of that, these results pro-

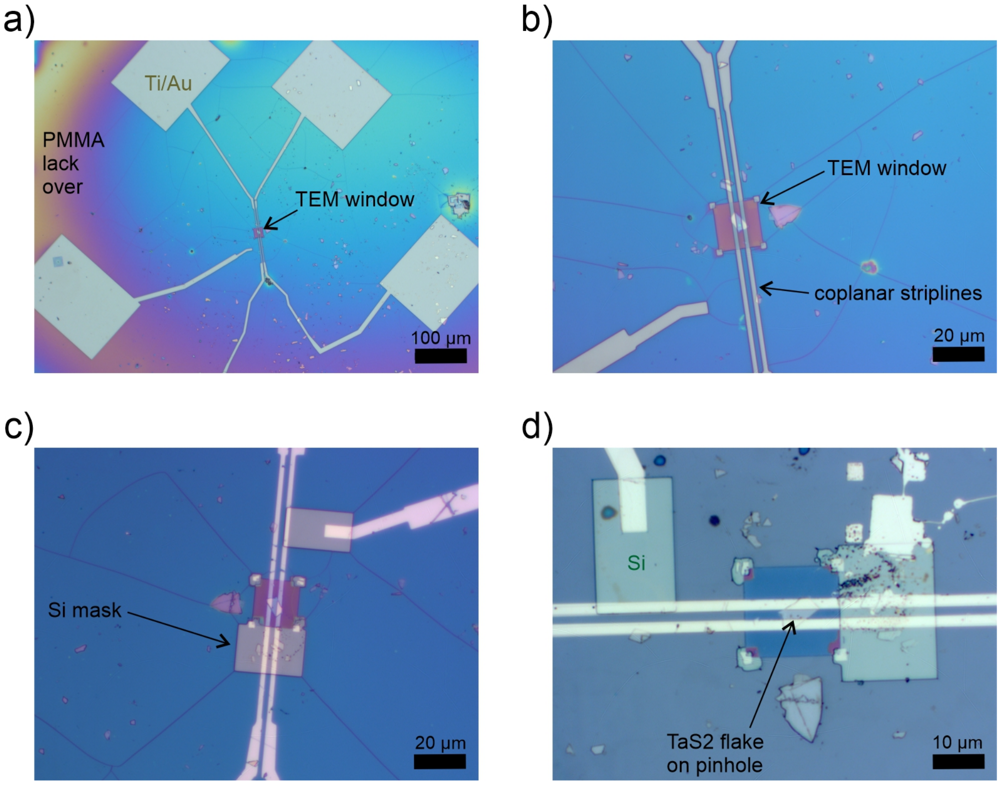

Figure A.6: Optical microscope images of the 1T-TaS_2 ultrafast electronic circuit fabrication. a) PMMA covered substrate after EBL and PVD of metallic contacts for the bond-wiring pads (Ti/Au) to electrically connect the coplanar striplines and the photoconductive switch. b) Closer look at the 1T-TaS_2 surroundings. c) Overview of the substrate after EBL and development of the photoconductive switch mask. d) Final result of the ultrafast electronic circuit after evaporation of Si as photoconductive switches (test structures).

vide a pathway for a successful fabrication of an electronic circuit with coplanar striplines and a photoconductive switch, fabricated on a TEM membrane with a pinhole covered by stamped 1T-TaS_2. Noteworthy, the 1T-TaS_2 flake on this sample is free-standing, as it is placed over a 1 µm diameter hole between the 1 µm separation of the striplines. This is beneficial for a better resolution of the measurements at the UTEM setup, as no additional crystalline or amorphous structure is between the detectors of the setup and the 1T-TaS_2 flake. A suggestion for future fabrication of samples as the presented here is to follow the same procedure, but exfoliating the 1T-TaS_2 flakes directly on the stamp. For instance, by an all-dry viscoelastic stamping technique [173]. This way, the use of PC film is not necessary and the use of chloroform is avoided. This suggestion is based on the observation that chloroform is the only chemical component that has not been used so far for the preparation of 1T-TaS_2 samples on TEM membranes within this thesis, and the results of its use indicate that it could be react with the SiNx membranes.

Bibliography

[1] S. Lebegue and O. Eriksson, “Electronic structure of two-dimensional crystals from ab initio theory,” *Physical Review B*, vol. 79, no. 11, p. 115409, 2009.

[2] K. S. Novoselov, A. K. Geim, S. V. Morozov, D.-e. Jiang, Y. Zhang, S. V. Dubonos, I. V. Grigorieva, and A. A. Firsov, “Electric field effect in atomically thin carbon films,” *science*, vol. 306, no. 5696, pp. 666–669, 2004.

[3] N. Mounet, M. Gibertini, P. Schwaller, D. Campi, A. Merkys, A. Marrazzo, T. Sohier, I. E. Castelli, A. Cepellotti, G. Pizzi, *et al.*, “Two-dimensional materials from high-throughput computational exfoliation of experimentally known compounds,” *Nature nanotechnology*, vol. 13, no. 3, pp. 246–252, 2018.

[4] A. McCreary, O. Kazakova, D. Jariwala, and Z. Y. Al Balushi, “An outlook into the flat land of 2D materials beyond graphene: synthesis, properties and device applications,” *2D Materials*, vol. 8, no. 1, p. 013001, 2020.

[5] K. S. Kim, Y. Zhao, H. Jang, S. Y. Lee, J. M. Kim, K. S. Kim, J.-H. Ahn, P. Kim, J.-Y. Choi, and B. H. Hong, “Large-scale pattern growth of graphene films for stretchable transparent electrodes,” *nature*, vol. 457, no. 7230, pp. 706–710, 2009.

[6] G. Fiori, F. Bonaccorso, G. Iannaccone, T. Palacios, D. Neumaier, A. Seabaugh, S. K. Banerjee, and L. Colombo, “Electronics based on two-dimensional materials,” *Nature nanotechnology*, vol. 9, no. 10, pp. 768–779, 2014.

[7] H. Jang, Y. J. Park, X. Chen, T. Das, M.-S. Kim, and J.-H. Ahn, “Graphene-based flexible and stretchable electronics,” *Advanced Materials*, vol. 28, no. 22, pp. 4184–4202, 2016.

[8] Y.-M. Lin, K. A. Jenkins, A. Valdes-Garcia, J. P. Small, D. B. Farmer, and P. Avouris, “Operation of graphene transistors at gigahertz frequencies,” *Nano letters*, vol. 9, no. 1, pp. 422–426, 2009.

[9] B. Zhan, C. Li, J. Yang, G. Jenkins, W. Huang, and X. Dong, “Graphene field-effect transistor and its application for electronic sensing,” *Small*, vol. 10, no. 20, pp. 4042–4065, 2014.

[10] B. Sensale-Rodriguez, “Graphene-based optoelectronics,” *Journal of Lightwave Technology*, vol. 33, no. 5, pp. 1100–1108, 2015.

[11] F. Bonaccorso, Z. Sun, T. Hasan, and A. Ferrari, “Graphene photonics and optoelectronics,” *Nature photonics*, vol. 4, no. 9, pp. 611–622, 2010.

[12] J. S. Ponraj, Z.-Q. Xu, S. C. Dhanabalan, H. Mu, Y. Wang, J. Yuan, P. Li, S. Thakur, M. Ashrafi, K. Mccoubrey, *et al.*, “Photonics and optoelectronics of two-dimensional materials beyond graphene,” *Nanotechnology*, vol. 27, no. 46, p. 462001, 2016.

[13] W. Han, R. K. Kawakami, M. Gmitra, and J. Fabian, “Graphene spintronics,” *Nature nanotechnology*, vol. 9, no. 10, pp. 794–807, 2014.

[14] X. Lin, W. Yang, K. L. Wang, and W. Zhao, “Two-dimensional spintronics for low-power electronics,” *Nature Electronics*, vol. 2, no. 7, pp. 274–283, 2019.

[15] H. Yang, S. O. Valenzuela, M. Chshiev, S. Couet, B. Dieny, B. Dlubak, A. Fert, K. Garello, M. Jamet, D.-E. Jeong, *et al.*, “Two-dimensional materials prospects for non-volatile spintronic memories,” *Nature*, vol. 606, no. 7915, pp. 663–673, 2022.

[16] R. Raccichini, A. Varzi, S. Passerini, and B. Scrosati, “The role of graphene for electrochemical energy storage,” *Nature materials*, vol. 14, no. 3, pp. 271–279, 2015.

[17] K. Khan, A. K. Tareen, M. Aslam, A. Mahmood, Y. Zhang, Z. Ouyang, Z. Guo, H. Zhang, *et al.*, “Going green with batteries and supercapacitor: Two dimensional materials and their nanocomposites based energy storage applications,” *Progress in solid state chemistry*, vol. 58, p. 100254, 2020.

[18] X. Liu and M. C. Hersam, “2D materials for quantum information science,” *Nature Reviews Materials*, vol. 4, no. 10, pp. 669–684, 2019.

[19] A. H. Castro Neto, F. Guinea, N. M. R. Peres, K. S. Novoselov, and A. K. Geim, "The electronic properties of graphene," *Rev. Mod. Phys.*, vol. 81, pp. 109–162, Jan 2009.

[20] M. Katsnelson, K. Novoselov, and A. Geim, "Chiral tunnelling and the Klein paradox in graphene," *Nature physics*, vol. 2, no. 9, pp. 620–625, 2006.

[21] Y. Cao, V. Fatemi, A. Demir, S. Fang, S. L. Tomarken, J. Y. Luo, J. D. Sanchez-Yamagishi, K. Watanabe, T. Taniguchi, E. Kaxiras, *et al.*, "Correlated insulator behaviour at half-filling in magic-angle graphene superlattices," *Nature*, vol. 556, no. 7699, pp. 80–84, 2018.

[22] Y. Cao, V. Fatemi, S. Fang, K. Watanabe, T. Taniguchi, E. Kaxiras, and P. Jarillo-Herrero, "Unconventional superconductivity in magic-angle graphene superlattices," *Nature*, vol. 556, no. 7699, pp. 43–50, 2018.

[23] M. Yankowitz, S. Chen, H. Polshyn, Y. Zhang, K. Watanabe, T. Taniguchi, D. Graf, A. F. Young, and C. R. Dean, "Tuning superconductivity in twisted bilayer graphene," *Science*, vol. 363, no. 6431, pp. 1059–1064, 2019.

[24] E. C. Regan, D. Wang, C. Jin, M. I. Bakti Utama, B. Gao, X. Wei, S. Zhao, W. Zhao, Z. Zhang, K. Yumigeta, *et al.*, "Mott and generalized Wigner crystal states in WSe2/WS2 moiré superlattices," *Nature*, vol. 579, no. 7799, pp. 359–363, 2020.

[25] L. An, X. Cai, D. Pei, M. Huang, Z. Wu, Z. Zhou, J. Lin, Z. Ying, Z. Ye, X. Feng, *et al.*, "Interaction effects and superconductivity signatures in twisted double-bilayer WSe 2," *Nanoscale horizons*, vol. 5, no. 9, pp. 1309–1316, 2020.

[26] L. Wang, E.-M. Shih, A. Ghiotto, L. Xian, D. A. Rhodes, C. Tan, M. Claassen, D. M. Kennes, Y. Bai, B. Kim, *et al.*, "Correlated electronic phases in twisted bilayer transition metal dichalcogenides," *Nature materials*, vol. 19, no. 8, pp. 861–866, 2020.

[27] Y. Tang, L. Li, T. Li, Y. Xu, S. Liu, K. Barmak, K. Watanabe, T. Taniguchi, A. H. MacDonald, J. Shan, *et al.*, "Simulation of Hubbard model physics in WSe2/WS2 moiré superlattices," *Nature*, vol. 579, no. 7799, pp. 353–358, 2020.

[28] R. Bistritzer and A. H. MacDonald, "Moiré bands in twisted double-layer graphene," *Proceedings of the National Academy of Sciences*, vol. 108, no. 30, pp. 12233–12237, 2011.

[29] A. Kerelsky, C. Rubio-Verdú, L. Xian, D. M. Kennes, D. Halbertal, N. Finney, L. Song, S. Turkel, L. Wang, K. Watanabe, *et al.*, "Moiréless correlations in ABCA graphene," *Proceedings of the National Academy of Sciences*, vol. 118, no. 4, p. e2017366118, 2021.

[30] G. Li, A. Luican, J. Lopes dos Santos, A. Castro Neto, A. Reina, J. Kong, and E. Andrei, "Observation of Van Hove singularities in twisted graphene layers," *Nature physics*, vol. 6, no. 2, pp. 109–113, 2010.

[31] L. Van Hove, "The occurrence of singularities in the elastic frequency distribution of a crystal," *Physical Review*, vol. 89, no. 6, p. 1189, 1953.

[32] F. Zhang, B. Sahu, H. Min, and A. H. MacDonald, "Band structure of A B C-stacked graphene trilayers," *Physical Review B*, vol. 82, no. 3, p. 035409, 2010.

[33] F. Zhang, J. Jung, G. A. Fiete, Q. Niu, and A. H. MacDonald, "Spontaneous quantum Hall states in chirally stacked few-layer graphene systems," *Physical review letters*, vol. 106, no. 15, p. 156801, 2011.

[34] F. Zhang, "Spontaneous chiral symmetry breaking in bilayer graphene," *Synthetic Metals*, vol. 210, pp. 9–18, 2015.

[35] H. Min and A. H. MacDonald, "Electronic structure of multilayer graphene," *Progress of Theoretical Physics Supplement*, vol. 176, pp. 227–252, 2008.

[36] M. Koshino, "Interlayer screening effect in graphene multilayers with ABA and ABC stacking," *Physical Review B*, vol. 81, no. 12, p. 125304, 2010.

[37] H. Zhou, T. Xie, T. Taniguchi, K. Watanabe, and A. F. Young, "Superconductivity in rhombohedral trilayer graphene," *Nature*, vol. 598, no. 7881, pp. 434–438, 2021.

[38] H. Zhou, T. Xie, A. Ghazaryan, T. Holder, J. R. Ehrets, E. M. Spanton, T. Taniguchi, K. Watanabe, E. Berg, M. Serbyn, *et al.*, "Half-and quarter-metals in rhombohedral trilayer graphene," *Nature*, vol. 598, no. 7881, pp. 429–433, 2021.

[39] Y. Lee, D. Tran, K. Myhro, J. Velasco, N. Gillgren, C. Lau, Y. Barlas, J. Poumirol, D. Smirnov, and F. Guinea, "Competition between spontaneous symmetry breaking and single-particle gaps in trilayer graphene," *Nature communications*, vol. 5, no. 1, pp. 1–5, 2014.

[40] Y. Shi, S. Xu, Y. Yang, S. Slizovskiy, S. V. Morozov, S.-K. Son, S. Ozdemir, C. Mullan, J. Barrier, J. Yin, *et al.*, "Electronic phase separation in multilayer rhombohedral graphite," *Nature*, vol. 584, no. 7820, pp. 210–214, 2020.

[41] H. Henck, J. Avila, Z. B. Aziza, D. Pierucci, J. Baima, B. Pamuk, J. Chaste, D. Utt, M. Bartos, K. Nogajewski, *et al.*, "Flat electronic bands in long sequences of rhombohedral-stacked graphene," *Physical Review B*, vol. 97, no. 24, p. 245421, 2018.

[42] H. Min, G. Borghi, M. Polini, and A. H. MacDonald, "Pseudospin magnetism in graphene," *Physical Review B*, vol. 77, no. 4, p. 041407, 2008.

[43] F. Zhang, H. Min, M. Polini, and A. MacDonald, "Spontaneous inversion symmetry breaking in graphene bilayers," *Physical Review B*, vol. 81, no. 4, p. 041402, 2010.

[44] J. Martin, B. E. Feldman, R. T. Weitz, M. T. Allen, and A. Yacoby, "Local compressibility measurements of correlated states in suspended bilayer graphene," *Physical review letters*, vol. 105, no. 25, p. 256806, 2010.

[45] R. T. Weitz, M. T. Allen, B. E. Feldman, J. Martin, and A. Yacoby, "Broken-symmetry states in doubly gated suspended bilayer graphene," *Science*, vol. 330, no. 6005, pp. 812–816, 2010.

[46] F. R. Geisenhof, F. Winterer, A. M. Seiler, J. Lenz, T. Xu, F. Zhang, and R. T. Weitz, "Quantum anomalous Hall octet driven by orbital magnetism in bilayer graphene," *Nature*, vol. 598, no. 7879, pp. 53–58, 2021.

[47] Y. Shi, S. Che, K. Zhou, S. Ge, Z. Pi, T. Espiritu, T. Taniguchi, K. Watanabe, Y. Barlas, R. Lake, *et al.*, "Tunable Lifshitz transitions and multiband transport in tetralayer graphene," *Physical review letters*, vol. 120, no. 9, p. 096802, 2018.

[48] K. I. Bolotin, K. J. Sikes, Z. Jiang, M. Klima, G. Fudenberg, J. Hone, P. Kim, and H. L. Stormer, "Ultrahigh electron mobility in suspended graphene," *Solid state communications*, vol. 146, no. 9-10, pp. 351–355, 2008.

[49] T. Wehling, E. Şaşıoğlu, C. Friedrich, A. Lichtenstein, M. Katsnelson, and S. Blügel, "Strength of effective coulomb interactions in graphene and graphite," *Physical review letters*, vol. 106, no. 23, p. 236805, 2011.

[50] B. Sipos, A. F. Kusmartseva, A. Akrap, H. Berger, L. Forró, and E. Tutiš, "From Mott state to superconductivity in 1T-TaS$_2$," *Nature materials*, vol. 7, no. 12, pp. 960–965, 2008.

[51] T.-R. T. Han, F. Zhou, C. D. Malliakas, P. M. Duxbury, S. D. Mahanti, M. G. Kanatzidis, and C.-Y. Ruan, "Exploration of metastability and hidden phases in correlated electron crystals visualized by femtosecond optical doping and electron crystallography," *Science advances*, vol. 1, no. 5, p. e1400173, 2015.

[52] T. Ritschel, J. Trinckauf, G. Garbarino, M. Hanfland, M. v. Zimmermann, H. Berger, B. Büchner, and J. Geck, "Pressure dependence of the charge density wave in 1T-TaS 2 and its relation to superconductivity," *Physical Review B*, vol. 87, no. 12, p. 125135, 2013.

[53] M. Yoshida, R. Suzuki, Y. Zhang, M. Nakano, and Y. Iwasa, "Memristive phase switching in two-dimensional 1T-TaS2 crystals," *Science advances*, vol. 1, no. 9, p. e1500606, 2015.

[54] A. Mohammadzadeh, A. Rehman, F. Kargar, S. Rumyantsev, J. Smulko, W. Knap, R. Lake, and A. Balandin, "Room temperature depinning of the charge-density waves in quasi-two-dimensional 1T-TaS2 devices," *Applied Physics Letters*, vol. 118, no. 22, p. 223101, 2021.

[55] A. K. Geim and K. S. Novoselov, "The rise of graphene," in *Nanoscience and technology: a collection of reviews from nature journals*, pp. 11–19, World Scientific, 2010.

[56] S. Z. Butler, S. M. Hollen, L. Cao, Y. Cui, J. A. Gupta, H. R. Gutiérrez, T. F. Heinz, S. S. Hong, J. Huang, A. F. Ismach, *et al.*, "Progress, challenges, and opportunities in two-dimensional materials beyond graphene," *ACS nano*, vol. 7, no. 4, pp. 2898–2926, 2013.

[57] H. R. Gutiérrez, "Two-dimensional layered materials offering expanded applications in flatland," 2020.

[58] M. I. Katsnelson, "Graphene: carbon in two dimensions," *Materials today*, vol. 10, no. 1-2, pp. 20–27, 2007.

[59] N. D. Mermin, "Crystalline order in two dimensions," *Physical Review*, vol. 176, no. 1, p. 250, 1968.

[60] P. R. Wallace, "The Band Theory of Graphite," *Phys. Rev.*, vol. 71, pp. 622–634, May 1947.

[61] C. Beenakker, "Colloquium: Andreev reflection and Klein tunneling in graphene," *Reviews of Modern Physics*, vol. 80, no. 4, p. 1337, 2008.

[62] D. DiVincenzo and E. Mele, "Self-consistent effective-mass theory for intralayer screening in graphite intercalation compounds," *Physical Review B*, vol. 29, no. 4, p. 1685, 1984.

[63] G. W. Semenoff, "Condensed-matter simulation of a three-dimensional anomaly," *Physical Review Letters*, vol. 53, no. 26, p. 2449, 1984.

[64] M. V. Berry, “Quantal phase factors accompanying adiabatic changes,” *Proceedings of the Royal Society of London. A. Mathematical and Physical Sciences*, vol. 392, no. 1802, pp. 45–57, 1984.

[65] E. McCann and M. Koshino, “The electronic properties of bilayer graphene,” *Reports on Progress in physics*, vol. 76, no. 5, p. 056503, 2013.

[66] E. McCann and V. I. Fal’ko, “Landau-level degeneracy and quantum Hall effect in a graphite bilayer,” *Physical review letters*, vol. 96, no. 8, p. 086805, 2006.

[67] J. Slonczewski and P. Weiss, “Band structure of graphite,” *Physical Review*, vol. 109, no. 2, p. 272, 1958.

[68] J. McClure, “Band structure of graphite and de Haas-van Alphen effect,” *Physical Review*, vol. 108, no. 3, p. 612, 1957.

[69] K. S. Novoselov, E. McCann, S. Morozov, V. I. Fal’ko, M. Katsnelson, U. Zeitler, D. Jiang, F. Schedin, and A. Geim, “Unconventional quantum Hall effect and Berry’s phase of 2π in bilayer graphene,” *Nature physics*, vol. 2, no. 3, pp. 177–180, 2006.

[70] G. Mikitik and Y. V. Sharlai, “Electron energy spectrum and the Berry phase in a graphite bilayer,” *Physical Review B*, vol. 77, no. 11, p. 113407, 2008.

[71] E. McCann, D. S. Abergel, and V. I. Fal’ko, “Electrons in bilayer graphene,” *Solid state communications*, vol. 143, no. 1-2, pp. 110–115, 2007.

[72] T. Ando, T. Nakanishi, and R. Saito, “Berry’s phase and absence of back scattering in carbon nanotubes,” *Journal of the Physical Society of Japan*, vol. 67, no. 8, pp. 2857–2862, 1998.

[73] F. Guinea, A. C. Neto, and N. Peres, “Electronic states and Landau levels in graphene stacks,” *Physical Review B*, vol. 73, no. 24, p. 245426, 2006.

[74] K. Myhro, S. Che, Y. Shi, Y. Lee, K. Thilahar, K. Bleich, D. Smirnov, and C. Lau, “Large tunable intrinsic gap in rhombohedral-stacked tetralayer graphene at half filling,” *2D Materials*, vol. 5, no. 4, p. 045013, 2018.

[75] M. Koshino and E. McCann, “Trigonal warping and Berry’s phase N π in ABC-stacked multilayer graphene,” *Physical Review B*, vol. 80, no. 16, p. 165409, 2009.

[76] J. L. Mañes, F. Guinea, and M. A. Vozmediano, “Existence and topological stability of Fermi points in multilayered graphene,” *Physical Review B*, vol. 75, no. 15, p. 155424, 2007.

[77] M. Aoki and H. Amawashi, “Dependence of band structures on stacking and field in layered graphene,” *Solid State Communications*, vol. 142, no. 3, pp. 123–127, 2007.

[78] M. Koshino and E. McCann, “Gate-induced interlayer asymmetry in ABA-stacked trilayer graphene,” *Physical Review B*, vol. 79, no. 12, p. 125443, 2009.

[79] H. Min and A. H. MacDonald, “Chiral decomposition in the electronic structure of graphene multilayers,” *Physical Review B*, vol. 77, no. 15, p. 155416, 2008.

[80] S. Slizovskiy, E. McCann, M. Koshino, and V. I. Fal’ko, “Films of rhombohedral graphite as two-dimensional topological semimetals,” *Communications Physics*, vol. 2, no. 1, pp. 1–10, 2019.

[81] L. Zhang, Y. Zhang, J. Camacho, M. Khodas, and I. Zaliznyak, “The experimental observation of quantum Hall effect of l= 3 chiral quasiparticles in trilayer graphene,” *Nature Physics*, vol. 7, no. 12, pp. 953–957, 2011.

[82] F. Zhang, H. Min, and A. MacDonald, “Competing ordered states in bilayer graphene,” *Physical Review B*, vol. 86, no. 15, p. 155128, 2012.

[83] S. Manzeli, D. Ovchinnikov, D. Pasquier, O. V. Yazyev, and A. Kis, “2D transition metal dichalcogenides,” *Nature Reviews Materials*, vol. 2, no. 8, pp. 1–15, 2017.

[84] Q. H. Wang, K. Kalantar-Zadeh, A. Kis, J. N. Coleman, and M. S. Strano, “Electronics and optoelectronics of two-dimensional transition metal dichalcogenides,” *Nature nanotechnology*, vol. 7, no. 11, pp. 699–712, 2012.

[85] K. Rossnagel, “On the origin of charge-density waves in select layered transition-metal dichalcogenides,” *Journal of Physics: Condensed Matter*, vol. 23, no. 21, p. 213001, 2011.

[86] Y. Ding, Y. Wang, J. Ni, L. Shi, S. Shi, and W. Tang, “First principles study of structural, vibrational and electronic properties of graphene-like MX2 (M= Mo, Nb, W, Ta; X= S, Se, Te) monolayers,” *Physica B: Condensed Matter*, vol. 406, no. 11, pp. 2254–2260, 2011.

[87] C. Ataca, H. Sahin, and S. Ciraci, “Stable, single-layer MX2 transition-metal oxides and dichalcogenides in a honeycomb-like structure,” *The Journal of Physical Chemistry C*, vol. 116, no. 16, pp. 8983–8999, 2012.

[88] K. Kam and B. Parkinson, “Detailed photocurrent spectroscopy of the semiconducting group VIB transition metal dichalcogenides,” *The Journal of Physical Chemistry*, vol. 86, no. 4, pp. 463–467, 1982.

[89] A. Kuc, N. Zibouche, and T. Heine, “Influence of quantum confinement on the electronic structure of the transition metal sulfide T S 2,” *Physical Review B*, vol. 83, no. 24, p. 245213, 2011.

[90] K. Kobayashi and J. Yamauchi, “Electronic structure and scanning-tunneling-microscopy image of molybdenum dichalcogenide surfaces,” *Physical Review B*, vol. 51, no. 23, p. 17085, 1995.

[91] T. Li and G. Galli, “Electronic properties of MoS_2 nanoparticles,” *The Journal of Physical Chemistry C*, vol. 111, no. 44, pp. 16192–16196, 2007.

[92] L. Liu, S. B. Kumar, Y. Ouyang, and J. Guo, “Performance limits of monolayer transition metal dichalcogenide transistors,” *IEEE Transactions on Electron Devices*, vol. 58, no. 9, pp. 3042–3047, 2011.

[93] M. Bernardi, M. Palummo, and J. C. Grossman, “Extraordinary sunlight absorption and one nanometer thick photovoltaics using two-dimensional monolayer materials,” *Nano letters*, vol. 13, no. 8, pp. 3664–3670, 2013.

[94] Z. Hu, Y. Ding, X. Hu, W. Zhou, X. Yu, and S. Zhang, “Recent progress in 2D group IV–IV monochalcogenides: synthesis, properties and applications,” *Nanotechnology*, vol. 30, no. 25, p. 252001, 2019.

[95] A. Y. Joe, L. A. Jauregui, K. Pistunova, A. M. M. Valdivia, Z. Lu, D. S. Wild, G. Scuri, K. De Greve, R. J. Gelly, Y. Zhou, *et al.*, “Electrically controlled emission from singlet and triplet exciton species in atomically thin light-emitting diodes,” *Physical Review B*, vol. 103, no. 16, p. L161411, 2021.

[96] A.-J. Cho, K. C. Park, and J.-Y. Kwon, “A high-performance complementary inverter based on transition metal dichalcogenide field-effect transistors,” *Nanoscale research letters*, vol. 10, no. 1, pp. 1–6, 2015.

[97] B. Das, D. Sen, and S. Mahapatra, “Tuneable quantum spin Hall states in confined 1T’transition metal dichalcogenides,” *Scientific reports*, vol. 10, no. 1, pp. 1–13, 2020.

[98] S. Wu, V. Fatemi, Q. D. Gibson, K. Watanabe, T. Taniguchi, R. J. Cava, and P. Jarillo-Herrero, “Observation of the quantum spin Hall effect up to 100 kelvin in a monolayer crystal,” *Science*, vol. 359, no. 6371, pp. 76–79, 2018.

[99] X. Qian, J. Liu, L. Fu, and J. Li, “Quantum spin Hall effect in two-dimensional transition metal dichalcogenides,” *Science*, vol. 346, no. 6215, pp. 1344–1347, 2014.

[100] K. Xu, P. Chen, X. Li, C. Wu, Y. Guo, J. Zhao, X. Wu, and Y. Xie, “Ultrathin nanosheets of vanadium diselenide: a metallic two-dimensional material with ferromagnetic charge-density-wave behavior,” *Angewandte Chemie*, vol. 125, no. 40, pp. 10671–10675, 2013.

[101] D. Voiry, H. Yamaguchi, J. Li, R. Silva, D. C. Alves, T. Fujita, M. Chen, T. Asefa, V. B. Shenoy, G. Eda, *et al.*, “Enhanced catalytic activity in strained chemically exfoliated WS2 nanosheets for hydrogen evolution,” *Nature materials*, vol. 12, no. 9, pp. 850–855, 2013.

[102] D. Sakabe, Z. Liu, K. Suenaga, K. Nakatsugawa, and S. Tanda, “Direct observation of mono-layer, bi-layer, and tri-layer charge density waves in 1T-TaS2 by transmission electron microscopy without a substrate,” *npj Quantum Materials*, vol. 2, no. 1, pp. 1–6, 2017.

[103] A. W. Tsen, R. Hovden, D. Wang, Y. D. Kim, J. Okamoto, K. A. Spoth, Y. Liu, W. Lu, Y. Sun, J. C. Hone, *et al.*, “Structure and control of charge density waves in two-dimensional 1T-TaS2,” *Proceedings of the National Academy of Sciences*, vol. 112, no. 49, pp. 15054–15059, 2015.

[104] E. H. Hall *et al.*, “On a new action of the magnet on electric currents,” *American Journal of Mathematics*, vol. 2, no. 3, pp. 287–292, 1879.

[105] D. Tong, “The quantum hall effect. TIFR infosys lectures,” *arXiv preprint arXiv:1606.06687*, 2016.

[106] K. Von Klitzing, “The quantized Hall effect,” *Reviews of Modern Physics*, vol. 58, no. 3, p. 519, 1986.

[107] H. L. Stormer, “Nobel lecture: the fractional quantum Hall effect,” *Reviews of Modern Physics*, vol. 71, no. 4, p. 875, 1999.

[108] K. v. Klitzing, G. Dorda, and M. Pepper, “New method for high-accuracy determination of the fine-structure constant based on quantized Hall resistance,” *Physical review letters*, vol. 45, no. 6, p. 494, 1980.

[109] D. A. Abanin and L. S. Levitov, “Conformal invariance and shape-dependent conductance of graphene samples,” *Physical Review B*, vol. 78, no. 3, p. 035416, 2008.

[110] J. R. Williams, D. A. Abanin, L. DiCarlo, L. S. Levitov, and C. M. Marcus, “Quantum Hall conductance of two-terminal graphene devices,” *Physical Review B*, vol. 80, no. 4, p. 045408, 2009.

[111] B. Jeckelmann and B. Jeanneret, “The quantum Hall effect as an electrical resistance standard,” *Reports on Progress in Physics*, vol. 64, no. 12, p. 1603, 2001.

[112] E. McCann, “Electronic properties of monolayer and bilayer graphene,” in *Graphene nanoelectronics*, pp. 237–275, Springer, 2011.

[113] Y. Barlas, K. Yang, and A. MacDonald, “Quantum Hall effects in graphene-based two-dimensional electron systems,” *Nanotechnology*, vol. 23, no. 5, p. 052001, 2012.

[114] Y. Barlas, R. Côté, K. Nomura, and A. MacDonald, “Intra-Landau-level cyclotron resonance in bilayer graphene,” *Physical Review Letters*, vol. 101, no. 9, p. 097601, 2008.

[115] Y. Lee, D. Tran, K. Myhro, J. Velasco Jr, N. Gillgren, J. Poumirol, D. Smirnov, Y. Barlas, and C. Lau, “Multicomponent quantum hall ferromagnetism and landau level crossing in rhombohedral trilayer graphene,” *Nano Letters*, vol. 16, no. 1, pp. 227–231, 2016.

[116] F. Zhang, D. Tilahun, and A. H. MacDonald, “Hund’s rules for the n= 0 landau levels of trilayer graphene,” *Physical Review B*, vol. 85, no. 16, p. 165139, 2012.

[117] M. Vojta, “Quantum phase transitions,” *Reports on Progress in Physics*, vol. 66, no. 12, p. 2069, 2003.

[118] S. Sachdev, “Quantum phase transitions,” *Physics world*, vol. 12, no. 4, p. 33, 1999.

[119] F. Krauss and D. Maitre, “Lecture 3: Phase transitions.” Available at `https://www.ippp.dur.ac.uk/%7Ekrauss/Lectures/NumericalMethods/PhaseTransitions/Lecture/pt3.html`.

[120] D. Yamamoto, T. Ozaki, C. A. S. de Melo, and I. Danshita, “First-order phase transition and anomalous hysteresis of bose gases in optical lattices,” *Physical Review A*, vol. 88, no. 3, p. 033624, 2013.

[121] V. Piazza, V. Pellegrini, F. Beltram, W. Wegscheider, T. Jungwirth, and A. H. MacDonald, “First-order phase transitions in a quantum Hall ferromagnet,” *Nature*, vol. 402, no. 6762, pp. 638–641, 1999.

[122] V. N. Kotov, B. Uchoa, V. M. Pereira, F. Guinea, and A. C. Neto, “Electron-electron interactions in graphene: Current status and perspectives,” *Reviews of modern physics*, vol. 84, no. 3, p. 1067, 2012.

[123] D. Xiao, M.-C. Chang, and Q. Niu, “Berry phase effects on electronic properties,” *Reviews of modern physics*, vol. 82, no. 3, p. 1959, 2010.

[124] R. Nandkishore and L. Levitov, “Dynamical screening and excitonic instability in bilayer graphene,” *Physical review letters*, vol. 104, no. 15, p. 156803, 2010.

[125] F. Zhang, J. Jung, and A. H. MacDonald, “Spontaneous quantum Hall states and novel luttinger liquids in chiral graphene,” in *Journal of Physics: Conference Series*, vol. 334, p. 012002, IOP Publishing, 2011.

[126] J. Velasco, L. Jing, W. Bao, Y. Lee, P. Kratz, V. Aji, M. Bockrath, C. Lau, C. Varma, R. Stillwell, *et al.*, “Transport spectroscopy of symmetry-broken insulating states in bilayer graphene,” *Nature nanotechnology*, vol. 7, no. 3, pp. 156–160, 2012.

[127] F. Freitag, M. Weiss, R. Maurand, J. Trbovic, and C. Schönenberger, “Spin symmetry of the bilayer graphene ground state,” *Physical Review B*, vol. 87, no. 16, p. 161402, 2013.

[128] Y. Lee, S. Che, J. Velasco Jr, X. Gao, Y. Shi, D. Tran, J. Baima, F. Mauri, M. Calandra, M. Bockrath, *et al.*, “Gate-tunable magnetism and giant magnetoresistance in suspended rhombohedral-stacked few-layer graphene,” *Nano Letters*, vol. 22, no. 13, pp. 5094–5099, 2022.

[129] G. Grüner, “The dynamics of charge-density waves,” *Reviews of modern physics*, vol. 60, no. 4, p. 1129, 1988.

[130] D. Graf, E. Choi, J. Brooks, M. Matos, R. Henriques, and M. Almeida, “High magnetic field induced charge density wave state in a quasi-one-dimensional organic conductor,” *Physical review letters*, vol. 93, no. 7, p. 076406, 2004.

[131] S. Pan, A. De Lozanne, and R. Fainchtein, “Scanning tunneling microscopy of quasi-one-dimensional organic conductors,” *Journal of Vacuum Science & Technology B: Microelectronics and Nanometer Structures Processing, Measurement, and Phenomena*, vol. 9, no. 2, pp. 1017–1021, 1991.

[132] J. Schäfer, E. Rotenberg, S. D. Kevan, P. Blaha, R. Claessen, and R. Thorne, “High-Temperature Symmetry Breaking in the Electronic Band Structure of the Quasi-One-Dimensional Solid NbSe3,” *Physical Review Letters*, vol. 87, no. 19, p. 196403, 2001.

[133] J. Wilson, F. Di Salvo, and S. Mahajan, "Charge-density waves in metallic, layered, transition-metal dichalcogenides," *Physical review letters*, vol. 32, no. 16, p. 882, 1974.

[134] J. A. Wilson, F. Di Salvo, and S. Mahajan, "Charge-density waves and superlattices in the metallic layered transition metal dichalcogenides," *Advances in Physics*, vol. 24, no. 2, pp. 117–201, 1975.

[135] P. Fazekas and E. Tosatti, "Charge carrier localization in pure and doped 1T-TaS2," *Physica B+ C*, vol. 99, no. 1-4, pp. 183–187, 1980.

[136] L. Stojchevska, I. Vaskivskyi, T. Mertelj, P. Kusar, D. Svetin, S. Brazovskii, and D. Mihailovic, "Ultrafast switching to a stable hidden quantum state in an electronic crystal," *Science*, vol. 344, no. 6180, pp. 177–180, 2014.

[137] I. Vaskivskyi, J. Gospodaric, S. Brazovskii, D. Svetin, P. Sutar, E. Goreshnik, I. A. Mihailovic, T. Mertelj, and D. Mihailovic, "Controlling the metal-to-insulator relaxation of the metastable hidden quantum state in 1T-TaS2," *Science advances*, vol. 1, no. 6, p. e1500168, 2015.

[138] Q. Stahl, M. Kusch, F. Heinsch, G. Garbarino, N. Kretzschmar, K. Hanff, K. Rossnagel, J. Geck, and T. Ritschel, "Collapse of layer dimerization in the photo-induced hidden state of 1T-TaS2," *Nature communications*, vol. 11, no. 1, pp. 1–7, 2020.

[139] Y. A. Gerasimenko, P. Karpov, I. Vaskivskyi, S. Brazovskii, and D. Mihailovic, "Intertwined chiral charge orders and topological stabilization of the light-induced state of a prototypical transition metal dichalcogenide," *npj Quantum Materials*, vol. 4, no. 1, pp. 1–9, 2019.

[140] Y. A. Gerasimenko, I. Vaskivskyi, M. Litskevich, J. Ravnik, J. Vodeb, M. Diego, V. Kabanov, and D. Mihailovic, "Quantum jamming transition to a correlated electron glass in 1t-tas2," *Nature materials*, vol. 18, no. 10, pp. 1078–1083, 2019.

[141] Y. Yu, F. Yang, X. F. Lu, Y. J. Yan, Y.-H. Cho, L. Ma, X. Niu, S. Kim, Y.-W. Son, D. Feng, *et al.*, "Gate-tunable phase transitions in thin flakes of 1T-TaS2," *Nature nanotechnology*, vol. 10, no. 3, pp. 270–276, 2015.

[142] I. Vaskivskyi, I. Mihailovic, S. Brazovskii, J. Gospodaric, T. Mertelj, D. Svetin, P. Sutar, and D. Mihailovic, "Fast electronic resistance switching involving hidden charge density wave states," *Nature communications*, vol. 7, no. 1, pp. 1–6, 2016.

[143] K. S. Novoselov, D. Jiang, F. Schedin, T. Booth, V. Khotkevich, S. Morozov, and A. K. Geim, "Two-dimensional atomic crystals," *Proceedings of the National Academy of Sciences*, vol. 102, no. 30, pp. 10451–10453, 2005.

[144] P. Blake, E. Hill, A. Castro Neto, K. Novoselov, D. Jiang, R. Yang, T. Booth, and A. Geim, "Making graphene visible," *Applied physics letters*, vol. 91, no. 6, p. 063124, 2007.

[145] M. Altissimo, "E-beam lithography for micro-/nanofabrication," *Biomicrofluidics*, vol. 4, no. 2, p. 026503, 2010.

[146] R. R. Nair, P. Blake, A. N. Grigorenko, K. S. Novoselov, T. J. Booth, T. Stauber, N. M. Peres, and A. K. Geim, "Fine structure constant defines visual transparency of graphene," *science*, vol. 320, no. 5881, pp. 1308–1308, 2008.

[147] L. A. Lyon, C. D. Keating, A. P. Fox, B. E. Baker, L. He, S. R. Nicewarner, S. P. Mulvaney, and M. J. Natan, "Raman spectroscopy," *Analytical Chemistry*, vol. 70, no. 12, pp. 341–362, 1998.

[148] R. Krishnan and R. Shankar, "Raman effect: History of the discovery," *Journal of Raman Spectroscopy*, vol. 10, no. 1, pp. 1–8, 1981.

[149] A. C. Ferrari and D. M. Basko, "Raman spectroscopy as a versatile tool for studying the properties of graphene," *Nature nanotechnology*, vol. 8, no. 4, pp. 235–246, 2013.

[150] A. C. Ferrari, "Raman spectroscopy of graphene and graphite: Disorder, electron–phonon coupling, doping and nonadiabatic effects," *Solid state communications*, vol. 143, no. 1-2, pp. 47–57, 2007.

[151] C. Casiraghi, "Doping dependence of the Raman peaks intensity of graphene close to the Dirac point," *Physical Review B*, vol. 80, no. 23, p. 233407, 2009.

[152] T. A. Nguyen, J.-U. Lee, D. Yoon, and H. Cheong, "Excitation energy dependent Raman signatures of ABA-and ABC-stacked few-layer graphene," *Scientific reports*, vol. 4, no. 1, pp. 1–5, 2014.

[153] Y. Hao, Y. Wang, L. Wang, Z. Ni, Z. Wang, R. Wang, C. K. Koo, Z. Shen, and J. T. Thong, "Probing layer number and stacking order of few-layer graphene by Raman spectroscopy," *small*, vol. 6, no. 2, pp. 195–200, 2010.

[154] C. H. Lui, Z. Li, Z. Chen, P. V. Klimov, L. E. Brus, and T. F. Heinz, "Imaging stacking order in few-layer graphene," *Nano letters*, vol. 11, no. 1, pp. 164–169, 2011.

[155] K. G. Wirth, J. B. Hauck, A. Rothstein, H. Kyoseva, D. Siebenkotten, L. Conrads, L. Klebl, A. Fischer, B. Beschoten, C. Stampfer, *et al.*, "Experimental observation of ABCB stacked tetralayer graphene," *ACS nano*, 2022.

[156] L. Ju, Z. Shi, N. Nair, Y. Lv, C. Jin, J. Velasco, C. Ojeda-Aristizabal, H. A. Bechtel, M. C. Martin, A. Zettl, *et al.*, "Topological valley transport at bilayer graphene domain walls," *Nature*, vol. 520, no. 7549, pp. 650–655, 2015.

[157] F. R. Geisenhof, F. Winterer, A. M. Seiler, J. Lenz, I. Martin, and R. T. Weitz, "Interplay between topological valley and quantum Hall edge transport," *Nature Communications*, vol. 13, no. 1, pp. 1–7, 2022.

[158] A. Rasmussen and V. Deckert, "New dimension in nano-imaging: breaking through the diffraction limit with scanning near-field optical microscopy," *Analytical and bioanalytical chemistry*, vol. 381, no. 1, pp. 165–172, 2005.

[159] G. Jeong, B. Choi, D.-S. Kim, S. Ahn, B. Park, J. H. Kang, H. Min, B. H. Hong, and Z. H. Kim, "Mapping of Bernal and non-Bernal stacking domains in bilayer graphene using infrared nanoscopy," *Nanoscale*, vol. 9, no. 12, pp. 4191–4195, 2017.

[160] D.-S. Kim, H. Kwon, A. Y. Nikitin, S. Ahn, L. Martin-Moreno, F. J. Garcia-Vidal, S. Ryu, H. Min, and Z. H. Kim, "Stacking structures of few-layer graphene revealed by phase-sensitive infrared nanoscopy," *ACS nano*, vol. 9, no. 7, pp. 6765–6773, 2015.

[161] J. A. Robinson, M. LaBella, M. Zhu, M. Hollander, R. Kasarda, Z. Hughes, K. Trumbull, R. Cavalero, and D. Snyder, "Contacting graphene," *Applied Physics Letters*, vol. 98, no. 5, p. 053103, 2011.

[162] W. Li, Y. Liang, D. Yu, L. Peng, K. P. Pernstich, T. Shen, A. Hight Walker, G. Cheng, C. A. Hacker, C. A. Richter, *et al.*, "Ultraviolet/ozone treatment to reduce metal-graphene contact resistance," *Applied Physics Letters*, vol. 102, no. 18, p. 183110, 2013.

[163] C. Wei Chen, F. Ren, G.-C. Chi, S.-C. Hung, Y. Huang, J. Kim, I. I. Kravchenko, and S. J. Pearton, "UV ozone treatment for improving contact resistance on graphene," *Journal of Vacuum Science & Technology B, Nanotechnology and Microelectronics: Materials, Processing, Measurement, and Phenomena*, vol. 30, no. 6, p. 060604, 2012.

[164] P. Walker and W. H. Tarn, *CRC handbook of metal etchants.* CRC press, 1990.

[165] LeicaMicrosystems, "Brief introduction to Critical Point Drying." Available at `https://www.leica-microsystems.com/science-lab/brief-introduction-to-critical-point-drying/`.

[166] J. Moser, A. Barreiro, and A. Bachtold, "Current-induced cleaning of graphene," *Applied Physics Letters*, vol. 91, no. 16, p. 163513, 2007.

[167] S. Tanaka, H. Goto, H. Tomori, Y. Ootuka, K. Tsukagoshi, and A. Kanda, "Effect of current annealing on electronic properties of multilayer graphene," in *Journal of Physics: Conference Series*, vol. 232, p. 012015, IOP Publishing, 2010.

[168] F. Pobell, *Matter and methods at low temperatures.* Springer Science & Business Media, 2007.

[169] F. S. Winterer, *Spontaneous symmetry-breaking in trilayer graphene.* PhD thesis, lmu, 2021.

[170] Norcada, "Norcada's TEM window array with 9 windows on a single frame for multiple analyses." Available at `https://www.norcada.com/products/nitride-windows-tem/`.

[171] P. Zomer, M. Guimarães, J. Brant, N. Tombros, and B. Van Wees, "Fast pick up technique for high quality heterostructures of bilayer graphene and hexagonal boron nitride," *Applied Physics Letters*, vol. 105, no. 1, p. 013101, 2014.

[172] D. Purdie, N. Pugno, T. Taniguchi, K. Watanabe, A. Ferrari, and A. Lombardo, "Cleaning interfaces in layered materials heterostructures," *Nature communications*, vol. 9, no. 1, pp. 1–12, 2018.

[173] A. Castellanos-Gomez, M. Buscema, R. Molenaar, V. Singh, L. Janssen, H. S. Van Der Zant, and G. A. Steele, "Deterministic transfer of two-dimensional materials by all-dry viscoelastic stamping," *2D Materials*, vol. 1, no. 1, p. 011002, 2014.

[174] R. W. Stark, T. Drobek, and W. M. Heckl, "Tapping-mode atomic force microscopy and phase-imaging in higher eigenmodes," *Applied Physics Letters*, vol. 74, no. 22, pp. 3296–3298, 1999.

[175] A. Feist, N. Bach, N. R. da Silva, T. Danz, M. Möller, K. E. Priebe, T. Domröse, J. G. Gatzmann, S. Rost, J. Schauss, *et al.*, "Ultrafast transmission electron microscopy using a laser-driven field emitter: Femtosecond resolution with a high coherence electron beam," *Ultramicroscopy*, vol. 176, pp. 63–73, 2017.

[176] T. Danz, T. Domröse, and C. Ropers, "Ultrafast nanoimaging of the order parameter in a structural phase transition," *Science*, vol. 371, no. 6527, pp. 371–374, 2021.

[177] C. Scruby, P. Williams, and G. Parry, "The role of charge density waves in structural transformations of 1T-TaS2," *Philosophical Magazine*, vol. 31, no. 2, pp. 255–274, 1975.

[178] H. van Elferen, A. Veligura, N. Tombros, E. Kurganova, B. Van Wees, J. Maan, and U. Zeitler, "Fine structure of the lowest landau level in suspended trilayer graphene," *Physical Review B*, vol. 88, no. 12, p. 121302, 2013.

[179] W. Bao, Z. Zhao, H. Zhang, G. Liu, P. Kratz, L. Jing, J. Velasco Jr, D. Smirnov, and C. N. Lau, "Magnetoconductance oscillations and evidence for fractional quantum hall states in suspended bilayer and trilayer graphene," *Physical Review Letters*, vol. 105, no. 24, p. 246601, 2010.

[180] G. Chen, A. L. Sharpe, P. Gallagher, I. T. Rosen, E. J. Fox, L. Jiang, B. Lyu, H. Li, K. Watanabe, T. Taniguchi, *et al.*, "Signatures of tunable superconductivity in a trilayer graphene moiré superlattice," *Nature*, vol. 572, no. 7768, pp. 215–219, 2019.

[181] X. Zhang, K.-T. Tsai, Z. Zhu, W. Ren, Y. Luo, S. Carr, M. Luskin, E. Kaxiras, and K. Wang, "Correlated insulating states and transport signature of superconductivity in twisted trilayer graphene superlattices," *Physical review letters*, vol. 127, no. 16, p. 166802, 2021.

[182] A. M. Seiler, F. R. Geisenhof, F. Winterer, K. Watanabe, T. Taniguchi, T. Xu, F. Zhang, and R. T. Weitz, "Quantum cascade of correlated phases in trigonally warped bilayer graphene," *Nature*, vol. 608, no. 7922, pp. 298–302, 2022.

[183] F. D. M. Haldane, "Model for a quantum hall effect without landau levels: Condensed-matter realization of the" parity anomaly"," *Physical review letters*, vol. 61, no. 18, p. 2015, 1988.

[184] S. Raghu, X.-L. Qi, C. Honerkamp, and S.-C. Zhang, "Topological mott insulators," *Physical review letters*, vol. 100, no. 15, p. 156401, 2008.

[185] P. Maher, C. R. Dean, A. F. Young, T. Taniguchi, K. Watanabe, K. L. Shepard, J. Hone, and P. Kim, "Evidence for a spin phase transition at charge neutrality in bilayer graphene," *Nature Physics*, vol. 9, no. 3, pp. 154–158, 2013.

[186] F. Freitag, J. Trbovic, M. Weiss, and C. Schönenberger, "Spontaneously gapped ground state in suspended bilayer graphene," *Physical review letters*, vol. 108, no. 7, p. 076602, 2012.

[187] W. Bao, J. Velasco Jr, F. Zhang, L. Jing, B. Standley, D. Smirnov, M. Bockrath, A. H. MacDonald, and C. N. Lau, "Evidence for a spontaneous gapped state in ultraclean bilayer graphene," *Proceedings of the National Academy of Sciences*, vol. 109, no. 27, pp. 10802–10805, 2012.

[188] R. Côté, M. Rondeau, A.-M. Gagnon, and Y. Barlas, "Phase diagram of insulating crystal and quantum hall states in abc-stacked trilayer graphene," *Physical Review B*, vol. 86, no. 12, p. 125422, 2012.

[189] I. L. Aleiner, P. W. Brouwer, and L. I. Glazman, "Quantum effects in coulomb blockade," *Physics Reports*, vol. 358, no. 5-6, pp. 309–440, 2002.

[190] F. Sols, F. Guinea, and A. C. Neto, "Coulomb blockade in graphene nanoribbons," *Physical Review Letters*, vol. 99, no. 16, p. 166803, 2007.

[191] Y. Nam, D.-K. Ki, D. Soler-Delgado, and A. F. Morpurgo, "A family of finite-temperature electronic phase transitions in graphene multilayers," *Science*, vol. 362, no. 6412, pp. 324–328, 2018.

[192] M. He, Y.-H. Zhang, Y. Li, Z. Fei, K. Watanabe, T. Taniguchi, X. Xu, and M. Yankowitz, "Competing correlated states and abundant orbital magnetism in twisted monolayer-bilayer graphene," *Nature Communications*, vol. 12, no. 1, pp. 1–8, 2021.

[193] C. Pfleiderer, "Why first order quantum phase transitions are interesting," *Journal of Physics: Condensed Matter*, vol. 17, no. 11, p. S987, 2005.

[194] W. Wang, D. Dietzel, and A. Schirmeisen, "Lattice discontinuities of 1T-TaS2 across first order charge density wave phase transitions," *Scientific reports*, vol. 9, no. 1, pp. 1–7, 2019.

[195] H. Lin, W. Huang, K. Zhao, S. Qiao, Z. Liu, J. Wu, X. Chen, and S.-H. Ji, "Scanning tunneling spectroscopic study of monolayer 1T-TaS2 and 1T-TaSe2," *Nano Research*, vol. 13, no. 1, pp. 133–137, 2020.

[196] A. K. Geremew, S. Rumyantsev, F. Kargar, B. Debnath, A. Nosek, M. A. Bloodgood, M. Bockrath, T. T. Salguero, R. K. Lake, and A. A. Balandin, "Bias-voltage driven switching of the charge-density-wave and normal metallic phases in 1T-TaS2 thin-film devices," *ACS nano*, vol. 13, no. 6, pp. 7231–7240, 2019.

[197] A. Mohammadzadeh, S. Baraghani, S. Yin, F. Kargar, J. P. Bird, and A. A. Balandin, "Evidence for a thermally driven charge-density-wave transition in 1T-TaS2 thin-film devices: Prospects for GHz switching speed," *Applied Physics Letters*, vol. 118, no. 9, p. 093102, 2021.

[198] L. Ma, C. Ye, Y. Yu, X. F. Lu, X. Niu, S. Kim, D. Feng, D. Tománek, Y.-W. Son, X. H. Chen, *et al.*, "A metallic mosaic phase and the origin of Mott-insulating state in 1T-TaS2," *Nature communications*, vol. 7, no. 1, pp. 1–8, 2016.

[199] A. J. Frenzel, A. S. McLeod, D. Z.-R. Wang, Y. Liu, W. Lu, G. Ni, A. W. Tsen, Y. Sun, A. N. Pasupathy, and D. Basov, "Infrared nanoimaging of the metal-insulator transition in the charge-density-wave van der Waals material 1T-TaS2," *Physical Review B*, vol. 97, no. 3, p. 035111, 2018.

[200] M. Yoshida, Y. Zhang, J. Ye, R. Suzuki, Y. Imai, S. Kimura, A. Fujiwara, and Y. Iwasa, "Controlling charge-density-wave states in nano-thick crystals of 1T-TaS2," *Scientific reports*, vol. 4, no. 1, pp. 1–5, 2014.

[201] C. Zhu, Y. Chen, F. Liu, S. Zheng, X. Li, A. Chaturvedi, J. Zhou, Q. Fu, Y. He, Q. Zeng, *et al.*, "Light-tunable 1T-TaS2 charge-density-wave oscillators," *ACS nano*, vol. 12, no. 11, pp. 11203–11210, 2018.

[202] D. R. Lide, *CRC handbook of chemistry and physics*, vol. 85. CRC press, 2004.

[203] B. Josephson, "Coupled superconductors," *Reviews of Modern Physics*, vol. 36, no. 1, p. 216, 1964.

[204] K. Likharev, "Superconducting weak links," *Reviews of Modern Physics*, vol. 51, no. 1, p. 101, 1979.

[205] M. Titov and C. W. Beenakker, "Josephson effect in ballistic graphene," *Physical Review B*, vol. 74, no. 4, p. 041401, 2006.

[206] X. Du, I. Skachko, and E. Y. Andrei, "Josephson current and multiple Andreev reflections in graphene SNS junctions," *Physical Review B*, vol. 77, no. 18, p. 184507, 2008.

[207] T. Li, J. C. Gallop, L. Hao, and E. J. Romans, "Josephson penetration depth in coplanar junctions based on 2d materials," *Journal of Applied Physics*, vol. 126, no. 17, p. 173901, 2019.

[208] H. B. Heersche, P. Jarillo-Herrero, J. B. Oostinga, L. M. Vandersypen, and A. F. Morpurgo, "Bipolar supercurrent in graphene," *Nature*, vol. 446, no. 7131, pp. 56–59, 2007.

[209] T. Li, J. Gallop, L. Hao, and E. Romans, "Ballistic josephson junctions based on cvd graphene," *Superconductor Science and Technology*, vol. 31, no. 4, p. 045004, 2018.

[210] G.-H. Lee, D. K. Efetov, W. Jung, L. Ranzani, E. D. Walsh, T. A. Ohki, T. Taniguchi, K. Watanabe, P. Kim, D. Englund, *et al.*, "Graphene-based Josephson junction microwave bolometer," *Nature*, vol. 586, no. 7827, pp. 42–46, 2020.

[211] A. W. Draelos, M.-T. Wei, A. Seredinski, H. Li, Y. Mehta, K. Watanabe, T. Taniguchi, I. V. Borzenets, F. Amet, and G. Finkelstein, "Supercurrent flow in multiterminal graphene Josephson junctions," *Nano letters*, vol. 19, no. 2, pp. 1039–1043, 2019.

[212] F. Amet, C. T. Ke, I. V. Borzenets, J. Wang, K. Watanabe, T. Taniguchi, R. S. Deacon, M. Yamamoto, Y. Bomze, S. Tarucha, *et al.*, "Supercurrent in the quantum Hall regime," *Science*, vol. 352, no. 6288, pp. 966–969, 2016.

[213] M. T. Allen, O. Shtanko, I. C. Fulga, J. I.-J. Wang, D. Nurgaliev, K. Watanabe, T. Taniguchi, A. R. Akhmerov, P. Jarillo-Herrero, L. S. Levitov, *et al.*, "Observation of electron coherence and Fabry–perot standing waves at a graphene edge," *Nano Letters*, vol. 17, no. 12, pp. 7380–7386, 2017.

[214] N. Mizuno, B. Nielsen, and X. Du, "Ballistic-like supercurrent in suspended graphene Josephson weak links," *Nature communications*, vol. 4, no. 1, pp. 1–6, 2013.

[215] M. Tomi, M. R. Samatov, A. S. Vasenko, A. Laitinen, P. Hakonen, and D. S. Golubev, "Joule heating effects in high-transparency Josephson junctions," *Physical Review B*, vol. 104, no. 13, p. 134513, 2021.

[216] M. Aziz, D. Christopher Hudson, and S. Russo, "Molybdenum-rhenium superconducting suspended nanostructures," *Applied Physics Letters*, vol. 104, no. 23, p. 233102, 2014.

[217] C. Karnetzky, P. Zimmermann, C. Trummer, C. Duque Sierra, M. Wörle, R. Kienberger, and A. Holleitner, "Towards femtosecond on-chip electronics based on plasmonic hot electron nano-emitters," *Nature communications*, vol. 9, no. 1, pp. 1–7, 2018.

[218] P. Gallagher, C.-S. Yang, T. Lyu, F. Tian, R. Kou, H. Zhang, K. Watanabe, T. Taniguchi, and F. Wang, "Quantum-critical conductivity of the Dirac fluid in graphene," *Science*, vol. 364, no. 6436, pp. 158–162, 2019.

[219] N. Fernandez, P. Zimmermann, P. Zechmann, M. Wörle, R. Kienberger, and A. Holleitner, "Toward femtosecond electronics up to 10 THz," in *Ultrafast Phenomena and Nanophotonics XXIII*, vol. 10916, pp. 63–73, SPIE, 2019.

[220] D. H. Auston, K. Cheung, J. Valdmanis, and D. Kleinman, "Cherenkov radiation from femtosecond optical pulses in electro-optic media," *Physical Review Letters*, vol. 53, no. 16, p. 1555, 1984.

[221] P. U. Jepsen, R. H. Jacobsen, and S. Keiding, "Generation and detection of terahertz pulses from biased semiconductor antennas," *JOSA B*, vol. 13, no. 11, pp. 2424–2436, 1996.

Abbreviations

Term	*Description*	*Term*	*Description*
2D	Two-dimmensional	s-SNOM	Scattering-type Scanning Near-Field Optical Microscopy
TMD	Transition-metal dichalcogenide	FWHM	Full Width at Half Maximum
CDW	Charge density wave	AFM	Atomic Force Microscope
TEM	Transmission Electron Microscopy	NIR	Near Infrared
C	Commensurate	e-beam	electron beam
NC	Nearly-commensurate	BOE	Buffered oxide etchant
IC	Incommensurate	SEM	Scanning Electron Microscopy
QHE	Quantum Hall effect	MIBK	Metyl isobutyl keton
LL	Landau level	IPA	Isopropanol
SWM	Slonczewski-Weiss-McClure	CPD	Critical point dryer
2DEG	Two-dimmensional electron gas	CNP	Charge neutrality point
2DES	Two-dimmensional electron system	PLD	Periodic lattice distorsion
D	Displacement field	FIB	Focused Ion Beam
n	Charge carrier density	PDMS	Polydimethylsiloxane
B	Magnetic field	PC	Polycarbonate
V_B	Bottom gate voltage	DF	Dark-field
V_T	Top gate voltage	UTEM	Ultrafast Transmission Electron Microscopy
$B_\parallel$	In-plane magnetic field	CCR	Closed-cycle refrigerator
$B_\perp$	Out-of-plane magnetic field	JJ	Josephson junction
G	Differential conductance	MoRe	Molybdenum Rhenium
ν	Filling factor	T_C	Critical temperature
EBL	Electron Beam Lithography	B_C	Critical magnetic field
PVD	Physical Vapor Deposition	I_C	Critical current

Acknowledgments

I would like to take this opportunity to express my most sincere gratitude to all the people who accompanied and supported me during my doctorate.

I am thankful to my supervisor Prof. Thomas Weitz for giving me the chance to work at his group, for his scientific insight, for the freedom to explore own ideas within my research topics and for his support and career advice. Also, thanks to Prof. Claus Ropers for the collaborative work, which has been an extremely valuable experience.

I am grateful to all members of my doctoral examination committee, especially to Prof. Thomas Weitz and Prof. Alexander Urban for reviewing this thesis.

I am also very grateful to Prof. Ignacio Cirac, for being a mentor whose guidance has helped me learn to overcome many challenges and stay on track to pursue my academic goals. I would also like to thank the International Max Planck Research School for Quantum Science and Technology (IMPRS-QST) for the opportunity of starting my doctoral thesis. In particular, to Sonya Gzyl, for her help and support to the IMPRS-QST students.

Many thanks as well to Philipp Altpeter and Christian Obermayer, who were always there to help immediately with any problems in the cleanroom at LMU. To Philipp Altpeter, in addition, for the discussions about sample fabrication techniques and for his support when trying out new ideas. To Mike Kanbach and Joachim Herbst, for their help on the technical matters in the cleanroom of the Universitiy of Göttingen. As well, to the technical team of the I. Physical Institute of the University of Göttingen, in particular, Uta Filippich, Kai Dörner, Carsten Mahn and Simon Stoldt, for being there to help when needed.

A big thank goes to my colleagues at the AG Weitz, for the great time during the past years. In particular, to Felix Winterer, Fabian Geisenhof, Lisa Walter, Jakob Lenz, James Borchert, Jakob Pöhls, Anna Seiler, Martin Statz, Lukas Renn, Chirstian Eckel and Francesca Falorsi. In addition, to Marco Dembecki, Daniela Priesack, Jakob, Gilles Rodway-Gant, Daniel Vitroler, Jonas Schröder, David Urbaniak and Monica Kolek Martinez de Azagra. Thank you all for the great work atmosphere, for the scientific discussions and coffee breaks, for lifting each other's spirits through the ups and downs of the laboratory work, for the delicious cakes and the fond memories, both in Munich as well as in Göttingen. Also, to Till Domröse from the AG Ropers for the work together.

Finally, a special thanks to my closest friends, to my family and to Daniel, for their love and support over the past years. Without you, this work would have not been possible.